Material flow in a silicon furnace



Matthew Shirley
St Anne's College
University of Oxford

A thesis submitted for the degree of
Doctor of Philosophy

Michaelmas 2022

Acknowledgements

Firstly, I would like to thank my academic supervisors Colin Please, Jim Oliver, and Madeleine Moore for all their guidance, encouragement, insight, and for being so generous with your time over the past four years.

I would also like to thank my industrial supervisors Harry Reynolds, Ben Sloman, Anne-Gry Messenlein, and Aasgeir Valderhaug at Elkem ASA for their insight, support, and continual drive to ensure my work is grounded in reality. I am also grateful to them and everyone else at Elkem who have made me feel so welcome on my visits to Norway.

I am grateful to Chris Breward and Colin Please for creating and running the InFoMM CDT which has played such a large role in turning me into the mathematician that I am today. I would also like to thank everyone else in OCIAM and InFoMM who have made the Maths Institute such an amazing environment to be in, both when working and not. In particular, Edwina Yeo, Helen Saville, Michael Negus, and Amy Kent, your friendship has been one of the best parts of these past four years, and is one of the main reasons I managed to reach this point.

Finally, thanks to my parents and Helen for all your unwavering love, support, and belief in me throughout everything.

Abstract

Silicon is produced in silicon furnaces through a series of chemical reactions, between the solid raw materials, which form a mixture called the charge material, and solid and gaseous intermediate products. The early stages of this process occur near the top of the furnace, when newly added cold charge material, moving downwards as the material below is consumed, meet hot gases flowing upwards, resulting in several exothermic chemical reactions occurring. The behaviour of silicon furnaces is therefore the result of a counter-current flow of gases and solids, and the heat transfer and mass transfer between them. This complicated coupling means that, generally, previous studies of silicon furnaces have either focused exclusively on modelling the flow of material, or on chemical and thermal effects, rather than the coupled behaviour.

In this thesis, we develop a model for the coupled behaviour, based on the idealisation of the microstructure of the charge material as a series of gas channels, filled with a binary gas mixture and surrounded by an impermeable solid. As laminar non-isothermal compressible flow through a channel is a relatively unstudied problem, we first investigate the flow of a single species of non-reacting gas, subject to an imposed wall temperature, by comparing the behaviour of full numerical simulations to the predictions of reduced models, derived using industrially relevant parameter values. We then build on this framework to solve numerically a simplified version of the model of the charge material. By considering the limit where viscous forces across the gas channels dominate, we are able to solve the problem using asymptotic methods to study the effect of a strongly temperature-dependent reaction rate.

The results of our model allow us to give new insight into important, industrially relevant questions about silicon furnaces, namely: the relationship between the flux of gas and the pressure in furnace; the rate of heat exchange between the gases and solid; and the effect of reactions on the gas flow.

Contents

1 Introduction **1**

1.1 Silicon production process and silicon furnaces . . . 3

1.1.1 Structure of the furnace . . . 3

1.1.2 Chemistry in the furnace . . . 4

1.2 Previous models of silicon furnaces . . . 7

1.3 Counter-current flows . . . 8

1.4 Compressible gas flow in channels . . . 9

1.5 Summary of the rest of the thesis . . . 11

1.6 Statement of originality . . . 12

2 Mathematical model of the charge material in a silicon furnace **13**

2.1 Problem formulation . . . 13

2.1.1 Gas channel . . . 15

2.1.1.1 Conservation of mass . . . 15

2.1.1.2 Conservation of momentum . . . 16

2.1.1.3 Conservation of energy . . . 19

2.1.1.4 Equation of state . . . 20

2.1.2 Solid . . . 21

2.1.3 Boundary conditions . . . 22

2.1.3.1 Charge-surface boundary . . . 22

2.1.3.2 Charge-crater boundary . . . 22

2.1.3.3 Interface . . . 23

2.1.3.4 Periodicity . . . 27

2.1.4 Fluxes . . . 27

2.1.5 Summary of the dimensional model . . . 28

2.2 Nondimensionalisation . . . 29

2.2.1 Scalings . . . 29

2.2.2 Dimensionless gas governing equations . . . 33

2.2.3 Dimensionless solid model 35
2.2.4 Dimensionless boundary conditions 37
2.2.5 Dimensionless fluxes 38
2.3 Discussion 39

3 Non-isothermal compressible flow in a narrow channel driven by a small pressure drop 40
3.1 A two-dimensional model of a single-phase gas 41
3.1.1 Two-dimensional geometry 41
3.1.2 Simplification of the model of the charge material 42
3.1.3 Problem statement 44
3.1.4 Numerical solution 46
3.2 Reduced single-phase models 46
3.2.1 Case I: Large reduced Reynolds number 47
3.2.2 Case II: Order unity reduced Reynolds number 48
3.2.3 Reformulation and numerical solution of cases I and II 50
3.2.4 Case III: Small reduced Reynolds number 52
3.2.4.1 $O(1)$ solution 53
3.2.4.2 $O(\epsilon^2 \mathrm{Re})$ solution 55
3.2.4.3 Behaviour of the mass flux 57
3.2.4.4 Behaviour of the energy flux 59
3.3 Results 61
3.3.1 Solutions comparison 61
3.3.2 Mass flux 65
3.3.3 Energy transfer 74
3.3.4 Varying the Prandtl number 77
3.4 Discussion 78

4 Counter-current flow of reacting gases and solids 81
4.1 Problem formulation 82
4.1.1 Simplifications 82
4.1.1.1 Geometry 82
4.1.1.2 Parameter sizes 83
4.1.2 Reduced solid model 86
4.1.3 Reduced gas model 88
4.1.4 Fluxes, efficiencies and averages 89
4.1.5 Simplification of the coupled model 92

4.2 Numerical solution . . . 92
4.2.1 Transformed problem . . . 92
4.2.1.1 Gas . . . 92
4.2.1.2 Solid . . . 94
4.2.2 Numerical scheme . . . 94
4.2.3 Shooting problem . . . 95
4.3 Coupled problem . . . 99
4.3.1 Results with reactions . . . 99
4.3.2 Results without reactions . . . 102
4.4 Prescribed solid temperature . . . 110
4.5 Discussion . . . 117

5 Counter-current flow of gases and solids in the small reduced Reynolds number limit 121
5.1 Assumptions . . . 121
5.2 Slow reactions model . . . 123
5.2.1 Reduction to a one-dimensional model . . . 124
5.2.2 No reactions solution . . . 131
5.2.3 General solution . . . 134
5.3 Fast reactions model . . . 138
5.3.1 Region I . . . 141
5.3.2 Region III . . . 142
5.3.3 Region II . . . 144
5.3.4 Solution to the outer problems . . . 150
5.4 Discussion . . . 153

6 Discussion 155
6.1 Summary of results . . . 155
6.2 Future work . . . 157
6.3 Industrial implications . . . 160

A Physical properties of CO, SiO, and gas mixtures 164
A.1 Kinetic gas theory for transport coefficients . . . 164
A.1.1 Viscosity . . . 165
A.1.2 Thermal conductivity . . . 166
A.1.3 Binary diffusion coefficient . . . 167
A.2 Specific heat capacity . . . 167

B Dimensionless governing equations for the gas in cylindrical coordinates **169**

C Finite difference schemes for solving reduced models **171**

C.1 Methodology 171

C.1.1 Gas 171

C.1.2 Solid 173

C.1.3 Initial conditions 174

C.2 Validation 174

D Special case of slow reaction asymptotic analysis **177**

Bibliography **180**

Chapter 1

Introduction

Silicon (Si) is a key material in the manufacture of many modern products including semiconductors, photovoltaic devices, and a range of metal alloys [67]. It is produced in submerged arc furnaces (SAFs), operated by metallurgical companies such as Elkem ASA, through a series of chemical reactions between solid raw materials and gaseous intermediate products. Similar processes also occur in SAFs used in the production of ferro-silicon [67], titanium oxide [38], and phosphorus [66], although we will focus on silicon production in this thesis. A schematic of the silicon production process, centred around a SAF, is shown in Figure 1.1. A medium-sized silicon furnace will have a height around 3 m and an internal diameter of 9 m. The electrical input into the furnace, allowing the endothermic silicon creating reactions to occur, will be between 15 to 45 MW, and the material in the furnace will reach temperatures over 2300 K [33].

The motivation for this thesis is to gain a greater understanding of the processes occurring within silicon producing SAFs and, in particular, the role of the flow of gas. For efficient furnace operation, it is important to manage the rate at which different reactions occur in the furnace, so that the amounts of the different chemical species remain in the correct ratio. Moreover, these reactions must occur at the correct location so that the reactants for all reactions are able to meet. The gas flow is important for this as silicon monoxide gas (SiO) is a key reactant in many reactions. Since the reactions in the furnace are strongly temperature-dependent, understanding the temperature distribution of the raw materials is also crucial for predicting where reactions occur, and hence managing furnace operation. In much of the furnace, it is the flow of hot gases created by reactions at the bottom of the furnace that is responsible for heating up the material, either directly through heat transfer, or indirectly by reacting with the raw materials in exothermic reactions [67].

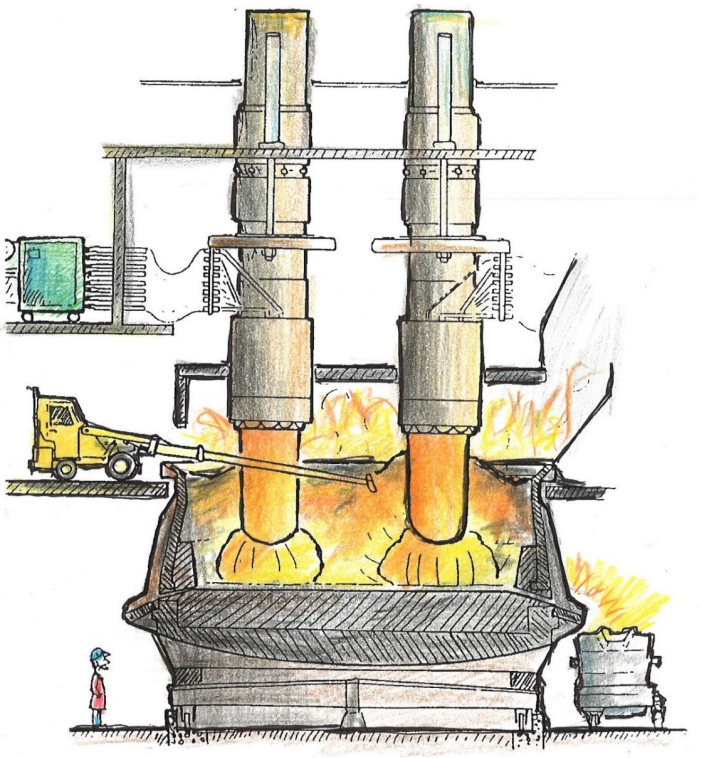


Figure 1.1: Schematic drawing of an operational silicon furnace [28].

The gas flow is therefore strongly coupled to both the thermal and chemical processes of the furnace, and so crucial to understanding its behaviour.

Since the extreme conditions inside the furnace make measurements of the interior almost impossible, previous studies of silicon furnaces (which we discuss in more detail in Section 1.2), have used mathematical models to gain insight into their behaviour. However, these previous studies have largely focused on the heat transfer, mass transfer, and electrical behaviour in the furnace, or considered the gas flow in isolation. The goal of this thesis is to improve upon these models by solving for the realistic behaviour of a compressible gas mixture in the furnace, coupled to the movement of the solid, temperature distribution, and exothermic chemical reactions. In particular, we focus on a model for the gas flow in the pore-space between the particles of raw material, idealised as a channel extending the entire height of the furnace. Using the results of this detailed mesoscale model, we to aim to identify the key physical and chemical processes governing the gas behaviour and its coupling with the other processes in the furnace, allowing for a more complete understanding, which can help its incorporation into macroscale model of the entire silicon production process in future.

The remainder of this first chapter is structured as follows. In Section 1.1, we will describe the silicon production process, and the challenges faced by furnace operators in greater detail. Then, in Section 1.2, we will discuss previous models of silicon furnaces. We also discuss the broader context of so-called 'counter-current' processes in Section 1.3. Due to its relevance to our modelling approach, in Section 1.4, we review previous work on compressible flows in a channel. We finish in Section 1.5 by outlining the structure of the remaining chapters of the thesis.

1.1 Silicon production process and silicon furnaces

1.1.1 Structure of the furnace

A simplified diagram of the structure inside a silicon furnace, typical of those used by Elkem ASA within the silicon production process, is given in Figure 1.2, with the main regions labelled. Solid raw materials are added at the top of the furnace. These raw materials, consisting of quartz rock (SiO_2), carbon-rich coal, and woodchips (both C), together form a granular mixture called the *charge material*. Energy for the endothermic, silicon creating chemical reactions is provided by an electric current passed into the charge material by an *arc* created by carbon *electrodes* in the furnace, with a furnace normally containing three electrodes arranged in a triangle [67]. The current heats up the material through Ohmic heating, with temperatures over 2300 K measured [67]. The endothermic reactions consume solid material near the bottom of the furnace, leading to a continuous downwards motion of the charge material, and also create hot gases which flow upwards through the charge material, and then escape out the top of the furnace [67]. The silicon created by the reactions flows downwards into a pool at the bottom the furnace, before being extracted from the furnace through a *taphole* [33, 63]. Around the base of each electrode a gas-filled cavity called the *crater* forms [36, 67].

As previously mentioned, there is a lack of measurements of the interior of silicon furnaces during operation, meaning that the majority of information about the internal structure comes from the excavation of shutdown furnaces. These excavations, described in [36], lead to diagrams such as Figure 1.3, which depicts the composition of the charge material in different regions of the furnace. However, such excavations can only provide limited insight into the operational behaviour, meaning mathematical modelling provides an important tool for understanding silicon furnaces.

For the work in this thesis, there does exist one set of measurements of the interior of the furnace, reported in [31, 33], which are of particular interest in developing

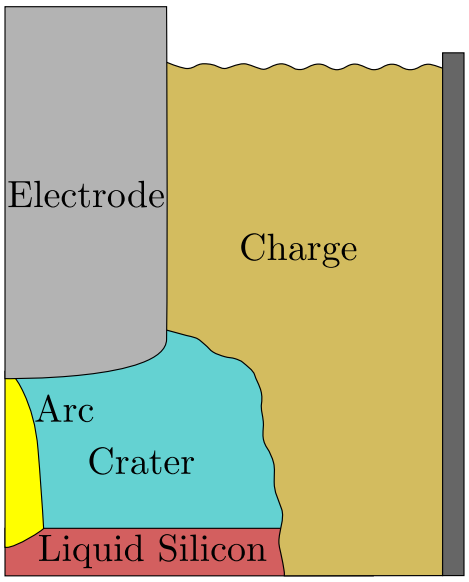


Figure 1.2: Schematic of a silicon furnace.

our model, as they give measurements of the pressure in the crater during normal operation. They find that the crater pressure varies between 0.04 to 0.1 atm above atmospheric pressure, which will drive the upwards flow of gas. Measurements of the off-gas, which consists predominately of carbon monoxide (CO) and unreacted SiO, are also reported in [31, 33], and they find temperatures over 1000 K; however, the measurements were taken after the off-gas combusted with oxygen in the air above the furnace (see [24]), then passed into a gas collection system, so it is unclear how this relates to temperature of the gas as it initially exits the charge material. In [24] a value of 1700 K is given for the temperature of the off-gas before combustion. Other measurements described in [67] have established the temperature in the crater to be at least 2300 K. Therefore, the temperature of the gas decreases as it passes through the charge material, but it appears to exit the charge material at a temperature hotter than the temperature of the newly added solid, which is believed to be between 600 to 1500 K at the surface [30, 32].

1.1.2 Chemistry in the furnace

The overall behaviour of the production process can be summarised by the reaction

$$\mathrm{SiO_2(s)} + 2\,\mathrm{C(s)} \longrightarrow \mathrm{Si(l)} + 2\,\mathrm{CO(g)}, \tag{1.1}$$

where the letter in brackets denotes the phase (s-solid, l-liquid, g-gas). However, in reality the chemical process is much more complicated, with silicon formation

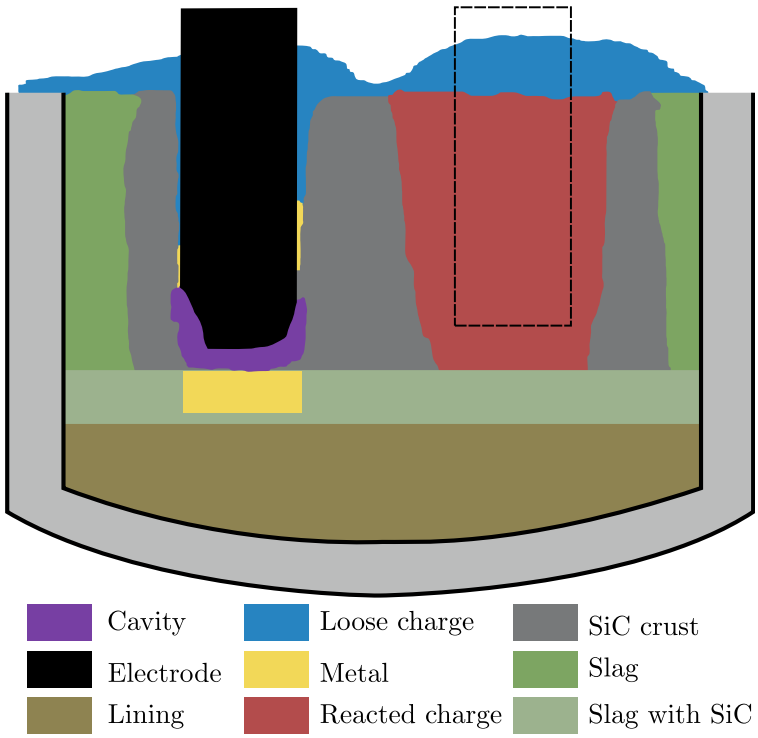


Figure 1.3: The different regions of a silicon furnace identified in the excavation of a 40 MW silicon furnace at Elkem Thamshavn (Figure reproduced with permission from [36]). The dashed box is the approximate position of another electrode.

happening in several stages, and with multiple possible chemical pathways. The most important reactions are generally agreed to be [2, 45, 67, 74]

$$\begin{aligned}
(i=1) \qquad & \mathrm{SiO\,(g)} + 2\,\mathrm{C\,(s)} \longrightarrow \mathrm{SiC\,(s)} + \mathrm{CO\,(g)}, \\
(i=2\rightarrow, i=3\leftarrow) \qquad & 2\,\mathrm{SiO\,(g)} \rightleftharpoons \mathrm{SiO_2(l)} + \mathrm{Si\,(l)}, \\
(i=4) \qquad & \mathrm{SiO_2(s)} \longrightarrow \mathrm{SiO_2(l)}, \\
(i=5) \qquad & \mathrm{SiO\,(g)} + \mathrm{SiC\,(s)} \longrightarrow 2\,\mathrm{Si\,(l)} + \mathrm{CO\,(g)}, \\
(i=6) \qquad & \mathrm{SiO_2(l)} + \mathrm{C\,(s)} \longrightarrow \mathrm{SiO\,(g)} + \mathrm{CO\,(g)}, \\
(i=7) \qquad & 2\,\mathrm{SiO_2(l)} + \mathrm{SiC\,(s)} \longrightarrow 3\,\mathrm{SiO\,(g)} + \mathrm{CO\,(g)},
\end{aligned} \tag{1.2}$$

which introduces two additional chemical species compared to (1.1), silicon carbide (SiC) and SiO. The reactions show that SiO is a key driver of the chemistry in the furnace, with every reaction, except reaction 4, the melting of quartz, either creating or consuming it. Hence, its distribution and flow through the furnace plays an important role in determining the chemical behaviour, and hence the temperature distribution. It is common to treat liquid quartz, $\mathrm{SiO_2(l)}$, as a distinct chemical species to solid quartz, $\mathrm{SiO_2(s)}$, since the rate of reaction 6 is almost zero for solid quartz

Reaction	Enthalpy change
1	$7.76 \times 10^4\,\mathrm{J\,mol^{-1}}$
2	$3.07 \times 10^5\,\mathrm{J\,mol^{-1}}$
3	$-6.05 \times 10^5\,\mathrm{J\,mol^{-1}}$
4	$-9.36 \times 10^4\,\mathrm{J\,mol^{-1}}$
5	$-1.67 \times 10^5\,\mathrm{J\,mol^{-1}}$
6	$-7.93 \times 10^5\,\mathrm{J\,mol^{-1}}$
7	$-1.38 \times 10^6\,\mathrm{J\,mol^{-1}}$

Table 1.1: Enthalpy change of reactions (1.2) in the furnace. Data from [33, 67, 75]

due to surface roughness creating a tiny contact area between particles [74]. Thus, we view the melting of quartz as a chemical reaction. Reasonably realistic functional forms of reactions 1-6 are given in [74]. Reaction 7 has been historically excluded from previous models of silicon furnaces, but is included here for completeness.

Although the overall reaction (1.1) is endothermic, the system of reactions given by (1.2) consists of a mixture of exothermic and endothermic reactions, whose enthalpies we give in Table 1.1. Throughout this thesis, we use the convention from [74] that exothermic reactions have positive enthalpies, as they give out heat to the surrounding, and endothermic negative enthalpies, as they take in heat, although in chemical engineering (see e.g. [33, 67]), the opposite convention is used. It is commonly assumed by furnace operators that the furnace consists of a hotter inner zone close to the crater, where the endothermic reactions (reactions 3-7) occur, and a cooler outer zone where the exothermic reaction 1 is the main reaction [67]. In [45], it is shown using a mathematical model of the combined electrical, thermal, and endothermic chemical processes in the furnace, that an endothermic reaction combining reactions 4 and 6 in (1.2) is indeed confined to a narrow layer close to the crater, unless there is a large exchange of heat between the gas and the solid, in which case endothermic reactions can occur throughout the domain.

Away from the inner zone, the main reaction is reaction 1, the exothermic creation of SiC by SiO flowing through the charge material. Maintaining a high conversion rate of C to SiC is important, as it captures silicon from SiO, which would otherwise be lost in the exiting gas, lowering the efficiency of the furnace. Moreover, reaction 7, where SiO_2(l) reacts with SiC provides a less endothermic reaction to produce the gases in the furnace, than reaction 6, where it reacts directly with carbon. Reaction 2, also called the *condensation reaction*, because it only occurs below a certain temperature, and deposits a very sticky material, which is referred to as the *condensate* [2, 8].

It also occurs in the outer zone of the furnace and is exothermic. Over time, the condensate deposited by this reaction can alter the permeability of the charge, and eventually cause clogging [63]. This is believed to lead to a build up of pressure in the crater which can lead to jets of flaming gas shooting out the taphole, posing a risk to furnace operators [33, 63]. Hence, furnace operators must regularly *stoke* the charge material with a stoking car (see Figure 1.1) every few hours, to break up the condensate and maintain a high permeability in the charge [8, 67].

1.2 Previous models of silicon furnaces

The stoichiometric model, described in [67], is a purely chemical model for the furnace, where the charge is divided up into a hot inner zone and a cool outer zone with different reactions occurring in each zone. It can only predict steady solutions for the furnace. Similar models that predict the evolution of the furnace over the timescale of days include the dynamic model [27], and Elkem's internal model SiMod [30]. All these models use lumped parameters which are tuned to give qualitatively correct results, rather than reflect physical or chemical properties.

The flow of gas through the furnace with imposed charge structure was simulated in [33] using the commercial computational fluid dynamics (CFD) package Fluent to solve the Navier-Stokes-Forchheimer-Brinkman equations with a k-ϵ model for turbulence. The temperature was assumed constant, and all chemical effects were neglected, with the production of gas a prescribed source term. Commercial CFD packages were also used to attempt to simulate the coupled thermal, chemical, and gas flow behaviour in silicon producing SAFs in [2] and phosphorus producing SAFs in [66]. Due to the extremely high computational cost, only a limited number of scenarios were investigated in both cases.

The coupled heat and mass transfer processes occurring in a pilot silicon furnace are analysed in the thesis [74] and its associated papers [75, 76, 77, 78]. Although the focus is on pilot silicon furnaces, which are used to carry out experiments, many of their results are applicable to industrial furnaces. In [76, 78], a detailed model of the mass transfer in the furnace is developed, encompassing reactions 1-6 in (1.2), with a particular focus on studying the formation of the crater and surrounding crust. The gas is assumed to always be at atmospheric pressure with its movement driven by displacement from newly created gases. The gases and solids are assumed to all share a single temperature. In [75], a model for the formation of a crust around the crater is developed by considering the temperature, flow, and movement of the charge

material, with the charge modelled as a viscous fluid with a temperature-dependent viscosity. The gas flow is entirely neglected in this model. In [77], a model for the gas-solid reactions within a carbon particle is developed. The model is then homogenised to provide a simple model for the dynamics of the entire particle.

The coupling between the electrical, thermal, and chemical processes in the furnace was studied in [45], and the associated papers [46, 47, 48]. In [47], a mathematical model is derived for the electrical arc in the crater, and the electric current in the surrounding charge. In [46], the arc and electrical model from the previous paper is incorporated into an equivalent circuit model for the whole furnace, over the timescale of the AC current applied to the furnace. In [48], the behaviour of a counter-current flow between a gas and solid with an endothermic reaction occurring between them is considered. Asymptotic solutions are found for the full range of sizes of the heat transfer coefficient between the gas and the solid. In all these papers, which together can be thought of as a model for the inner zone of the furnace, the pressure is assumed atmospheric throughout the furnace, with the flow of gas driven by displacement due to newly created gas.

Our goal in this thesis is to model the behaviour of the movement of the gases and solids, and the coupled chemical and thermal processes in the outer zone of the furnace. This will allow for a more complete understanding of the behaviour of the charge material, and complement the detailed study of the inner zone undertaken in [45].

1.3 Counter-current flows

In a silicon furnace, the gases flow upwards, and the solids move downwards, with both heat and mass moving from one phase to the other. This is an example of a counter-current flow, i.e. a system where two materials flow in opposite directions whilst exchanging mass or heat. Other examples of counter-current systems with mass exchange are the production of urine [93], some designs of bioreactors [49], and the separation of chemical species [80]. Examples of counter-current heat exchange systems are blood flow through the body [50], coolant systems, for example in the nuclear industry [16], and volcanic conduits [20].

Mathematical studies of counter-current flow include [50], who treat the two materials as mixed, with a bulk transfer coefficient between them, and [19, 26] who treat the two materials as separated with diffusion processes on the interface between them governing the exchange of mass. The forward/backwards nature of the diffusion

problems in the latter papers highlight the difficulty in ensuring well-possedness and solving counter-current problems. Possible methods to solve counter-current flow problems include half-range eigenfunction expansions [25] and projection methods [85]. When reactions between the materials occur, counter-current effects are usually neglected from mathematical models, with those studies considering the coupling focused on flames and combustion, with many models assuming the two species to share a common temperature [81]. However, there do exist some studies of two temperature counter-current reacting flows, focusing on catalytic converters [9], filtration combustion [10], and the combustion of rocket fuel [35], respectively.

An assumption common to all the theoretical works mentioned where the two materials are assumed to have distinct temperatures, is that the heat exchange between the two materials at a point is linearly proportional to the difference in temperatures between the materials at that point. In fact, this constitutive relation is used far more generally when modelling porous media out of local thermal equilibrium (LTNE) [6, 55], although questions have been raised about its validity [82]. There have been some papers [22, 52] which consider upscaling microscale models to deduce the macroscale energy equations for porous media in LTNE, but they both assume a linear relation during the upscaling procedure. A goal for this thesis will therefore be to assess the validity of this linear relationship for the heat flux between the phases, in the particular case of the charge material of a silicon furnace.

1.4 Compressible gas flow in channels

Besides the microstructure inside silicon furnaces, modelling subsonic non-isothermal compressible flow through narrow channels is also relevant to understanding other industrial applications including: gas channelling in blast furnaces [95]; coolant for super-conducting magnets [70]; optimising the post-combustion capture of CO_2 [39]; and controlling chemical vapour deposition reactors [18]. It also occurs in a large number of micro-fluidic devices, as reviewed in [65].

Despite this large array of applications, there have been relatively few theoretical studies of laminar compressible flow in the continuum limit. Of the theoretical works that do exist, most have focused on incorporating the relationship between density and pressure, and so find generalisations of the Hagen-Poiseuille equation relating the mass flux and pressure drop for incompressible flows [68]. To this end [1, 92], found similarity solutions to a reduced model derived from the Navier-Stokes equations for flow in a channel with insulated walls by assuming an adiabatic flow and a viscosity

linearly proportional to temperature. By assuming isothermal and unidirectional flow, approximate solutions to the compressible Navier-Stokes equations were found for flow in narrow pipes with insulated walls for an ideal gas and a general equation of state, by [61] and [4], respectively, using double perturbation expansions in the aspect ratio and dimensionless compressibility. The assumption that a flow in a channel with insulated walls may be regarded as isothermal was justified in [5], where it was shown that internal heating of the gas by the work done due to compression and viscous heating will be a small effect, unless the gas is very compressible. However, [83] showed a unidirectional assumption used by [4, 61] to be inconsistent with the equations of motion, with terms of the same order retained in some equations, but neglected in others. Instead, [83] found a perturbation solution to the vorticity-streamfunction formulation of a weakly compressible Newtonian gas in a pipe using the dimensionless compressibility as a small parameter, but not the aspect ratio (i.e. without the lubrication approximation). This analysis was extended to two-dimensional channels in [84] with the predictions compared to experimental results. Isothermal flow was also considered by [69] who assumed the solution only varied slowly along the length of the channel. They found, for moderate values of the Reynolds number, that the analytical solution cannot be continued beyond a certain point when the speed is near sonic, a phenomenon they call mathematical choking.

For non-isothermal flows, [70] consider subsonic, viscous-dominated gas flow in a narrow pipe with a constant heat flux supplied through the walls, heating the gas flow driven by a finite pressure gradient. Utilising a perturbation solution of the compressible Navier-Stokes equations, as well as exploiting the small aspect ratio and reduced Reynolds number, they showed that a steady solution can exist only below a critical heat input through the walls. When the critical value is exceeded in time dependent simulations, the flow reverses against the imposed pressure gradient and flows out of both the inlet and outlet. They also found that a temperature-dependent viscosity leads to the existence of multiple steady solutions. These results were extended to channels with a slowly varying cross-section in [17]. In [40], a modification of triple-deck theory is used to analyse the perturbation of a compressible Poiseuille flow between two plates at high Reynolds number when the temperature of the lower plate suddenly increases by a small amount. They assume a vanishingly small Eckert number, and so neglect entirely the effect of viscous heating and the work done due to compression, meaning that the temperature variation is due to conduction, forced convection, and natural convection.

In the limit of rarefield gas, i.e. where the assumptions of continuum mechanics break down, there does exist previous work on both isothermal and non-isothermal compressible flow in channels, see the reviews in [73, 79]. However, in the furnace, we expect the substantial proportion of the gas flow to occur between individual particles of solid, not within them and hence the typical lengthscale will be of the order of millimetres, not the micrometres required for rarefield effects to become important. As a result, we do not discuss these studies in any more detail here.

Other models of relevance are those which consider gas flows in channels where a multiphase mixture of gas undergoes reaction on the walls. These include [13, 34] who model the gas flow through a solid oxide fuel cell and its coupling to the electrochemistry in the surrounding components, and [37, 42] who consider models of the multiphase gas flow in chemical vapour deposition reactors. The clogging of a gas channel in a silicon furnace due to condensate deposited by reaction 2 in (1.2) also has several similarities to the solidification of an incompressible fluid in a channel. Previous studies of this phenomena have considered: clogging of reactive filters [7]; development of lava tubes [44]; and the formation of ice in pipes [86].

None of the previous works on non-isothermal flow have considered the behaviour when there is a balance between viscous and inertial effects in the gas at leading-order. Further, none of them have considered the role of internal heating of the gas outside of the viscous dominated regime. For reactive flows no previous studies have considered the simultaneous coupling between compressibility, multiple gas species, reactions, and heat transfer.

1.5 Summary of the rest of the thesis

In Chapter 2, we develop a mathematical model for the charge material in a silicon furnace, based on the idealisation of the microstructure as an impermeable solid perforated by a regular array of channels filled with a binary mixture of CO and SiO gas. Focusing on the behaviour relevant to the outer zone of the furnace, we couple the behaviour of the gases and solids through exothermic reactions occurring on the walls of the channel. The resulting model is complicated due to the non-linear governing equations for the gases, counter-current flow, and disparate length-scales, so we do not attempt to solve it in its entirety. We present a nondimensionalisation of the model, based on estimates of industrially-relevant parameter values. The remainder of the thesis consists of analysing simplifications of this dimensionless model.

In Chapter 3, we consider the steady laminar flow of a single species of gas through a channel, subject to an imposed temperature on the walls, to gain insight into the behaviour of the gas in our coupled model. Motivated by the size of the industrially-relevant parameter values, we consider a range of reduced models in the limit of small channel aspect ratio and small pressure drop, with the limits differing by the assumed size of the reduced Reynolds number. These reduced models are also validated against numerical solutions of the full compressible Navier-Stokes equations.

In Chapter 4, we consider a simplified version of the coupled model for the gases and solid in the industrially-relevant limit of order unity reduced Reynolds number. We solve this coupled model numerically by building on numerical methods developed for the gas only problem in the previous chapter. We find that in this limit, steady solutions exist in which the gas and solid temperatures differ. Due to difficulties in obtaining solutions in the industrially-relevant parameter regime, we also consider the sub-problems of a coupled gas and solid model without reactions, and of the gas model with reactions, but an imposed solid temperature.

In Chapter 5, we study the alternative, but still industrially-relevant limit of our coupled model where the reduced Reynolds number is small. In this limit we find the gases and solid to have the same temperature. We consider the behaviour when the reaction rates are small and reactions occur along the entire length of the channel, and when the reaction rate is order unity and highly temperature dependent, meaning the reaction only occurs in a narrow layer.

In Chapter 6, we summarise our results and highlight avenues for future work. We also discuss the implications of our results for furnace operators and for the incorporation of gas dynamics into future modelling for silicon furnaces.

1.6 Statement of originality

The modelling, analysis, and numerical results in this thesis are the work of M. D. Shirley, under the supervision of C. P. Please, J. M. Oliver, and M. R. Moore. At the time of submission none of the work presented in this thesis has been submitted for publication.

Chapter 2

Mathematical model of the charge material in a silicon furnace

2.1 Problem formulation

In this chapter, we present a model for the coupled flow, heat transfer, and mass transfer occurring between the gases and solids in the charge material of a silicon furnace. Our model is based on the idealisation of the microstruture of the charge material as an impermeable solid perforated by a periodic array of vertical gas channels, as depicted in Figure 2.1. We work in a Cartesian coordinate system (x^*, y^*, z^*) with standard basis vectors $\mathbf{i}$, $\mathbf{j}$, and $\mathbf{k}$, such that the axial direction along the channels is parallel to the z^* axis. Within the gas channels, denoted Ω^*_{g}, we will model the temperature and fluid flow of multiple gas species, while in the solid region, denoted Ω^*_{s}, we will model the movement and temperature of a single, representative solid species. On the interface between the gas and solid regions, denoted $\partial\Omega^*_{\mathrm{Inter}}$, we will model the gas-solid reactions that occur within the so-called 'outer zone' furnace, reactions 1 and 2 in (1.2), which are the formation of SiC, and the 'condensation' of SiO, respectively. At the bottom of the domain, denoted $\partial\Omega^*_{\mathrm{crat}} = \partial\Omega^*_{\mathrm{g,crat}} \cup \partial\Omega^*_{\mathrm{s,crat}}$, we will model where the charge material ends, and the crater begins, by imposing boundary conditions based on measurements of the conditions in the crater of industrial furnaces. However, we will neglect modelling the evolution of the charge-crater boundary, instead taking it to be fixed, and also ignore the effect of electrical heating and endothermic gas-creating chemical reactions (reactions 3-7 in (1.2)), which are believed to be restricted to a narrow region of charge material near the edge of the crater and were studied in detail in [47]. Similarly, at the top of the domain, denoted $\partial\Omega^*_{\mathrm{surf}} = \partial\Omega^*_{\mathrm{g,surf}} \cup \partial\Omega^*_{\mathrm{s,surf}}$, we will model the surface where fresh charge material is deposited by applying boundary conditions based on measurements of the surface of

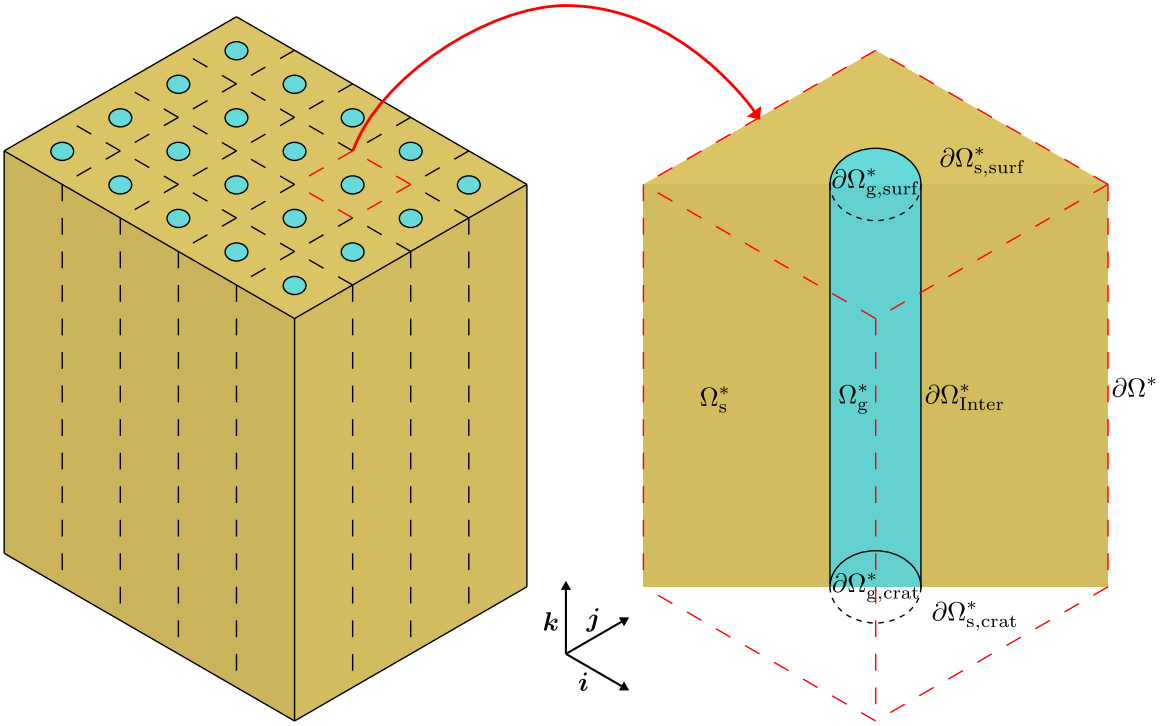


Figure 2.1: (left) The assumed periodic microstructure of the charge material with the solid shown in brown and the gas channels in blue. (right) A cross-section of a single periodic region with the regions and boundaries labelled.

the charge material in industrial furnaces. However, we will neglect modelling the effect of volatile gases being released from the newly added carbon material and the combustion of SiO(g) and CO(g) with oxygen in the air above the charge, as considered in [24]. We will assume that the rate at which new solid material is constantly deposited is chosen so that the location of the upper surface of the charge material remains fixed. Finally, to simplify the analysis in this thesis, we will assume the solution of our model to be periodic in the plane perpendicular to the channels, and so only need to consider the behaviour of our model in a single gas channel, and its surrounding solid material, shown by red dashed lines in Figure 2.1. We will denote the remaining boundaries introduced by considering this smaller region by $\partial\Omega^*$. It is possible to consider more general solutions on the periodic domain depicted in Figure 2.1. For example, the macroscale behaviour of many channels could be studied using homogenisation via the method of multiple scales [15], and we discuss this further in the future work section in Chapter 6.

Although we will not attempt to solve the full model presented in this chapter, it will form the basis of the reduced models studied in subsequent chapters. As discussed in Chapter 1, the relationship between the pressure build-up in the crater and the mass

flux of gas through the charge is not fully understood, and there is some uncertainty as to whether the gas and solids locally share a common temperature. By writing down a comprehensive microscale model for the coupled gas and solid dynamics in a single channel, we have a model that can be used to address these questions. The insight gained from studying simplified versions of this model in subsequent chapters will help shed light on the key underlying physical and chemical processes that dictate how this model will behave, whilst being more easily tractable. We will discuss these insights and relate them back to the full model in chapter 6.

2.1.1 Gas channel

In this section, we present a multiphase continuum model for a miscible mixture of SiO and CO inside the gas channel Ω_{g}^* based on conservation of mass, momentum, and energy for each species. This derivation is adapted from previous studies of multiphase gas dynamics in [53, 60, 88, 89, 90, 96].

2.1.1.1 Conservation of mass

Let $\rho_{\mathrm{CO}}^*, \rho_{\mathrm{SiO}}^*$, be the mass density [$\mathrm{kg\,m^{-3}}$] of SiO and CO respectively, where the mass density is defined as the total mass of that species within a representative elementary volume (REV) divided by the volume of the REV. The total mass of gas ρ^* is thus

$$\rho^* = \rho_{\mathrm{CO}}^* + \rho_{\mathrm{SiO}}^*, \tag{2.1}$$

which is the total mass of gas within the REV divided by the volume of the REV. Hence, the mass fraction of each species is given by

$$Y_{\mathrm{SiO}} = \frac{\rho_{\mathrm{SiO}}^*}{\rho^*}, \quad Y_{\mathrm{CO}} = \frac{\rho_{\mathrm{CO}}^*}{\rho^*}, \tag{2.2}$$

and we note that, from (2.1), $Y_{\mathrm{CO}} + Y_{\mathrm{SiO}} = 1$. Later, it will be convenient to express parts of the model in a molar formulation rather than a mass formulation. We therefore note that the molar concentration of each species [$\mathrm{mol\,m^{-3}}$] is related to the mass density via

$$c_{\mathrm{SiO}}^* = \frac{\rho_{\mathrm{SiO}}^*}{M_{\mathrm{SiO}}^*}, \quad c_{\mathrm{CO}}^* = \frac{\rho_{\mathrm{CO}}^*}{M_{\mathrm{CO}}^*}, \tag{2.3}$$

where M_{SiO}^* and M_{CO}^* are the molar weights [$\mathrm{kg\,mol^{-1}}$], and the total molar concentration of the mixture is thus given by

$$c^* = c_{\mathrm{SiO}}^* + c_{\mathrm{CO}}^*. \tag{2.4}$$

Assuming that no chemical reactions occur between the gas species, conservation of mass for each species gives the equations

$$\frac{\partial \rho^*_{\mathrm{CO}}}{\partial t^*} + \boldsymbol{\nabla} \cdot (\rho^*_{\mathrm{CO}} \boldsymbol{u}^*_{\mathrm{CO}}) = 0, \quad \frac{\partial \rho^*_{\mathrm{SiO}}}{\partial t^*} + \boldsymbol{\nabla} \cdot (\rho^*_{\mathrm{SiO}} \boldsymbol{u}^*_{\mathrm{SiO}}) = 0, \tag{2.5}$$

where $\boldsymbol{u}^*_{\mathrm{CO}}$ and $\boldsymbol{u}^*_{\mathrm{SiO}}$ are the velocities of CO and SiO gas, respectively, and t^* is time. The mass-averaged or barycentric velocity of the mixture is defined as

$$\boldsymbol{u}^* = Y_{\mathrm{CO}} \boldsymbol{u}^*_{\mathrm{CO}} + Y_{\mathrm{SiO}} \boldsymbol{u}^*_{\mathrm{SiO}}. \tag{2.6}$$

Using this definition of the average velocity, it is natural to define the total momentum of the gas in the REV to be $\rho^* \boldsymbol{u}^*$, since this is equivalent to the sum of the momentum of each species. With this average velocity, each individual species velocity can now be rewritten as the averaged velocity plus a deviation from the average, called the diffusion velocity,

$$\boldsymbol{u}^*_{\mathrm{SiO}} = \boldsymbol{u}^* + \boldsymbol{U}^*_{\mathrm{SiO}}, \quad \boldsymbol{u}^*_{\mathrm{CO}} = \boldsymbol{u}^* + \boldsymbol{U}^*_{\mathrm{CO}}. \tag{2.7}$$

By multiplying each equation in (2.7) by its respective species density, it can be shown the diffusion velocities are related via $\rho^*_{\mathrm{SiO}} \boldsymbol{U}^*_{\mathrm{SiO}} + \rho^*_{\mathrm{CO}} \boldsymbol{U}^*_{\mathrm{CO}} = 0$. Using these diffusion velocities, the conservation of mass equations for each species, (2.5), can be rewritten as

$$\frac{\partial \rho^*_{\mathrm{CO}}}{\partial t^*} + \boldsymbol{\nabla} \cdot (\rho^*_{\mathrm{CO}} \boldsymbol{u}^*) = -\boldsymbol{\nabla} \cdot (\rho^*_{\mathrm{CO}} \boldsymbol{U}^*_{\mathrm{CO}}), \tag{2.8}$$

$$\frac{\partial \rho^*_{\mathrm{SiO}}}{\partial t^*} + \boldsymbol{\nabla} \cdot (\rho^*_{\mathrm{SiO}} \boldsymbol{u}^*) = -\boldsymbol{\nabla} \cdot (\rho^*_{\mathrm{SiO}} \boldsymbol{U}^*_{\mathrm{SiO}}), \tag{2.9}$$

and by summing them, the conservation of total mass can be expressed as

$$\frac{\partial \rho^*}{\partial t^*} + \boldsymbol{\nabla} \cdot (\rho^* \boldsymbol{u}^*) = 0. \tag{2.10}$$

2.1.1.2 Conservation of momentum

To determine both the mass-averaged velocity and the diffusion velocities we must consider conservation of momentum for each species. Our derivation follows that described in [87, 89, 90], so we only sketch the main argument, stating the key assumptions.

The starting point is to consider conservation of momentum for each individual species. For SiO, this is given by

$$\frac{\partial}{\partial t^*} (\rho^*_{\mathrm{SiO}} \boldsymbol{u}^*_{\mathrm{SiO}}) + \boldsymbol{\nabla} \cdot (\rho^*_{\mathrm{SiO}} \boldsymbol{u}^*_{\mathrm{SiO}} \otimes \boldsymbol{u}^*_{\mathrm{SiO}}) = \boldsymbol{\nabla} \cdot \boldsymbol{T}^*_{\mathrm{SiO}} + \boldsymbol{P}^*_{\mathrm{SiOCO}}, \tag{2.11}$$

where $\otimes$ is the outer product, $\boldsymbol{T}^*_{\mathrm{SiO}}$ is the species stress tensor for SiO, and $\boldsymbol{P}^*_{\mathrm{SiOCO}}$ is the force per unit volume exerted by the CO on the SiO, also called the diffusive force. The corresponding equation for CO is readily obtained by swapping the subscripts in (2.11). The species momentum equations for SiO and CO can be summed to express conservation of total momentum, which after using the requirement $\boldsymbol{P}^*_{\mathrm{SiOCO}} = -\boldsymbol{P}^*_{\mathrm{COSiO}}$, and performing some algebraic manipulations to rewrite the left-hand side in terms of ρ^* and $\boldsymbol{u}^*$, is given by

$$\frac{\partial}{\partial t^*}\left(\rho^* \boldsymbol{u}^*\right) + \boldsymbol{\nabla} \cdot \left(\rho^* \boldsymbol{u}^* \otimes \boldsymbol{u}^*\right) = \boldsymbol{\nabla} \cdot \boldsymbol{T}^*, \tag{2.12}$$

where $\boldsymbol{T}^*$ is the total stress tensor for the mixture, defined as

$$\boldsymbol{T}^* = \boldsymbol{T}^*_{\mathrm{SiO}} + \boldsymbol{T}^*_{\mathrm{CO}} - \rho^*_{\mathrm{SiO}} \boldsymbol{U}^*_{\mathrm{SiO}} \otimes \boldsymbol{U}^*_{\mathrm{SiO}} - \rho^*_{\mathrm{CO}} \boldsymbol{U}^*_{\mathrm{CO}} \otimes \boldsymbol{U}^*_{\mathrm{CO}}. \tag{2.13}$$

Now, we assume each of the species stress tensors to be of the form

$$\boldsymbol{T}^*_{\mathrm{SiO}} = -p^*_{\mathrm{SiO}} \boldsymbol{I} + \boldsymbol{\tau}^*_{\mathrm{SiO}}, \quad \boldsymbol{T}^*_{\mathrm{CO}} = -p^*_{\mathrm{CO}} \boldsymbol{I} + \boldsymbol{\tau}^*_{\mathrm{CO}}, \tag{2.14}$$

where $\boldsymbol{I}$ is the identity matrix, p^*_{SiO}, p^*_{CO} are the partial pressures, and $\boldsymbol{\tau}^*_{\mathrm{SiO}}$, $\boldsymbol{\tau}^*_{\mathrm{CO}}$ are the species viscous stress tensors of the SiO and CO, respectively. We further assume the gases to form an ideal mixture, meaning the partial pressures of each species are given by

$$\frac{p^*_{\mathrm{SiO}}}{p^*} = \frac{c^*_{\mathrm{SiO}}}{c^*}, \quad \frac{p^*_{\mathrm{CO}}}{p^*} = \frac{c^*_{\mathrm{CO}}}{c^*}, \tag{2.15}$$

where p^* is the total pressure of the mixture. By substituting (2.14)–(2.15) into the expression for $\boldsymbol{T}^*$ (2.13), the conservation of total momentum (2.12), can be re-expressed as

$$\frac{\partial}{\partial t^*}\left(\rho^* \boldsymbol{u}^*\right) + \boldsymbol{\nabla} \cdot \left(\rho^* \boldsymbol{u}^* \otimes \boldsymbol{u}^*\right) = -\boldsymbol{\nabla} p^* + \boldsymbol{\nabla} \cdot \boldsymbol{\tau}^*, \tag{2.16}$$

where

$$\boldsymbol{\tau}^* = \boldsymbol{\tau}^*_{\mathrm{SiO}} + \boldsymbol{\tau}^*_{\mathrm{CO}} - \rho^*_{\mathrm{SiO}} \boldsymbol{U}^*_{\mathrm{SiO}} \otimes \boldsymbol{U}^*_{\mathrm{SiO}} - \rho^*_{\mathrm{CO}} \boldsymbol{U}^*_{\mathrm{CO}} \otimes \boldsymbol{U}^*_{\mathrm{CO}}, \tag{2.17}$$

is the total viscous stress tensor. To obtain the simplest possible model, we now assume the mixture will behave as a Newtonian fluid, meaning $\boldsymbol{\tau}^*$ is linearly proportional to the strain rate, and further assume the Stokes hypothesis holds, so that the bulk viscosity of the mixture is zero [68]. This means the total viscous stress is given by

$$\boldsymbol{\tau}^* = \mu^* \left(\boldsymbol{\nabla} \boldsymbol{u}^* + \left(\boldsymbol{\nabla} \boldsymbol{u}^*\right)^{\mathrm{T}}\right) - \frac{2}{3}\mu^* \left(\boldsymbol{\nabla} \cdot \boldsymbol{u}^*\right) \boldsymbol{I}, \tag{2.18}$$

where μ^* is the dynamic viscosity of the mixture. The assumption of a bulk viscosity of zero can only be shown to be true for monatomic gases [58], which SiO and CO are not, but as it is almost impossible to measure bulk viscosity experimentally, we use this assumption to simplify our model. To estimate the value of the dynamic viscosity of the mixture, we use the kinetic theory of dilute gases, which is discussed in detail in Appendix A.

We now have a governing equation for the total conservation of momentum, equivalent to the compressible Navier-Stokes equations for a single-phase fluid, from which we can determine the average velocity, but we still require an expression for the diffusive velocities. To obtain this, we must consider the species momentum equations (2.11) further, and so need an expression for the diffusive force $\boldsymbol{P}^*_{\mathrm{SiOCO}}$. For this, we use the Maxwellian representation of the drag force between the species

$$\boldsymbol{P}^*_{\mathrm{SiOCO}} = \frac{p^* c^*_{\mathrm{SiO}} c^*_{\mathrm{CO}} \left(\boldsymbol{U}^*_{\mathrm{SiO}} - \boldsymbol{U}^*_{\mathrm{CO}}\right)}{\left(c^*\right)^2 \mathcal{D}^*_{\mathrm{SiOCO}}}, \tag{2.19}$$

where $\mathcal{D}^*_{\mathrm{SiOCO}}$ is the binary diffusion coefficient of the SiO-CO mixture [$\mathrm{m^2\,s^{-1}}$] [11]. This expression was developed using statistical mechanics, under the assumption the gas mixture is dilute, meaning that all the collisions are assumed to occur between two molecules [11, 29]. For denser gases this assumption will not hold and so the model will not be valid. As with the dynamic viscosity, the value of $\mathcal{D}^*_{\mathrm{SiOCO}}$ can be estimated using the kinetic theory of dilute gases, which is discussed in detail in Appendix A.

Substituting the expressions for the species stress tensors, partial pressures, and diffusive force, (2.14), (2.15), and (2.19) respectively, into the species momentum equation (2.11), we obtain

$$\begin{aligned}\frac{1}{p^*}\left(\frac{\partial}{\partial t^*}\left(\rho^*_{\mathrm{SiO}}\boldsymbol{u}^*_{\mathrm{SiO}}\right) + \boldsymbol{\nabla}\cdot\left(\rho^*_{\mathrm{SiO}}\boldsymbol{u}^*_{\mathrm{SiO}}\otimes\boldsymbol{u}^*_{\mathrm{SiO}}\right) + \frac{c^*_{\mathrm{SiO}}}{c^*}\boldsymbol{\nabla}p^* - \boldsymbol{\nabla}\cdot\boldsymbol{\tau}^*_{\mathrm{SiO}}\right)& \\ = -\boldsymbol{\nabla}\left(\frac{c^*_{\mathrm{SiO}}}{c^*}\right) + \frac{c^*_{\mathrm{SiO}}c^*_{\mathrm{CO}}\left(\boldsymbol{U}^*_{\mathrm{SiO}} - \boldsymbol{U}^*_{\mathrm{CO}}\right)}{\left(c^*\right)^2\mathcal{D}^*_{\mathrm{SiOCO}}}.&\end{aligned} \tag{2.20}$$

We now follow [90], and assume the left-hand side of (2.20) is small compared to the right-hand side, so can be neglected. This reduces the equation (2.20) to the classical form of the Stefan-Maxwell equation [29],

$$0 = -\boldsymbol{\nabla}\left(\frac{c^*_{\mathrm{SiO}}}{c^*}\right) + \frac{c^*_{\mathrm{SiO}}c^*_{\mathrm{CO}}\left(\boldsymbol{U}^*_{\mathrm{SiO}} - \boldsymbol{U}^*_{\mathrm{CO}}\right)}{\left(c^*\right)^2\mathcal{D}^*_{\mathrm{SiOCO}}}. \tag{2.21}$$

The choice to start with the species momentum equation for SiO was arbitrary, and starting with the equation for CO would result in an equivalent expression to (2.21).

The above derivation may be easily extended to a mixture of N different gas species, and results in a total momentum equation coupled to $N-1$ Stefan-Maxwell equations. However, in the two-species case we consider here, it is possible to simplify further, and through a series of algebraic manipulations detailed in [89], show that (2.21) can be rewritten as

$$\rho^*_{\mathrm{SiO}} \boldsymbol{U}^*_{\mathrm{SiO}} = -\rho^* \mathcal{D}^*_{\mathrm{SiOCO}} \boldsymbol{\nabla} Y_{\mathrm{SiO}}, \tag{2.22}$$

the classical form of Fick's law of diffusion. This expression determines the diffusion velocity, and may be substituted into (2.9) to give an advection-diffusion equation for Y_{SiO},

$$\frac{\partial}{\partial t^*}\left(\rho^* Y_{\mathrm{SiO}}\right) + \boldsymbol{\nabla} \cdot \left(\rho^* \boldsymbol{u}^* Y_{\mathrm{SiO}}\right) = \boldsymbol{\nabla} \cdot \left(\rho^* \mathcal{D}^*_{\mathrm{SiOCO}} \boldsymbol{\nabla} Y_{\mathrm{SiO}}\right), \tag{2.23}$$

where the diffusion will be nonlinear due to the factor of ρ^*.

Note that in presenting this model we have assumed there to be no body force due to gravity acting on the gas. The derivation is also valid when a body force is included, but upon the nondimensionalisation in Section 2.2, it would be found that the Froude number is large, implying the effect gravity can be neglected, so it was omitted here for simplicity.

2.1.1.3 Conservation of energy

The derivation of the energy equation proceeds similarly to the momentum equation, and so we omit the details. We assume the gases to be in local thermal equilibrium, so that they share a common temperature T^*. Thus, only a single energy equation will be required and so we can add the conservation of energy equation for each species, and neglect terms related to the diffusion velocities (see [88] for details), to find

$$\frac{\partial}{\partial t^*}\left(\rho^* h^*\right) + \boldsymbol{\nabla} \cdot \left(\rho^* h^* \boldsymbol{u}^*\right) = \boldsymbol{\nabla} \cdot \left(k^*_{\mathrm{g}} \boldsymbol{\nabla} T^*\right) + \frac{\partial p^*}{\partial t^*} + \boldsymbol{u}^* \cdot \boldsymbol{\nabla} p^* + \Phi^*, \tag{2.24}$$

$$\Phi^* = \boldsymbol{\tau}^* : \boldsymbol{\nabla} \boldsymbol{u}^*, \tag{2.25}$$

where k^*_{g} is the thermal conductivity of the mixture [$\mathrm{W\,m^{-1}\,K^{-1}}$], Φ^* is the viscous dissipation, $:$ is the double-dot product, and h^* is the mass-averaged specific enthalpy of the mixture [$\mathrm{J\,kg^{-1}}$], given by

$$h^* = Y_{\mathrm{SiO}} h^*_{\mathrm{SiO}} + Y_{\mathrm{CO}} h^*_{\mathrm{CO}}, \tag{2.26}$$

where h^*_{SiO} and h^*_{CO} are the specific enthalpies of SiO and CO, respectively. In order, the terms in (2.24) represent advection of heat, conduction of heat, the work done by

compression of the gas, and viscous heating, respectively. Similarly to the dynamic viscosity, we estimate the value of the thermal conductivity, k_{g}^*, using the kinetic theory of dilute gases, which is discussed in detail in Appendix A.

Since we are considering an ideal mixture of gases, and assuming the gases to be in local thermal equilibrium, the individual species specific enthalpies are given by

$$h_{\mathrm{SiO}}^* = c_{p,\mathrm{SiO}}^* T^*, \quad h_{\mathrm{CO}}^* = c_{p,\mathrm{CO}}^* T^*, \tag{2.27}$$

where $c_{p,\mathrm{SiO}}^*$ and $c_{p,\mathrm{CO}}^*$ are the specific heat capacities of SiO and CO at constant pressure $[\mathrm{J\,kg^{-1}\,K^{-1}}]$, respectively, which we will assume to be constants. Using these expressions, we can rewrite h^*, defined in (2.26), as

$$h^* = c_{p,\mathrm{CO}}^* \left(1 - \left(1 - \frac{c_{p,\mathrm{SiO}}^*}{c_{p,\mathrm{CO}}^*}\right) Y_{\mathrm{SiO}}\right) T^*, \tag{2.28}$$

and so rewrite the conservation of energy equation, (2.24), as

$$\begin{aligned} &\frac{\partial}{\partial t^*}\left(\rho^* c_{p,\mathrm{CO}}^* T^*\right) + \boldsymbol{\nabla}\cdot\left(\rho^* c_{p,\mathrm{CO}}^* \boldsymbol{u}^* T^*\right) \\ &\qquad - \left(1 - \frac{c_{p,\mathrm{SiO}}^*}{c_{p,\mathrm{CO}}^*}\right)\left(\frac{\partial}{\partial t^*}\left(\rho^* c_{p,\mathrm{CO}}^* T^* Y_{\mathrm{SiO}}\right) + \boldsymbol{\nabla}\cdot\left(\rho^* c_{p,\mathrm{CO}}^* \boldsymbol{u}^* T^* Y_{\mathrm{SiO}}\right)\right) \\ &\qquad\qquad = \boldsymbol{\nabla}\cdot\left(k_{\mathrm{g}}^* \boldsymbol{\nabla} T^*\right) + \frac{\partial p^*}{\partial t^*} + \boldsymbol{u}^*\cdot\boldsymbol{\nabla} p^* + \Phi^*, \end{aligned} \tag{2.29}$$

Due to the lack of experimental data for $c_{p,\mathrm{SiO}}^*$, we estimate the values of the specific heat capacities of both species using statistical mechanics, which is discussed in detail in Appendix A.

2.1.1.4 Equation of state

Finally, we require an equation of state to close the model. This was already fixed in Section 2.1.1.2, when it was assumed the gas forms an ideal mixture, and so each species behaves as an ideal gas. Hence, we find the total pressure to be given by

$$p^* = \rho_{\mathrm{SiO}}^* \frac{R^*}{M_{\mathrm{SiO}}^*} T^* + \rho_{\mathrm{CO}}^* \frac{R^*}{M_{\mathrm{CO}}^*} T^* = \frac{\rho^* R^* T^*}{M_{\mathrm{CO}}^*}\left(1 - \left(1 - \frac{M_{\mathrm{CO}}^*}{M_{\mathrm{SiO}}^*}\right) Y_{\mathrm{SiO}}\right), \tag{2.30}$$

where R^* is the universal gas constant $[\mathrm{J\,K^{-1}\,mol^{-1}}]$ and the second equality follows from using (2.1) and (2.2).

2.1.2 Solid

In this section, we present a simple model for the solid in the charge region of a silicon furnace based on conservation of mass and energy. As discussed in Chapter 1, there are multiple solid species in the porous granular mixture, with the solid particles being porous themselves [77]. However, for simplicity in this model, we will take the charge material as an impermeable region containing a single solid species whose physical properties are derived from the material in a real furnace by assuming a constant ratio between quartz and carbon.

We let the density of the solid material be ρ_{s}^*, whose temperature dependence is specified by a constitutive law, possibly obtained by fitting to data available in [62]. Assuming no reactions consuming or creating solid occur within Ω_{s}^*, and neglecting any compressive effects from the weight of the material above, the conservation of mass equation for the solid is given by

$$\frac{\partial \rho_{\mathrm{s}}^*}{\partial t^*} + \boldsymbol{\nabla} \cdot (\rho_{\mathrm{s}}^* \boldsymbol{u}_{\mathrm{s}}^*) = 0, \tag{2.31}$$

where $\boldsymbol{u}_{\mathrm{s}}^*$ the solid velocity. We now assume the solid velocity to be purely vertical, with non-zero component w_{s}^*, simplifying (2.31) to

$$\frac{\partial \rho_{\mathrm{s}}^*}{\partial t^*} + \frac{\partial}{\partial z^*} (\rho_{\mathrm{s}}^* w_{\mathrm{s}}^*) = 0. \tag{2.32}$$

Thus, by fixing the flux of incoming solid material, the velocity will be fixed everywhere in Ω_{s}^*.

To model the temperature evolution in the solid we consider conservation of energy. Assuming the only heat transport mechanisms are advection and conduction, we obtain the equation

$$\frac{\partial}{\partial t^*} \left(\rho_{\mathrm{s}}^* c_{p,\mathrm{s}}^* T^* \right) + \boldsymbol{\nabla} \cdot \left(\rho_{\mathrm{s}}^* c_{p,\mathrm{s}}^* \boldsymbol{u}_{\mathrm{s}}^* T^* \right) = \boldsymbol{\nabla} \cdot \left(k_{\mathrm{s}}^* \boldsymbol{\nabla} T^* \right), \tag{2.33}$$

where $c_{p,\mathrm{s}}^*$ is the specific heat capacity of the solid at constant pressure and k_{s}^* is the thermal conductivity of the solid. As the solid is an idealisation of multiple species, $c_{p,\mathrm{s}}^*$ and k_{s}^* will depend on the volume fraction and physical properties of each species, and in the latter case on the temperature. We could extend this equation to additionally model the effect of radiation between the particles, by adding to the right-hand side of (2.33) a nonlinear diffusion term $\boldsymbol{\nabla} \cdot (k_{\mathrm{rad}} T^3 \boldsymbol{\nabla} T)$, where k_{rad} is a constant. A term of this form was used in [9] and [74] to model radiative transfer in a porous material, and it has also been derived rigorously via homogenisation in [64]. However, as we are not considering radiative transfer through Ω_{g}^*, it would be inconsistent to include it here.

2.1.3 Boundary conditions

In this section, we prescribe the boundary conditions on each interface in the domain. The locations of the boundaries are shown in Figure 2.1.

2.1.3.1 Charge-surface boundary

At the top of the gas channel $\partial\Omega^*_{\mathrm{g,surf}}$, we impose the normal stress to equal atmospheric pressure, zero tangential stress, and no diffusive flux of heat and of SiO, i.e.

$$(-p^*\boldsymbol{I}+\boldsymbol{\tau}^*)\cdot\boldsymbol{n}_{\mathrm{g}}=-p^*_{\mathrm{surf}}\boldsymbol{n}_{\mathrm{g}},\quad \boldsymbol{\nabla}T^*\cdot\boldsymbol{n}_{\mathrm{g}}=0,\quad \boldsymbol{\nabla}Y_{\mathrm{SiO}}\cdot\boldsymbol{n}_{\mathrm{g}}=0\quad \text{at } \partial\Omega^*_{\mathrm{g,surf}}, \tag{2.34}$$

where $\boldsymbol{n}_{\mathrm{g}}$ is the outwards pointing unit normal to Ω^*_{g} and p^*_{surf} is taken to be atmospheric pressure. The zero tangential stress condition, zero conductive flux, and zero diffusive flux condition are chosen as they are passive boundary conditions, commonly used for outlets which are not expected to alter the gas solution far upstream.

At the top solid boundary $\partial\Omega^*_{\mathrm{s,surf}}$, we impose the rate at which new solid material is added $w^*_{\mathrm{s,surf}}$, and the temperature of the incoming solid material T^*_{surf},

$$w^*_{\mathrm{s}}=w^*_{\mathrm{s,surf}},\quad T^*=T^*_{\mathrm{surf}}\ \text{ at }\ \partial\Omega^*_{\mathrm{s,surf}}, \tag{2.35}$$

where $\boldsymbol{n}_{\mathrm{s}}$ is the outwards pointing unit normal from Ω^*_{s}.

2.1.3.2 Charge-crater boundary

At the bottom of the gas channel $\partial\Omega^*_{\mathrm{g,crat}}$ we impose the normal stress of the gas so that the gas pressure approximately equals pressure measurements of the crater p^*_{crat}, and assume a unidirectional flow. We also fix the gas temperature T^*_{crat} and the mass fraction of SiO, Y_{crat}, based on industrial measurements. Thus, the boundary conditions at the charge-crater boundary are given by

$$\boldsymbol{n}_{\mathrm{g}}\cdot(-p^*\boldsymbol{I}+\boldsymbol{\tau}^*)\cdot\boldsymbol{n}_{\mathrm{g}}=-p^*_{\mathrm{crat}},\ \boldsymbol{u}^*\times\boldsymbol{n}_{\mathrm{g}}=\boldsymbol{0},\ T^*=T^*_{\mathrm{crat}},\ Y_{\mathrm{SiO}}=Y_{\mathrm{crat}}\ \text{ at }\ \partial\Omega^*_{\mathrm{g,crat}}. \tag{2.36}$$

For the solid boundary at the bottom of the domain $\partial\Omega^*_{\mathrm{s,crat}}$, we impose the temperature to be equal to that imposed on the gas,

$$T^*=T^*_{\mathrm{crat}}\ \text{ at }\ \partial\Omega^*_{\mathrm{s,crat}}. \tag{2.37}$$

This boundary condition is a very crude model for the effect of radiative heating in the crater on the surrounding solid material, which is beyond the scope of our analysis but is discussed in detail in [45].

2.1.3.3 Interface

We now consider the appropriate boundary conditions for the interface $\partial\Omega^*_{\text{Inter}}$ between the gas and the solid. This is the location at which we assume the gas-solid reactions occur. For simplicity, it is assumed that there are always sufficient solid reactants available on the interface for all the reactions considered.

As mentioned in the introduction to the chapter, we will assume the interface's position is fixed for all time, implying no additional material is being deposited by the reactions. Since we will account for the mass of gas consumed by these reactions in the boundary conditions presented below, this implies that mass is not being conserved across the interface. Nevertheless, the assumption of a fixed interface is reasonable when only considering reaction 1 in (1.2), where the amount of mass deposited will be quite small, with each mole of SiO that reacts depositing $M^*_{\text{SiO}} - M^*_{\text{CO}}$ solid mass. In fact, in Chapters 4 and 5, the molar masses of the two gas species are assumed to be equal, implying the interface is fixed. However, in reaction 2 in (1.2), all the mass in the gaseous reactants is transformed into condensate, making the fixed interface assumption less justifiable when reaction 2 is included. Modifications to these boundary conditions to allow the interface to evolve are therefore an important area for future work, and are discussed in detail in Chapter 6.

We denote by $\mathcal{Q}^*_{i,X}$ the rate at which mass of species X is produced by reaction i on the interface [$\text{kg}\,\text{m}^{-2}\,\text{sec}^{-1}$], and write

$$\mathcal{Q}^*_{i,X} = \nu_{i,X} M^*_X \mathcal{R}^*_i, \tag{2.38}$$

where $\mathcal{R}^*_i$ is the rate of reaction i per unit area [$\text{mol}\,\text{m}^{-2}\,\text{sec}^{-1}$] and the dimensionless quantity $\nu_{i,X}$ encodes the stoichiometry of species X in reaction i: $\nu_{i,X} < 0$ when species i is consumed and $\nu_{i,X} > 0$ when species i is produced.

By considering conservation of mass for each gas species, we obtain the following boundary conditions

$$\rho^*_{\text{SiO}} \boldsymbol{u}^*_{\text{SiO}} \cdot \boldsymbol{n}_{\text{g}} = -\sum_i \mathcal{Q}^*_{i,\text{SiO}}, \quad \rho^*_{\text{CO}} \boldsymbol{u}^*_{\text{CO}} \cdot \boldsymbol{n}_{\text{g}} = -\sum_i \mathcal{Q}^*_{i,\text{CO}} \quad \text{on } \partial\Omega^*_{\text{Inter}}. \tag{2.39}$$

Using the definitions of the mass fraction and mass-averaged velocity, (2.2) and (2.6) respectively, these conditions can be combined to derive an expression for the total mass flux of gas into the boundary, namely

$$\rho^* \boldsymbol{u}^* \cdot \boldsymbol{n}_{\text{g}} = -\sum_i \left(\mathcal{Q}^*_{i,\text{CO}} + \mathcal{Q}^*_{i,\text{SiO}} \right) \quad \text{on } \partial\Omega^*_{\text{Inter}}. \tag{2.40}$$

We can also use the expression for the diffusion velocity, (2.22), to rewrite the condition for the mass flux of SiO as

$$(\rho^* Y_{\mathrm{SiO}} \boldsymbol{u}^* - \rho^* \mathcal{D}^*_{\mathrm{SiOCO}} \nabla Y_{\mathrm{SiO}}) \cdot \boldsymbol{n}_{\mathrm{g}} = -\sum_i \mathcal{Q}^*_{i,\mathrm{SiO}} \quad \text{on } \partial\Omega^*_{\mathrm{Inter}}. \tag{2.41}$$

Next, as we are considering a viscous gas, we must impose conditions on the other components of velocity and so consider what slip condition is appropriate. Calculating the Knudsen number Kn, defined as the ratio of the mean-free path of the gas to the radius of the channel using the formula for mean-free path in [65] and values from tables 2.1 and 2.2, we see that $\mathrm{Kn} = 4.3 \times 10^{-4} < 10^{-3}$. This implies that viscous slip on the interface will be negligible. For a single-phase gas we could therefore conclude that a continuum model with a no-slip condition is valid [65]. However, for a multi-component mixture of gases, diffusive slip, where the mass-averaged velocity of the mixture is non-zero, can occur at any Knudsen number, and may be significant if the effect of mixture density gradient is greater than the effect of total pressure gradient [3, 96]. Using the expression for the diffusive slip derived in [96], the appropriate slip boundary conditions for the binary gas mixture are therefore

$$\begin{aligned}(\boldsymbol{u}^* - \boldsymbol{u}^*_{\mathrm{s}}) \times \boldsymbol{n}_{\mathrm{g}} \\ = -\left(\frac{(M^*_{\mathrm{CO}})^{-1/2} \rho^*_{\mathrm{CO}} \boldsymbol{U}^*_{\mathrm{CO}} + (M^*_{\mathrm{SiO}})^{-1/2} \rho^*_{\mathrm{SiO}} \boldsymbol{U}^*_{\mathrm{SiO}}}{(M^*_{\mathrm{CO}})^{-1/2} \rho^*_{\mathrm{CO}} + (M^*_{\mathrm{SiO}})^{-1/2} \rho^*_{\mathrm{SiO}}} \right) \times \boldsymbol{n}_{\mathrm{g}} \quad \text{on } \partial\Omega^*_{\mathrm{Inter}},\end{aligned} \tag{2.42}$$

where the second term on the left-hand side accounts for the movement of the solid material. This condition may be rewritten to eliminate the diffusive velocities, using (2.2) and (2.22), as

$$\begin{aligned}(\boldsymbol{u}^* - \boldsymbol{u}^*_{\mathrm{s}}) \times \boldsymbol{n}_{\mathrm{g}} \\ = \mathcal{D}^*_{\mathrm{SiOCO}} \left(\frac{1 - \left(\frac{M^*_{\mathrm{CO}}}{M^*_{\mathrm{SiO}}} \right)^{-1/2}}{Y_{\mathrm{SiO}} + \left(\frac{M^*_{\mathrm{CO}}}{M^*_{\mathrm{SiO}}} \right)^{-1/2} (1 - Y_{\mathrm{SiO}})} \right) \boldsymbol{\nabla} Y_{\mathrm{SiO}} \times \boldsymbol{n}_{\mathrm{g}} \quad \text{on } \partial\Omega^*_{\mathrm{Inter}}.\end{aligned} \tag{2.43}$$

Finally, we require two boundary conditions for the energy equations. The first is to require continuity of temperature across the interface,

$$\lim_{\Omega^*_{\mathrm{g}} \to \partial\Omega^*_{\mathrm{Inter}}} T^* = \lim_{\Omega^*_{\mathrm{s}} \to \partial\Omega^*_{\mathrm{Inter}}} T^* \quad \text{on } \partial\Omega^*_{\mathrm{Inter}}, \tag{2.44}$$

where $\lim_{A \to \partial A}$ implies the limit approaching the boundary of a set A from the interior of A. The second condition, derived similarly to the Stefan condition in a phase-change problem, says that the change in heat flux across the boundary is equal to

enthalpy change due to the reaction,

$$\lim_{\Omega_{\mathrm{g}}^* \to \partial\Omega_{\mathrm{Inter}}^*} \left(\left(\rho^* c_{p,\mathrm{CO}}^* \boldsymbol{u}^* T^* - \left(1 - \frac{c_{p,\mathrm{SiO}}^*}{c_{p,\mathrm{CO}}^*} \right) \rho^* c_{p,\mathrm{CO}}^* \boldsymbol{u}^* T^* Y_{\mathrm{SiO}} - k_{\mathrm{g}}^* \nabla T^* \right) \cdot \boldsymbol{n}_{\mathrm{g}} \right) + \lim_{\Omega_{\mathrm{s}}^* \to \partial\Omega_{\mathrm{Inter}}^*} \left((-k_{\mathrm{s}}^* \nabla T^*) \cdot \boldsymbol{n}_{\mathrm{s}} \right) = -\sum_i \mathcal{S}_i^*, \quad (2.45)$$

on $\partial\Omega_{\mathrm{Inter}}^*$, where $\mathcal{S}_i^*$ is the enthalpy change due to reaction i, $[\mathrm{J\,m^{-2}\,sec^{-1}}]$ given by

$$\mathcal{S}_i^* = \mathcal{R}_i^* \Delta H_i^* \quad (2.46)$$

in terms of the standard enthalpy of reaction of reaction i, ΔH_i^* $[\mathrm{J\,mol^{-1}}]$. As we are primarily interested in the change in temperature in the local surrounding region caused by the reaction, we will follow [74] and have $\Delta H_i^* > 0$ for exothermic reactions, and $\Delta H_i^* < 0$ for endothermic reactions, which is consistent with exothermic reactions acting as heat sources, and endothermic reactions acting as heat sinks. However, we note that this is the opposite convention to the majority of the chemical engineering literature (see for example [33]).

The first two terms in (2.45) represents the thermal energy of the mass of gas consumed by the reaction, the third and fourth terms are the conductive heat transfer in the gas and solids respectively, and the final term is the enthalpy of reaction. Here the enthalpy of reaction acts as a heat source or sink, just as the latent heat does in a phase-change problem.

Although, as discussed above, the fixed position of the interface implies that the total mass of the system is not conserved, (2.45) is defined so that the total energy in the system is conserved, as the internal energy of the gas consumed and created by the reactions is correctly accounted for. However, with no new solid being deposited, none of the energy flux from the reaction will be allocated to the internal energy of the new material, meaning the pre-existing solid material will receive a larger heat flux than it would in reality, and hence its temperature will be over-predicted. It is possible to partially correct for this over-prediction by reducing the value of the standard enthalpy of reaction ΔH_i^* by an amount equal to the internal energy of the newly created solid products. For example, denoting the modified values of ΔH_i^* by $\widetilde{\Delta H}_i^*$, the modified value for reaction 2 would be given by

$$\widetilde{\Delta H}_2^* = \Delta H_2^* - \frac{1}{2} \left(c_{p,\mathrm{SiO2}}^* T^* M_{\mathrm{SiO2}}^* + c_{p,\mathrm{Si}}^* T^* M_{\mathrm{Si}}^* \right), \quad (2.47)$$

where M_{SiO2}^* and M_{Si}^* are the molar weights of SiO_2(l) and Si, and $c_{p,\mathrm{SiO2}}^*$ and $c_{p,\mathrm{Si}}^*$ are the specific heat capacities of SiO_2(l) and Si, respectively. The factor of a half

comes from the stoichiometry in (1.2). However, using this modified value would mean the model under-estimates the contribution of the chemical energy when comparing the relative amounts of heating provide to the solid raw material by different sources. Moreover, unlike ΔH_i^* , $\widetilde{\Delta H}_i^*$ is temperature dependent, which introduces an additional complication in the analysis of the model. Hence, we continue to use the unmodified values for the remainder of the thesis.

This completes the boundary conditions on $\partial\Omega^*_{\text{Inter}}$, up to the choice of model for the reaction rates, $\mathcal{R}_i^*$. For the majority of this thesis we will leave both the number and form of the reactions arbitrary, so that the models may be more easily applied to other processes. However, we propose the following forms of $\mathcal{R}_i$ as suitable models for reactions 1 and 2 in (1.2), the formation of SiC, and the condensation of SiO respectively.

Previous studies of reactions 1 and 2 have focused on modelling a volumetric, not a surface reaction rate. This makes it difficult to use the limited amount of data in the literature to parameterise our model, but we can reasonably expect the functional form of the reaction rate's dependence on local environmental factors such as the temperature and the partial pressure to remain unchanged. In [2] and [78], the rates of both reactions 1 and 2 are modelled to be zero when the partial pressure of SiO was below the temperature-dependent equilibrium partial pressure of the reaction, and linearly increasing with partial pressure above it. We will adopt the simpler model that the reaction rate is linearly proportional to the molar concentration of the reactant gas species SiO, and also proportional to an arbitrary dimensionless function of temperature $F_i\left(T^*\right)$, so that the rate of reaction i per unit area, is given by

$$\mathcal{R}_i^* = \zeta_i^* c_{\text{SiO}}^* F_i\left(T^*\right) = \zeta_i^* M_{\text{SiO}}^* \rho^* Y_{\text{SiO}} F_i\left(T^*\right), \tag{2.48}$$

for $i = 1, 2$, where ζ_i^* is the reaction constant $[\mathrm{m\,sec^{-1}}]$, and the second equality follows from (2.2)–(2.3).

For reaction 1, the equilibrium partial pressure remains less than 1 % across the entire temperature range of interest and there is no large energy barrier to overcome [74], implying the temperature dependence of reaction 1 is a small effect (at least above the minimum temperature in the furnace). Hence, we take

$$F_1\left(T^*\right) = 1, \tag{2.49}$$

implying temperature has no direct effect on reaction 1.

In contrast, reaction 2 is known to be highly temperature dependent. Above 2080 K SiO gas is stable, and reaction 2 never occurs. Below this temperature, the

reaction increases rapidly to a maximum rate, found to occur at 1920 K in an experimental study in [8]. This is accounted for by [2] and [78] through the equilibrium partial pressure rapidly changing. We will approximate this using a logistic function,

$$F_2\left(T^*\right) = \frac{1}{1 + \exp\left(\dfrac{T^* - T^*_{\text{cond}}}{\xi^*}\right)}, \tag{2.50}$$

where $T^*_{\text{cond}} = 2000\,\text{K}$, which we will refer to as the 'condensation temperature', is the centre of this smoothed Heavyside function, and ξ^* is a constant [K] controlling the rate of increase. Below 1920 K, [8] found that the reaction rate decreased as temperature decreased, which they modelled with an Arrhenius function. However, we will follow [2] and [78] and assume the activation energy of this reaction is small, and neglect this effect.

2.1.3.4 Periodicity

On the outer boundary $\partial\Omega^*$ of the solid around each channel, we will assume the solution to be periodic

$$T^* \text{ periodic} \qquad \text{on } \partial\Omega^*, \tag{2.51}$$

and further assume that the temperature varies smoothly over $\partial\Omega^*$.

2.1.4 Fluxes

Sections 2.1.1–2.1.3 fully specify the model of the charge material. However, to interpret solutions of the model, it is useful to also define quantities associated with the overall fluxes of mass and energy through the charge. These will be used regularly throughout the subsequent chapters to quantify the overall behaviour of the model.

The total mass flux of gas along the channel [$\text{kg}\,\text{s}^{-1}$] in the axial direction is given by

$$Q^*_{\text{g}} = \int_{\mathcal{C}^*_{\text{g}}} \rho^* \boldsymbol{u}^* \cdot \boldsymbol{k}\,\mathrm{d}A, \tag{2.52}$$

where $\mathcal{C}^*_{\text{g}}$ is the cross-section of Ω^*_{g} perpendicular to the axial direction. The mass fluxes of the individual gas species are given by

$$Q^*_{\text{SiO}} = \int_{\mathcal{C}^*_{\text{g}}} \rho^* Y_{\text{SiO}} \boldsymbol{u}^* \cdot \boldsymbol{k}\,\mathrm{d}A, \quad Q^*_{\text{CO}} = \int_{\mathcal{C}^*_{\text{g}}} \rho^* \left(1 - Y_{\text{SiO}}\right) \boldsymbol{u}^* \cdot \boldsymbol{k}\,\mathrm{d}A. \tag{2.53}$$

The total mass flux of solid in the vertical direction is defined as

$$Q^*_{\text{s}} = \int_{\mathcal{C}^*_{\text{s}}} \rho^*_{\text{s}} \boldsymbol{u}^*_{\text{s}} \cdot \boldsymbol{k}\,\mathrm{d}A, \tag{2.54}$$

where $\mathcal{C}_{\mathrm{s}}^*$ is the cross-section of Ω_{s}^* perpendicular to the axial direction of the gas channel.

The total outwards energy fluxes [$\mathrm{J\,s^{-1}}$] through $\partial\Omega_{\mathrm{g,crat}}^*$ and $\partial\Omega_{\mathrm{g,surf}}^*$ respectively, are given by

$$E_{\mathrm{g,crat}}^* = \int_{\partial\Omega_{\mathrm{g,crat}}^*} \left(\rho^* c_{p,\mathrm{CO}}^* \boldsymbol{u}^* T^* - \left(1 - \frac{c_{p,\mathrm{SiO}}^*}{c_{p,\mathrm{CO}}^*}\right) \rho^* c_{p,\mathrm{CO}}^* \boldsymbol{u}^* T^* Y + \frac{1}{2}\rho^* \left\|\boldsymbol{u}^*\right\|_2^2 \boldsymbol{u}^* - \boldsymbol{\tau}^* \boldsymbol{u}^* - k_g^* \boldsymbol{\nabla} T \right) \cdot \boldsymbol{n}_{\mathrm{g}} \,\mathrm{d}A, \quad (2.55a)$$

$$E_{\mathrm{g,surf}}^* = \int_{\partial\Omega_{\mathrm{g,surf}}^*} \left(\rho^* c_{p,\mathrm{CO}}^* \boldsymbol{u}^* T^* - \left(1 - \frac{c_{p,\mathrm{SiO}}^*}{c_{p,\mathrm{CO}}^*}\right) \rho^* c_{p,\mathrm{CO}}^* \boldsymbol{u}^* T^* Y + \frac{1}{2}\rho^* \left\|\boldsymbol{u}^*\right\|_2^2 \boldsymbol{u}^* - \boldsymbol{\tau}^* \boldsymbol{u}^* - k_g^* \boldsymbol{\nabla} T \right) \cdot \boldsymbol{n}_{\mathrm{g}} \,\mathrm{d}A, \quad (2.55b)$$

where $\|\boldsymbol{u}^*\|_2$ is the two-norm of $\boldsymbol{u}^*$. The total outwards energy fluxes through $\partial\Omega_{\mathrm{s,crat}}^*$ and $\partial\Omega_{\mathrm{s,surf}}^*$ are given by

$$E_{\mathrm{s,crat}}^* = \int_{\partial\Omega_{\mathrm{s,crat}}^*} \left(\rho_{\mathrm{s}}^* c_{p,\mathrm{s}}^* \boldsymbol{u}_{\mathrm{s}}^* T^* - k_{\mathrm{s}}^* \boldsymbol{\nabla} T^*\right) \cdot \boldsymbol{n}_{\mathrm{s}} \,\mathrm{d}A, \quad (2.56a)$$

$$E_{\mathrm{s,surf}}^* = \int_{\partial\Omega_{\mathrm{s,surf}}^*} \left(\rho_{\mathrm{s}}^* c_{p,\mathrm{s}}^* \boldsymbol{u}_{\mathrm{s}}^* T^* - k_{\mathrm{s}}^* \boldsymbol{\nabla} T^*\right) \cdot \boldsymbol{n}_{\mathrm{s}} \,\mathrm{d}A. \quad (2.56b)$$

The thermal energy removed from $\Omega_{\mathrm{s}} \cup \Omega_{\mathrm{g}}$ per unit time due to the reactions is given by

$$E_{\mathrm{React}}^* = -\int_{\partial\Omega_{\mathrm{Inter}}^*} \sum_i \mathcal{S}_i^* \,\mathrm{d}A. \quad (2.57)$$

Since we have periodic boundary conditions on $\partial\Omega^*$, there is no flux of energy through $\partial\Omega^*$. Hence, for steady solutions to the model, we have that conservation of energy is given by

$$E_{\mathrm{g,crat}}^* + E_{\mathrm{g,surf}}^* + E_{\mathrm{s,crat}}^* + E_{\mathrm{s,surf}}^* + E_{\mathrm{React}}^* = 0. \quad (2.58)$$

2.1.5 Summary of the dimensional model

In summary, our model for the gas flow in Ω_{g}^* consists of five governing equations: conservation of total mass (2.10); conservation of total momentum (2.16); conservation of mass of SiO(g) (2.23); conservation of energy (2.29); and the equation of state (2.30), which are written in terms of five variables, namely $\rho^*, \boldsymbol{u}^*, p^*, T^*$ and Y_{SiO}.

This is coupled to the model for the solid in Ω_{s}^*, consisting of two governing equation for conservation of mass (2.32); and conservation of energy (2.33), which may be written in terms of two variables, w_{s}^* and T^*. The boundary conditions, which couple the gas and solid's behaviour, are given by (2.34)–(2.37), (2.40)–(2.41), (2.43)–(2.45), and (2.51). Values of the parameters in this model, based, where possible, on measurements of industrial furnaces are given in Table 2.1. We use their values to determine the scalings used in the nondimensionalisation of the model in the next section.

However, before carrying out the nondimensionalisation, it is useful to first introduce an alternative cylindrical coordinate system (r^*, θ, z^*), with

$$x^* = r^* \cos(\theta), \quad y^* = r^* \sin(\theta). \tag{2.59}$$

We adopt this mix of Cartesian and cylindrical coordinates, as although Ω_{g}^* is cylindrical, Ω_{s}^* is not, and so there is no reason to expect the solution to be axisymmetric in Ω_{g}^*, and hence simplify in cylindrical coordinates. (Indeed, showing the gas problem to be approximately axisymmetric will form an important part of the asymptotic analysis considered in Chapter 5.) When in the Cartesian coordinate system we will write the components of the gas velocity as $\boldsymbol{u}^* = \left(u_x^*, v_y^*, w_z^*\right)$, while in cylindrical coordinates we will write $\boldsymbol{u}^* = (u_r^*, v_\theta^*, w_z^*)$.

2.2 Nondimensionalisation

2.2.1 Scalings

We will nondimensionalise the problem using the following scalings

$$\begin{gathered}
t^* = [t]t, \quad (x^*, y^*, z^*) = h^*(\epsilon x, \epsilon y, z), \\
(u_x^*, v_y^*, w_z^*) = [w_{\mathrm{g}}](\epsilon u_x, \epsilon v_y, w_z), \quad w_{\mathrm{s}}^* = [w_{\mathrm{s}}]w_{\mathrm{s}}, \\
p^* = p_{\mathrm{crat}}^* + \Delta p^* p, \quad T^* = T_{\mathrm{crat}}^* T, \quad \rho^* = [\rho_{\mathrm{g}}]\rho, \\
\mu^* = [\mu]\mu, \quad k_{\mathrm{g}}^* = [k_{\mathrm{g}}]k_{\mathrm{g}}, \quad \mathcal{D}_{\mathrm{SiOCO}}^* = [\mathcal{D}_{\mathrm{SiOCO}}]\mathcal{D}, \quad \boldsymbol{\tau}^* = \frac{[\mu][w_{\mathrm{g}}]}{\epsilon h^*}\boldsymbol{\tau}, \\
k_{\mathrm{s}}^* = [k_{\mathrm{s}}]k_{\mathrm{s}}, \quad \rho_{\mathrm{s}}^* = [\rho_{\mathrm{s}}]\rho_{\mathrm{s}}, \quad \mathcal{R}_i^* = [\mathcal{R}_i]\mathcal{R}_i, \\
(Q^*, Q_{\mathrm{SiO}}^*, Q_{\mathrm{CO}}^*, Q_{\mathrm{s}}^*) = [Q]\left(Q, Q_{\mathrm{SiO}}, Q_{\mathrm{CO}}, Q_{\mathrm{s}}\right), \\
\left(E_{\mathrm{g,crat}}^*, E_{\mathrm{s,crat}}^*, E_{\mathrm{g,surf}}^*, E_{\mathrm{s,surf}}^*, E_{\mathrm{React}}^*\right) = [E]\left(E_{\mathrm{g,crat}}, E_{\mathrm{s,crat}}, E_{\mathrm{g,surf}}, E_{\mathrm{s,surf}}, E_{\mathrm{React}}\right),
\end{gathered} \tag{2.60}$$

where $\epsilon = a^*/h^*$ is the aspect ratio of a gas channel, and $\Delta p^* = p_{\mathrm{crat}}^* - p_{\mathrm{surf}}^*$ is the dimensional pressure drop. The definition of the characteristic values, denoted by square brackets, is given below. We also write $Y_{\mathrm{SiO}} = Y$ to simplify the notation.

Parameter	Value	Reference
a^*	1×10^{-3} to $1 \times 10^{-2}\,\mathrm{m}$	[30]
h^*	$3\,\mathrm{m}$	[67]
T^*_{crat}	$2273\,\mathrm{K}$	[67]
T^*_{surf}	$523\,\mathrm{K}$	[67, 32]
p^*_{crat}	$1.04 \times 10^5\,\mathrm{Pa}$	[31, 33]
p^*_{surf}	$1.00 \times 10^5\,\mathrm{Pa}$	[33]
Y_{crat}	0.61	[30]
$c^*_{p,\mathrm{CO}}$	$1.34 \times 10^3\,\mathrm{J\,kg^{-1}\,K^{-1}}$	Equation (A.10)
$c^*_{p,\mathrm{SiO}}$	$8.49 \times 10^2\,\mathrm{J\,kg^{-1}\,K^{-1}}$	Equation (A.10)
R^*	$8.314\,\mathrm{J\,K^{-1}\,mol^{-1}}$	Universal gas constant
M^*_{CO}	$2.801 \times 10^{-2}\,\mathrm{kg\,mol^{-1}}$	Molar weight CO
M^*_{SiO}	$4.408 \times 10^{-2}\,\mathrm{kg\,mol^{-1}}$	Molar weight SiO
$c^*_{p,\mathrm{s}}$	$1.47 \times 10^3\,\mathrm{J\,kg^{-1}\,K^{-1}}$	[30]
$w^*_{\mathrm{s,surf}}$	$2.78 \times 10^{-4}\,\mathrm{m\,s^{-1}}$	[45]
ΔH^*_1	$7.76 \times 10^4\,\mathrm{J\,mol^{-1}}$	[33]
ΔH^*_2	$3.07 \times 10^5\,\mathrm{J\,mol^{-1}}$	[33]
$\nu_{1,\mathrm{SiO}}$	-1	Equation (1.2)
$\nu_{1,\mathrm{CO}}$	1	Equation (1.2)
$\nu_{2,\mathrm{SiO}}$	-2	Equation (1.2)
$\nu_{2,\mathrm{CO}}$	0	Equation (1.2)

Table 2.1: Dimensional parameter values.

In nondimensionalising the coordinate system, we have scaled the x- and y-coordinates by a factor of ϵ, in anticipation of exploiting the small aspect ratio to derive a simplified model. Consequently the corresponding components of velocity are also rescaled by the factor ϵ to retain a balance in (2.10). The pressure is scaled according to the imposed pressure gradient based on the measurements of an industrial furnace. The gas mixture's viscosity, binary diffusion coefficient, and thermal conductivity are all scaled by reference values taken to be the conditions at $\partial\Omega^*_{\mathrm{crat,g}}$, while the solid's density and thermal conductivity are scaled by reference values taken at $\partial\Omega^*_{\mathrm{surf,s}}$. The mass fluxes for the different gas species and the solid are scaled by the natural scaling for the total mass flux of gas. The choice of the gas and solid velocity scales $[w_{\mathrm{g}}]$ and $[w_{\mathrm{s}}]$, along with the gas density scale $[\rho_{\mathrm{g}}]$, the mass flux scale $[Q]$, the energy flux scale $[E]$, the reaction rate scales $[\mathcal{R}_i]$ for all i, and the timescale $[t]$ are discussed in more detail below. We will write Ω_{g} and Ω_{s} for the dimensionless gas and solid regions respectively, as illustrated in Figure 2.2, together with the dimensionless independent variables in both coordinate systems.

The gas density scaling $[\rho_{\mathrm{g}}]$ is chosen so that the equation of state (2.30) exactly

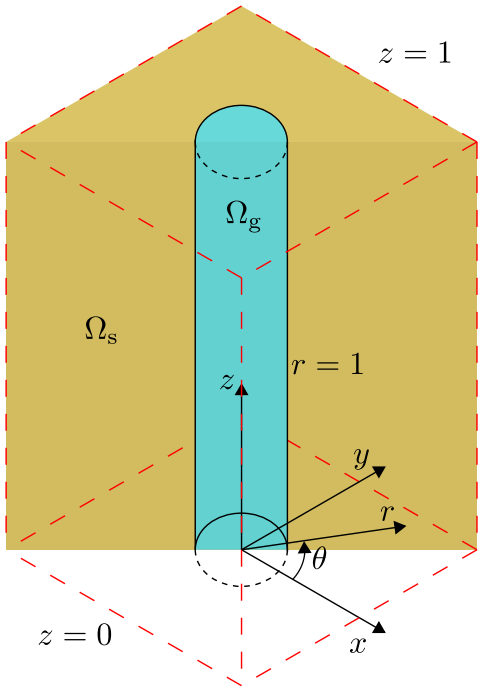


Figure 2.2: The dimensionless Cartesian and polar coordinate systems.

balances for a flow of pure CO(g) at $\partial\Omega_{\text{crat}}$, i.e.

$$[\rho_g] = \frac{M_{CO} p_{\text{crat}}}{R T_{\text{crat}}}. \tag{2.61}$$

The gas velocity scale $[w_g]$ is chosen so that pressure in the axial momentum equation (2.68d) balances the perpendicular viscous forces,

$$[w_g] = \frac{\epsilon^2 \Delta p^* h^*}{[\mu]}. \tag{2.62}$$

Thus $[w_g]$ can be interpreted as the velocity of a purely viscous flow along the channel, driven by the pressure drop measured for an industrial furnace, in the absence of reactions and density variations. We pick this velocity scale as the viscous-dominated limit of our model will be shown later to be of industrial relevance, and the focus of study in chapter 5. This choice of gas velocity scale also sets the scaling for the mass fluxes:

$$[Q] = \epsilon^2 (h^*)^2 [\rho_g][w_g]. \tag{2.63}$$

We choose to scale the energy fluxes by the thermal energy of the gas, so that

$$[E] = \epsilon^2 (h^*)^2 [\rho_g][w_g] c^*_{p,\text{CO}} T^*_{\text{crat}}, \tag{2.64}$$

as we know from industrial measurements this should change significantly between the charge-crater and charge-surface boundaries.

Parameter	Value	Reference
$[\rho_{\mathrm{g}}]$	$0.154\,\mathrm{kg\,m^{-3}}$	Equation (2.61)
$[w_{\mathrm{g}}]$	1.82×10^{1} to $1.82 \times 10^{3}\,\mathrm{m\,s^{-1}}$	Equation (2.62)
$[Q]$	2.81×10^{-6} to $2.81 \times 10^{-2}\,\mathrm{kg\,s^{-1}}$	Equation (2.63)
$[E]$	8.30 to $8.30 \times 10^{4}\,\mathrm{J\,s^{-1}}$	Equation (2.64)
$[w_{\mathrm{s}}]$	$2.78 \times 10^{-4}\,\mathrm{m\,s^{-1}}$	Equation (2.66)
$[t]$	$1.08 \times 10^{4}\,\mathrm{s}$	Equation (2.67)
$[\mu]$	$7.32 \times 10^{-5}\,\mathrm{kg\,m^{-1}\,s^{-1}}$	Equation (A.3)
$[k_{\mathrm{g}}]$	$9.60 \times 10^{-2}\,\mathrm{J\,m^{-1}\,s^{-1}\,K^{-1}}$	Equation (A.7)
$[\mathcal{D}_{\mathrm{SiOCO}}]$	$5.10 \times 10^{-4}\,\mathrm{m^{2}\,s^{-1}}$	Equation (A.9)
$[\rho_{\mathrm{s}}]$	$2.1 \times 10^{3}\,\mathrm{kg\,m^{-3}}$	[45]
$[k_{\mathrm{s}}^{*}]$	$10\,\mathrm{J\,m^{-1}\,s^{-1}\,K^{-1}}$	[2]

Table 2.2: Values of the dimensional scaling chosen in (2.60).

For each reaction we scale the reaction by a different constant $[\mathcal{R}_i]$, so that the maximum dimensionless rate $\mathcal{R}_i$ is order unity for all i. As the definition of $[\mathcal{R}_i]$ will depend on the particular choice of reaction model, we will present the remainder of the derivation in terms of an arbitrary scaling. However, for the form of the reactions rate given in (2.48) to model reactions in the furnace, the scaling is given by

$$[\mathcal{R}_i] = \zeta_i^{*} M_{\mathrm{SiO}}^{*} [\rho_{\mathrm{g}}]. \tag{2.65}$$

As the solid is moving much more slowly than the gas, we scale the solid velocity by the rate at which new material is being added to the top surface of the charge, (2.35),

$$[w_{\mathrm{s}}] = w_{\mathrm{s,surf}}^{*}. \tag{2.66}$$

There are a large number of possible timescales to consider in the model. Those associated with the gas phase are of a size of at most seconds, while the timescale of the motion of the solid through the charge is on the order of hours, and conduction of heat through the solid is on the order of days. We choose to focus on the timescale of advection in the solid, as this is the timescale of greatest industrial interest, being close to the time between stoking cycles for a typical furnace [67]. Hence, we pick $[t]$ to give a balance between the time derivative and advective term in (2.33), meaning

$$[t] = \frac{h}{[w_{\mathrm{s}}]}. \tag{2.67}$$

The value of the scalings described above, are given in Table 2.2, based on the parameter values in Table 2.1. With the dimensional scalings for the industrially-relevant parameter values fully determined, we now present the dimensionless model.

2.2.2 Dimensionless gas governing equations

We first substitute the scalings (2.60) into the governing equations for the gas, which consist of (2.10), (2.16), (2.23), (2.29), and (2.30). We present the resulting equations here in Cartesian coordinates, but for reference, they are also stated in cylindrical coordinates in Appendix B. Thus, in the gas channel Ω_{g}, ρ, u_x, v_y, w_z, p, Y, and T are governed by

$$\alpha\frac{\partial\rho}{\partial t}+\frac{\partial\left(\rho u_x\right)}{\partial x}+\frac{\partial\left(\rho v_y\right)}{\partial y}+\frac{\partial\left(\rho w_z\right)}{\partial z}=0, \tag{2.68a}$$

$$\begin{aligned}\epsilon^2\mathrm{Re}\left(\alpha\frac{\partial\left(\rho u_x\right)}{\partial t}+\frac{\partial\left(\rho u_x u_x\right)}{\partial x}+\frac{\partial\left(\rho u_x v_y\right)}{\partial y}+\frac{\partial\left(\rho u_x w_z\right)}{\partial z}\right)\\ =-\frac{1}{\epsilon^2}\frac{\partial p}{\partial x}+\frac{1}{\epsilon}\frac{\partial\tau_{xx}}{\partial x}+\frac{1}{\epsilon}\frac{\partial\tau_{xy}}{\partial y}+\frac{\partial\tau_{xz}}{\partial z},\end{aligned} \tag{2.68b}$$

$$\begin{aligned}\epsilon^2\mathrm{Re}\left(\alpha\frac{\partial\left(\rho v_y\right)}{\partial t}+\frac{\partial\left(\rho u_x v_y\right)}{\partial x}+\frac{\partial\left(\rho v_y v_y\right)}{\partial y}+\frac{\partial\left(\rho v_y w_z\right)}{\partial z}\right)\\ =-\frac{1}{\epsilon^2}\frac{\partial p}{\partial y}+\frac{1}{\epsilon}\frac{\partial\tau_{xy}}{\partial y}+\frac{1}{\epsilon}\frac{\partial\tau_{yy}}{\partial y}+\frac{\partial\tau_{yz}}{\partial z},\end{aligned} \tag{2.68c}$$

$$\begin{aligned}\epsilon^2\mathrm{Re}\left(\alpha\frac{\partial\left(\rho w_z\right)}{\partial t}+\frac{\partial\left(\rho u_x w_z\right)}{\partial x}+\frac{\partial\left(\rho v_y w_z\right)}{\partial y}+\frac{\partial\left(\rho w_z w_z\right)}{\partial z}\right)\\ =-\frac{\partial p}{\partial z}+\frac{\partial\tau_{xz}}{\partial r}+\frac{\partial\tau_{yz}}{\partial y}+\epsilon\frac{\partial\tau_{zz}}{\partial z},\end{aligned} \tag{2.68d}$$

$$\begin{aligned}&\epsilon^2\mathrm{Re}\left(\alpha\frac{\partial\left(\rho T\right)}{\partial t}+\frac{\partial\left(\rho u_x T\right)}{\partial x}+\frac{\partial\left(\rho v_y T\right)}{\partial y}+\frac{\partial\left(\rho w_z T\right)}{\partial z}\right)\\ &\quad-\epsilon^2\mathrm{Re}\left(1-\kappa\right)\left(\alpha\frac{\partial\left(\rho TY\right)}{\partial t}+\frac{\partial\left(\rho u_x TY\right)}{\partial x}+\frac{\partial\left(\rho v_y TY\right)}{\partial y}+\frac{\partial\left(\rho w_z TY\right)}{\partial z}\right)\\ &\qquad=\frac{1}{\mathrm{Pr}}\frac{\partial}{\partial x}\left(k\frac{\partial T}{\partial x}\right)+\frac{1}{\mathrm{Pr}}\frac{\partial}{\partial y}\left(k\frac{\partial T}{\partial y}\right)+\frac{\epsilon^2}{\mathrm{Pr}}\frac{\partial}{\partial z}\left(k\frac{\partial T}{\partial z}\right)\\ &\qquad\quad+\mathrm{Ec}\left(\alpha\frac{\partial p}{\partial t}+u_x\frac{\partial p}{\partial x}+v_y\frac{\partial p}{\partial y}+w_z\frac{\partial p}{\partial z}\right)+\epsilon^2\mathrm{Ec}\Phi,\end{aligned} \tag{2.68e}$$

$$\begin{aligned}\epsilon^2\mathrm{Re}\left(\alpha\frac{\partial\left(\rho Y\right)}{\partial t}+\frac{\partial\left(\rho u_x Y\right)}{\partial x}+\frac{\partial\left(\rho v_y Y\right)}{\partial y}+\frac{\partial\left(\rho w_z Y\right)}{\partial z}\right)\\ =\frac{1}{\mathrm{Sc}}\frac{\partial}{\partial x}\left(\rho\mathcal{D}\frac{\partial Y}{\partial x}\right)+\frac{1}{\mathrm{Sc}}\frac{\partial}{\partial y}\left(\rho\mathcal{D}\frac{\partial Y}{\partial y}\right)+\frac{\epsilon^2}{\mathrm{Sc}}\frac{\partial}{\partial z}\left(\rho\mathcal{D}\frac{\partial Y}{\partial z}\right),\end{aligned} \tag{2.68f}$$

$$\Delta p\, p + 1 = \rho T \left(1 - (1 - \mathcal{M})\, Y\right), \tag{2.68g}$$

where the components of the dimensionless viscous stress tensor are given by

$$\tau_{xx} = \epsilon\mu \left(2\frac{\partial u_x}{\partial x} - \frac{2}{3}\left(\frac{\partial u_x}{\partial x} + \frac{\partial v_y}{\partial y} + \frac{\partial w_z}{\partial z}\right)\right), \tag{2.69a}$$

$$\tau_{yy} = \epsilon\mu \left(2\frac{\partial v_y}{\partial y} - \frac{2}{3}\left(\frac{\partial u_x}{\partial x} + \frac{\partial v_y}{\partial y} + \frac{\partial w_z}{\partial z}\right)\right), \tag{2.69b}$$

$$\tau_{zz} = \epsilon\mu \left(2\frac{\partial w_z}{\partial z} - -\frac{2}{3}\left(\frac{\partial u_x}{\partial x} + \frac{\partial v_y}{\partial y} + \frac{\partial w_z}{\partial z}\right)\right), \tag{2.69c}$$

$$\tau_{xy} = \epsilon\mu \left(\frac{\partial v_y}{\partial x} + \frac{\partial u_x}{\partial y}\right), \tag{2.69d}$$

$$\tau_{xz} = \mu \left(\frac{\partial w_z}{\partial x} + \epsilon^2\frac{\partial u_x}{\partial z}\right), \tag{2.69e}$$

$$\tau_{yz} = \mu \left(\epsilon^2\frac{\partial v_y}{\partial z} + \frac{\partial w_z}{\partial y}\right), \tag{2.69f}$$

and Φ is the dimensionless viscous dissipation, given by

$$\begin{aligned}\frac{\Phi}{\mu} = 2\Bigg(&\left(\frac{\partial u_x}{\partial x}\right)^2 + \left(\frac{\partial v_y}{\partial y}\right)^2 + \left(\frac{\partial w_z}{\partial z}\right)^2\Bigg) \\ &+ \left(\frac{\partial v_y}{\partial x} + \frac{\partial u_x}{\partial y}\right)^2 + \left(\frac{1}{\epsilon}\frac{\partial w_z}{\partial y} + \epsilon\frac{\partial v_y}{\partial z}\right)^2 \\ &+ \left(\epsilon\frac{\partial u_x}{\partial z} + \frac{1}{\epsilon}\frac{\partial w_z}{\partial x}\right)^2 - \frac{2}{3}\left(\frac{\partial u_x}{\partial x} + \frac{\partial v_y}{\partial y} + \frac{\partial w_z}{\partial z}\right)^2.\end{aligned} \tag{2.70}$$

Nondimensionalising the gas region introduced the following eight dimensionless parameters into the model:

$$\begin{aligned}&\mathrm{Re} = \frac{[\rho_\mathrm{g}][w_\mathrm{g}]h^*}{[\mu]}, \quad \mathrm{Pr} = \frac{c^*_{p,\mathrm{CO}}[\mu]}{[k_\mathrm{g}]}, \quad \mathrm{Sc} = \frac{[\mu]}{[\rho_\mathrm{g}][\mathcal{D}_{\mathrm{SiOCO}}]}, \\ &\Delta p = \frac{\Delta p^*}{p^*_\mathrm{crat}}, \quad \kappa = \frac{c^*_{p,\mathrm{SiO}}}{c^*_{p,\mathrm{SiO}}}, \quad \gamma = \frac{c^*_{p,\mathrm{CO}}}{c^*_{v,\mathrm{CO}}}, \quad \alpha = \frac{[w_\mathrm{s}]}{[w_\mathrm{g}]}, \quad \mathcal{M} = \frac{M^*_\mathrm{CO}}{M^*_\mathrm{SiO}},\end{aligned} \tag{2.71}$$

which are the Reynolds number; Prandtl number; Schmidt number; the dimensionless pressure change; the ratio of specific heat capacities at constant pressure of SiO and CO; the ratio of specific heat capacities of CO at constant pressure and at constant volume; the ratio of solid to gas velocity scales; and the ratio of molar weights, respectively. We have introduced the specific heat capacity at constant volume, given by

$$\frac{R^*}{M^*_\mathrm{CO}} = c^*_{p,\mathrm{CO}} - c^*_{v,\mathrm{CO}}, \tag{2.72}$$

since CO is assumed to be an ideal gas, in order to be consistent with the standard non-dimensionalisation of the Navier-Stokes equations (see, for example [68, 91]). Note that by using values of specific heat capacity given by (A.10) implies that $\kappa = \mathcal{M}$, but we will distinguish between them for the remainder of this chapter, as this will not hold in general. The Reynolds number measures the ratio of axial inertial to viscous forces, while the Prandtl and Schmidt numbers measure the relative importance of advective to diffusive transport of heat and mass in the gas, respectively.

The parameters, given by (2.71), form the basis which determine the value of all the dimensionless parameter groupings appearing in the gas model. Their values, based on the dimensional parameters and scalings in Tables 2.1 and 2.2, are given in Table 2.3. However, it the analysis in subsequent chapters, it will emerge that two groupings of these dimensionless parameters are particularly important to understanding the behaviour of the model. The first of these is the reduced Reynolds number, $\epsilon^2\mathrm{Re}$, which gives the ratio between axial inertial forces and transversal viscous forces. The other is the Eckert number, which appears in the energy equation (2.68e). It is defined as

$$\mathrm{Ec} = \frac{[w_\mathrm{g}]^2}{c_p^* T^*_\mathrm{crat}} = \epsilon^2 \mathrm{Re}(1-\gamma^{-1})\Delta p, \tag{2.73}$$

and expresses the relative importance of terms representing internal heating in the gas. From (2.73) it is clear that the Ec is proportional to both the reduced Reynolds number and the dimensionless pressure drop, which will become important in Chapter 3, when we consider different limits of the model. Therefore, we will use (2.73) to compactly write the Eckert number for the remainder of this chapter, then switch to its definition for the remainder of the thesis. Values of the reduced Reynolds number and the Eckert number, based on the industrially-relevant dimensionless parameter values in Table 2.3, are given in Table 2.4.

2.2.3 Dimensionless solid model

Substituting the scalings (2.60) into the governing equations for the solid (2.32)–(2.33), we find that they become, in Cartesian coordinates,

$$\frac{\partial \rho_\mathrm{s}}{\partial t} + \frac{\partial}{\partial z}\left(\rho_\mathrm{s} w_\mathrm{s}\right) = 0, \tag{2.74a}$$

Parameter	Value
ϵ	3.333×10^{-4} to 3.333×10^{-3}
Re	1.15×10^{5} to 1.15×10^{7}
Pr	0.991
Sc	0.931
Δp	3.85×10^{-2}
κ	0.635
γ	1.3
α	1.53×10^{-7} to 1.53×10^{-5}
$\mathcal{M}$	0.635
$\mathrm{Pe_s}$	2.57×10^{2}
Λ	9.60×10^{-3}
η_1	0.596
η_2	2.36

Table 2.3: Values of the dimensionless parameters defined in (2.71), (2.75), and (2.79).

Parameter	Value
$\epsilon^2\mathrm{Re}$	1.28×10^{-2} to 1.28×10^{2}
Ec	1.14×10^{-4} to 1.14
$\epsilon^2\mathrm{Pe_s}$	2.85×10^{-5} to 2.85×10^{-3}

Table 2.4: Important groupings of the dimensionless parameters in Table 2.3.

$$\frac{\partial}{\partial t}\left(\rho_{\mathrm{s}} T\right) + \frac{\partial}{\partial z}\left(\rho_{\mathrm{s}} w_{\mathrm{s}} T\right) = \frac{1}{\epsilon^2 \mathrm{Pe_s}} \frac{\partial}{\partial x}\left(k_{\mathrm{s}} \frac{\partial T}{\partial x}\right) + \frac{1}{\epsilon^2 \mathrm{Pe_s}} \frac{\partial}{\partial y}\left(k_{\mathrm{s}} \frac{\partial T}{\partial y}\right) + \frac{1}{\mathrm{Pe}} \frac{\partial}{\partial z}\left(k_{\mathrm{s}} \frac{\partial T}{\partial z}\right), \quad (2.74b)$$

where, we have introduced another new dimensionless number

$$\mathrm{Pe_s} = \frac{[\rho_{\mathrm{s}}][w_{\mathrm{s}}] h^* c^*_{p,\mathrm{s}}}{[k_{\mathrm{s}}]}, \quad (2.75)$$

the Péclet number of the solid, which describes the relative importance of advective and conductive heat transport in the axial direction. Equation (2.74b) also contains an important parameter grouping, $\epsilon^2\mathrm{Pe_s}$, the reduced Péclet number, which describes the relative importance of advective transport in the axial direction and conductive transport in the transverse direction. The value of $\mathrm{Pe_s}$, based on the dimensional parameter values in Tables 2.1 and 2.2, is given in Table 2.3 and the value of $\epsilon^2\mathrm{Pe_s}$ is given in Table 2.4. Note that the timescale $[t]$ was chosen so that the rate of change of solid temperature balances the advection of heat in the solid in (2.74).

2.2.4 Dimensionless boundary conditions

We now nondimensionalise the boundary conditions from Section 2.1.3 using the scalings (2.60). The boundary conditions on the charge-surface boundary are given by

$$\tau_{xz} = 0,\ \ \tau_{yz} = 0,\ \ p - \epsilon\tau_{zz} = -1,\ \ \frac{\partial T}{\partial z} = 0,\ \ \frac{\partial Y}{\partial z} = 0 \quad \text{at } \partial\Omega_{\text{surf,g}}, \tag{2.76a}$$

$$w_{\text{s}} = -1,\ \ T = T_{\text{surf}} \quad \text{at } \partial\Omega_{\text{surf,s}}, \tag{2.76b}$$

where $T_{\text{surf}} = T^*_{\text{surf}}/T^*_{\text{crat}}$ is the dimensionless surface temperature of the solid, while the boundary conditions on the charge-crater boundary become

$$u_x = 0,\ \ v_y = 0,\ \ p - \epsilon\tau_{zz} = 0,\ \ T = 1,\ \ Y = Y_{\text{crat}} \quad \text{on } \partial\Omega_{\text{crat,g}}, \tag{2.77a}$$

$$T_{\text{s}} = 1 \quad \text{on } \partial\Omega_{\text{crat,s}}. \tag{2.77b}$$

Due to the geometry of the interface between the gas and the solid it is simplest to state the boundary conditions here in the cylindrical coordinate system, and so they are given by

$$\epsilon^2 \text{Re}\rho u_r = -\sum_i \frac{\text{Da}_i}{\text{Sc}} \left(\nu_{i,\text{SiO}} + \mathcal{M}\nu_{i,\text{CO}}\right) \mathcal{R}_i, \tag{2.78a}$$

$$\epsilon^2 \text{Re}\rho Y u_r - \frac{1}{\text{Sc}}\rho\mathcal{D}\frac{\partial Y}{\partial r} = -\sum_i \frac{\text{Da}_i \nu_{i,\text{SiO}}}{\text{Sc}} \mathcal{R}_i, \tag{2.78b}$$

$$v_\theta = \frac{1}{\epsilon^2 \text{ReSc}} \mathcal{D} \left(\frac{1 - (\mathcal{M})^{-1/2}}{Y + (\mathcal{M})^{-1/2}(1 - Y)} \right) \frac{1}{r} \frac{\partial Y}{\partial \theta}, \tag{2.78c}$$

$$w - \alpha w_{\text{s}} = \frac{1}{\text{ReSc}} \mathcal{D} \left(\frac{1 - (\mathcal{M})^{-1/2}}{Y + (\mathcal{M})^{-1/2}(1 - Y)} \right) \frac{\partial Y}{\partial z}, \tag{2.78d}$$

$$T\big|_{r=1-} = T\big|_{r=1+}, \tag{2.78e}$$

$$k_{\text{s}} \frac{\partial T}{\partial r}\bigg|_{r=1+} = \Lambda \Bigg(\left(-\epsilon^2 \text{RePr} \left(1 - (1 - \kappa) Y\right) \rho u T + k_{\text{g}} \frac{\partial T}{\partial r} \right)\bigg|_{r=1-} - \sum_i \frac{\text{Da}_i \eta_i \text{Pr}}{\text{Sc}} \mathcal{R}_i\big|_{r=1} \Bigg), \tag{2.78f}$$

on $\partial\Omega_{\text{Inter}}$, where

$$\Lambda = \frac{[k_{\text{g}}]}{[k_{\text{s}}]}, \quad \text{Da}_i = \frac{\epsilon h^* [\mathcal{R}_i] M^*_{\text{SiO}}}{[\rho_{\text{g}}][\mathcal{D}_{\text{SiOCO}}]}, \quad \eta_i = \frac{\Delta H^*_i}{c^*_{p,\text{CO}} T^*_{\text{crat}} M^*_{\text{SiO}}}, \tag{2.79}$$

are further dimensionless parameters introduced by the nondimensionalisation. Here Λ is the ratio of the thermal conductivities of the gas and solid; Da_i is the surface

Damköhler number of reaction i, which expresses the ratio of the reaction rate i and the mass diffusion rate of SiO; η_i is the ratio of the reaction's energy, and the thermal energy of the gas. Thus, η_i can be thought of as the reactive analogue of the Stefan number in a phase-change problem. The values of these dimensionless parameters, based on the dimensional parameters and scalings in Tables 2.1 and 2.2, are given in Table 2.3.

The boundary condition on the edge of the solid region surrounding a single channel, (2.51), becomes

$$T \text{ periodic} \qquad \text{on } \partial\Omega. \tag{2.80}$$

The dimensionless form for reaction rates given by (2.48) is

$$\mathcal{R}_i = \rho Y F_i(T), \tag{2.81}$$

for all i. In terms of dimensionless temperature, the temperature dependence functions (2.49)–(2.50) are

$$F_1(T) = 1, \quad F_2(T) = \frac{1}{1 + \exp\left(\dfrac{T - T_{\text{cond}}}{\xi}\right)}, \tag{2.82}$$

where $T_{\text{cond}} = T^*_{\text{cond}}/T^*_{\text{crat}}$ and $\xi = \xi^*/T^*_{\text{crat}}$ are the dimensionless condensation temperature and the constant controlling the rate of increase, respectively.

2.2.5 Dimensionless fluxes

Applying the scalings (2.60) to the definition of the fluxes in (2.52)–(2.57) in Section 2.1.4, we find that the dimensionless mass fluxes become

$$Q = \int_{\mathcal{C}_{\text{g}}} \rho w_z \, \mathrm{d}A, \tag{2.83}$$

$$Q_{\text{SiO}} = \int_{\mathcal{C}_{\text{g}}} \rho w_z Y \, \mathrm{d}A, \tag{2.84}$$

$$Q_{\text{CO}} = \int_{\mathcal{C}_{\text{g}}} \rho w_z (1 - Y) \, \mathrm{d}A, \tag{2.85}$$

$$Q_{\text{s}} = \frac{[\rho_{\text{s}}][w_{\text{s}}]}{[\rho_{\text{g}}][w_{\text{g}}]} \int_{\mathcal{C}_{\text{s}}} \rho_{\text{s}} w_{\text{s}} \, \mathrm{d}A, \tag{2.86}$$

where $\mathcal{C}_{\text{g}}$ and $\mathcal{C}_{\text{s}}$ are the dimensionless cross-sections (perpendicular to z) of the gas and solid regions, respectively. Similarly, the energy fluxes through the boundaries

and the rate at which energy is consumed by the reactions become

$$E_{\mathrm{g,crat}} = -\int_{\mathcal{C}_\mathrm{g}} \Bigg(\rho w_z T - (1-\kappa)\,\rho w_z T Y + \frac{1}{2}\mathrm{Ec}\rho w_z^3 + \frac{4}{3}\frac{\mathrm{Ec}}{\mathrm{Re}}\mu w_z \frac{\partial w_z}{\partial z} - \frac{1}{\mathrm{RePr}} k \frac{\partial T}{\partial z} \Bigg)\Bigg|_{z=0} \mathrm{d}A, \quad (2.87)$$

$$E_{\mathrm{g,surf}} = \int_{\mathcal{C}_\mathrm{g}} \Bigg(\rho w_z T - (1-\kappa)\,\rho w_z T Y + \frac{1}{2}\mathrm{Ec}\rho w_z^3 + \frac{4}{3}\frac{\mathrm{Ec}}{\mathrm{Re}}\mu w_z \frac{\partial w_z}{\partial z} - \frac{1}{\mathrm{RePr}} k \frac{\partial T}{\partial z} \Bigg)\Bigg|_{z=1} \mathrm{d}A, \quad (2.88)$$

$$E_{\mathrm{s,crat}} = -\int_{\mathcal{C}_\mathrm{s}} \left(\frac{\epsilon^2 \mathrm{Pe_s}}{\epsilon^2 \mathrm{RePr}\Lambda} \rho_\mathrm{s} w_\mathrm{s} T - \frac{1}{\mathrm{RePr}\Lambda} k_\mathrm{s} \frac{\partial T}{\partial z} \right)\Bigg|_{z=0} \mathrm{d}A, \quad (2.89)$$

$$E_{\mathrm{s,surf}} = \int_{\mathcal{C}_\mathrm{s}} \left(\frac{\epsilon^2 \mathrm{Pe_s}}{\epsilon^2 \mathrm{RePr}\Lambda} \rho_\mathrm{s} w_\mathrm{s} T - \frac{1}{\mathrm{RePr}\Lambda} k_\mathrm{s} \frac{\partial T}{\partial z} \right)\Bigg|_{z=1} \mathrm{d}A, \quad (2.90)$$

$$E_{\mathrm{React}} = -\int_{\partial\Omega_{\mathrm{Inter}}} \sum_i \frac{\mathrm{Da}_i \eta_i}{\epsilon^2 \mathrm{ReSc}} \mathcal{R}_i \,\mathrm{d}A, \quad (2.91)$$

where

$$E_{\mathrm{g,crat}} + E_{\mathrm{g,surf}} + E_{\mathrm{s,crat}} + E_{\mathrm{s,surf}} + E_{\mathrm{React}} = 0. \quad (2.92)$$

2.3 Discussion

In this chapter, we have presented a model for the mass and heat transport of the gas and solid in the charge material of the silicon furnace, coupled by the reactions occurring on the interface between them. We have nondimensionalised this model, choosing a scaling based on realistic parameter values for a silicon furnace. This allowed us to determine the critical dimensionless numbers that dictate the dynamics of the model. We will discuss the implications of the size of these parameters fully in the upcoming chapters, but note two properties immediately. Firstly, the aspect ratio of the channel is very small, immediately suggesting it will be possible derive reduced models where many of the physical processes can be neglected. Secondly, the reduced Reynolds number lies between 0.01 to 100. Therefore, our estimates of the industrially-relevant parameter values suggest the gas behaviour could be anything from a viscous dominated flow to an inertial dominated one. Much of the remainder of the thesis will be concerned with investigating different possible limits of the size of the reduced Reynolds number, and its implications for the gas flow and the behaviour of silicon furnaces.

Chapter 3

Non-isothermal compressible flow in a narrow channel driven by a small pressure drop

In this chapter, we study the flow of a single-phase compressible viscous gas through a narrow two-dimensional channel. As discussed in Chapter 1, non-isothermal compressible flow through channels has not received much attention in the literature, so we consider this simple problem, in order to develop an intuition for the behaviour of the gas flow in the model of the charge material described in Chapter 2. The remainder of the chapter is structured as follows. In Section 3.1, we describe how the model for the binary gas mixture in Chapter 2 can reduced to a model for a single-phase gas flow, and introduce the two-dimensional geometry that we will focus on in this chapter. We discuss how this model can be solved numerically. In Section 3.2, we exploit the small size of the aspect ratio and dimensionless pressure drop to derive a series of three reduced models, differing by the assumed size of the reduced Reynolds number. The first two reduced models include inertia at leading-order so must be solved numerically, which we do using a shooting method. The models differ through the inclusion of internal heating of the gas. In the third reduced model, viscous forces across the channel dominate, and the model can be solved using asymptotic methods. In Section 3.3, we compare the solutions of the different reduced models and the compressible Navier-Stokes equations, demonstrating they are in agreement when their range of validity overlaps. In particular, we consider the dependence of the mass and energy flux on the various parameters in the problem. We discuss the implications of these results in Section 3.4.

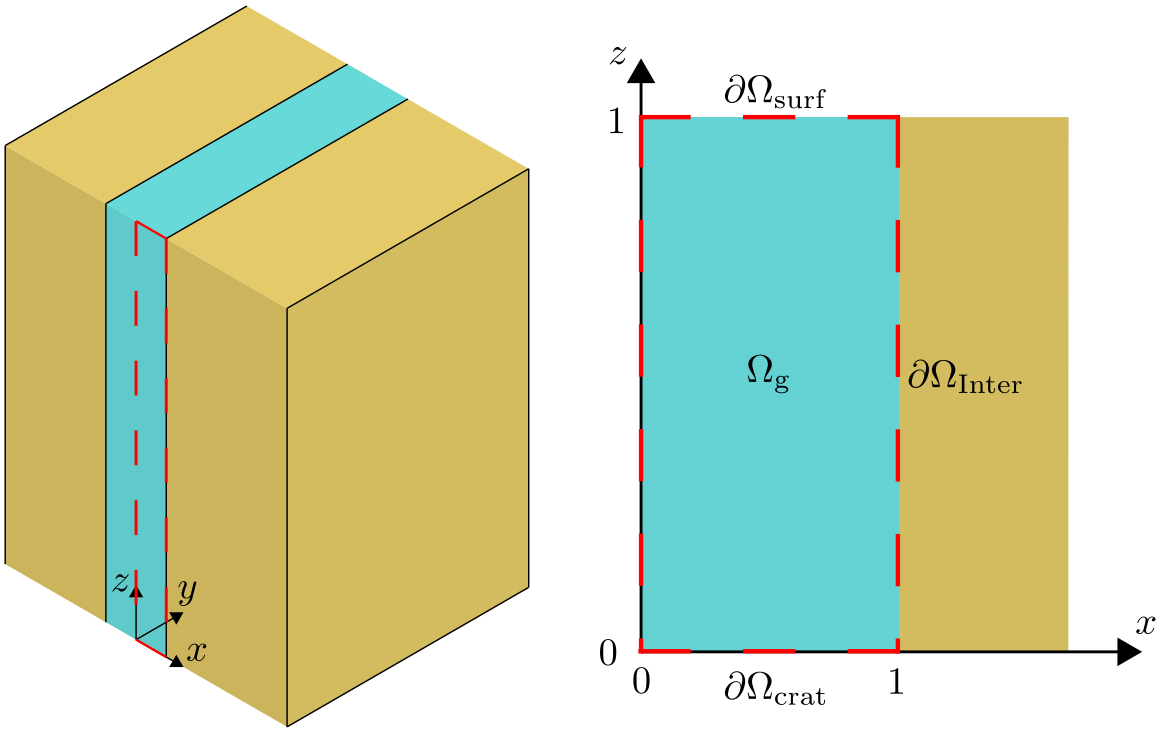


Figure 3.1: The coordinate system we use to model the flow through a long, narrow channel. The cross-section modelled in this chapter is highlighted by a red box.

3.1 A two-dimensional model of a single-phase gas

3.1.1 Two-dimensional geometry

In this chapter, we will consider the problem in a simpler geometry to the cylindrical channel described in Chapter 2. We still assume the gas channel to rise vertically through the charge material, hence occupying a long and thin region in the xz-plane, but now additionally assume that the cross-section in the xy-plane is narrow, as depicted in Figure 3.1. This will slightly simplify our analysis, but we expect similar results to hold in the original geometry.

While this new geometry is not suitable as an idealisation of the microstructure of the granular charge material, it has some industrial relevance. It has been observed that large amounts of gas sometimes exit the charge around the perimieter of the electrode, suggesting the possibility of a large channel around the edge of the electrode [30]. Evidence for such a channel is given in the results of the furnace excavation depicted in Figure 1.3, specifically by all the loose unreacted charge around the edge of the electrode. This must have been added after the electrode was shutdown, or, being adjacent to the electrode, it would have reacted. Hence, there must have been

a void for the charge added after the shutdown to fill.

Modelling the entirety of such a channel would require working in a curvilinear coordinate system aligned with the centreline of the channel. However, due to the large radius of the electrode compared to the channel width, we will assume that locally the two interfaces may be taken to be infinite parallel plates, and so work in a Cartesian coordinate system with the plates fixed at $x = \pm 1$, as depicted in Figure 3.1. Then, we focus our attention on two-dimensional solutions that are independent of y, so that we need only model a cross-section of the channel in the xz-plane. It is convenient at this point to abuse notation and let Ω_{g} denote this cross-section of the gas channel, and let the gas's boundaries with the crater $\partial\Omega_{\mathrm{crat}}$, the solid $\partial\Omega_{\mathrm{Inter}}$, and the surface $\partial\Omega_{\mathrm{surf}}$, also denote their naturally defined lower dimensional analogues. We also let $\mathcal{C}_{\mathrm{g}}$ denote the transverse cross-section of the two-dimensional channel. We also make the simplifying assumption that the temperatures on the interfaces at $x = \pm 1$ are equal, implying that the solution is symmetric about $x = 0$, so that we only need model the channel in $x > 0$. It is worth noting that, for a channel separating the charge material and the electrode, this assumption may not hold due to the differing properties of the charge material and the electrode, but it is straightforward to extend the analysis herein to study such non-symmetric behaviour.

In the new two-dimensional geometry, the non-dimensionalisation given by (2.60) is unchanged, except for the heat and mass flux scalings. These are now fluxes per unit length (in the y-direction), with corresponding scalings

$$[Q] = \epsilon h^* [\rho_{\mathrm{g}}][w_{\mathrm{g}}], \quad [E] = \epsilon h^* [\rho_{\mathrm{g}}][w_{\mathrm{g}}] c^*_{p,\mathrm{g}} T^*_{\mathrm{crat}}, \tag{3.1}$$

with the new values given in Table 3.1.

3.1.2 Simplification of the model of the charge material

We now describe the simplifications that reduce the model from Chapter 2 to a model of single-phase gas flow in a channel. As we are only interested in the gas dynamics in this chapter, we take the velocity of the solid to be zero, and the temperature in the solid to be a prescribed function, T_{s}, depending only on z, and satisfying the surface and crater boundary conditions, (2.76b) and (2.77b), respectively. This means that the boundary conditions on the gas-solid interface, (2.78), become over-specified and so we neglect the heat flux boundary condition, (2.78f), noting that the temperature continuity condition, (2.78e), simplifies to a Dirichlet condition for the temperature in the gas.

Parameter	Value	Reference
$[w_g]$	1.97×10^1 to $1.97 \times 10^3\,\mathrm{m\,s^{-1}}$	Equation (2.62)
$[Q]$	3.04×10^{-3} to $3.04\,\mathrm{kg\,s^{-1}}$	Equation (3.1)
$[E]$	8.98×10^3 to $8.98 \times 10^6\,\mathrm{J\,s^{-1}}$	Equation (3.1)
$[\mu]$	$6.76 \times 10^{-5}\,\mathrm{kg\,m^{-1}\,s^{-1}}$	[91]
$[k_g]$	$1.22 \times 10^{-1}\,\mathrm{J\,m^{-1}\,s^{-1}\,K^{-1}}$	[91]

Table 3.1: Values of the dimensional scalings in (2.60) for pure CO in a two-dimensional cross-section of a channel.

Parameter	Value
ϵ	3.333×10^{-4} to 3.333×10^{-3}
Re	1.35×10^5 to 1.35×10^7
Pr	0.720
Δp	3.85×10^{-2}
γ	1.3

Table 3.2: Value of the dimensionless parameters values in the model of flow of pure CO in a two-dimensional cross-section of a channel.

Moving on to the model for the gas, we assume there is no SiO present, implying that $Y = 0$ everywhere, and so the conservation of SiO equation, (2.68f) is automatically satisfied. We also assume that the CO gas undergoes no reactions, so that $\mathcal{R}_i = 0$ for all i. The remaining governing equations in (2.68) are then equivalent to those derived directly for a single-phase compressible viscous gas, and the remaining boundary conditions (2.76a), (2.77a), and (2.78), match those imposed for single-phase flow through a channel with a varying temperature on the walls. As we are no longer considering a mixture of gases, we replace the reference values for viscosity and thermal conductivity given in Table 2.2, based on values for a mixture, with values for pure CO, given in Table 3.1. This modifies the value of $[w_g]$ and the dimensionless parameters given in Table 2.3. However, the new values of the dimensionless parameters, given in Table 3.2, are all of the same orders of magnitude as their original values, suggesting the qualitative behaviour for the two regimes will be similar.

As the prescribed solid temperature depends only on z, we should rescale time by $t = \alpha\tilde{t}$ in order to work on the timescale of the gas dynamics. However, from Table 2.3, α, the ratio of axial speed of the solid and the gas, is very small, suggesting the gas flow in the coupled model in Chapter 2 can be taken as quasi-steady. We will therefore restrict ourselves to studying steady solutions of the model of single-phase flow in this chapter, as they are most relevant to interpreting the behaviour of the full model.

3.1.3 Problem statement

As we will only be working in a two-dimensional Cartesian coordinate system (x, z) throughout this chapter, we drop the subscripts on the velocities used in Chapter 2 and can write $\boldsymbol{u} = (u, w)$ without ambiguity. Then, under the simplifications discussed above, the dimensionless equations governing the gas flow, (2.68), become

$$\frac{\partial(\rho u)}{\partial x} + \frac{\partial(\rho w)}{\partial z} = 0, \tag{3.2a}$$

$$\epsilon^2 \mathrm{Re}\left(\frac{\partial(\rho u u)}{\partial x} + \frac{\partial(\rho u w)}{\partial z}\right) = -\frac{1}{\epsilon^2}\frac{\partial p}{\partial x} + 2\frac{\partial}{\partial x}\left(\mu\frac{\partial u}{\partial x}\right) + \epsilon^2\frac{\partial}{\partial z}\left(\mu\frac{\partial u}{\partial z}\right) + \frac{\partial}{\partial z}\left(\mu\frac{\partial w}{\partial x}\right) - \frac{2}{3}\frac{\partial}{\partial x}\left(\mu\left(\frac{\partial u}{\partial x} + \frac{\partial w}{\partial z}\right)\right), \tag{3.2b}$$

$$\epsilon^2 \mathrm{Re}\left(\frac{\partial(\rho u w)}{\partial x} + \frac{\partial(\rho w w)}{\partial z}\right) = -\frac{\partial p}{\partial z} + \frac{\partial}{\partial x}\left(\mu\frac{\partial w}{\partial x}\right) + 2\epsilon^2\frac{\partial}{\partial z}\left(\mu\frac{\partial w}{\partial z}\right) + \epsilon^2\left(\frac{\partial}{\partial x}\left(\mu\frac{\partial u}{\partial z}\right) - \frac{2}{3}\frac{\partial}{\partial z}\left(\mu\left(\frac{\partial u}{\partial x} + \frac{\partial w}{\partial z}\right)\right)\right), \tag{3.2c}$$

$$\epsilon^2 \mathrm{Re}\left(\frac{\partial(\rho u T)}{\partial x} + \frac{\partial(\rho w T)}{\partial z}\right) = \frac{1}{\mathrm{Pr}}\frac{\partial}{\partial x}\left(k\frac{\partial T}{\partial x}\right) + \frac{\epsilon^2}{\mathrm{Pr}}\frac{\partial}{\partial z}\left(k\frac{\partial T}{\partial z}\right) + (1-\gamma^{-1})\epsilon^2 \mathrm{Re}\Delta p\left(u\frac{\partial p}{\partial x} + w\frac{\partial p}{\partial z} + \epsilon^2\Phi\right), \tag{3.2d}$$

$$\Delta p\, p + 1 = \rho T, \tag{3.2e}$$

which are the conservation of mass, conservation of momentum, conservation of energy, and the equation of state, respectively. Here, we write the dimensionless dissipation function Φ in terms of the dimensionless viscosity,

$$\frac{\Phi}{\mu} = 2\left(\frac{\partial u}{\partial x}\right)^2 + \epsilon^2\left(\frac{\partial u}{\partial z}\right)^2 + \frac{\partial u}{\partial z}\frac{\partial w}{\partial x} + \frac{1}{\epsilon^2}\left(\frac{\partial w}{\partial x}\right)^2 + 2\left(\frac{\partial w}{\partial z}\right)^2 - \frac{2}{3}\left(\frac{\partial u}{\partial x} + \frac{\partial w}{\partial z}\right)^2. \tag{3.2f}$$

These governing equations contain only five dimensionless parameters, namely the aspect ratio ϵ, the Reynolds number Re, the Prandtl number Pr, the ratio of specific heat capacities at constant pressure and volume γ, and the dimensionless pressure

change Δp, all of which are defined in (2.71). Note that we have rewritten the Eckert number, defined in (2.73), it terms of these parameters, to make the relative size of all the terms clear.

The boundary conditions are given by the corresponding two-dimensional version of (2.76)–(2.78): the crater boundary conditions are

$$u = 0, \quad p + \epsilon^2 \mu \left(\frac{2}{3} \frac{\partial u}{\partial x} - \frac{4}{3} \frac{\partial w}{\partial z} \right) = 0, \quad T = 1 \ \text{ at } 0 < x < 1,\ z = 0, \tag{3.3a}$$

the interface boundary conditions are

$$u = 0, \quad w = 0, \quad T = T_{\mathrm{s}}(z) \ \text{ at } x = 1,\ 0 < z < 1, \tag{3.3b}$$

and the surface boundary conditions are

$$\epsilon^2 \mu \frac{\partial u}{\partial z} + \mu \frac{\partial w}{\partial x} = 0, \ p + \epsilon^2 \mu \left(\frac{2}{3} \frac{\partial u}{\partial x} - \frac{4}{3} \frac{\partial w}{\partial z} \right) = -1,$$

$$\frac{\partial T}{\partial z} = 0 \ \text{ at } 0 < x < 1,\ z = 1. \tag{3.3c}$$

We also introduce the symmetry boundary conditions at the centreline

$$u = 0, \quad \frac{\partial w}{\partial x} = 0, \quad \frac{\partial T}{\partial x} = 0 \ \text{ at } x = 0,\ 0 < z < 1. \tag{3.3d}$$

The total mass flux of gas per unit length (in the y-direction) is given by

$$Q = 2 \int_0^1 \rho w \, \mathrm{d}x, \tag{3.4}$$

while the energy fluxes per unit length (in the y-direction) through $\partial\Omega_{\mathrm{crat}}$, $\partial\Omega_{\mathrm{surf}}$, and $\partial\Omega_{\mathrm{Inter}}$ respectively are given by

$$E_{\mathrm{crat}} = -2 \int_0^1 \left(\rho T w + \frac{1}{2} \mathrm{Ec} \rho w^3 + \frac{4}{3} \frac{\mathrm{Ec}}{\mathrm{Re}} \mu w \frac{\partial w}{\partial z} - \frac{1}{\mathrm{RePr}} k \frac{\partial T}{\partial z} \right) \Bigg|_{z=0} \mathrm{d}x, \tag{3.5a}$$

$$E_{\mathrm{surf}} = 2 \int_0^1 \left(\rho T w + \frac{1}{2} \mathrm{Ec} \rho w^3 + \frac{4}{3} \frac{\mathrm{Ec}}{\mathrm{Re}} \mu w \frac{\partial w}{\partial z} - \frac{1}{\mathrm{RePr}} k \frac{\partial T}{\partial z} \right) \Bigg|_{z=1} \mathrm{d}x, \tag{3.5b}$$

$$E_{\mathrm{Inter}} = \frac{2}{\epsilon^2 \mathrm{RePr}} \int_0^1 -k \left. \frac{\partial T}{\partial x} \right|_{x=1}, \tag{3.5c}$$

which satisfy $E_{\mathrm{crat}} + E_{\mathrm{surf}} + E_{\mathrm{Inter}} = 0$. We have introduced E_{Inter} to denote the energy flux from the gas into the surrounding solid. In this model, this energy flux from the gas to the solid, due to conductive heat transfer, represents the only possible mechanism for energy to not be lost from the furnace. Therefore, it is natural to define the energy efficiency of a particular channel to be

$$\mathcal{E} = \left| \frac{E_{\mathrm{Inter}}}{E_{\mathrm{crat}}} \right| = -\frac{E_{\mathrm{Inter}}}{E_{\mathrm{crat}}}, \tag{3.6}$$

i.e. the proportion of energy inputted into the channel that is subsequently transferred to the solid.

3.1.4 Numerical solution

We can solve (3.2)–(3.3) numerically using the finite element software COMSOL multiphysics® v5.5. We use a triangular mesh of 68667 domain elements and 2181 boundary elements. We use Taylor-Hood elements to discreteise the velocity and pressure and use order one Lagrange elements for the temperature. It typically takes 20 minutes to converge to a solution with relative and absolute tolerances of 1×10^{-3} on a standard desktop computer. However, to achieve this convergence, we must restrict the size of the aspect ratio of the channel, taking $\epsilon = 0.05$ for all the computations. This restriction on the aspect ratio occurs because we use COMSOL's built-in solver for the compressible Navier-Stokes equations, which requires us to preform the calculations in a coordinate system where distance is scaled the same in all directions. Consequently, meshing the long-thin domain, while avoiding elements which are too stretched, requires a huge number of elements to achieve sufficient resolution in the x-direction, with the number of elements increasing as ϵ decreases. Although the value of ϵ is larger than the size given for a silicon furnace in Table 2.3, we still expect the results to provide good qualitative insight into the behaviour in the limit $\epsilon \ll 1$. Results from these simulations are given in Section 3.3.

Since we are restricted from studying the most industrially-relevant behaviour of ϵ, and the solution time limits our exploration of parameter space, we choose to instead focus on using asymptotic analysis to exploit the small size of the aspect ratio, by deriving reduced models, which include only the most important physical effects. We therefore use these COMSOL results to guide our asymptotic analysis, and act as validation for the behaviour reduced models we develop.

3.2 Reduced single-phase models

Based on the size of the dimensionless parameters given in Table 3.2, some physical effects in the furnace will only play a small role in the behaviour of the solution and so may reasonably be neglected, allowing a reduced model to be considered. Since the aspect ratio of the channel, ϵ, is small, the fluid's behaviour is characterised not by the size of the Reynolds number, and rather by the size of the reduced Reynolds number, which we discuss in more detail below. The dimensionless pressure drop, Δp, is also a small parameter (although larger than the aspect ratio), whose size implies the effect of changes in pressure will be small. The Prandtl number is of order unity, and so the behaviour of the temperature will mirror that of momentum, in the sense that the relative sizes of advection and conduction will be the same of those of inertia and

momentum. The ratio of specific heat capacities at constant pressure and constant volume are of order unity, as is typical for the majority of gases [91].

From Table 3.2, the reduced Reynolds number, $\epsilon^2\mathrm{Re}$, can be reasonably justified in being small, of order unity, or large, which would imply transverse viscous forces to be the dominant effect; transverse viscous forces to balance inertia in the axial momentum equation; or inertial effects to dominate, respectively. We will derive a reduced model for each of these possibilities in the following sections, before comparing their behaviour in Section 3.3.

3.2.1 Case I: Large reduced Reynolds number

Motivated by the discussion above, we first consider the limit where

$$\epsilon^2 \ll \Delta p \ll 1, \quad \mathrm{Pr},\, \gamma = O(1), \quad \epsilon^2\mathrm{Re} = O(\Delta p^{-1}), \tag{3.7}$$

which we refer to as case I. We note this particular size of $\epsilon^2\mathrm{Re}$ implies, the Eckert number, Ec, defined in (2.73), to be order unity. If we naively sought a regular asymptotic solution to the full problem (3.2)–(3.3), then at leading-order, viscosity and conductivity would be neglected in both directions, reducing the governing equations to those for an inviscid gas, which are lower order, meaning we would be unable to impose all the boundary conditions, and in particular the wall temperature. This could be resolved by using the method matched asymptotics, by introducing a boundary layer near the interface at $x = 1$, where the compressible boundary layer equations would hold [68]. However, we instead choose to construct a model that is consistent with (3.7), but not an asymptotic limit. We do this by retaining terms of both size and $O(1)$ and $O\big((\epsilon^2\mathrm{Re})^{-1}\big)$ in (3.2c) and (3.2d) so that we can satisfy all the boundary conditions on $\partial\Omega_{\mathrm{Inter}}$, (3.3b). This results in the set of governing equations,

$$\frac{\partial(\rho u)}{\partial x} + \frac{\partial(\rho w)}{\partial z} = 0, \tag{3.8a}$$

$$0 = \frac{\partial p}{\partial x}, \tag{3.8b}$$

$$\epsilon^2\mathrm{Re}\left(\frac{\partial(\rho u w)}{\partial x} + \frac{\partial(\rho w w)}{\partial z}\right) = -\frac{\partial p}{\partial z} + \frac{\partial}{\partial x}\left(\mu\frac{\partial w}{\partial x}\right), \tag{3.8c}$$

$$\epsilon^2\mathrm{Re}\left(\frac{\partial(\rho u T)}{\partial x} + \frac{\partial(\rho w T)}{\partial z}\right) = \frac{1}{\mathrm{Pr}}\frac{\partial}{\partial x}\left(k\frac{\partial T}{\partial x}\right) + \mathrm{Ec}\left(w\frac{\partial p}{\partial z} + \mu\left(\frac{\partial w}{\partial x}\right)^2\right), \tag{3.8d}$$

$$\rho T = 1, \tag{3.8e}$$

for $0 < x < 1$, $0 < z < 1$. Thus, the governing equations (3.8a)–(3.8d), are identical to the compressible boundary layer equations including internal heating of the gas (see, for example [68]) We will see in Section 3.2.2, that the model for case II, which is derived using rigorous asymptotic methods when $\epsilon^2\mathrm{Re} = O(1)$, is identical to (3.8), but with the internal heating terms removed from the energy equation (3.8d). From left to right, the internal heating terms in (3.8d) represent the work done compressing the gas and the heat generated by viscous forces, respectively. Using the same assumptions for deriving the governing equations, the boundary conditions (3.3) become

$$u = 0,\ p = 0,\ T = 1 \quad \text{for} \quad 0 < x < 1,\ z = 0, \tag{3.9a}$$

$$u = 0,\ \frac{\partial w}{\partial x} = 0,\ \frac{\partial T}{\partial x} = 0 \quad \text{at} \quad x = 0,\ 0 < z < 1, \tag{3.9b}$$

$$u = 0,\ w = 0,\ T = T_{\mathrm{s}}(z) \quad \text{at} \quad x = 1,\ 0 < z < 1, \tag{3.9c}$$

$$p = -1 \quad \text{at} \quad 0 < x < 1,\ z = 1. \tag{3.9d}$$

We note that by neglecting axial viscous forces and conduction in (3.8), we have still lowered the order of the governing equations, implying that the tangential stress and no conductive heat flux conditions at the outlet can no longer be satisfied (cf. (3.3c)). This suggests there is a boundary region close to the outlet where these conditions are met, but we ignore analysing this layer, anticipating that they will have negligible effect on the solution upstream. We later confirm this in Section 3.3, by comparing to the COMSOL solution of the full problem (3.2)–(3.3).

While this approach does not provide a valid asymptotic model, it does result in a composite problem whose solution describes the behaviour over the entire channel. The model is also closely related to the asymptotic model obtained in the limit where $\epsilon^2\mathrm{Re} = O(1)$ and $\Delta p = O(1)$, which is discussed in Section 6.2. Solutions to (3.8)–(3.9) requires a numerical method, which we discuss in Section 3.2.3.

3.2.2 Case II: Order unity reduced Reynolds number

We now consider the second limit where

$$\epsilon^2 \ll \Delta p \ll 1, \quad \mathrm{Pr},\ \gamma,\ \epsilon^2\mathrm{Re} = O(1), \tag{3.10}$$

which we refer to as case II. With the parameter sizes given in (3.10), seeking an asymptotic solution, we obtain the leading-order governing equations

$$\frac{\partial(\rho u)}{\partial x} + \frac{\partial(\rho w)}{\partial z} = 0, \tag{3.11a}$$

$$0 = \frac{\partial p}{\partial x}, \tag{3.11b}$$

$$\epsilon^2 \mathrm{Re}\left(\frac{\partial(\rho u w)}{\partial x} + \frac{\partial(\rho w w)}{\partial z}\right) = -\frac{\partial p}{\partial z} + \frac{\partial}{\partial x}\left(\mu \frac{\partial w}{\partial x}\right), \tag{3.11c}$$

$$\epsilon^2 \mathrm{Re}\left(\frac{\partial(\rho u T)}{\partial x} + \frac{\partial(\rho w T)}{\partial z}\right) = \frac{1}{\mathrm{Pr}}\frac{\partial}{\partial x}\left(k \frac{\partial T}{\partial x}\right), \tag{3.11d}$$

$$\rho T = 1, \tag{3.11e}$$

whose appropriate boundary conditions are the same as for case I, so given again by (3.9). Unlike the governing equations for case I (3.8), are the result of a valid asymptotic limit. These governing equations are identical to case I, except the internal heating terms do not appear in the energy equation (3.11d). Thus, the governing equations for case II, (3.11), are obtained from those of case I, (3.8), by setting $\Delta p = 0$ (i.e. $\mathrm{Ec} = 0$).

As previously mentioned, the assumption $\epsilon^2 \mathrm{Re} = O(1)$, implies inertia balances transverse viscous forces in the axial momentum equation in (3.11c), and, since $\mathrm{Pr} = O(1)$ advection balances transverse conduction in the energy equation (3.11d). The small aspect ratio implies the pressure does not vary in the transverse direction, (3.11b). The equation of state (3.11e), has simplified due to the small pressure change assumption, and implies the density and temperature to be inverses of each other. This simplified equation of state is unusual, and we have only found it appearing previously in the literature in [12] and [40]. In [12], it arises from assuming *a priori* that the equation of state of a gas is given by Charles' law of gases, which states that *'When the pressure on a sample of a dry gas is held constant, the Kelvin temperature and the volume will be in direct proportion'* [21]. Here we have shown systematically, through our asymptotic analysis, that despite the pressure changing globally, locally the pressure appears constant, in the sense that Charles' law is approximately valid. In [40] this equation of state of state is valid in a boundary layer around a sudden jump in temperature on the wall of a pipe.

As for case I, the problem defined by (3.9), (3.11) requires a numerical solution which we discuss in Section 3.2.3.

3.2.3 Reformulation and numerical solution of cases I and II

Due to the nonlinear advective terms in both cases I and II, they must be solved numerically. As case II is a special case of case I we will discuss our method for case I, and describe how it can be simplified for case II, leading to greatly reduce the computational time.

To reduce the number of variables in the problem we introduce the compressible streamfunction, ψ, defined by

$$\frac{\partial \psi}{\partial x} = \rho w, \ \frac{\partial \psi}{\partial z} = -\rho u. \tag{3.12}$$

Using (3.8e) to eliminate ρ, and differentiating (3.8c) with respect to x to make it independent of p, the system (3.8) can be reduced to

$$\epsilon^2 \mathrm{Re}\left(\psi_{xxz}\psi_x T + 2\psi_{xx}\psi_x T_z + \psi_x^2 T_{xz} - \psi_z \left(\psi_x T\right)_{xx}\right) = \left(\left(\mu \left(\psi_x T\right)_x\right)\right)_{xx}, \tag{3.13a}$$

$$\epsilon^2 \mathrm{Re}\left(\psi_x T_z - \psi_z T_x\right) = \frac{1}{\mathrm{Pr}} \left(k T_x\right)_x + \mathrm{Ec}\left(\psi_x T p_z + \mu \left(\left(\psi_x T\right)_x\right)^2\right), \tag{3.13b}$$

for ψ and T, where we have used subscripts x and z to denote partial derivatives with respect to x and z respectively. To obtain an additional equation to determine p, we integrate (3.8c) from $x = 0$ to $x = 1$, and apply the boundary conditions (3.9b)–(3.9c). Then by introducing a new variable H, defined as the integral of the stress across the channel,

$$H(z) = p + \epsilon^2 \mathrm{Re} \int_0^1 \psi_x^2 T \, \mathrm{d}x, \tag{3.14}$$

we obtain an ordinary differential equation (ODE) for H, given by

$$\frac{\mathrm{d}H}{\mathrm{d}z} = \left(\mu \left(\psi_x T\right)_x\right)\Big|_{x=1}. \tag{3.15}$$

The no-flux condition (3.9b) on the line of symmetry gives that $\psi_z = 0$ at $x = 0$, implying that ψ is constant along $x = 0$, which we take to be zero without loss of generality. Substituting (3.12) into (3.4) then implies that $\psi = Q/2$ at $x = 1$. Therefore, in terms of our new variables, the boundary conditions are given by

$$\frac{\partial \psi}{\partial z} = 0, \ T = 1, \ p = 0, \ H = \epsilon^2 \mathrm{Re} \int_0^1 \psi_x^2 T \, \mathrm{d}x \quad \text{at } z = 0, \tag{3.16a}$$

$$\psi = 0, \ \psi_{xx} = 0, \ T_x = 0 \quad \text{at } x = 0, \tag{3.16b}$$

$$\psi = \frac{Q}{2}, \ \psi_x = 0, \ T = T_{\mathrm{s}}(z) \quad \text{at } x = 1, \tag{3.16c}$$

$$p = -1, \ H = -1 + \epsilon^2 \mathrm{Re} \int_0^1 \psi_x^2 T \, \mathrm{d}x \quad \text{at } z = 1. \tag{3.16d}$$

For a given value of Q, (3.13a)–(3.16c) is a parabolic-type problem for ψ and T, with z acting as a time-like variable, with ψ and T determining H and p. Hence, we solve (3.13a)–(3.16) numerically, using a shooting method to converge to a value of Q such that (3.16d) is satisfied. To a obtain a numerical solution we apply the method lines in the axial direction to (3.13a)–(3.16), discretising the x derivatives using second-order accurate central differences on a uniformly-spaced mesh. As (3.13a) is fourth-order in x, we use a ghost point near each x-boundary to retain second-order accuracy. To ensure we have enough equations to uniquely determine the value of the solution at the ghost points we also require that (3.13b) holds at the x-boundaries. The resulting set of equations form a system of differential-algebraic equations (DAE) which is solved using MATLAB's built-in solver ode15s [72], using adaptive time-stepping to take the largest step possible, satisfying the required absolute and relative tolerances, which we set to be 10^{-6}. Further details of the finite difference approximations and its implementation are given in Appendix C.

As the numerical scheme involves the solution of a DAE, the numerical integrator requires both an initial condition and an initial slope (the z-derivative) at $z = 0$ for all the dependent variables such that the governing equations are satisfied [72]. To determine the information not given in (3.16a), the main difficulty is finding $\psi\big|_{z=0}$, with the remaining terms being readily calculated from the governing equations.

We first let $\Psi(x) = \psi\big|_{z=0}$. Then, to derive an equation for Ψ, we start by substituting the boundary conditions at $z = 0$, (3.9a), into the governing equations (3.8). Then, subtracting $w(x, 0)$ times the energy equation (3.8d) from the momentum equation (3.8c), and substituting in the definition of the streamfunction (3.12) (which we also evaluate at $z = 0$, to find $\mathrm{d}\Psi/\mathrm{d}x = w(x, 0)$), we obtain the ODE

$$\Psi''' = \mathrm{Ec}\Psi' \left(\Psi''\right)^2 + \mathrm{Ec}\lambda \left(\Psi'\right)^2 + \lambda, \tag{3.17}$$

where $\Psi' = \mathrm{d}\Psi/\mathrm{d}x$, and $\lambda = \mathrm{d}p/\mathrm{d}z\big|_{z=0}$ is an unknown constant to be determined as part of the solution. From (3.16b)–(3.16c), we obtain the boundary conditions

$$\Psi = 0, \quad \Psi'' = 0, \quad \text{at } x = 0, \tag{3.18a}$$

$$\Psi = \frac{Q}{2}, \quad \Psi' = 0, \quad \text{at } x = 1, \tag{3.18b}$$

where we assume Q is given by the shooting method. Thus, (3.17)–(3.18) consists of a third order ODE with one unknown parameter and four boundary conditions, so is a well posed problem. For case II, we set $\mathrm{Ec} = 0$, and can solve exactly,

$$\Psi = \frac{3Q}{4}\left(1 - x^2\right), \quad \lambda = -\frac{3Q}{2}, \tag{3.19}$$

which, in terms of velocity and pressure, is seen to be just a Posiseuille flow. For case I, we must solve the problem numerically, which can be done so using MATLAB's built-in BVP solver bvp5c, given a sufficiently good initial guess. For small values of Ec, (3.19) is a suitable initial guess. For larger values we either use continuation, or in a parameter sweep, the solution at the previous step. Alternatively, it is possible to find an asymptotic solution for large Ec, but as the three approaches produce the same result, we do not discuss it further.

Once ψ and T are found numerically, (3.8e), and (3.12) can be used to find ρ, u, and w using numerical differentiation formulas. The details of this calculation are also in Appendix C.

Given this method to solve the problem for a given mass flux Q, we use MATLAB's built-in root finding algorithm fzero, to carry out the shooting problem of finding a value of Q such that (3.9d) is satisfied. In our results we have found Q to a tolerance of 10^{-6}. Convergence tests are given in Appendix C, and a comparison to the COMSOL solution of the full system (3.2)–(3.3) is given in Section 3.3.

When solving case II, (3.13) becomes independent of p, and so we can omit (3.14), from the set of equations solved by ode15s, only calculating p once we have converged to a Q such that the boundary condition for H in (3.16d) is satisfied. This greatly reduces the computation time for the numerical solution of case II compared to case I, since (3.14) depends on ψ and T at every mesh point, meaning the Jacobian of the DAE for case II is much sparser. The computation time of case II is also sped up by not having to numerically solve (3.17)–(3.18).

Once we have computed solutions to cases I and II, we can use them to evaluate the energy fluxes. Under the assumptions for case I, given in (3.7), the total energy fluxes (3.5) simplify to

$$E_{\text{crat}} = -2\int_0^1 \left(\rho T w + \frac{1}{2}\text{Ec}\rho w^3\right)\Big|_{z=0} \,\mathrm{d}x, \tag{3.20a}$$

$$E_{\text{surf}} = 2\int_0^1 \left(\rho T w + \frac{1}{2}\text{Ec}\rho w^3\right)\Big|_{z=1} \,\mathrm{d}x, \tag{3.20b}$$

$$E_{\text{Inter}} = \frac{2}{\epsilon^2 \text{RePr}}\int_0^1 -k\,\frac{\partial T}{\partial x}\Big|_{x=1} \,\mathrm{d}z, \tag{3.20c}$$

and to obtain the expressions for case II, we just set $\text{Ec} = 0$ in (3.20).

3.2.4 Case III: Small reduced Reynolds number

Before presenting the results of solving cases I and II numerically, we consider the final industrially-relevant limit, that of small reduced Reynolds number. Specifically,

we assume that

$$\epsilon^2 \ll \Delta p \ll \epsilon^2 \mathrm{Re} \ll 1, \quad \mathrm{Pr},\, \gamma = O(1), \tag{3.21}$$

and refer to the resulting model as case III. We make the assumption that $\Delta p \ll \epsilon^2 \mathrm{Re}$, so that to $O(\epsilon^2 \mathrm{Re})$, the model derived in this section is a sub-limit of cases I and II. This provides us with a valuable check on the numerical solutions to cases I and II. This limit is very similar to the model of heated gas flow in a pipe considered in [70], although they assumed $\Delta p = O(1)$, and imposed the heat flux into the channel, rather than a temperature profile on the walls. That model was later extended to channels of varying width in [17].

Given the assumptions (3.21), we seek an asymptotic solution to (3.2)–(3.3) of the form

$$\begin{aligned}(u, w, p, \rho, T, Q) \sim (u^{(0)}, w^{(0)}, p^{(0)}, \rho^{(0)}, T^{(0)}, Q^{(0)}) \\ + \epsilon^2 \mathrm{Re}(u^{(1)}, w^{(1)}, p^{(1)}, \rho^{(1)}, T^{(1)}, Q^{(1)}) + o\left(\epsilon^2 \mathrm{Re}\right)\end{aligned} \tag{3.22}$$

as $\epsilon^2 \mathrm{Re} \to 0$, with the solution presented as follows. In Sections 3.2.4.1 and 3.2.4.2, we present and solve the $O(1)$ and $O(\epsilon^2 \mathrm{Re})$ problems, respectively. Then in Sections 3.2.4.3 and 3.2.4.4, we use these solutions to investigate how the parameters in the problem affect the mass flux and energy efficiency, respectively. The asymptotic solutions are subsequently compared to the numerical solutions of cases I and II, and the full compressible Navier-Stokes in Section 3.3.1.

3.2.4.1 $O(1)$ solution

Substituting (3.22) into (3.2), to leading-order, we obtain the following set of governing equations

$$\frac{\partial \left(\rho^{(0)} u^{(0)}\right)}{\partial x} + \frac{\partial \left(\rho^{(0)} w^{(0)}\right)}{\partial z} = 0, \tag{3.23a}$$

$$0 = \frac{\partial p^{(0)}}{\partial x}, \tag{3.23b}$$

$$\frac{\partial p^{(0)}}{\partial z} = \frac{\partial}{\partial x}\left(\mu\left(T^{(0)}\right)\frac{\partial w^{(0)}}{\partial x}\right), \tag{3.23c}$$

$$0 = \frac{\partial}{\partial x}\left(k\left(T^{(0)}\right)\frac{\partial T^{(0)}}{\partial x}\right), \tag{3.23d}$$

$$\rho^{(0)} T^{(0)} = 1, \tag{3.23e}$$

for $0 < x < 1$, $0 < z < 1$, which are subject to the boundary conditions

$$p^{(0)} = 0 \quad \text{at} \quad z = 0, \tag{3.24a}$$

$$u^{(0)} = 0, \ \frac{\partial w^{(0)}}{\partial x} = 0, \ \frac{\partial T^{(0)}}{\partial x} = 0 \quad \text{at} \quad x = 0, \tag{3.24b}$$

$$u^{(0)} = 0, \ w^{(0)} = 0, \ T^{(0)} = T_{\mathrm{s}}(z) \quad \text{at} \quad x = 1, \tag{3.24c}$$

$$p^{(0)} = -1 \quad \text{at} \quad z = 1. \tag{3.24d}$$

Note that in the boundary conditions at $z = 0$, (3.24a), we did not include the unidirectional flow and gas temperature conditions in (3.9a), as they are not required to construct the leading-order solution (3.27). We will see below they are trivially satisfied at leading order. However, if we were to consider a problem where $T_{\mathrm{s}}(0) \neq 1$, then a boundary layer analysis at $z = 0$ would be required to determine how the temperature of the gas adjusts to the interface temperature. Just as for cases I and II, we neglected the boundary layer near $z = 1$, as we do not expect it to have a significant effect on the solution elsewhere.

To solve (3.23)–(3.24) we begin by integrating (3.23d) twice with respect to x, and by using (3.24), see that the temperature equals the solid temperature, and so depends only on z. Moreover, by (3.23d), the density is the inverse of the solid temperature, and so also depends only on z. Next, integrating (3.23c) twice, we can find $w^{(0)}$ in terms of the pressure gradient, with

$$w^{(0)} = -\frac{1}{2\mu\left(T^{(0)}\right)} \frac{\mathrm{d}p^{(0)}}{\mathrm{d}z} \left(1 - x^2\right), \tag{3.25}$$

from which we see the axial velocity has the expected quadratic dependence on x for laminar flow in a pipe. By substituting the expressions for $\rho^{(0)}$ and $w^{(0)}$ into (3.4), which can be shown to be a constant using (3.23a), we obtain the following relationship between $p^{(0)}$, $Q^{(0)}$ and $T^{(0)}$,

$$\frac{\mathrm{d}p^{(0)}}{\mathrm{d}z} = -\frac{3}{2} Q^{(0)} T^{(0)} \mu\left(T^{(0)}\right). \tag{3.26}$$

Integrating this expression and using the pressure boundary conditions at $z = 0, 1$ determines the pressure and the value of $Q^{(0)}$. Finally, substituting all the other variables into (3.23a) gives that the transverse velocity must be zero. In summary,

the leading-order solution is given by

$$u^{(0)} = 0, \tag{3.27a}$$

$$w^{(0)} = \frac{3}{4}Q^{(0)}T_{\mathrm{s}}(z)\left(1-x^2\right), \tag{3.27b}$$

$$p^{(0)} = -\frac{3}{2}Q^{(0)}\int_0^z T_{\mathrm{s}}(\tilde{z})\mu\left(T_{\mathrm{s}}(\tilde{z})\right)\,\mathrm{d}\tilde{z}, \tag{3.27c}$$

$$\rho^{(0)} = \frac{1}{T_{\mathrm{s}}(z)}, \tag{3.27d}$$

$$T^{(0)} = T_{\mathrm{s}}(z), \tag{3.27e}$$

$$Q^{(0)} = \frac{2}{3\int_0^1 T_{\mathrm{s}}(z)\mu\left(T_{\mathrm{s}}(z)\right)\,\mathrm{d}z}. \tag{3.27f}$$

Examining (3.27), we can see that the gas temperature is equal to the solid temperature, and so case III is not a good model of the situation when gas exits the furnace at a hotter temperature than the solid surface temperature. The velocity solution is essentially a modification to the Poiseuille solution for incompressible flow between two plates, and the two coincide exactly if $T_{\mathrm{s}} \equiv 1$. However, when T_{s} decreases, the gas becomes denser, and so must go slower so that the mass flux remains constant. Conversely, an increasing wall temperature would accelerate the gas.

3.2.4.2 $O(\epsilon^2\mathrm{Re})$ solution

Substituting the asymptotic expansion (3.22) into the governing equations (3.2) and equating coefficients at $O(\epsilon^2\mathrm{Re})$ gives the governing equations

$$\frac{\partial}{\partial x}\left(\rho^{(0)}u^{(1)}\right) + \frac{\partial}{\partial z}\left(\rho^{(0)}w^{(1)} + \rho^{(1)}w^{(0)}\right) = 0, \tag{3.28a}$$

$$0 = \frac{\partial p^{(1)}}{\partial x}, \tag{3.28a}$$

$$\rho^{(0)}w^{(0)}\frac{\partial w^{(0)}}{\partial z} = -\frac{\partial p^{(1)}}{\partial z} + \frac{\partial}{\partial x}\left(\mu\left(T^{(0)}\right)\frac{\partial w^{(1)}}{\partial x} + \mu'\left(T^{(0)}\right)T^{(1)}\frac{\partial w_0}{\partial x}\right), \tag{3.28b}$$

$$\frac{\partial w^{(0)}}{\partial z} = \frac{1}{\mathrm{Pr}}\frac{\partial}{\partial x}\left(k\left(T^{(0)}\right)\frac{\partial T^{(1)}}{\partial x}\right), \tag{3.28c}$$

$$\rho^{(0)}T^{(1)} + \rho^{(1)}T^{(0)} = 0, \tag{3.28d}$$

for $0 < x < 1$, $0 < z < 1$, with an appropriate subset of the boundary conditions (3.9) giving

$$p^{(1)} = 0 \quad \text{at} \quad z = 0, \tag{3.29a}$$

$$u^{(1)} = 0, \ \frac{\partial w^{(1)}}{\partial x} = 0, \ \frac{\partial T^{(1)}}{\partial x} = 0 \quad \text{at} \quad x = 0, \tag{3.29b}$$

$$u^{(1)} = 0, \ w^{(1)} = 0, \ T^{(1)} = 0 \quad \text{at} \quad x = 1, \tag{3.29c}$$

$$p^{(1)} = 0 \quad \text{at} \quad z = 1. \tag{3.29d}$$

Note that in stating (3.28), we have exploited the fact that $u^{(0)} = 0$ and $T^{(0)} = T^{(0)}(z)$ to simplify the statement of the problem. The solution, found using an identical method as used for (3.23)–(3.24), is given by

$$\begin{aligned} u^{(1)} = &-\frac{3}{1120}(Q^{(0)})^2 T_{\mathrm{s}} \frac{\mathrm{d}}{\mathrm{d}z}\left(\frac{1}{T_{\mathrm{s}}\mu(T_{\mathrm{s}})}\frac{\mathrm{d}T_{\mathrm{s}}}{\mathrm{d}z}\right)\left(x^7 - 7x^5 + 11x^3 - 5x\right) \\ &+ \frac{1}{2240}\mathrm{Pr}(Q^{(0)})^2 T_{\mathrm{s}} \frac{\mathrm{d}}{\mathrm{d}z}\left(\frac{\mu'(T_{\mathrm{s}})}{k(T_{\mathrm{s}})\mu(T_{\mathrm{s}})}\frac{\mathrm{d}T_{\mathrm{s}}}{\mathrm{d}z}\right)\left(5x^7 - 63x^5 + 111x^3 - 53x\right) \\ &+ \frac{3}{2240}\mathrm{Pr}(Q^{(0)})^2 T_{\mathrm{s}} \frac{\mathrm{d}}{\mathrm{d}z}\left(\frac{1}{T_{\mathrm{s}}k(T_{\mathrm{s}})}\frac{\mathrm{d}T_{\mathrm{s}}}{\mathrm{d}z}\right)\left(5x^7 - 49x^5 + 83x^3 - 39x\right), \end{aligned} \tag{3.30a}$$

$$\begin{aligned} w^{(1)} = &\frac{3}{4}Q^{(1)}T_{\mathrm{s}}(z)\left(1 - x^2\right) - \frac{51}{280}\mathrm{Pr}(Q^{(0)})^2 \frac{1}{k(T_{\mathrm{s}})}\frac{\mathrm{d}T_{\mathrm{s}}}{\mathrm{d}z}\left(1 - x^2\right) \\ &+ \frac{3}{1120}(Q^{(0)})^2 \frac{1}{\mu(T_{\mathrm{s}})}\frac{\mathrm{d}T_{\mathrm{s}}}{\mathrm{d}z}\left(7x^6 - 35x^4 + 33x^2 - 5\right) \\ &- \frac{1}{2240}\mathrm{Pr}(Q^{(0)})^2 \frac{\mu'(T_{\mathrm{s}})}{k(T_{\mathrm{s}})\mu(T_{\mathrm{s}})} T_{\mathrm{s}} \frac{\mathrm{d}T_{\mathrm{s}}}{\mathrm{d}z}\left(35x^6 - 315x^4 + 333x^2 - 53\right), \end{aligned} \tag{3.30b}$$

$$\begin{aligned} p^{(1)} = &\frac{51}{140}\mathrm{Pr}(Q^{(0)})^2 \int_0^z \frac{\mu(T_{\mathrm{s}})}{k(T_{\mathrm{s}})}\frac{\mathrm{d}T_{\mathrm{s}}}{\mathrm{d}\tilde{z}}\,\mathrm{d}\tilde{z} + \frac{27}{70}(Q^{(0)})^2\left(1 - T_{\mathrm{s}}\right) \\ &+ \frac{6}{35}\mathrm{Pr}(Q^{(0)})^2 \int_0^z \frac{\mu'(T_{\mathrm{s}})}{k(T_{\mathrm{s}})} T_{\mathrm{s}} \frac{\mathrm{d}T_{\mathrm{s}}}{\mathrm{d}z}\,\mathrm{d}\tilde{z} - \frac{3}{2}Q^{(1)} \int_0^z T_{\mathrm{s}}\mu(T_{\mathrm{s}})\,\mathrm{d}\tilde{z}, \end{aligned} \tag{3.30c}$$

$$\rho^{(1)} = -\frac{1}{16}\mathrm{Pr}Q^{(0)} \frac{1}{T_{\mathrm{s}}^2 k(T_{\mathrm{s}})}\frac{\mathrm{d}T_{\mathrm{s}}}{\mathrm{d}z}\left(6x^2 - x^4 - 5\right), \tag{3.30d}$$

$$T^{(1)} = \frac{1}{16}\mathrm{Pr}Q^{(0)} \frac{1}{k(T_{\mathrm{s}})}\frac{\mathrm{d}T_{\mathrm{s}}}{\mathrm{d}z}\left(6x^2 - x^4 - 5\right), \tag{3.30e}$$

$$\begin{aligned} Q^{(1)} = &\frac{51}{140}\mathrm{Pr}(Q^{(0)})^3 \int_0^1 \frac{\mu(T_{\mathrm{s}})}{k(T_{\mathrm{s}})}\frac{\mathrm{d}T_{\mathrm{s}}}{\mathrm{d}z}\,\mathrm{d}z + \frac{27}{70}(Q^{(0)})^3 \Delta T \\ &+ \frac{6}{35}\mathrm{Pr}(Q^{(0)})^3 \int_0^1 \frac{\mu'(T_{\mathrm{s}})}{k(T_{\mathrm{s}})} T_{\mathrm{s}} \frac{\mathrm{d}T_{\mathrm{s}}}{\mathrm{d}z}\,\mathrm{d}z, \end{aligned} \tag{3.30f}$$

where $\Delta T = 1 - T_{\text{surf}}$ is the dimensionless difference in temperature between the crater and surface, we have written $\mu' = \mathrm{d}\mu/\mathrm{d}T$, and suppressed the dependence of T_{s} on z (and $\tilde{z}$) for compactness. From (3.30), we see that there is both transverse variation in temperature, and a non-zero transverse velocity at $O(\epsilon^2\text{Re})$. This transverse velocity of the fluid is being driven by the transverse temperature variations, since from (3.28a), it is clear that $p^{(1)}$ depends only on z.

Unlike the leading-order solution (3.27), $u^{(1)}$ and $T^{(1)}$ do not satisfy the unidirectional flow and imposed temperature boundary conditions at $z = 0$ given in (3.9a). This suggests that the method of matched asymptotics must be used to construct a uniformly valid $O(\epsilon^2\text{Re})$ asymptotic solution for the flow, by considering an additional region close to $z = 0$. Whilst we do not do that here, it is a relatively straightforward to show that the leading-order form of (3.2b) and (3.2c) imply that pressure must be constant in both x and z in the narrow region, implying the composite solution for $p^{(1)}$, and hence the value of $Q^{(1)}$ will be unaffected by this inner region.

3.2.4.3 Behaviour of the mass flux

Having constructed the asymptotic solution up to order $\epsilon^2\text{Re}$, we now use it to study the relationship between $\epsilon^2\text{Re}$ and Q in the limit where case III is valid. This relationship is an important because Q is the shooting parameter in our numerical simulations of cases I and II described in Section 3.2.3, so understanding its behaviour in a particular limit helps select reasonable initial estimates. Moreover, the relationship can be used to infer the dependence of the dimensional mass flux Q^* on the pressure drop driving the flow. However, this is slightly non-trivial, since using our choice of scalings, given by (2.60), (2.71) and (3.1), the dimensional mass flux, Q^*, is

$$Q^* = \frac{[\mu]}{\epsilon}\epsilon^2\text{Re}Q. \tag{3.31}$$

Hence, the dimensional mass flux is a scalar multiple of $\epsilon^2\text{Re}Q$, and not Q, as $\epsilon^2\text{Re}$ varies. For cases II and III, varying $\epsilon^2\text{Re}$ while keeping all the other parameters fixed is equivalent to varying the pressure in the crater, since $\epsilon^2\text{Re}$ is linearly proportional to Δp^*. However, for case I, varying Δp^* also varies Δp, and so we cannot vary only a single parameter to obtain the dimensional behaviour of varying pressure. To understand the effect of varying channel radius, varying $\epsilon^2\text{Re}$ alone is sufficient for all three reduced models, as ϵ does not appear independently in them.

For case III, we have that

$$Q^* = \frac{[\mu]}{\epsilon}\epsilon^2\text{Re}\left(Q^{(0)} + \epsilon^2\text{Re}Q^{(1)} + o(\epsilon^2\text{Re})\right) \tag{3.32}$$

as $\epsilon^2\mathrm{Re} \to 0$. Thus, to leading-order we have that the dimensional mass flux increases linearly with $\epsilon^2\mathrm{Re}$, and so with Δp^*. This is identical to the exact scaling for a laminar incompressible flow through a channel, [68]. The constant of proportionality varies with $Q^{(0)}$, which depends on T_s and μ only. Unlike the incompressible case, this linear relationship is not exact, and so we must proceed to next order to see if the growth is sub-linear (when $Q^{(1)} < 0$), or super-linear ($Q^{(1)} > 0$).

We start by noting (3.30f) can be rewritten, using a change of variables, as

$$Q^{(1)} = \frac{27}{70}\left(Q^{(0)}\right)^3 \left(\Delta T - \frac{17}{18}\mathrm{Pr}\int_{1-\Delta T}^{1} \frac{\mu(T)}{k(T)} + \frac{8}{17}\frac{\mu'(T)T}{k(T)}\,\mathrm{d}T\right). \tag{3.33}$$

From this we can see that if $\Delta T = 0$, then $Q^{(1)} = 0$, irrespective of the variation of the solid temperature for $0 < z < 1$. This implies that the scaling between Q^* and Δp^* is indeed linear, with a $o\left(\epsilon^2\mathrm{Re}\right)$ correction.

Now assuming $\Delta T \neq 0$, we investigate the sign of $Q^{(1)}$. Since the viscosity of most gases is an increasing function of temperature [91], we assume that $\mu'(T)$ is non-negative. If the solid temperature is decreasing with increasing z, so that $\Delta T > 0$ and the Prandtl number satisfies

$$\mathrm{Pr} < \mathrm{Pr_c} = \frac{18}{17}\Delta T\left(\int_{1-\Delta T}^{1} \frac{\mu(T)}{k(T)} + \frac{8}{17}\frac{\mu'(T)T}{k(T)}\,\mathrm{d}T\right)^{-1}, \tag{3.34}$$

then $Q^{(1)} > 0$ and Q^* is a super-linearly increasing function of $\epsilon^2\mathrm{Re}$. However, if the solid temperature is increasing with increasing z, so that $\Delta T < 0$, then $Q^{(1)} > 0$ and Q is an increasing function of $\epsilon^2\mathrm{Re}$ provided $\mathrm{Pr} > \mathrm{Pr_c}$. However, we will not consider the increasing wall temperature further in this thesis, as it is not relevant for silicon furnaces.

To interpret (3.34), we now consider two possible models for μ and k. Firstly, when the viscosity and thermal conductivity are constant, $\mu \equiv k \equiv 1$, then (3.34) reduces to $\mathrm{Pr} < \mathrm{Pr_c} = 18/17$. If instead we adopt the common power law models for variation with temperature, discussed in Appendix A, then the bound becomes

$$\mathrm{Pr} < \mathrm{Pr_c} = \frac{18}{17}\Delta T\frac{n-\nu+1}{1+\frac{8}{17}n}\left(1-(1-\Delta T)^{n-\nu+1}\right)^{-1}. \tag{3.35}$$

Note that in the special case where $n = \nu$, an approximation used previously in [68, 70], the bound simplifies to $\mathrm{Pr} < 18/(8\nu + 17)$, and as for the constant case, is independent of the temperature distribution.

We plot (3.35) in Figure 3.2, using values of n and ν for five common gases, given in Table 3.3. It is immediately clear that when using the more realistic temperature

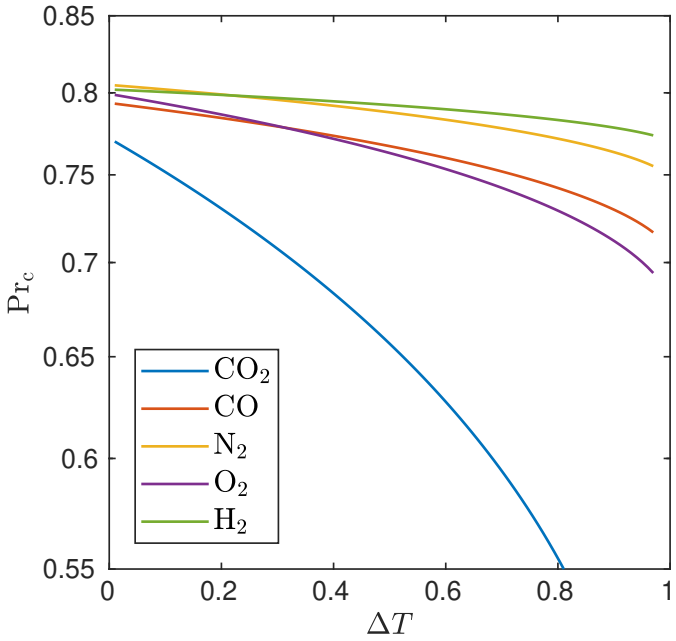


Figure 3.2: The critical value of the Prandtl number, $\mathrm{Pr_c}$, (3.35), determining if $Q^{(1)}$ is positive or negative, evaluated for five common gases: CO_2, CO, N_2, O_2, and H_2, based on power law models for the viscosity and thermal conductivity using data from [91].

Gas	n	ν
CO_2	0.79	1.30
CO	0.71	0.82
N_2	0.67	0.74
O_2	0.69	0.84
H_2	0.68	0.72

Table 3.3: Experimental values for the parameters n and ν in the power laws for viscosity (A.5) and thermal conductivity (A.8), respectively. Data from [91].

dependent viscosity model, the bound on the Prandtl number is much stricter than for the constant case. However, for temperatures below 1000 K, all the gases shown in Figure 3.2 still have a Prandtl number satisfying (3.34). Thus, for these common gases we conclude that when case III is valid, $Q^{(1)}$ is positive, implying that the dimensional mass flux increases super-linearly with the dimensional pressure drop when gas flows along a channel with an imposed, decreasing wall temperature.

3.2.4.4 Behaviour of the energy flux

We now proceed to discuss the behaviour of the energy flux and energy efficiency, as functions of the reduced Reynolds number. As with the mass flux, we begin by

remarking on the general differences between the behaviour of the dimensionless and dimensional energy fluxes, before discussing case III in particular.

Using (2.60), (2.71) and (3.1), the dimensional energy fluxes may be written as

$$(E^*_{\rm crat}, E^*_{\rm Inter}, E^*_{\rm surf}) = \frac{[\mu] c^*_{p,{\rm g}} T^*_{\rm crat}}{\epsilon} \epsilon^2 {\rm Re}\, (E_{\rm crat}, E_{\rm Inter}, E_{\rm surf})\,. \tag{3.36}$$

Hence, the dimensional energy fluxes are proportional to the reduced Reynolds number, and so behave in a similar manner as the dimensional mass flux. In contrast, the energy efficiency (3.6) has an identical value whether it represents the proportion of dimensional or dimensionless energy transferred from the gas to the solid.

Moving onto case III in particular, we substitute (3.22) into (3.5) and (3.6), and expanding

$$\begin{aligned}(E_{\rm crat}, E_{\rm surf}, E_{\rm Inter}, \mathcal{E}) \sim (E^{(0)}_{\rm crat}, E^{(0)}_{\rm surf}, E^{(0)}_{\rm Inter}, \mathcal{E}^{(0)}) \\ + \epsilon^2 {\rm Re}(E^{(1)}_{\rm crat}, E^{(1)}_{\rm surf}, E^{(1)}_{\rm Inter}, \mathcal{E}^{(1)}) + \cdots\end{aligned} \tag{3.37}$$

as $\epsilon^2 {\rm Re} \to 0$, in order to obtain the asymptotic behaviour of the energy fluxes and energy efficiency. We find, using (3.27) and (3.30), that the leading-order energy fluxes are given by

$$E^{(0)}_{\rm crat} = -2 \int_0^1 w^{(0)}\big|_{z=0}\, {\rm d}x \qquad = -Q^{(0)}, \tag{3.38a}$$

$$E^{(0)}_{\rm Inter} = \frac{2}{\rm Pr} \int_0^1 k\left(T^{(0)}\right) \left.\frac{\partial T^{(1)}}{\partial x}\right|_{x=1} {\rm d}z = Q^{(0)} \Delta T, \tag{3.38b}$$

$$E^{(0)}_{\rm surf} = 2 \int_0^1 w^{(0)}\big|_{z=1}\, {\rm d}x \qquad = Q^{(0)}\,(1 - \Delta T)\,, \tag{3.38c}$$

which satisfy $E^{(0)}_{\rm crat} + E^{(0)}_{\rm Inter} + E^{(0)}_{\rm surf} = 0$, as expected. Further, the $O(\epsilon^2 {\rm Re})$ energy fluxes through the crater and the surface are given by

$$E^{(1)}_{\rm crat} = -2 \int_0^1 w_1\big|_{z=0}\, {\rm d}x = -Q^{(1)} + \frac{17}{70} {\rm Pr} (Q^{(0)})^2 \left.\frac{1}{k(T_{\rm s})} \frac{{\rm d}T_{\rm s}}{{\rm d}z}\right|_{z=0}, \tag{3.39a}$$

$$E^{(1)}_{\rm surf} = 2 \int_0^1 w^{(1)}\big|_{z=1}\, {\rm d}x = Q^{(1)}\,(1 - \Delta T) - \frac{17}{70} {\rm Pr} (Q^{(0)})^2 \left.\frac{1}{k(T_{\rm s})} \frac{{\rm d}T_{\rm s}}{{\rm d}z}\right|_{z=1}, \tag{3.39b}$$

respectively. However, we cannot directly evaluate $E^{(1)}_{\rm Inter}$ because it depends on $T^{(2)}$. Instead, we use $E^{(1)}_{\rm crat} + E^{(1)}_{\rm Inter} + E^{(1)}_{\rm surf} = 0$, to find that

$$\begin{aligned} E^{(1)}_{\rm Inter} &= -E^{(1)}_{\rm crat} - E^{(1)}_{\rm surf} \\ &= Q^{(1)} \Delta T + \frac{17}{70} {\rm Pr} (Q^{(0)})^2 \left(\left.\frac{1}{k(T_{\rm s})} \frac{{\rm d}T_{\rm s}}{{\rm d}z}\right|_{z=1} - \left.\frac{1}{k(T_{\rm s})} \frac{{\rm d}T_{\rm s}}{{\rm d}z}\right|_{z=0} \right). \end{aligned} \tag{3.39c}$$

From these we can calculate the first two terms for the energy efficiency, namely

$$\mathcal{E}^{(0)} = -\frac{E^{(0)}_{\text{Inter}}}{E^{(0)}_{\text{crat}}} = \Delta T, \tag{3.40}$$

and

$$\begin{aligned}\mathcal{E}^{(1)} &= \frac{E^{(1)}_{\text{crat}} E^{(0)}_{\text{Inter}} - E^{(0)}_{\text{crat}} E^{(1)}_{\text{Inter}}}{\left(E^{(0)}_{\text{crat}}\right)^2} \\ &= \frac{17}{70}\text{Pr}Q^{(0)} \left(\frac{1}{k(T_\text{s})} \frac{\mathrm{d}T_\text{s}}{\mathrm{d}z}\bigg|_{z=1} - (1-\Delta T)\, \frac{1}{k(T_\text{s})} \frac{\mathrm{d}T_\text{s}}{\mathrm{d}z}\bigg|_{z=0} \right). \end{aligned} \tag{3.41}$$

As the leading-order dimensionless energy fluxes are constant, we know that the dimensional energy fluxes will grow linearly with reduced Reynolds number, and hence dimensional pressure drop. The leading-order efficiency, (3.40), implies that the proportion of either dimensionless, or dimensional, energy transferred to the gas depends only on the temperature at the crater and the surface. Physically this makes sense, as the only term included in the leading-order energy fluxes (3.38a), (3.38c) is the internal energy of the gas, which depends on the mass flux, and the temperature of the gas, which, by (3.27e) is equal to the solid temperature.

3.3 Results

In this section, we will compare numerical solutions of cases I and II to the asymptotic solution of case III, and the numerical solution of the compressible Navier-Stokes equations (3.2)–(3.3). For simplicity, we restrict T_s to be a linear function of z,

$$T_\text{s}(z) = 1 - \Delta T z, \tag{3.42}$$

so that it only depends on a single parameter, ΔT. For the remainder of this chapter we will assume the viscosity and thermal conductivity of the gas are constant, i.e. $\mu \equiv k \equiv 1$. We have also considered the behaviour of the model when viscosity and temperature vary as power laws with temperature, as discussed in Appendix A, but found no qualitative difference in the behaviour compared to the constant case, and so omit those results.

3.3.1 Solutions comparison

We begin by comparing solutions of the different models. This will demonstrate the typical behaviour of solutions to the different models and show that they are in agreement when their various ranges of validity overlap.

In Figure 3.3a, we present cross-sectional profiles of the axial velocity and temperature at $z = 0, 0.25, 0.5, 075$, and 1, alongside the pressure for $0 < z < 1$, when $\epsilon^2\mathrm{Re} = 0.1$, $\Delta T = 0.5$, and $\Delta p = 1/26$. As the reduced Reynolds number is small, these parameter values are representative of the regime where case III is valid. We therefore compare the leading-order asymptotic solution to case III, given by (3.27), to the solution obtained numerically by solving the compressible Navier-Stokes equations (3.2)–(3.3) using COMSOL, and the solution obtained numerically for case I, (3.9) and (3.8). We do not include a numerical solution to case II (3.11)– (3.9), as for these parameter values, the solution is indistinguishable from that for case I. Note that both cases I and II do not have unique steady solutions, and in Figure 3.3a we have picked the solution to case I that best agrees with the solutions of the other models. We defer further discussion of these multiple steady solutions until Section 3.3.2.

For all three of the solution components depicted in Figure 3.3a, there is very good agreement between the two numerical solutions for the compressible Navier-Stokes equations and case I, except near $z = 1$, where the Navier-Stokes solution becomes hotter than the case I solution. This is due to the incompatibility of the reduced models with the outlet boundary conditions (3.3c) at $z = 1$. We also see clear justification in these results for our earlier assumption that the effect of these conditions is confined to a boundary layer. Both the numerical solutions shown also agree with the leading-order asymptotic solution to case III. However, as the leading-order solution for temperature (3.27e) in case III depends only on z, inclusion of the $O(\epsilon^2\mathrm{Re})$ solution (3.30e) would be necessary to capture the small increase in temperature towards the centreline found by the other models, which is caused by advective transport of heat. Indeed, if the $O(\epsilon^2\mathrm{Re})$ terms are included, then all the plots of the variables in the problem in the case I and case III solutions would be indistinguishable. The small size of this discrepancy in transverse variation in temperature confirms that the gas cannot be significantly hotter than the surrounding solid in this parameter regime, and so is not representative of the conditions in a furnace when gas is exiting at temperatures hotter than the surface temperature of the solid material.

Figure 3.3b similarly compares the axial velocity and temperature cross-sectional profiles, and the pressure variation with z when $\epsilon^2\mathrm{Re} = 10$, $\Delta T = 0.5$, and $\Delta p = 1/26$. Case III is not valid for these parameter values, so we compare only the numerical solution for case I to the numerical solution of the compressible Navier-Stokes equations, omitting the numerical solution of case II since it is indistinguishable

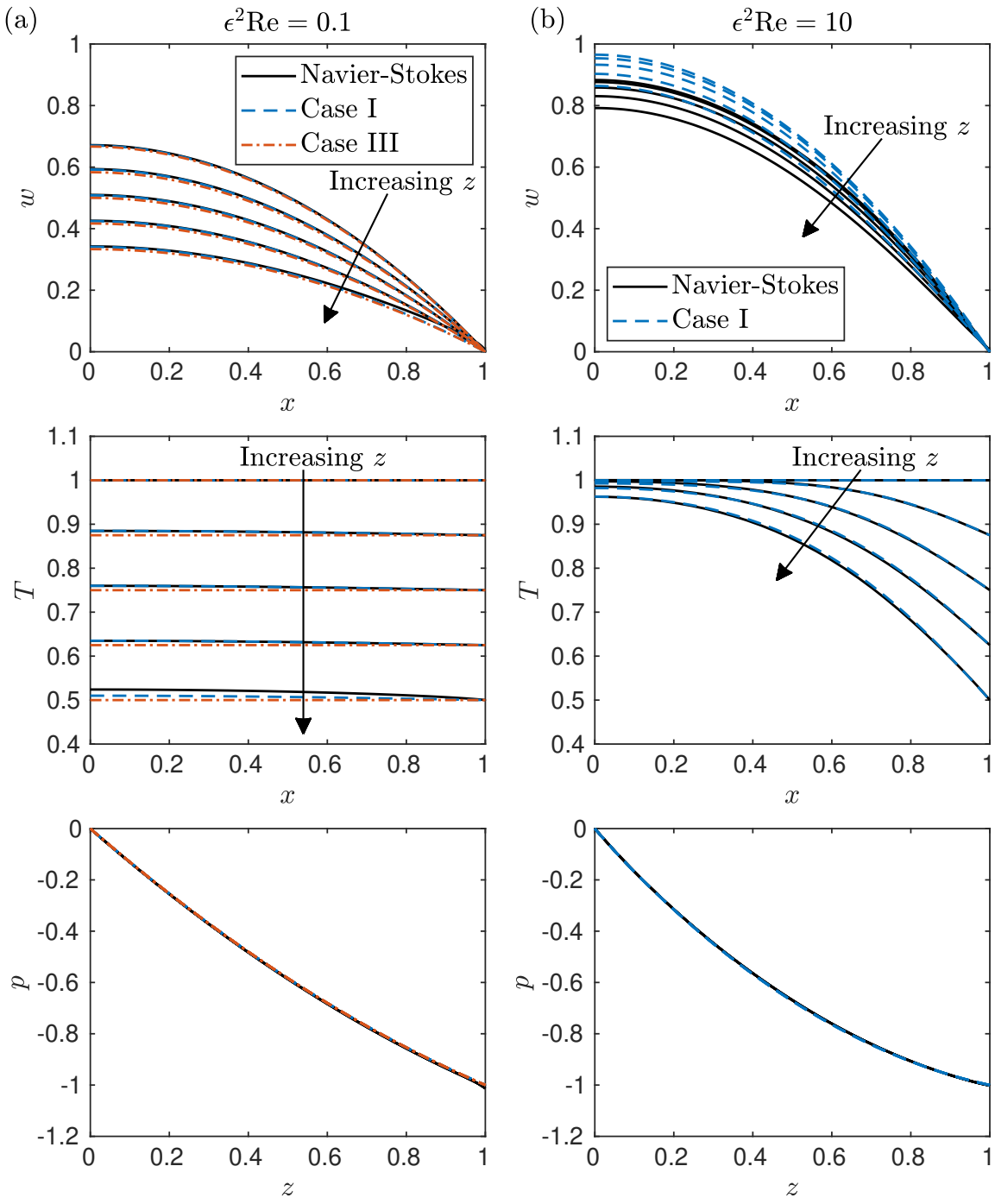


Figure 3.3: Cross-sections of the axial velocity w, and temperature T taken at $z = 0, 0.25, 0.5, 0.75, 1$, along with pressure profiles varying with z. Numerical solutions of the Navier-Stokes equations are shown by solid black lines, and of case I by dot-dash blue lines. The leading-order asymptotic solution to case III is shown by red dashed lines. The parameter values are (a) $\epsilon^2\mathrm{Re} = 0.1$ and (b) $\epsilon^2\mathrm{Re} = 10$, with $\Delta T = 0.5$ and $\Delta p = 1/26$.

from the numerical solution for case I. The agreement between the two models is very good for the temperature and pressure. In particular, the temperature profiles confirm that in the parameter range of order unity reduced Reynolds number, steady solutions for the gas may have a significantly higher temperature than the surrounding solid. However, the solution for case I overestimates the axial velocity compared to the COMSOL results. This effect can entirely be explained by the differing mass fluxes with $Q = 1.28$ and $Q = 1.18$ for case I and the Navier-Stokes equations respectively. If both solutions are normalised by their respective values of Q, then the axial velocity, and temperature profiles would overlay each other.

Finally, we compare the transverse velocity profiles u for both solutions given in Figure 3.3. As these do not vary monotonically with z, they are shown in Figure 3.4 as heat maps. We do not plot the leading-order asymptotic solution for case III, (3.27a), as it is zero. We would therefore expect the transverse velocities obtained by solving case I and the compressible Navier-Stokes equations to be small. However, the solution obtained for the compressible Navier-Stokes equations shows that the transverse velocity is of order unity near $z = 1$. As before, this can be explained by noting that, if we were to enforce the boundary conditions at $z = 1$, (3.3c), in the reduced models, we would need to perform a boundary layer analysis around $z = 1$. Hence, to ensure the conservation of mass equation, (3.2a), remains fully balanced, the transverse velocity would have to become large. This makes it difficult to use Figure 3.4 to directly compare the velocities. Therefore, in Figure 3.5 we plot the absolute value of the differences between the transverse velocities for case I and the compressible Navier-Stokes equations, along the line $x = 1/2$ for both $\epsilon^2\mathrm{Re} = 0.1$ and $\epsilon^2\mathrm{Re} = 10$. The value of ϵ^2, based on the value used in the COMSOL calculations is also shown as a dotted line. Apart from the pressure term in (3.2e), the terms of size $O(\epsilon^2)$ are the largest omitted in case I. Figure 3.5 shows that away from $z = 0$ and $z = 1$, the error almost exactly matches what we should expect when $\epsilon^2\mathrm{Re} = 10$, and is much smaller when $\epsilon^2\mathrm{Re} = 0.1$. The error near $z = 1$ is caused by the previously discussed boundary layer. The error near $z = 0$ is caused by a spike in the value of u given by case I. This sudden increase, most clearly shown for $\epsilon^2\mathrm{Re} = 0.1$, is caused by small errors in the discretised, transformed problem, in enforcing the boundary condition $u = 0$ in (3.9a). The size and shape of this error is dependent on both the number of mesh points and the tolerances used by ode15s. However, as can be seen from Figure 3.5, the error does not appear to propagate downstream, and the error between the solutions quickly reduces to its expected size.

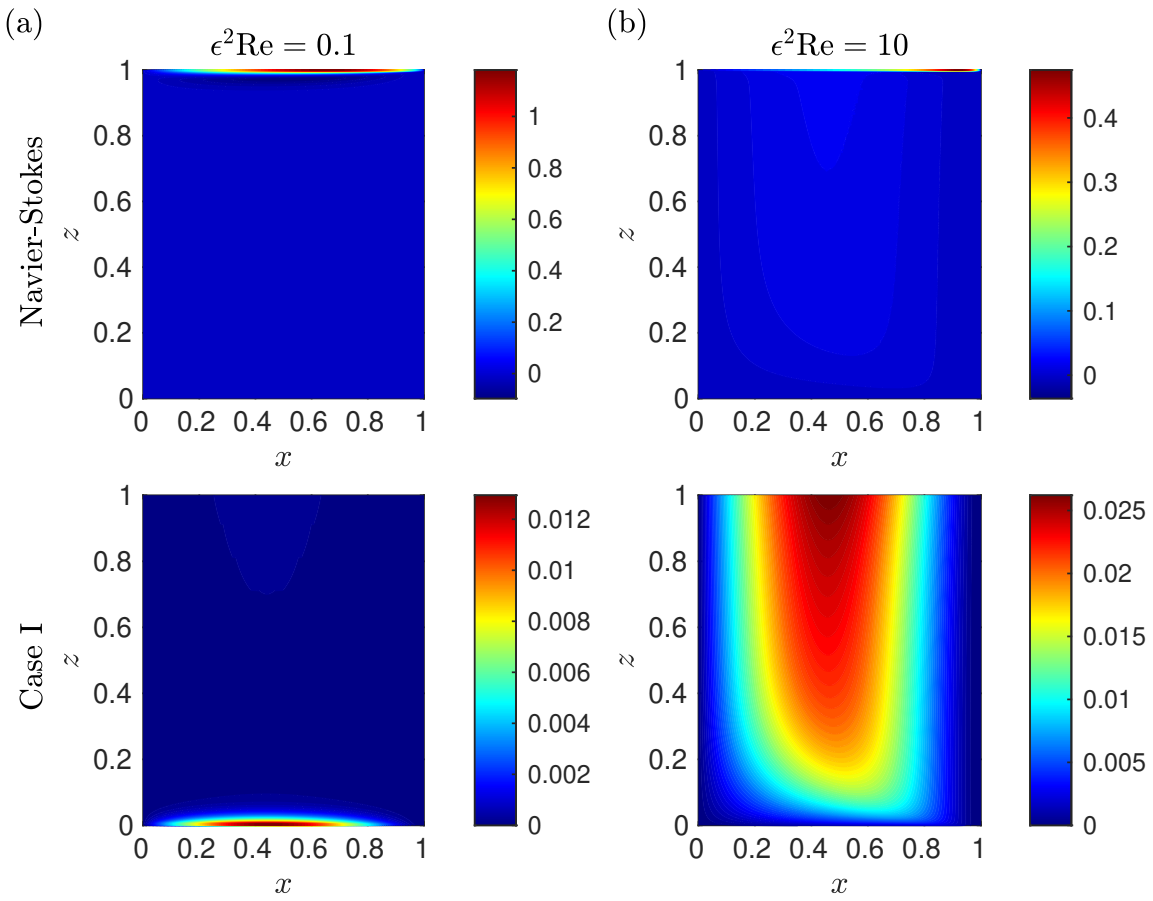


Figure 3.4: The transverse velocity u found by solving case I and the compressible Navier-Stokes equations when (a) $\epsilon^2\mathrm{Re} = 0.1$ and (b) $\epsilon^2\mathrm{Re} = 10$, with $\Delta T = 0.5$ and $\Delta p = 1/26$.

The comparison in this section demonstrates good agreement between the numerical solution of case I using the method described in Section 3.2.3, the numerical solution of the compressible Navier-Stokes equations using the commerical finite element package COMSOL, and an asymptotic solution in the limit $\epsilon^2\mathrm{Re} \to 0$. Together with the convergence tests in Appendix C, this demonstrates the method described in Section 3.2.3 has been correctly implemented. We therefore proceed to use it to investigate the dependence of the mass and energy flux on the parameters in the problem.

3.3.2 Mass flux

We now discuss in detail the relationship between the mass flux and reduced Reynolds number in detail. We will present all our results in dimensionless quantities, but using the relationship discussed in Section 3.2.4.3, will then interpret their meaning for the

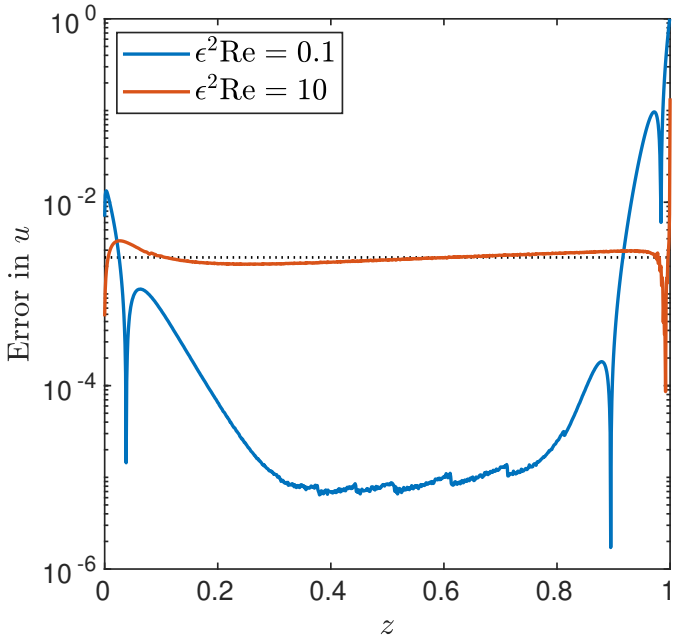


Figure 3.5: The absolute value of the difference between the transverse velocity u for the numerical solutions of the Navier-Stokes equations and of Case I, at $x = 1/2$, as a function of z. The error when $\Delta T = 0.5$, $\Delta p = 1/26$, and $\epsilon^2\mathrm{Re} = 0.1$ is shown by a solid blue line, while the error when $\epsilon^2\mathrm{Re} = 10$ is shown by a solid red line. The value of ϵ^2 used in computing the solutions to the compressible Navier-Stokes is shown by a black dotted line.

dimensional mass flux.

In Figure 3.6 we plot the mass flux Q, defined by (3.4), as a function of the reduced Reynolds number $\epsilon^2\mathrm{Re}$, with each panel calculated for a different dimensionless temperature drop ΔT. Within each panel, we show results from case I as lines and results from the full Navier-Stokes equations as symbols, using different colours to denote different values of the dimensionless pressure drops Δp. We vary Δp to investigate the behaviour of the case I reduced model as it tends towards the case II reduced model, the results from which have also been plotted in the figure using black lines. From these results it is immediately clear that the reduced models demonstrate non-uniqueness of steady solutions and, for case II, non-existence for values of $\epsilon^2\mathrm{Re}$ above a critical value, for all values of ΔT and Δp. However, for $\Delta T = 0.25$ and $\Delta p = 1/26$, the solutions of the full compressible Navier-Stokes equations predict solutions exceeding this critical value, indicating that the non-existence of solutions to case II must be due to some physical process missing from that model. This demonstrates the importance of considering case I, despite not being a valid asymptotic limit, it is able to match the behaviour of the compressible Navier-Stokes equations

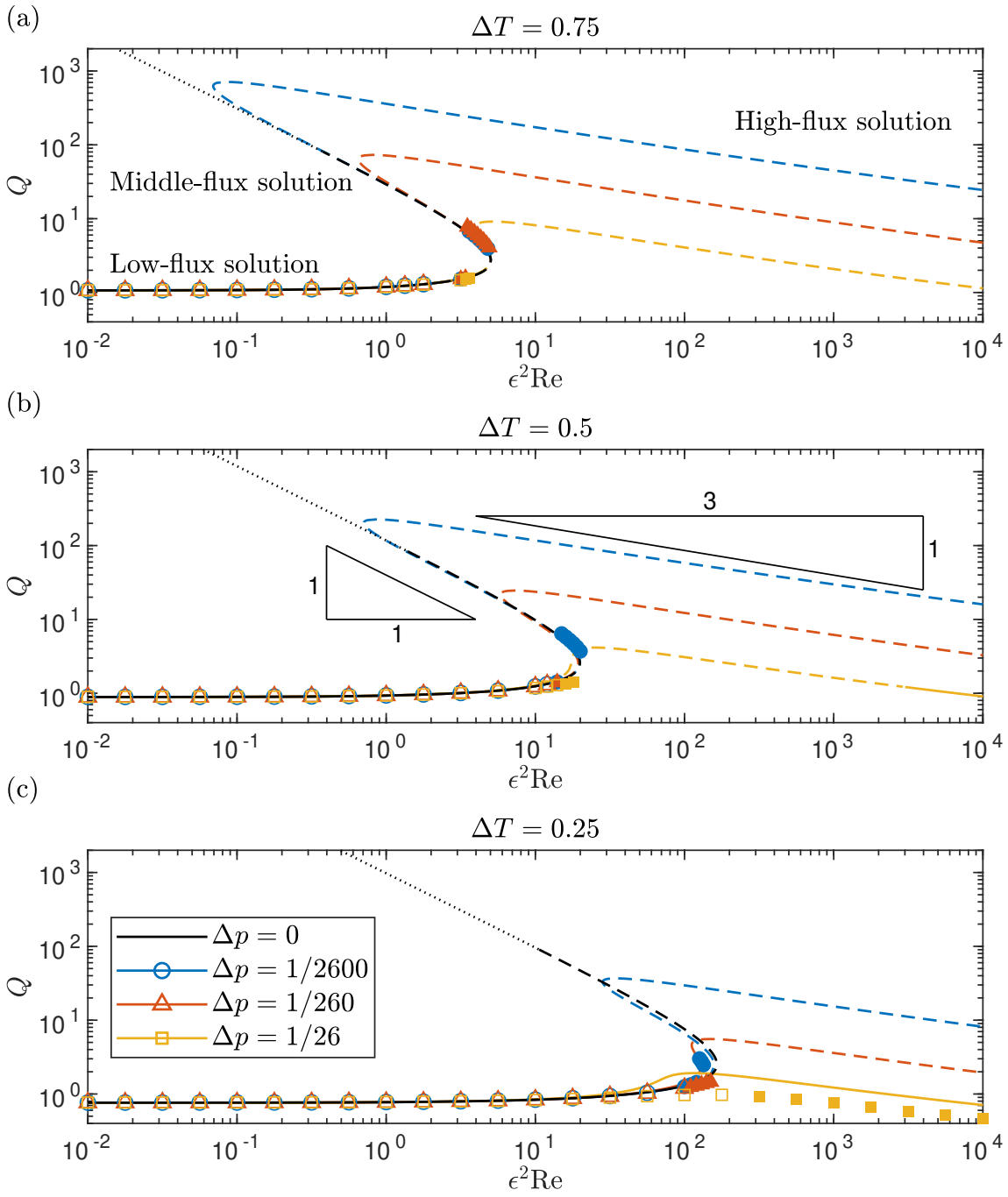


Figure 3.6: The mass flux Q as a function of the reduced Reynolds number ϵ^2Re for different pressure drops Δp when the temperature drop is: (a) $\Delta T = 0.75$, (b) $\Delta T = 0.5$, (c) $\Delta T = 0.25$. Numerical solutions to case I (3.9), (3.8) are shown by coloured lines, and numerical solutions of the compressible Navier-Stokes equations (3.2)–(3.3) are shown by coloured symbols where: $\Delta p = 1/2600$ blue circles; $\Delta p = 1/260$ red triangles; $\Delta p = 1/26$ yellow squares. Numerical solutions to case II ($\Delta p = 0$) are shown by black lines. A solution with a non-montonic pressure profile is shown by a dashed lines or filled symbol. Solutions to case II where the dimensional pressure becomes negative, when $\Delta p = 1/26$, are shown by a dotted line.

when the model from the valid asymptotic limit, case II, is unable to do so.

For all sets of parameter values shown in Figure 3.6, there is a solution branch along which Q tends to a constant as $\epsilon^2\mathrm{Re} \to 0$. This solution is found for all three models in the figure, and it is these solutions that were discussed in Section 3.3.1. The values of Q predicted by all three models are in excellent agreement along this branch. When $\epsilon^2\mathrm{Re} \ll 1$, they are also in excellent agreement with the value of the leading-order asymptotic solution Q_0, (3.27f), although this is not shown in the figure to improve readability. However, the behaviour of the other solutions to the models are not in such clear agreement; we discuss each model in turn.

The numerical solution of case I, (3.9) and (3.8), shown by coloured lines in Figure 3.6, form 'S'-shaped curves for the majority of parameter values shown, meaning there exists an interval of reduced Reynolds number values for which three different steady solutions exist. We will call the solution with the lowest flux as $\epsilon^2\mathrm{Re} \to 0$ the 'low-flux' solution, while we will refer to the other solutions as the 'middle-' and 'high-flux' solutions respectively, as labelled in Figure 3.6. Outside this interval a single steady solution exists for a given value of $\epsilon^2\mathrm{Re}$, connecting to the low-flux solution for $\epsilon^2\mathrm{Re} \to 0$, and the high-flux solution for $\epsilon^2\mathrm{Re} \to \infty$. The position of this interval moves to the right as ΔT decreases. The exception to this behaviour is the $\Delta p = 1/26$ curves for $\Delta T = 0.25$ and 0.5 which do not form 'S'-shapes and instead have a unique solution for all $\epsilon^2\mathrm{Re}$. These curves still follow the trend of the low- and high-flux solutions as $\epsilon^2\mathrm{Re} \to 0$ and $\epsilon^2\mathrm{Re} \to \infty$, respectively, with the transition between them happening in a narrow region.

To illustrate the difference between the low-, middle- and high-flux solutions to case I, in Figure 3.7 we plot all three solutions when $\epsilon^2\mathrm{Re} = 2$, $\Delta p = 1/2600$, and $\Delta T = 0.75$. The velocity profiles show that the maximum velocity in the solution increases with mass flux, and in all of the solutions there is a non-zero transverse component to the velocity moving the gas towards the wall. From the isotherms, we see that the low-flux solution is the only solution where the gas cools significantly across the entire width of the channel. This is why the velocity profile for the low-flux solution shows the velocity decreasing as z increases. In both the middle- and high-flux solutions, the gas cools in a boundary layer region near the wall, with the boundary layer for the high-flux solution being noticeably thinner. The high-flux solution also cools near the centreline and has a region where $T > 1$, and so the gas has heated, not cooled. We can interpret the position and shape of these regions in the high-flux solution by considering the sign of the terms multiplied by the Eckert number in the energy equation. The viscous dissipation (the shear rate squared)

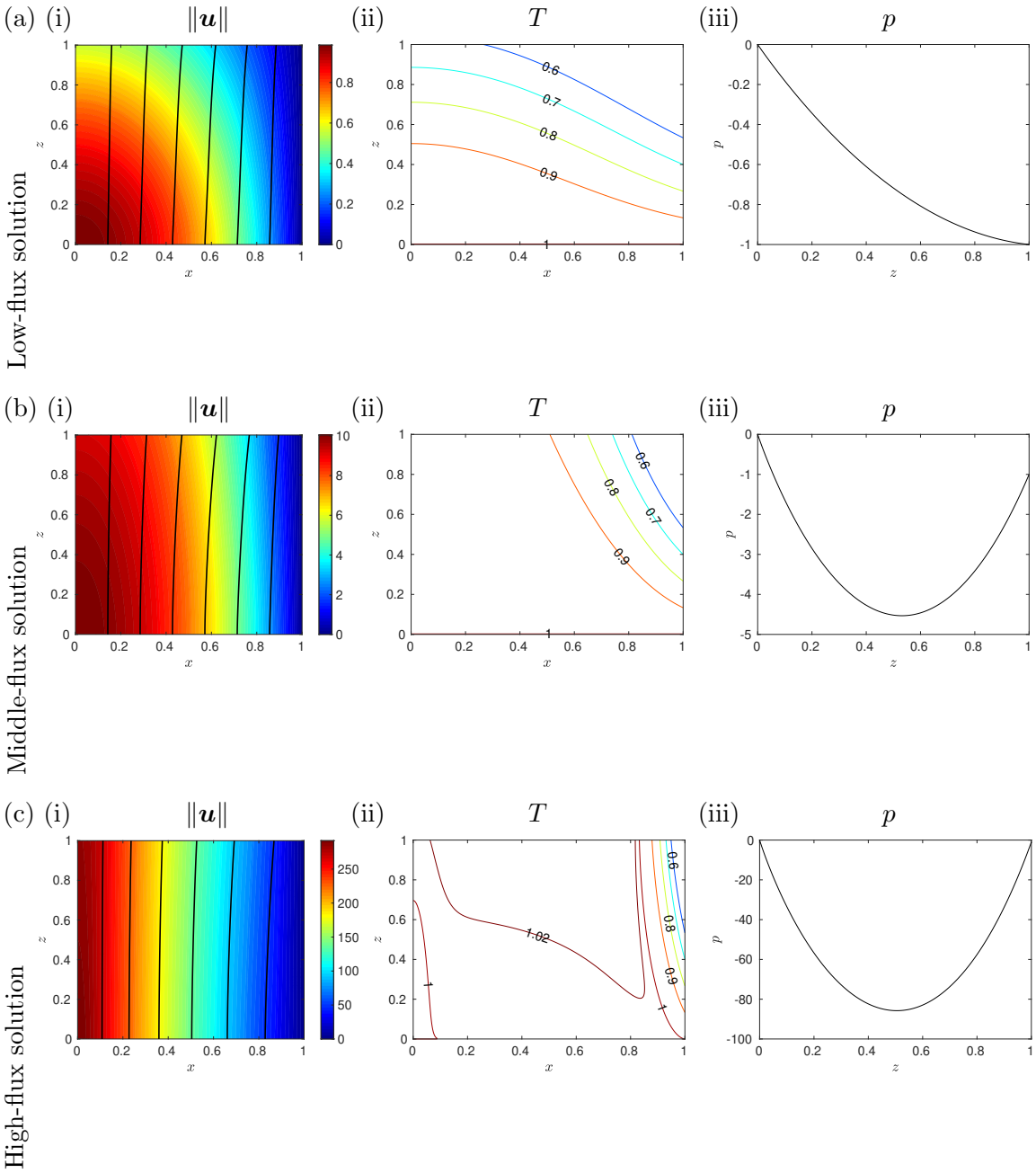


Figure 3.7: The velocity magnitude $\|\boldsymbol{u}\|$, temperature T, and pressure p of the three steady solutions to case I when $\epsilon^2\mathrm{Re} = 2$, $\Delta p = 1/2600$ and $\Delta T = 0.75$. The mass flux of the respective solutions are (a) $Q = 1.32$, (b) $Q = 13.5$, and (c) $Q = 288$. The black lines in (a)(i),(b)(i), and (c)(i) are streamlines.

cannot be negative, so will always act as a heat source. Since the velocity solution has an approximately Poiseuille shape, the shear rate increases as x increases, and hence is greatest near the wall. This is why the region of heated gas starts just outside the boundary layer where cooling occurs near the wall. The work done by compression (the axial velocity times the pressure gradient) will normally act as a heat sink, since the flow direction will be opposite to the pressure gradient. However, from the pressure profiles in Figure 3.7, we see that the high-flux solution actually has an adverse pressure gradient for $z > 0.5$. We discuss the full consequences of this below, and for now just note that this implies the work done by compression will actually be acting as a heat source for $z > 0.5$ as the two terms have the same sign. Since the pressure is x-independent by (3.8b), the magnitude of the work done by compression is largest near $x = 0$, since that is where the axial velocity is largest. Hence, we see that for $z < 0.5$, the gas cools near the centreline due to the work done by compression acting as a heat sink, but that region quickly disappears once it becomes a heat source. For $z > 0.5$, the growth of the region of heated gas towards the centreline also rapidly increases, as there is no longer a heat sink to oppose the viscous heating. We do not observe similar regions in the low- and middle- flux solutions as the size of the velocity and pressure in those solutions is small enough for the size of the viscous dissipation and the work the done by compression in the energy equation to be small.

As mentioned above, the high-flux solution, and the middle-flux solution to case I in Figure 3.7 have non-monotonic pressure profiles. We have indicated those solutions to case I which have non-monotonic pressure profiles in Figure 3.6 using dashed lines. This shows that the transition to non-monotonic pressure solutions actually occurs before the transition between the low- and middle-flux solutions. Moreover, the non-monotonic pressure solutions are not confined to the region of multiple solutions, with the high-flux solution continuing to display non-monotonic pressure as $\epsilon^2\mathrm{Re}$ becomes large.

To explore the dynamics of the pressure further, in Figure 3.8 we plot how the minimum pressure varies for the solutions shown in Figure 3.6. From Figure 3.8, we see that for case I, the lowest minimum pressure occurs close to the transition between middle- to high-flux solution, which also corresponds to the largest possible value of Q. This means the minimum pressure is increasing along the high-flux solution branch, and, for the $\Delta p = 1/26$, $\Delta T = 0.5$ solutions again have a monotonic pressure profile when $\epsilon^2\mathrm{Re}$ is above 3000.

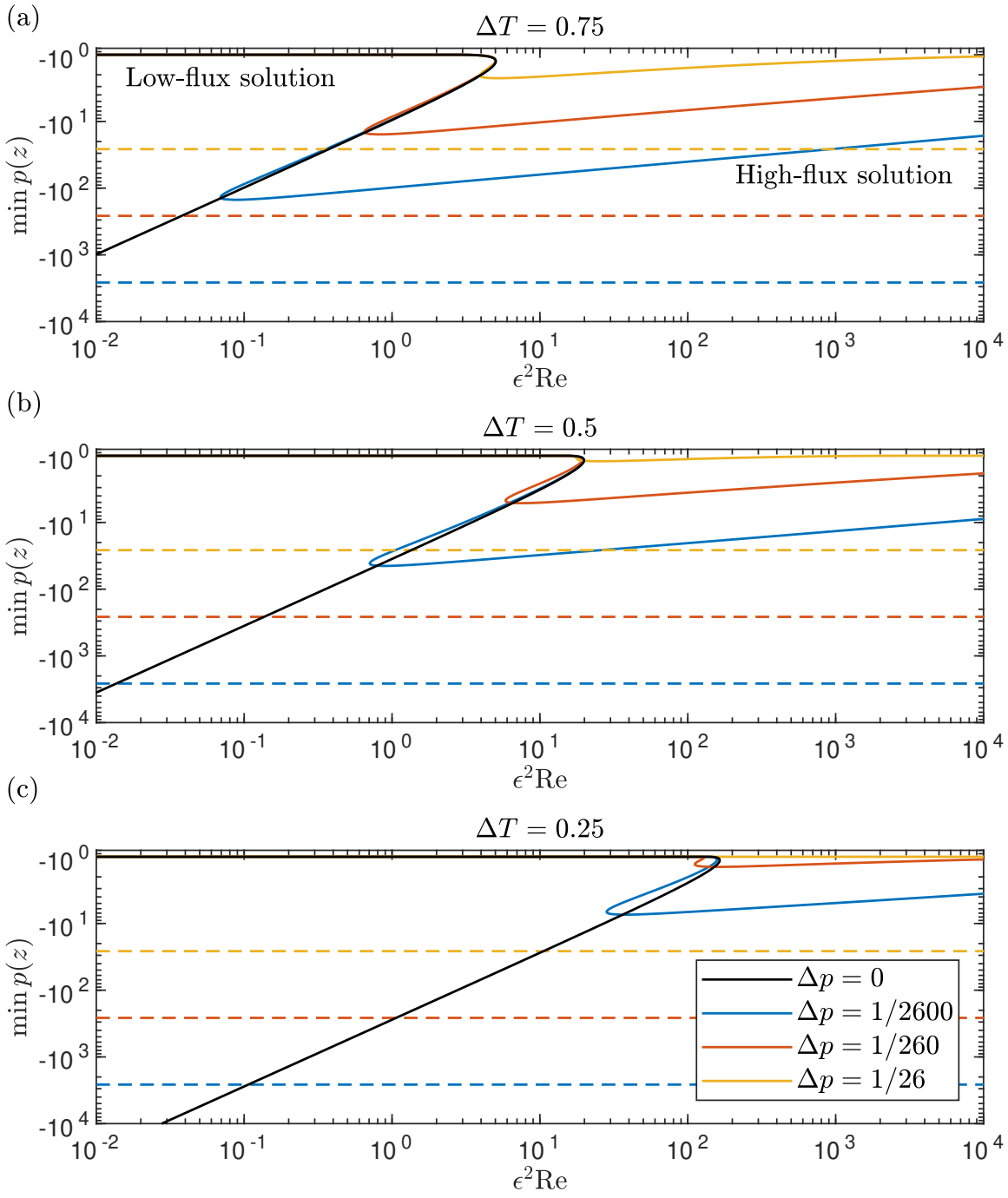


Figure 3.8: The minimum pressure in the solution as a function of the reduced Reynolds number for different dimensionless pressure drops Δp when the temperature drop is: (a) $\Delta T = 0.75$, (b) $\Delta T = 0.5$, (c) $\Delta T = 0.25$. The values for case I, (3.9), (3.20) are shown by coloured solid lines, with: $\Delta p = 1/2600$ blue; $\Delta p = 1/260$ red; $\Delta p = 1/26$ yellow. The smallest physically possible value of pressure, $-(\Delta p)^{-1}$, is shown for each value of Δp by a coloured dashed line. The value of minimum pressure for case II, (3.11)–(3.9), equivalent to case I with $\Delta p = 0$, are shown by a black line.

We now move on to discuss case II, (3.9) and (3.11), the limit of case I as $\Delta p \to 0$, whose results are shown in Figure 3.6 by a black line. Its behaviour mimics case I in the transition from the low- to middle-flux solution. However, unlike case I, case II never transitions from the middle-flux solution to the high-flux solution. Instead, case II continues along the same trajectory of the middle flux solution to case I, as $\epsilon^2\mathrm{Re} \to 0$. Hence, we have found that the case II parameter space is divided into two regions; below a critical reduced Reynolds number two steady solutions exist, while above it none exist.

We can be confident in our assertion that case II has no additional steady solutions, not shown in Figure 3.6, due to the method used to solve it numerically. Since we use a shooting method based on finding a Q such that $p\big|_{z=1} = -1$, and evaluating the model for a given Q takes at most seconds on a typical laptop, it is possible to perform an exhaustive sweep of all possible values of Q. A useful way to visualise this is to perform such a sweep for different values of $\epsilon^2\mathrm{Re}$, and then plot the contours of $p\big|_{z=1}$ as a function of both Q and $\epsilon^2\mathrm{Re}$. The solution curves in Figure 3.6 are then equivalent to the contour defined by $p\big|_{z=1} = -1$. Examples of such a contour plot are given in Figure 3.9, for both cases I and II when $\Delta T = 0.5$ and $\Delta p = 1/2600$, showing the behaviour around the transition between the different solution branches. This plot demonstrates how the inclusion of internal heating in case I causes the switch from the middle- to the high-flux solution branch, by changing the limit as $\epsilon^2\mathrm{Re} \to \infty$ and $Q \to \infty$ from $p\big|_{z=1} \to \infty$ in case II, to $p\big|_{z=1} \to -\infty$ for case I. The plot also demonstrates the lack of a solution to case II above the low- to middle-flux solution transition.

As in case I, the middle-flux solution to case II has a non-monotonic pressure profile. However, from Figure 3.8, where the minimum pressure of solutions for case II are displayed as black lines, we see that size of the minimum pressure continues to decrease along the middle-flux branch as $\epsilon^2\mathrm{Re} \to 0$ and $Q \to \infty$. In particular, this means the pressure for case II solutions goes below $-(\Delta p)^{-1}$, shown by dashed lines in the figure, meaning that the dimensional pressure would be negative, which is physically impossible. In contrast, the minimum pressures of solutions to case I, shown in Figure 3.8, remain above these lower bounds. Therefore, one of the internal heating terms, most likely the work done by compression since it contains a gradient of pressure, is providing an energetic penalisation to the non-monotonic pressure, preventing them becoming unphysical.

The solutions for the full Navier-Stokes equations shown in Figure 3.6 agree with both cases I and II along the low-flux solution branch. In particular, they also predict

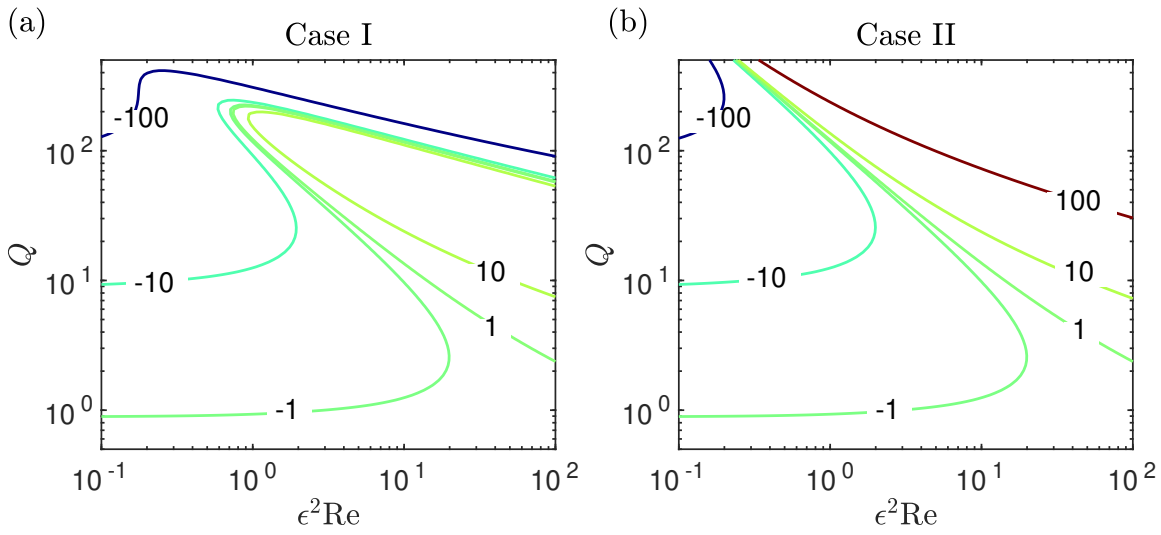


Figure 3.9: Contour plots of the pressure at the outlet $p|_{z=1}$, as the reduced Reynolds number ϵ^2Re and the mass flux Q vary for: (a) Case I and (b) case II, with $\Delta T = 0.5$ and $\Delta p = 1/2600$.

a transition to non-monotonic solutions on the low-flux solution branch, shown using filled symbols, at a similar value to that predicted by cases I and II. For $\Delta p = 1/260$ and $1/2600$, COMSOL also converged to solutions on the middle-flux solution branch for a small range of ϵ^2Re, close to the low- to middle-flux transition. However, attempting to use continuation methods to find solutions further along the middle-flux solution branch was unsuccessful, unless an impractically small step was taken. For values of ϵ^2Re larger than the low- to middle-flux solution, COMSOL would not converge to any steady solution, with the exception of the parameter values $\Delta p = 1/26$, $\Delta T = 0.25$, for which a solution was found for all values of ϵ^2Re. Moreover, this is the only set of parameter values in Figure 3.6 for which case I predicted a monotonic pressure for all values of ϵ^2Re. While the COMSOL solutions for these parameter values are marked as non-monotonic, the pressure minimum stays close to $z = 1$ in these solutions, and the non-monotonicity appears to be caused by the normal stress near $z = 1$, rather than the pressure, being imposed in (3.3c). The values of Q found with this set of parameters show the largest discrepancy between the reduced and full models, with mass flux predicted by solving the compressible Navier-Stokes equations noticably lower than that predicted by case I. However, beyond the low- to middle-flux solution transition, they both decrease at the same rate (cf. Figure 3.6c). It would be interesting to try applying continuation in Δp rather than ϵ^2Re in the COMSOL solutions, to try and find solutions to the compressible Navier-Stokes equations, on the high-flux solution branches for other parameter values.

So far the discussion in this section has been confined to the behaviour of the dimensionless mass flux, whose behaviour in Figure 3.6, could be approximately described as follows: Q is constant on the low-flux solution branch when $\epsilon^2\mathrm{Re} \ll 1$ and increasing when $\epsilon^2\mathrm{Re} = O(1)$; $Q \propto (\epsilon^2\mathrm{Re})^{-1}$ on the middle-flux solution branch; and $Q \propto (\epsilon^2\mathrm{Re})^{-1/3}$, on the high-flux solution branch. However, by the discussion from Section 3.2.4.3, we know that the dimensional mass flux Q^* is a scalar multiple of $\epsilon^2\mathrm{Re}Q$, not Q. Hence, recalling that $\epsilon^2\mathrm{Re}$ is proportional to the dimensional pressure drop Δp^*, the behaviour of Q^* can be summarised as follows. On the low-flux solution branch, if $\epsilon^2\mathrm{Re} \ll 1$ then $Q^* \propto \Delta p^*$ with a $O(\epsilon^2\mathrm{Re})$ correction, while if $\epsilon^2\mathrm{Re} = O(1)$, then Q^* grows super-linearly. On the middle-flux solution branch, Q^* is approximately a constant for all values of Δp^*. On the high-flux solution branch $Q^* \propto (\epsilon^2\mathrm{Re})^{2/3}$. However, we cannot directly infer the scaling of Q^* with Δp^* on the high-flux branch, since varying Δp^* also varies Δp, which was held fixed for each set of results in Figure 3.6. For the other solution branches this did not matter, as the results coincided for all values of $\Delta p \ll 1$, but on the high-flux solution branch they are distinct. Nevertheless, from the trend between the different sets of results as Δp varies, we can see that Q will decrease faster as Δp^* varies. Hence, Q^* will grow slower than $(\Delta p^*)^{2/3}$. This behaviour is reminiscent of the transition undergone when incompressible flow in a channel changes from a laminar flow, where $Q^* \propto \Delta p^*$, to a turbulent flow where $Q^* \propto (\Delta p^*)^{1/2}$ [68, 91]. However, there is nothing in the behaviour of individual high-flux solutions indicative of turbulent behaviour, and, as far as we are aware, no solutions to the incompressible case exhibit the adverse pressure gradient seen in the present analysis.

3.3.3 Energy transfer

In Figure 3.10, we plot the dimensionless total energy flux from the crater to the gas channel, $|E_{\mathrm{crat}}|$, and the dimensionless total energy flux from the gas channel to the surrounding solid, E_{Inter}. We show values obtained numerically for the compressible Navier-Stokes, (3.5), and cases I and II, (3.20), which correspond to the mass fluxes shown in Figure 3.6. The corresponding energy efficiency $\mathcal{E}$, defined in (3.6), is shown in Figure 3.11.

Along the low flux solution branch, the energy fluxes for cases I and II both tend to a constant value as $\epsilon^2\mathrm{Re} \to 0$, equal to that predicted using the leading-order asymptotic solution to case III, (3.38). Similarly, their energy efficiency tends to the asymptotically predicted value (3.40). In contrast, the energy efficiencies calculated from the compressible Navier-Stokes solutions, and shown in Figure 3.11, only agree

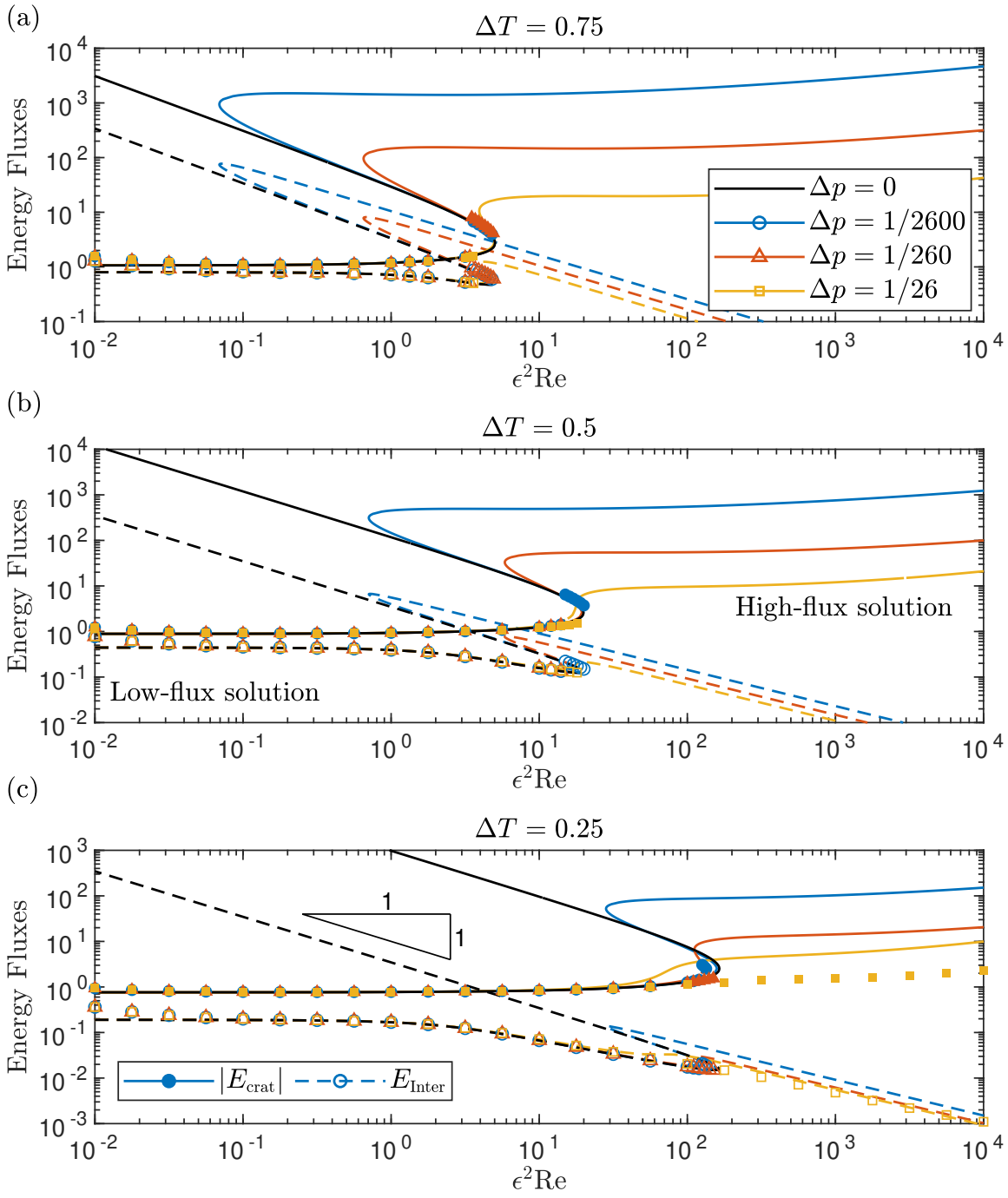


Figure 3.10: The total energy flux from the crater to the gas channel, $|E_{\rm crat}|$, shown by solid lines and filled symbols, and from the channel to the surrounding solid, $E_{\rm Inter}$, shown by dashed lines and unfilled symbols, as a function of reduced Reynolds number ϵ^2Re, when the temperature drop is: (a) $\Delta T = 0.75$, (b) $\Delta T = 0.5$, (c) $\Delta T = 0.25$. Numerical solutions to case I (3.24), (3.8) are shown by coloured lines, and numerical solutions of the compressible Navier-Stokes equations (3.2)–(3.3) are shown by coloured symbols with: $\Delta p = 1/2600$ blue circles; $\Delta p = 1/260$ red triangles; $\Delta p = 1/26$ yellow squares. The numerical solution to case II is shown by black lines.

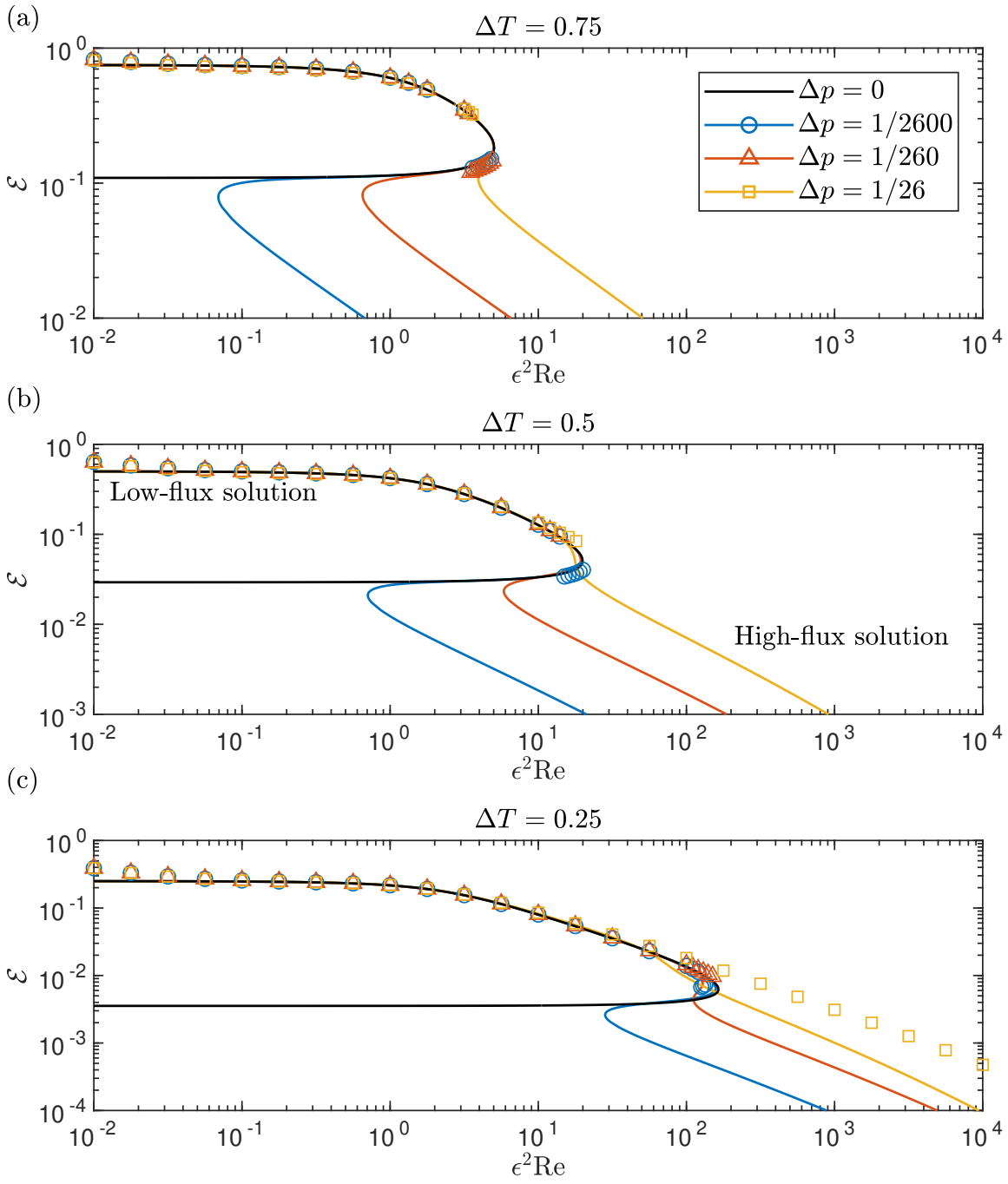


Figure 3.11: The energy efficiency (3.6) as a function of the reduced Reynolds number ϵ^2Re for different pressure drops Δp when the temperature drop is: (a) $\Delta T = 0.75$, (b) $\Delta T = 0.5$, (c) $\Delta T = 0.25$. Numerical solutions to case I (3.24), (3.8) are shown by coloured lines, and numerical solutions of the compressible Navier-Stokes equations (3.2)–(3.3) are shown by coloured symbols where: $\Delta p = 1/2600$ blue circles; $\Delta p = 1/260$ red triangles; $\Delta p = 1/26$ yellow squares. Numerical solutions to case II ($\Delta p = 0$) are shown by a black line.

with the value predicted by cases I and II along the low-flux solution when $\epsilon^2\mathrm{Re} > 0.03$. The discrepancy in the behaviour of the energy efficiency for lower reduced Reynolds numbers can be explained by noting that, as discussed in Section 3.1.4, the solutions to the compressible Navier-Stokes were all obtained with $\epsilon = 0.05$, meaning that $\epsilon^2\mathrm{Re} = 0.03$ implies $\mathrm{Re} = 12$, so that the assumption $\mathrm{Re} \gg 1$ is called into question.

When $\epsilon^2\mathrm{Re} = O(1)$, along the low-flux solution branch, the energy flux from the crater increases, while the energy flux into the solid decreases. This causes the energy efficiency to decrease rapidly. From Figure 3.11, we see that when $\Delta T = 0.75$ (the industrially-relevant value,) the proportion of thermal energy in the gas transferred to the solid falls from 75 % to less than 20 % as $\epsilon^2\mathrm{Re}$ increases from 0.7 to 7. Since only a small increase in pressure in the crater, or in the width of the channel is necessary to alter the reduced Reynolds number by that amount, this mechanism could cause a significant loss of energy efficiency in the furnace in practice.

Along the middle-flux solution branch, both $|E_{\mathrm{crat}}|$ and E_{Inter} approximately scale like $(\epsilon^2\mathrm{Re})^{-1}$. Recalling the discussion from Section 3.2.4.4, this means that the dimensional energy fluxes are both approximately constant along the middle-flux solution branch. As the two fluxes are constant on this solution branch, their energy efficiency does not vary.

Along the high-flux solution branch, E_{Inter} continues to scale like $(\epsilon^2\mathrm{Re})^{-1}$, meaning the dimensional energy flux E^*_{Inter} is approximately constant. This is expected, as from Figure 3.7, there is boundary layer-type behaviour near the interface, and it is this local behaviour that is determining E_{Inter}, rather than the behaviour in the rest of the channel. In contrast to Q, $|E_{\mathrm{crat}}|$ is an increasing function of $\epsilon^2\mathrm{Re}$ along the high-flux solution branch. Hence, unlike Q^* which increased sub-linearly with $\epsilon^2\mathrm{Re}$, $|E^*_{\mathrm{crat}}|$ increases super-linearly. Since E^*_{Inter} remains constant, but $|E^*_{\mathrm{crat}}|$ increases, the energy efficiency of the high-flux solution branch rapidly decreases.

3.3.4 Varying the Prandtl number

We now consider how varying the Prandtl number affects the relationship between mass flux and reduced Reynolds number. Our motivation for this comes from Section 3.2.4.3, where it was predicted, using the solution to case III, that when the Prandtl number exceeds a critical value, $\mathrm{Pr_c}$, given by (3.35), the mass flux Q would begin decreasing with increasing $\epsilon^2\mathrm{Re}$ rather than increasing, as we observed in Figure 3.6, for the industrially-relevant Prandtl number. Since a gas with constant viscosity and thermal conductivity has $\mathrm{Pr_c} = 18/17$, we show in Figure 3.12 the mass flux Q,

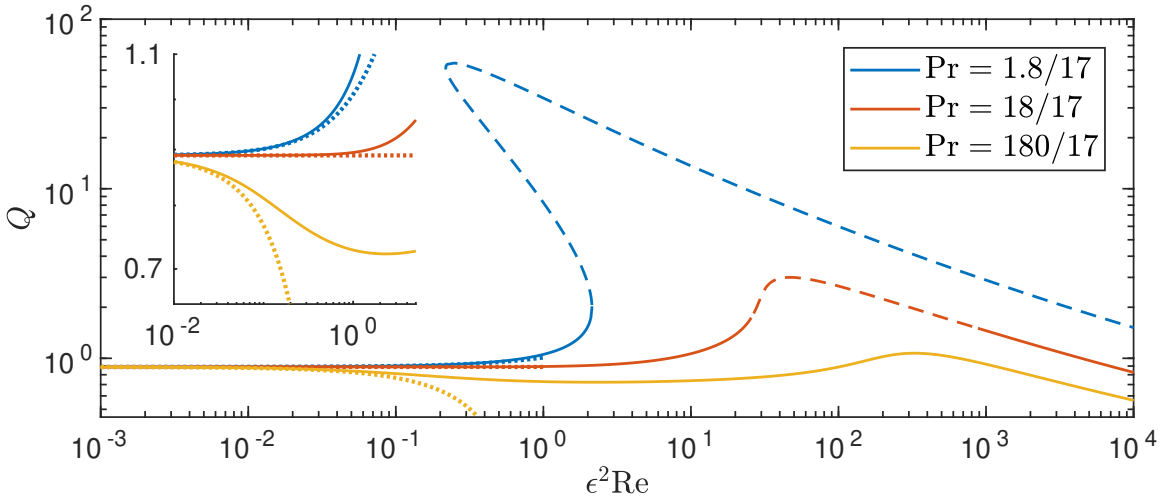


Figure 3.12: The mass flux Q as a function of the reduced Reynolds number $\epsilon^2\mathrm{Re}$ for different Prandtl numbers Pr when $\Delta T = 0.5$ and $\Delta p = 1/26$. Numerical solutions of case I (3.9), (3.8) are shown by solid coloured lines, when the presure is monotonic, and dashed lines when it is not. The first two terms of the asymptotic solution to case III, given by (3.27f) and(3.30f), are shown by dotted lines.

predicted by cases I and III, as functions of $\epsilon^2\mathrm{Re}$, for $\mathrm{Pr} = 1.8/17, 18$, and $180/17$. The results show excellent agreement between the numerical solution to case I, and the $O(\epsilon^2\mathrm{Re})$ asymptotic solution to case III, given by (3.27f) and (3.30f), for $\epsilon^2\mathrm{Re} \ll 1$. Moreover, the numerical results match the asymptotic prediction that Q will: increase for $\mathrm{Pr} < \mathrm{Pr_c}$; remain constant for $\mathrm{Pr} = \mathrm{Pr_c}$; and decrease for $\mathrm{Pr} > \mathrm{Pr_c}$. However, when the reduced Reynolds number becomes order unity, Q starts increasing for all values of the Prandtl number. The value of the Prandtl number still has an effect on the solution above this value, as we only get the non-monotonic pressure, and 'S' shaped curve for the lower values of Pr. Hence, reducing Pr has the same qualitative effect as reducing Δp whenever $\epsilon^2\mathrm{Re} = O(1)$.

3.4 Discussion

In Section 3.1, we presented a model for the non-isothermal compressible flow of a single gas species through a two dimensional channel based on the compressible Navier-Stokes equations, and discussed its solution using the finite element software COMSOL multiphysics. In Section 3.2, motivated by the size of the industrially-relevant parameter values, namely the small aspect ratio ϵ and small pressure drop Δp, we have derived three reduced models, who differ according to the assumed size of the reduced Reynolds number $\epsilon^2\mathrm{Re}$, all of which may be industrially-relevant.

The first of these, which we refer to as case I, assumes the reduced Reynolds number is large, $\epsilon^2\mathrm{Re} = O\left((\Delta p)^{-1}\right)$, so that the terms representing internal heating of the gas in the energy equation are of order unity. As asymptotic analysis of this problem results in a challenging singular perturbation problem, we instead considered a composite model, where terms of size $O\big(\left(\epsilon^2\mathrm{Re}\right)^{-1}\big)$ are retained in the axial momentum and energy equation, so that the boundary conditions on the walls of the channel can be satisfied. This approach led to a single set of governing equations to describe the behaviour over the whole channel. Solving this model numerically for industrially-relevant parameter values, we found the relationship between mass flux Q and $\epsilon^2\mathrm{Re}$ to be characterised by an 'S'-shaped curve, meaning their exists a range of $\epsilon^2\mathrm{Re}$ where three solutions exist. Along two of these solution branches the pressure became non-monotonic.

We also considered the limit where $\epsilon^2\mathrm{Re} = O(1)$, which we referred to as case II. In this limit, we found the governing equations were almost identical to those of case I, except internal heating of the gas due to the work done by compression and viscous heating were neglected. However, unlike case I, the case II problem forms a valid asymptotic limit of the full model. Solving case II numerically, we found that two steady solutions with different mass fluxes Q existed for a given $\epsilon^2\mathrm{Re}$ below a critical value of $\epsilon^2\mathrm{Re}$, and no steady solutions existed above. Along one of these solution branches, the pressure was non-monotonic, with the minimum pressure decreasing unboundedly. This leads to solutions which are certainly unphysical since the absolute pressure of the gas is negative. In contrast, in the previously mentioned non-monotonic solutions to case I, the minimum pressure remains bounded, meaning the solutions are physical plausible, albeit unlikely. This result demonstrates one of the reasons why we consider the composite model for case I, namely that its internal heating term provides an energetic penalty to large pressure gradients, preventing these unphysical solutions.

Finally, we considered the viscous dominated limited where $\epsilon^2\mathrm{Re} \ll 1$, which we referred to as case III. In this limit it was possible to solve the problem asymptotically, similar to the method described in [70]. We found excellent agreement between the asymptotic and numerical solutions for values of $\epsilon^2\mathrm{Re} < 1$.

All of the reduced models were validated against the numerical solutions of the compressible Navier-Stokes equations, and we found good agreement. Moreover, we found that for one set of parameter values, we could converge to solutions of the compressible Navier-Stokes equations for all $\epsilon^2\mathrm{Re}$, i.e. above the maximum value for solutions predicted by case II. Moreover, we found reasonable agreement between the

compressible Navier-Stokes soltuions, and the solutions to case I above the maximum value. This shows case I has the ability to predict behaviour of the full compressible Navier-Stokes equations case II cannot, demonstrating it is a useful model to study, despite its less rigorous derivation.

We found that, with few exceptions, COMSOL was unable to converge to any solution, where cases I and II predicted that solution to be non-monotonic. We conjecture that this is because these solutions are unstable, although time dependent simulations would be required to verify this. We discuss the difficulties of carrying out such simulations, and show some preliminary results in the future work in Chapter 6.

From our modelling, we have found that the temperature of the gas in the channel is heavily dependent on the reduced Reynolds number. In case III, when $\epsilon^2\mathrm{Re} \ll 1$, the gas temperature is almost equal to the solid temperature at the same height in the solid. However, in cases I and II, when $\epsilon^2\mathrm{Re} > 1$, the gas temperature is significantly hotter than the surrounding solid. Since industrial measurements indicate the gas to likely be exiting the furnace at a higher temperature than the solid surface temperature, it is likely case I or II is more representative of the typical conditions in a silicon furnace. However, the considerable simplifications offered by case III allowed for an analytical solution to be obtained, allowing for greater insight into the underlying physics. We shall therefore pursue both limits further in the upcoming chapters. In Chapter 4, we will study the charge material model from Chapter 2 in the limit $\epsilon^2\mathrm{Re} = O(1)$ in the two-dimensional geometry used in this chapter, by building on the numerical techniques described in Section 3.2.3. In Chapter 5, we will analyse the model from Chapter 2 in the limit $\epsilon^2\mathrm{Re} \ll 1$ and so gain mechanistic insight into the role different parameters play in the solution. Further, using the method of matched asymptotic expansions, we will be able to study the effect of strongly temperature dependent reaction rates.

Chapter 4

Counter-current flow of reacting gases and solids

In this chapter, we develop a simplified version of the model for the charge material that still includes the essential ingredients believed to be important in silicon furnaces, namely, the multiple gas species, counter-current flow, exothermic reactions, and differing gas and solid temperatures. Guided by the results of Chapter 3, we anticipate having to work in a regime in which inertia is non-negligible, in order to achieve the differing gas and solid temperatures.

This chapter is structured as follows. In Section 4.1, we consider the modifications necessary to pose the model for the charge material from Chapter 2 in a two-dimensional geometry, similar to that considered in Chapter 3. We then exploit the size of the industrially-relevant dimensionless parameters to derive a simplified, leading-order model. Based on the results from Chapter 3, we take the reduced Reynolds number to be of order unity in order to allow the gas and solid temperatures to differ. In Section 4.2, we present an extension of the numerical method presented in Section 3.2.3 that can solve the resulting coupled problem for the gas and solid, under the simplifying assumption that the molar weights of the two gas species are equal. We then carry out some numerical experiments to explore why our scheme usually fails to converge for industrially-relevant parameter values. Due to these difficulties, in Section 4.3 we explore the behaviour of our coupled gas-solid model without reaction rates, and in Section 4.4 explore the behaviour of the gas part of model subject to reactions, but with an imposed solid temperature. The results in these sections give insight into the energy transfer between the gas and solids, and the recovery of SiO from the gas phase respectively. We discuss the implications of these results, and how they relate back to the full problem in Section 4.5.

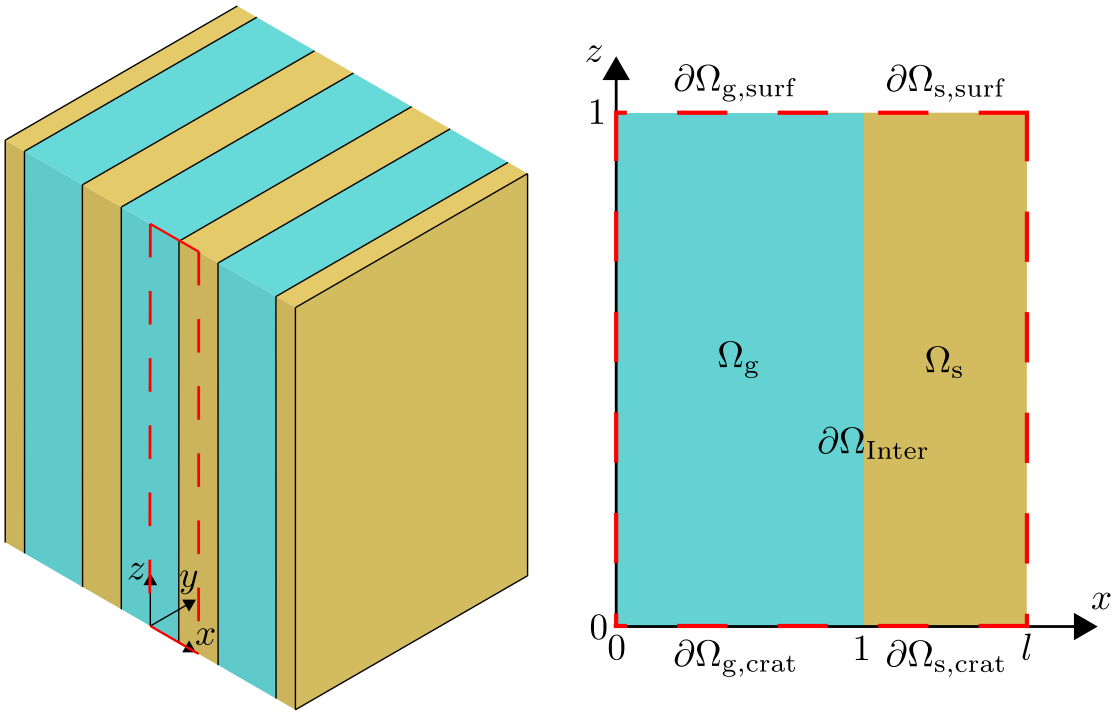


Figure 4.1: The coordinate system used in Chapter 4 to model the flow through a long, narrow channel and the surrounding solid. The cross-section considered in this chapter is highlighted by a red box.

4.1 Problem formulation

4.1.1 Simplifications

4.1.1.1 Geometry

We consider the full dimensionless model (2.68)–(2.80), but with the geometry of the gas channels taken to be long and narrow in the xy-plane, allowing us to focus on solutions which are independent of y, just as in Chapter 3. In fact, we go further and assume that the charge material consists of many such long and narrow channels in parallel, as depicted in Figure 4.1, so that the geometry is periodic. We assume further that the solution will be periodic in the x-direction, with the same period as the geometry. Moreover, we assume the solution to be symmetric about the centreline of each channel. We therefore, need only model a cross-section from the centreline of a channel, at $x = 0$, to the centreline line of the adjacent solid region, at $x = l$, as depicted in Figure 4.1. The gas-solid interface is located at $x = 1$. In this geometry, we pose symmetry boundary conditions on the solution at both $x = 0$ and $x = l$.

4.1.1.2 Parameter sizes

As in Chapter 3, we will exploit the size of the dimensionless parameters to obtain a reduced model, we will refer to as the coupled model, that is easier to solve than the model in Chapter 2, whilst still capturing the important physical processes. As mentioned at the start of the chapter, we will restrict ourselves to considering a limit where we anticipate the gas temperature differs significantly from the solid temperature, as this is believed to occur in real furnaces. In Chapter 3, both cases I and II had gas temperatures significantly exceeding the prescribed solid temperature. We will follow the assumptions of case II, and assume $\epsilon^2\mathrm{Re} = O(1)$, and also keep the same assumptions on $\epsilon, \Delta p, \mathrm{Pr}, \gamma$, and Re as given in (3.10). We choose case II, as not only is it quicker and simpler to solve than case I, it can also derived rigorously as the leading-order problem resulting from an asymptotic expansion. This is important in the derivation of the coupled model presented in this chapter, as deriving the governing equation for the leading-order temperature in the solid will require us to consider higher-order behaviour to obtain a closure condition. However, as discussed in Chapter 3, there are disadvantages of case II as a model compared to case I, namely the non-existence of solutions to the model beyond a critical value of $\epsilon^2\mathrm{Re}$. This suggests our model will be unable to give predictions for some industrially-relevant values of $\epsilon^2\mathrm{Re}$.

Therefore, based on the size of industrially-relevant values given in Table 2.3 and on the assumptions for case II in (3.10), we assume that

$$\epsilon,\ \Delta p,\ \Lambda,\ \alpha \ll 1, \tag{4.1a}$$

with the relationships between them discussed below, and

$$\epsilon^2\mathrm{Re},\ \mathrm{Pr},\ \mathrm{Sc},\ \mathrm{Pe_s},\ \gamma,\ \mathcal{M},\ \mathrm{Da}_1,\ \mathrm{Da}_2,\ \eta_1,\ \eta_2 = O(1). \tag{4.1b}$$

The significance of the sizes of ϵ, $\epsilon^2\mathrm{Re}$, Pr, γ, and Δp, has already been discussed in Section 3.2. The only novel consequence of their size in the binary mixture model, is that due to the small aspect ratio and order unity reduced Reynolds number, the diffusive slip in the axial direction, (2.78d) is a small, and the condition simplifies to no-slip.

Based on its value in Table 2.3, it would be reasonable to treat the the solid's Péclet number, $\mathrm{Pe_s}$, as large, and indeed this was done so when modelling the charge material of a silicon furnace in [48]. A large Péclet number implies that axial conduction in the solid is a small effect compared to advection of heat, and so may be

neglected. However, this would prevent the solid temperature from satisfying the boundary conditions at both $z = 0$ and $z = 1$. This could be resolved through the method of matched asymptotics, but this is complicated by the multiple sub-cases depending on the net direction of advection of heat (see Chapter 5 for further discussion of this). Ignoring the boundary condition at the crater is also impractical, as it introduces a discontinuity between gas and solid temperature on $\partial\Omega_{\text{Inter}}$ at $z = 0$. Therefore, to maintain tractability we take the Péclet number to be order unity in our asymptotic analysis, but explore its behaviour for large values in the subsequent numerical simulations.

We treat the (surface) Damköhler numbers, Da_i, as being of order unity throughout this chapter, in order to obtain a full balance in (2.78a)–(2.78b). The reaction rate $\mathcal{R}_i$ of some chemical reactions are highly temperature dependent, for example, in our model the rate of reaction 2 in (1.2), given by (2.81)–(2.82), is exponentially small for T close to one. However, letting $\mathcal{R}_i \to 0$ in part of the channel does not invalidate any of our analysis. Therefore, we derive and solve the model assuming $\mathcal{R}_i = O(1)$ throughout.

The Schmidt number, Sc, is the mass transfer analogue of the Prandtl number, so our comments on an order unity Prandtl number in Section 3.2 immediately generalise to the Schmidt number. The dimensionless enthalpies η_i are assumed to be order unity based on the industrially-relevant parameter values. Assuming the gas's specific heat capacities are given by (A.10), we have that $\kappa = \mathcal{M}$, reducing the number of parameters in the problem. Before solving the problem numerically, we will assume that the molar masses of SiO and CO are the same, i.e. $\mathcal{M} = 1$, in order to simplify the problem. However, we will derive the model for a general $\mathcal{M} = O(1)$, before making that assumption, whose consequences we discuss in Section 4.1.5.

We now consider the two small parameters in (4.1a), not appearing in Chapter 3. The first of these is the ratio of the gas and solid velocities, α, whose size implies that the interface between the gas and solid will appear stationary to the gas, implying the gas may be taken to have zero velocity at the interface. For the unsteady problem, the size of α also implies the gas to be quasi-steady. However, for tractability we will restrict ourselves to considering steady behaviour of the model in this chapter. Based on Table 2.3, α is the smallest parameter of the model.

The ratio of thermal conductivities, Λ, is also small, and implies that the flux of energy into the solid is small. To obtain the relative size of Λ to the other small

parameters, we note that, by the definition of the Péclet number (2.75), we have

$$\mathrm{Pe_s} = \mathrm{RePr}\Lambda \frac{[w_\mathrm{s}][\rho_\mathrm{s}][c_{p,\mathrm{s}}]}{[w_\mathrm{g}][\rho_\mathrm{g}][c_{p,\mathrm{CO}}]}. \tag{4.2}$$

From Table 2.3 it is clear that $[c_{p,\mathrm{s}}]/[c_{p,\mathrm{CO}}] = O(1)$. Moreover, in the furnace, all the gas flowing upwards must be created by reactions between the solid raw materials, which, in our model, we assume to occur in the crater. Therefore, assuming temporarily that the entire process is governed by the overall reaction (1.1), and that complete silicon recovery is achieved in the crater, conservation of mass implies the upwards mass flux of gas through the charge must be two-thirds the downwards mass flux of solid. In reality the crater will not be 100 % efficient, but this will only increase the total mass flux of gas. Hence, the sizes of Q^* and Q^*_s must be comparable, and by (2.86), this implies $([w_\mathrm{s}][\rho_\mathrm{s}]) \,/\, ([w_\mathrm{g}][\rho_\mathrm{g}]) = O(1)$. Thus, (4.2) can be rewritten as

$$\epsilon^2 = A_\epsilon \Lambda, \quad \text{where} \quad A_\epsilon = \frac{\epsilon^2 \mathrm{RePr}}{\mathrm{Pe_s}} \frac{[w_\mathrm{s}][\rho_\mathrm{s}][c_{p,\mathrm{s}}]}{[w_\mathrm{g}][\rho_\mathrm{g}][c_{p,\mathrm{CO}}]} = O(1), \tag{4.3}$$

giving us the relation between the sizes of Λ and ϵ. However, using the industrially-relevant parameter values given in Table 2.3, we find the value of A_ϵ is between 1.16×10^{-5} and 1.16×10^{-3}. This discrepancy is due to our previous decision to treat $\mathrm{Pe_s}$ as $O(1)$, when in practice $\mathrm{Pe_s^{-1}} = 3.89 \times 10^{-3}$. With a truly order unity Péclet number, the $A_\epsilon = O(1)$ is indeed valid. In practice we find our numerical solver is unable to converge for very small values of A_ϵ, and so all the simulations presented are carried out with $A_\epsilon = 0.02$, corresponding to a channel whose width is 0.12 m. In Chapter 5, we will explore an alternative limit where $\Lambda = O(\epsilon)$, giving much better agreement with Table 2.3. In summary, the relative sizes of the small parameters in (4.1a) are assumed to be

$$\alpha \ll \epsilon^2 \sim \Lambda \ll \Delta p. \tag{4.4}$$

When deriving case II in Chapter 3, we did not explicitly state the asymptotic expansion used to obtain the model, instead skipping straight to the problem resulting at leading-order from a regular asymptotic expansion. However in this chapter, the derivation of the model is less straightforward, as we are required to proceed to higher-orders in order to obtain a closure condition for the solid temperature. Hence, we must be more precise about the asymptotic series used. From our assumption (4.4), we expect the first correction to be of size $O(\Delta p)$. However, as we will only require higher order terms in the model for the solid, we simplify the derivation by seek a solution of the form

$$T \sim T^{(0)} + \Lambda T^{(1)} + \cdots, \tag{4.5}$$

and similarly for the other variables.

4.1.2 Reduced solid model

In the two-dimensional cross-section, the dimensionless governing equations for the solid (2.74) become

$$\frac{\partial}{\partial z}\left(\rho_{\mathrm{s}} w_{\mathrm{s}}\right) = 0, \tag{4.6a}$$

$$\epsilon^2 \mathrm{Pe}_{\mathrm{s}} \frac{\partial}{\partial z}\left(\rho_{\mathrm{s}} w_{\mathrm{s}} T\right) = \frac{\partial}{\partial x}\left(k_{\mathrm{s}} \frac{\partial T}{\partial x}\right) + \epsilon^2 \frac{\partial}{\partial z}\left(k_{\mathrm{s}} \frac{\partial T}{\partial z}\right), \tag{4.6b}$$

for $1 < x < l$, $0 < z < 1$, with boundary conditions

$$T = 1 \quad \text{at } z = 0, \tag{4.7a}$$

$$\frac{\partial T}{\partial x} = 0 \quad \text{at } x = l, \tag{4.7b}$$

$$w_{\mathrm{s}} = -1, \quad T = T_{\mathrm{surf}} \quad \text{at } z = 1, \tag{4.7c}$$

and

$$\frac{k_{\mathrm{s}}}{\Lambda} \frac{\partial T}{\partial x}\bigg|_{x=1+} + \sum_i \frac{\mathrm{Da}_i \eta_i \mathrm{Pr}}{\mathrm{Sc}} \mathcal{R}_i\big|_{x=1} = \left(-\epsilon^2 \mathrm{RePr}\left(1 - (1-\mathcal{M})\, Y\right) \rho u T + k_{\mathrm{g}} \frac{\partial T}{\partial x}\right)\bigg|_{x=1-}, \tag{4.7d}$$

$$T\big|_{x=1+} = T\big|_{x=1-},$$

at $x = 1$.

Using (4.6a) and (4.7c) we find that

$$\rho_{\mathrm{s}} w_{\mathrm{s}} = -1 \tag{4.8}$$

for all z, allowing (4.6b) to be simplified to a problem for T only.

We now substitute in our asymptotic expansion (4.5), into (4.6b) and (4.7), then (using (4.3) to rewrite ϵ^2,) equate powers of Λ, to obtain the leading-order problem

$$0 = \frac{\partial}{\partial x}\left(k_{\mathrm{s}}\left(T^{(0)}\right) \frac{\partial T^{(0)}}{\partial x}\right), \tag{4.9}$$

with

$$\frac{\partial T^{(0)}}{\partial x}\bigg|_{x=1+} = 0, \quad T^{(0)}\big|_{x=1+} = T^{(0)}\big|_{x=1-} \tag{4.10a}$$

and

$$\frac{\partial T^{(0)}}{\partial x} = 0 \quad \text{at } x = l. \tag{4.10b}$$

Integrating twice with respect to x, we find that $T^{(0)} = T^{(0)}(z)$, for $1 < x < l$, and $0 < z < 1$. However, to determine $T^{(0)}$ we must obtain a closure condition from the next-order problem. By equating terms of size Λ, we obtain the problem

$$-A_\epsilon \mathrm{Pe} \frac{\mathrm{d}T^{(0)}}{\mathrm{d}z} = \frac{\partial}{\partial x}\left(k_\mathrm{s}\left(T^{(0)}\right)\frac{\partial T^{(1)}}{\partial x}\right) + A_\epsilon \frac{\mathrm{d}}{\mathrm{d}z}\left(k_\mathrm{s}\left(T^{(0)}\right)\frac{\mathrm{d}T^{(0)}}{\mathrm{d}z}\right), \tag{4.11}$$

with boundary conditions

$$\begin{aligned} &k_\mathrm{s}\left(T^{(0)}\right)\frac{\partial T^{(1)}}{\partial x}\bigg|_{x=1+} + \sum_i \frac{\mathrm{Da}_i \eta_i \mathrm{Pr}}{\mathrm{Sc}} \mathcal{R}_i^{(0)}\big|_{x=1} \\ &\quad = \left(-\epsilon^2 \mathrm{RePr}\left(1-(1-\mathcal{M})\,Y^{(0)}\right)\rho^{(0)}u^{(0)}T^{(0)} + k_\mathrm{g}\left(T^{(0)}\right)\frac{\partial T^{(0)}}{\partial x}\right)\bigg|_{x=1-}, \end{aligned} \tag{4.12a}$$

and

$$\frac{\partial T^{(1)}}{\partial x} = 0 \quad \text{at } x = l, \tag{4.12b}$$

where $\mathcal{R}_i^{(0)}$ is the leading-order reaction rate, defined by substituting (4.5) into the definition of $\mathcal{R}_i$ and grouping terms $\mathcal{R}_i = \mathcal{R}_i^{(0)} + \Lambda \mathcal{R}_i^{(1)} + \cdots$. By integrating (4.11) from $x = 1$ to $x = l$ and using (4.12), we obtain

$$\begin{aligned} 0 = \mathrm{Pe}_\mathrm{s}\frac{\mathrm{d}T^{(0)}}{\mathrm{d}z} + \frac{\mathrm{d}}{\mathrm{d}z}\left(k_\mathrm{s}\frac{\mathrm{d}T^{(0)}}{\mathrm{d}z}\right) + \sum_i \frac{\mathrm{Da}_i\eta_i\mathrm{Pr}}{\mathrm{Sc}A_\epsilon|\mathcal{C}_\mathrm{s}|}\mathcal{R}_i^{(0)}\big|_{x=1} \\ + \frac{1}{A_\epsilon|\mathcal{C}_\mathrm{s}|}\left(\epsilon^2\mathrm{RePr}\left(1-(1-\mathcal{M})\,Y^{(0)}\right)\rho^{(0)}u^{(0)}T^{(0)} - k\left(T^{(0)}\right)\frac{\partial T^{(0)}}{\partial x}\right)\bigg|_{x=1-}, \end{aligned} \tag{4.13}$$

where $|\mathcal{C}_\mathrm{s}| = l - 1$. This is the closure condition allowing us to determine $T^{(0)}$. As a final step we write $T_\mathrm{s}(z) = T^{(0)}(1, z)$, and drop the superscripts from all the other variables, since we will only consider the leading-order behaviour of the model for the remainder of the chapter, meaning (4.13) may written more compactly, as

$$\begin{aligned} 0 = \mathrm{Pe}_\mathrm{s}\frac{\mathrm{d}T_\mathrm{s}}{\mathrm{d}z} + \frac{\mathrm{d}}{\mathrm{d}z}\left(k_\mathrm{s}\frac{\mathrm{d}T_\mathrm{s}}{\mathrm{d}z}\right) + \sum_i \frac{\mathrm{Da}_i\eta_i\mathrm{Pr}}{\mathrm{Sc}A_\epsilon|\mathcal{C}_\mathrm{s}|}\mathcal{R}_i\big|_{x=1} \\ + \frac{1}{A_\epsilon|\mathcal{C}_\mathrm{s}|}\left(\epsilon^2\mathrm{RePr}\left(1-(1-\mathcal{M})\,Y\right)\rho u T - k\frac{\partial T}{\partial x}\right)\bigg|_{x=1-}, \end{aligned} \tag{4.14}$$

with boundary conditions

$$T_\mathrm{s} = 1 \quad \text{at } z = 0, \tag{4.15a}$$

$$T_\mathrm{s} = T_\mathrm{surf} \quad \text{at } z = 1. \tag{4.15b}$$

Thus, the solid model is reduced to a one-dimensional advection-reaction-diffusion equation for how the solid temperature varies with z, where the reaction term depends on the solution to the gas model and accounts for both heat transfer from the gas and enthalpy released by the reactions.

4.1.3 Reduced gas model

The derivation of the leading-order model for the gas is simpler, as no closure conditions are required, and proceeds almost identically to the derivation of case II in Chapter 3. Therefore, we omit the details, and go straight to the leading-order problem for ρ, u, w, p, T, and Y in $0 < x < 1$, $0 < z < 1$, which is given by

$$\frac{\partial(\rho u)}{\partial x} + \frac{\partial(\rho w)}{\partial z} = 0, \tag{4.16a}$$

$$0 = \frac{\partial p}{\partial x}, \tag{4.16b}$$

$$\epsilon^2 \mathrm{Re}\left(\frac{\partial(\rho u w)}{\partial x} + \frac{\partial(\rho w w)}{\partial z}\right) = -\frac{\partial p}{\partial z} + \frac{\partial}{\partial x}\left(\mu \frac{\partial w}{\partial x}\right), \tag{4.16c}$$

$$\begin{aligned}&\epsilon^2 \mathrm{Re}\left(\frac{\partial(\rho u T)}{\partial x} + \frac{\partial(\rho w T)}{\partial z}\right)\\ &-\epsilon^2 \mathrm{Re}\,(1-\mathcal{M})\left(\frac{\partial(\rho u T Y)}{\partial x} + \frac{\partial(\rho w T Y)}{\partial z}\right) = \frac{1}{\mathrm{Pr}}\frac{\partial}{\partial x}\left(k\frac{\partial T}{\partial x}\right),\end{aligned} \tag{4.16d}$$

$$\epsilon^2 \mathrm{Re}\left(\frac{\partial(\rho u Y)}{\partial x} + \frac{\partial(\rho w Y)}{\partial z}\right) = \frac{1}{\mathrm{Sc}}\frac{\partial}{\partial x}\left(\rho \mathcal{D}\frac{\partial Y}{\partial x}\right), \tag{4.16e}$$

$$\rho T\left(1 - (1-\mathcal{M})\, Y\right) = 1. \tag{4.16f}$$

We similarly find the boundary conditions to be given by

$$u = 0, \quad p = 0, \quad T = 1, \quad Y = Y_{\mathrm{crat}} \quad \text{at} \quad z = 0, \tag{4.17a}$$

$$u = 0, \quad \frac{\partial w}{\partial x} = 0, \quad \frac{\partial T}{\partial x} = 0, \quad \frac{\partial Y}{\partial x} = 0 \quad \text{at} \quad x = 0, \tag{4.17b}$$

$$\left.\begin{aligned} \epsilon^2 \mathrm{Re}\rho u &= -\sum_i \frac{\mathrm{Da}_i}{\mathrm{Sc}}\left(\nu_{i,\mathrm{SiO}} + \mathcal{M}\nu_{i,\mathrm{CO}}\right)\mathcal{R}_i,\\ w &= 0,\\ T &= T_{\mathrm{s}}(z),\\ \epsilon^2 \mathrm{Re}\rho Y u - \frac{1}{\mathrm{Sc}}\rho\mathcal{D}\frac{\partial Y}{\partial r} &= -\sum_i \frac{\mathrm{Da}_i}{\mathrm{Sc}}\nu_{i,\mathrm{SiO}}\mathcal{R}_i \end{aligned}\right\} \quad \text{at } x = 1, \tag{4.17c}$$

and

$$p = -1 \quad \text{at} \quad z = 1, \tag{4.17d}$$

at the crater, centreline, interface, and surface, respectively. As for the reduced models in Chapter 3, we are unable to satisfy all the boundary conditions at $z = 1$ in (3.3c), but motivated by our analysis of the single-phase case, assume they do not have a significant effect upstream. Equations (4.14)–(4.17) fully specify the coupled problem for the gas and solid.

4.1.4 Fluxes, efficiencies and averages

We also need to determine the leading-order forms of the quantities of interest, introduced in Section 2.1.4, in the two-dimensional geometry.

In the two-dimensional geometry the total mass flux of gas per unit length (in the y-direction) is given by

$$Q = 2\int_0^1 \rho w \,\mathrm{d}x, \tag{4.18}$$

while the total mass flux of SiO and CO per unit length (in the y-direction) are given by

$$Q_{\mathrm{SiO}} = 2\int_0^1 \rho Y w \,\mathrm{d}x, \quad Q_{\mathrm{CO}} = 2\int_0^1 \rho\,(1-Y)\, w \,\mathrm{d}x, \tag{4.19}$$

respectively. Unlike Chapter 3, where Q was shown to be a constant, in this chapter the mass fluxes can vary with z due to the reactions. Using these mass fluxes, it is straightforward to compute the proportion of SiO gas lost from the furnace $\mathcal{L}$, as

$$\mathcal{L} = \frac{Q_{\mathrm{SiO}}\big|_{z=1}}{Q_{\mathrm{SiO}}\big|_{z=0}}. \tag{4.20}$$

This definition allows us to quantity the efficiency of the system in recovering silicon from the gas phase, an important industrial measure as unrecovered silicon represents a waste of raw materials and the energy used to create the SiO.

The outward energy fluxes per unit length (in the y-direction) from each boundary of the gas channel are given by

$$E_{\mathrm{g,crat}} = -2\int_0^1 \rho\,(1-(1-\mathcal{M})\,Y)\, wT\Big|_{z=0} \,\mathrm{d}x, \tag{4.21a}$$

$$E_{\mathrm{g,surf}} = 2\int_0^1 \rho\,(1-(1-\mathcal{M})\,Y)\, wT\Big|_{z=1} \,\mathrm{d}x. \tag{4.21b}$$

For the energy flux from the solid, at the crater and the solid, both advection and diffusion transport remain at leading-order. However, the two mechanisms transport energy in the opposite directions, and so we consider each of them separately. The outwards advective energy fluxes per unit length (in the y-direction) are given by,

$$E_{\mathrm{s,crat,A}} = 2\int_1^l \frac{A_\epsilon \mathrm{Pe_s}}{\epsilon^2 \mathrm{RePr}} T\Big|_{z=0} \,\mathrm{d}x, \quad E_{\mathrm{s,surf,A}} = -2\int_1^l \frac{A_\epsilon \mathrm{Pe_s}}{\epsilon^2 \mathrm{RePr}} T\Big|_{z=1} \,\mathrm{d}x, \tag{4.22a}$$

through the crater and surface, respectively. The outwards diffusive energy fluxes per unit length (in the y-direction) are given by

$$E_{\mathrm{s,crat,D}} = 2\int_1^l \frac{A_\epsilon}{\epsilon^2 \mathrm{RePr}} k_{\mathrm{s}} \frac{\partial T}{\partial z}\Big|_{z=0} \,\mathrm{d}x, \quad E_{\mathrm{s,surf,D}} = -2\int_1^l \frac{A_\epsilon}{\epsilon^2 \mathrm{RePr}} k_{\mathrm{s}} \frac{\partial T}{\partial z}\Big|_{z=1} \,\mathrm{d}x, \tag{4.22b}$$

through the crater and surface, respectively.

The rate at which energy is consumed by the chemical reactions in the channel per unit length (in the y-direction) is given by

$$E_{\text{React}} = -2 \int_0^1 \sum_i \frac{\text{Da}_i \eta_i}{\epsilon^2 \text{ReSc}} \mathcal{R}_i \bigg|_{x=1} \, \mathrm{d}z. \tag{4.23}$$

Thus, with these definitions, the total conservation of energy for the model may be expressed as

$$E_{\text{g,crat}} + E_{\text{g,surf}} + E_{\text{s,crat,A}} + E_{\text{s,surf,A}} + E_{\text{s,crat,D}} + E_{\text{s,surf,D}} + E_{\text{React}} = 0. \tag{4.24}$$

We must now specify how to combine these quantities in order to obtain a measure of the energy efficiency of the furnace, analogous to (3.6) for the gas only model. We do this by assigning each term as either an input of energy, a useful output, or a loss of energy, then define the efficiency as the useful output divided by the the input. We summarise our interpretation of each term schematically in Figure 4.2, and discuss the reasoning below.

It is straightforward to see that $E_{\text{g,crat}}$ and $E_{\text{s,surf,A}}$ are always inputs of energy to the system, as is E_{React}, provided we only consider exothermic reaction. It is also clear that $E_{\text{s,crat,A}}$ represents the useful output, as heating up the solid raw materials is required to produce silicon, while $E_{\text{g,surf}}$ must represent lost energy, as it is energy exiting the furnace. However, the roles of the conductive energy fluxes from the solid is less clear, as unlike the other terms they may change direction. Provided that $T_{\text{surf}} \leq T_{\text{s}} \leq 1$ everywhere, which is always true if no reactions occur, then heat must conduct from the crater into the solid, making $E_{\text{s,crat,D}}$ an input of energy, and heat will conduct out of the solid at the surface, making $E_{\text{s,surf,D}}$ a loss of energy. However, if a sufficient amount of exothermic reaction occurs that $T > 1$ adjacent to the crater, then heat will start conducting from the solid into the crater, making $E_{\text{s,crat,D}}$ a useful output of energy. As this possibility is unlikely to occur physically, we assume the temperature varies monotonically, and so define the efficiency as

$$\begin{aligned} \mathcal{E} &= \frac{|E_{\text{s,crat,A}}|}{|E_{\text{g,crat}} + E_{\text{s,crat,D}} + E_{\text{s,surf,A}} + E_{\text{React}}|} \\ &= -\frac{E_{\text{s,crat,A}}}{E_{\text{g,crat}} + E_{\text{s,crat,D}} + E_{\text{s,surf,A}} + E_{\text{React}}}. \end{aligned} \tag{4.25}$$

This is by no means the only sensible definition of the energy efficiency of the coupled model. Firstly, we have only considered a balance of thermal energy, with the exothermic reaction acting as a heat source, of size E_{React} within the domain. We

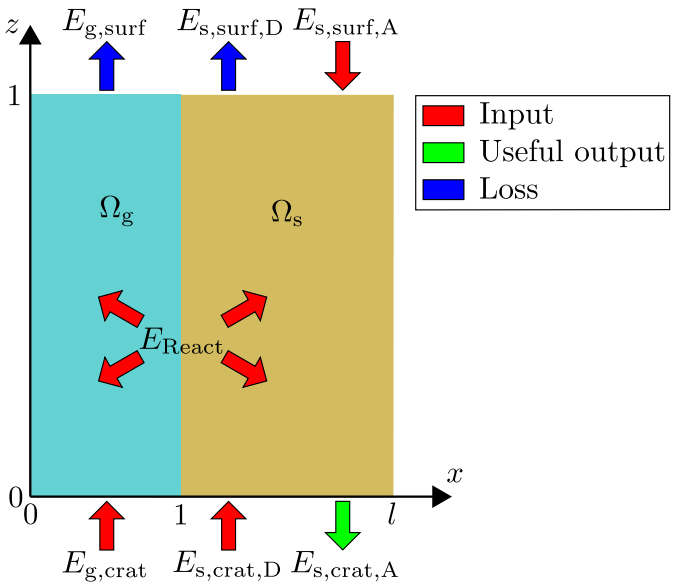


Figure 4.2: The direction and meaning of the energy fluxes in the coupled gas-solid model.

could have instead introduced a chemical potential energy to account for the energy stored within chemical bonds. Then E_{React} could be replaced by the flux of chemical energy through the crater and surface. However, when considering multiple reactions, it is not obvious how to define the chemical potential energy, as different reactions will release different amounts of energy. Another deficiency of (4.25), is that it does not account for the fact that adding the same amount of energy by two different mechanisms would not have the same economic cost. Specifically, the energy inputted by $E_{\mathrm{s,surf,A}}$ is just the intrinsic energy the material already has to exist at room temperature. In contrast, increasing $E_{\mathrm{s,crat,D}}$ can be interpreted as increasing the power into the electrodes of the furnace to deliver additional heat to the crater, which would increase the operating costs of the furnace. Our definition (4.25) should therefore be viewed as an illustrative tool to demonstrate how the furnace behaviour changes, and not a detailed cost-benefit analysis.

Another useful quantity for interpreting the output of solutions is the average temperature in the gas $T_{\mathrm{g}}(z)$. The correct form of this average could be derived rigorously through a homogenisation procedure, but that is beyond the scope of this thesis. Instead, we choose to define $T_{\mathrm{g}}(z)$ as the arithmetic mean,

$$T_{\mathrm{g}}(z) = \int_0^1 T(x,z)\,\mathrm{d}x, \tag{4.26}$$

as this is the simplest possible choice.

4.1.5 Simplification of the coupled model

Before discussing the numerical solution of (4.14)–(4.17), we make a final assumption, to simplify the solution process. This is to assume that the molar weights of CO and SiO are equal, so that

$$\mathcal{M} = 1. \tag{4.27}$$

This implies that (4.16a)-(4.16d), (4.16f) become identical to the governing equations for case II of the single-phase model (3.11). Hence, to solve the problem for a reacting binary gas mixture for a given solid temperature, we need to incorporate an advection-diffusion equation for Y into the single-phase model and change the boundary conditions to account for reactions on the interface.

Whilst the same techniques given in Section 4.2 could be used to solve the coupled model without this assumptions, we will see below the simplified version already provides a considerable challenge, and we leave the discussion of relaxing this assumption to the future work section in Chapter 6.

4.2 Numerical solution

4.2.1 Transformed problem

To solve (4.14)–(4.17) we use a modification of the method developed in Chapter 3 for the single-phase gas problem. Firstly, we transform the problem into new variables that reduce the total number of variables and make the governing equations a first order system in z. We then describe how the boundary conditions at $z = 1$ can be replaced by boundary conditions at $z = 0$, whose value must be determined using a shooting method. We will then outline a numerical method to integrate the problem forward in z for a given set of shooting parameters, and discuss how converge to a set of shooting parameters such that the boundary conditions at $z = 1$ are satisfied.

4.2.1.1 Gas

As in Section 3.2.3, we will rewrite the gas problem in terms of a streamfunction

$$\frac{\partial \psi}{\partial x} = \rho w, \ \frac{\partial \psi}{\partial z} = -\rho u, \tag{4.28}$$

defined identically to (4.28). Substituting (4.28) into (4.16), and differentiating the momentum equation to remove pressure, we obtain the governing equations

$$\epsilon^2\mathrm{Re}\left(\psi_{xxz}\psi_x T + 2\psi_{xx}\psi_x T_z + \psi_x^2 T_{xz} - \psi_z\left(\psi_x T\right)_{xx}\right) = \left(\left(\mu\left(\psi_x T\right)_x\right)\right)_{xx}, \tag{4.29a}$$

$$\epsilon^2\mathrm{Re}\left(\psi_x T_z - \psi_z T_x\right) = \frac{1}{\mathrm{Pr}}\left(kT_x\right)_x, \tag{4.29b}$$

$$\epsilon^2\mathrm{Re}\left(\psi_x Y_z - \psi_z Y_x\right) = \frac{1}{\mathrm{Sc}}\left(\frac{\mathcal{D}}{T}Y_x\right)_x, \tag{4.29c}$$

where we are again using subscript notation to denote partial derivatives with resepct to x and z. The choice to fix $\mathcal{M} = 1$, means that (4.29a)–(4.29b) are identical to the transformed equations for case II of the single-phase model in Chapter 3. As is that chapter, we introduce a new variable $H(z)$, the integral of the stress over the cross-section, given by

$$H(z) = p + \epsilon^2\mathrm{Re}\int_0^1 \psi_x^2 T\,\mathrm{d}x, \tag{4.30}$$

and satisfying

$$\frac{\mathrm{d}H}{\mathrm{d}z} = \left(\mu\left(\psi_x T\right)_x\right)\big|_{x=1}, \tag{4.31}$$

in order to determine the pressure after ψ, T, and H are found. Finally, we require an equation for how Q changes with z, since it will appear in the boundary conditions for ψ, but, unlike the single-phase case, it now varies with z. To obtain this equation, we integrate the conservation of mass equation (4.16a) from $x = 0$ to $x = 1$, and use the definition of the mass flux (3.4), along with the boundary conditions (4.17b)–(4.17c), to deduce that Q satisfies

$$\frac{\mathrm{d}Q}{\mathrm{d}z} = \frac{2}{\epsilon^2\mathrm{Re}}\sum_i \frac{\mathrm{Da}_i}{\mathrm{Sc}}\left(\nu_{i,\mathrm{SiO}} + \nu_{i,\mathrm{CO}}\right)\mathcal{R}_i. \tag{4.32}$$

The transformed boundary conditions are given by

$$\psi_z = 0, \quad T = 1, \quad Y = Y_{\mathrm{crat}}, \quad p = 0, \quad H = \epsilon^2\mathrm{Re}\int_0^1 \psi_x^2 T\,\mathrm{d}x \quad \text{at } z = 0, \tag{4.33a}$$

$$\psi = 0, \quad \psi_{xx} = 0, \quad T_x = 0, \quad Y_x = 0, \quad \text{at } x = 0, \tag{4.33b}$$

$$\left.\begin{aligned} \psi = \frac{Q}{2}, \quad \psi_x = 0, \quad T = T_{\mathrm{s}}(z), \\ \rho\mathcal{D}Y_x = -\sum_i \mathrm{Da}_i\left(\left(Y-1\right)\nu_{\mathrm{SiO},i} + Y\nu_{\mathrm{CO},i}\right)\mathcal{R}_i, \end{aligned}\right\} \quad \text{at } x = 1, \tag{4.33c}$$

$$p = -1, \quad H = -1 + \epsilon^2\mathrm{Re}\int_0^1 \psi_x^2 T\,\mathrm{d}x \quad \text{at } z = 1. \tag{4.33d}$$

The boundary condition for Y_x at $x = 1$ is derived by multiplying the total mass flux condition in (4.17c) by Y then subtracting the flux of SiO condition also in (4.17c).

We note that while the main topic of this chapter is the solution of the coupled gas and solid problem, if we impose the solid temperature T_s then (4.29)–(4.33) form a well-posed problem for the resulting gas behaviour. There is only a single shooting parameter Q_crat, which can be found using identical techniques as described for the single-phase problem in Section 3.2.3. We we study solutions of this prescribed solid temperature problem in Section 4.4.

4.2.1.2 Solid

To solve the coupled gas and solid problem numerically, we need to convert the solid energy equation (4.14) to a first order system in z. We do this by introducing q, the conductive heat flux in the negative z-direction, given by

$$q = k_\mathrm{s}\frac{\mathrm{d}T_\mathrm{s}}{\mathrm{d}z}. \tag{4.34}$$

Using (4.34), we can rewrite (4.14) as

$$0 = \frac{\mathrm{Pe}_\mathrm{s}}{k_\mathrm{s}}q + q_z + \sum_i \frac{\mathrm{Da}_i\eta_i\mathrm{Pr}}{\mathrm{Sc}A_\epsilon|\mathcal{C}_\mathrm{s}|}\mathcal{R}_i\big|_{x=1} - \frac{1}{A_\epsilon|\mathcal{C}_\mathrm{s}|}\left(\epsilon^2\mathrm{RePr}\psi_z T + kT_x\right)\big|_{x=1-}, \tag{4.35}$$

The boundary conditions (4.15), remain

$$T_\mathrm{s} = 1, \quad \text{at } z = 0, \tag{4.36a}$$

$$T_\mathrm{s} = T_\mathrm{surf}, \quad \text{at } z = 1. \tag{4.36b}$$

4.2.2 Numerical scheme

We now need to convert (4.29)–(4.36) to a form we can solve numerically. We do this by introducing two shooting parameters, Q_crat and q_crat, defined by

$$Q = Q_\mathrm{crat}, \quad q = q_\mathrm{crat} \quad \text{at } z = 0, \tag{4.37}$$

so that Q_crat is the dimensionless total mass flux of gas from the crater, and q_crat is the diffusive heat flux from the crater into the solid. Then, for given values of Q_crat and q_crat, the behaviour of the coupled system at $z = 0$ is known, and since (4.29) is parabolic, we can integrate the whole system forwards in z. The correct values of Q_crat and q_crat are determined using the boundary conditions for the gas and solid

at $z = 1$, (4.33d) and (4.36b), respectively. To solve the problem for given shooting parameters numerically, we discretise it the x-direction, using second order accurate central finite differences on a uniformly spaced mesh, then solve the resulting system of ODEs and algebraic equations using MATLAB's built-in DAE solver ode15s [72]. This is the same approach as used for the single-phase problem in Section 3.2.3. The details of the finite difference scheme are given in Appendix C.

In order to avoid numerical issues caused by the discontinuity in boundary conditions for u at $x = 1$, $z = 0$, ($u = 0$ by (4.17a), but $u \neq 0$ if $\mathcal{R}_i \neq 0$ by (4.17c),) we multiply $\mathcal{R}_i$ by a logistic regularisation function in z, so that the reaction smoothly turns on in a narrow region near $z = 0$. Therefore, in the numerical implementation, all the reaction rates $\mathcal{R}_i$ are replaced with a new rate $\tilde{\mathcal{R}}_i$, defined by multiply $\mathcal{R}_i$ by a logistic function in z,

$$\tilde{\mathcal{R}}_i = \left(\frac{1}{1 + \exp\left(-200\left(z - 0.025\right)\right)} \right) \mathcal{R}_i, \tag{4.38}$$

for all i. While this method works for small reaction rates, ode15s will sometimes reject initial conditions as being inconsistent. This is because the reaction rate is not exactly zero at $z = 0$, even after the smoothing is applied.

To solve the shooting problem of converging to a correct pair $Q_{\text{crat}}, q_{\text{crat}}$ such that the conditions at $z = 1$, (4.33d) and (4.36b) are satisfied, we use MATLAB's built-in non-linear system solve fsolve.

For the remainder of this chapter, we will assume, for simplicity, that the viscosity, binary diffusion coefficient, and thermal conductivity of both the gas and the solid are constant. All the solutions taken in this chapter use parameter values from Table 2.3, except when noted in a caption, or for A_ϵ, which, as previously discussed, is taken to equal 0.02. Throughout this chapter we will also assume the width of the solid to be equal to that of the gas, and so take $|\mathcal{C}_{\text{s}}| = 1$.

4.2.3 Shooting problem

Before discussing the results of the coupled model in detail, we first discuss the behaviour of the system of nonlinear equations that must be solved to obtain a solution to the shooting problem for Q_{crat} and q_{crat}, and explain the difficulties in converging to a solution of the system.

In Chapter 3, we were able to visualise the nonlinear function solved to obtain the shooting parameter Q such that $p\big|_{z=1} = -1$, by plotting the values of $p\big|_{z=1}$ as Q varied. For example, in Figure 3.9 we showed how the behaviour of the function

changes as $\epsilon^2\text{Re}$ varies using a contour plot. This allowed us to demonstrate that we had identified all possible steady solutions to our reduced models for a given value of $\epsilon^2\text{Re}$. We extend this idea to the nonlinear system for determining q_{crat} and Q_{crat} by overlaying, in Figure 4.3, the contours of $p\big|_{z=1}$, shown with blue lines, with those of $T_{\text{s}}\big|_{z=1}$, shown with red lines, as q_{crat} and Q_{crat} vary. Unlike in Chapter 3, each contour plot now represents a single set of parameter values, with the solutions of the coupled model corresponding to points where the $p\big|_{z=1} = -1$ contour intersects with the $T_{\text{s}}\big|_{z=1} = T_{\text{surf}}$ contour. Therefore, to show how the behaviour of the system changes with $\epsilon^2\text{Re}$, we show several such sets of contours, taking $\text{Da}_1 = \text{Da}_2 = 0$, so that no reations occur.

As T_{surf} does not appear within the equations (4.29)–(4.36a) used to evaluate the height of the contours in Figure 4.3, these contours plots show how the values of the shooting parameters will change as T_{surf} varies. Specifically, for all values of $\epsilon^2\text{Re}$ shown, we observe that as the size of T_{surf} increases, the value of q_{crat} decreases. Physically, this means that if the temperature of the newly added solid is increased, then less heating of the solid by diffusive heat transfer from the crater is required. We also see that, for a given value of $\epsilon^2\text{Re}$, there is a minimum value of T_{surf} for which a solution exists. Moreover, as the value of $\epsilon^2\text{Re}$ increases, this minimum value of T_{surf} increases. Physically, this is saying that for faster gas flows, hotter material must be added for a solution to exist. For values of T_{surf} over this minimum value there appears to always exist two solutions, due to the $p\big|_{z=1} = -1$ contour turning back on itself, as a function of q_{crat}. However, as Q_{crat} becomes large, q_{crat} becomes small for all the contours, and a finer sweep of that region would be necessary to fully understand the dynamics there.

When sweeping over q_{crat} and Q_{crat} to make Figure 4.3, we found a region of parameter space for which ode15s failed to converge before reaching $z = 1$, and depict it in the figure as a grey region. Examining the solution, just before ode15s fails, we see that the solid temperature is tending to zero, suggesting it becomes negative at the point where ode15s failed. Indeed, from the trend of the contours of red $T_{\text{s}}\big|_{z=1}$, we see that $T_{\text{s}}\big|_{z=1} \to 0$ as we approach the grey region. Since, a negative temperature is physically impossible, the model is no longer valid, so the failure of ode15s is to be expected. Therefore, we may be confident no physically relevant solutions lie in the grey region, and the solutions identified outside of it will represent the complete set of possible solutions to the coupled model, within the range of q_{crat} and Q_{crat} considered in the figure.

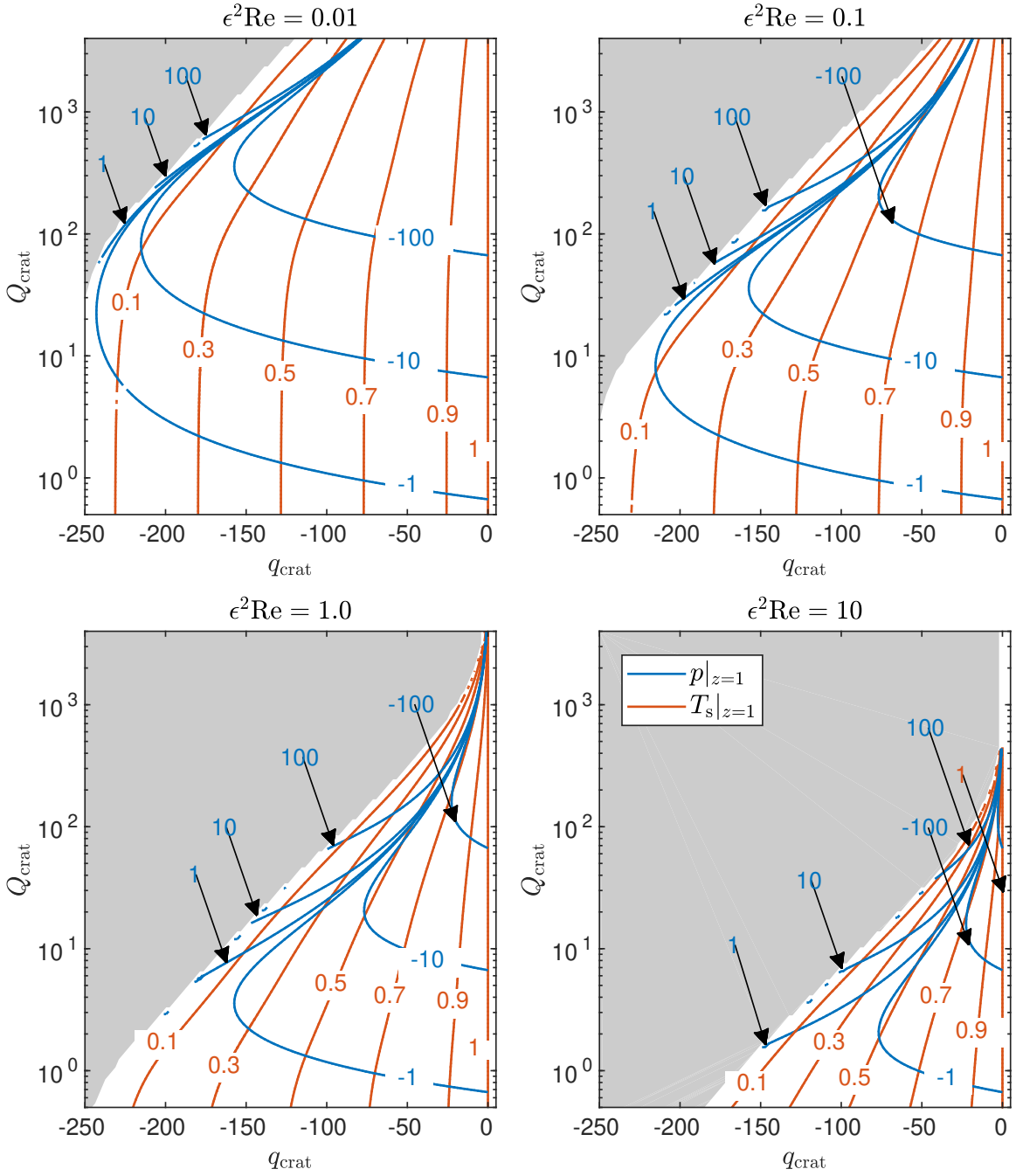


Figure 4.3: Contours of pressure at the surface $p\big|_{z=1}$, shown in blue, and solid temperature at the surface $T_{\mathrm{s}}\big|_{z=1}$, shown in red, as predicted by the coupled gas-solid model as Q_{crat} and q_{crat} vary for: (a) $\epsilon^2\mathrm{Re} = 0.01$, (b) $\epsilon^2\mathrm{Re} = 0.1$, (c) $\epsilon^2\mathrm{Re} = 1$, (d) $\epsilon^2\mathrm{Re} = 10$. In all cases $\mathrm{Da}_1 = \mathrm{Da}_2 = 0$.

Previous studies of compressible flow in channels have observed similar behaviour where the solution ceases to exist beyond a finite distance along the channel. In [69], where an isothermal compressible flow is considered, it is found that, for steady solutions, the pressure will vanish, and the velocity will become unbounded a finite distance along the channel, a phenomena they called 'mathematical choking'. In [70], where non-isothermal compressible flow with a constant heat flux on the walls is considered in the small reduced Reynolds number limit, it is found that above a critical heat flux the axial velocity tends to zero a finite distance along the channel and the temperature goes to infinity. However, the models of the gas flow we considered in Chapter 3 did not show this behaviour. In case III, our equivalent of the analysis of [70], the viscous dominated limit, we found no analogous result, which we conjecture is because we imposed the wall temperature and not the wall flux, ensuring the temperature remained bounded. The non-existence of solutions to case II, and the coupled model in this chapter, beyond a critical value of $\epsilon^2\mathrm{Re}$ is above a critical value, seems reminiscent of this behaviour, but the solution at the critical value of $\epsilon^2\mathrm{Re}$ is well-behaved, with no variables becoming negative or diverging to infinity, and there is no evidence of separation of the flow from the channel wall.

The contour plots in Figure 4.3 help illustrate some of the challenges faced in solving the shooting problem for the model in this chapter, even in the simplest case without reactions. In the industrially-relevant regimes T_{surf} will be small, implying the solutions will lie close to the boundary of the grey region. As we solve the shooting problem using a gradient-descent based method, it is common for the solver to take a step moving it into the grey region, and hence crash. Based on our attempts to converge to solutions when the reaction rates are non-zero, the $T\big|_{z=1}$ contours shrink closer together as the reaction rates increase, exacerbating this difficulty. Physically, this makes sense as increasing the reaction rate, will increase the size of energy released by the reactions (assuming not all the SiO was being consumed), and hence, lead to larger changes in $T\big|_{z=1}$.

Since the position of the boundary of the grey region cannot be known *a priori*, there is no way to directly force a nonlinear solver to remain outside of the grey region. It is possible to use an event function within ode15s to detect when a set of values of q_{crat} and Q_{crat} lie in the grey region, but is then unclear how to assign the value of $p\big|_{z=1}$ and $T\big|_{z=1}$ at that point. If we created a bespoke implementation an algorithm for nonlinear systems, such as the Levenberg-Marquardt Algorithm [51], we could modify the iterative rule to shrink the update until the new point was outside the grey region, but that is beyond the scope of the thesis. Consequently,

in Section 4.3, we will present and discuss a representative solution to the coupled problem including both reactions, to demonstrate that we can obtain solutions to the complete problem, but then focus on simplified versions of the problem. We first consider the coupled problem when the reaction rates are zero in order to gain insight into how the solutions and the energy transfer between the gases and solid vary. Then, in Section 4.4, we will consider the behaviour of the model for the reacting gas, (4.29)–(4.33), subject to an imposed solid temperature, allowing us to perform parameter sweeps as the Damköhler numbers vary, giving us insight into their effect on the gas flow. The combined insights from these two approaches will then be used to conjecture the behaviour of the coupled model with reactions in Section 4.5.

4.3 Coupled problem

4.3.1 Results with reactions

In Figure 4.4, we plot a solution to the coupled model when $\epsilon^2\mathrm{Re} = 1$, $T_{\mathrm{surf}} = 0.75$, $\mathrm{Pe_s} = 257$, $A_\epsilon = 0.02$, $\mathrm{Da}_1 = \mathrm{Da}_2 = 0.1$, for the reaction rates given by (2.81)–(2.82) with $T_{\mathrm{cond}} = 0.88$ and $\xi = 0.05$. The remaining parameter values are given in Table 2.3. This solution is the closest to the industrially-relevant parameter regime we were able to converge to, with only A_ϵ and T_{surf} too large, by an order of magnitude and a factor of 0.5, respectively. The solution was found using continuation from a solution with no reactions by slowly varying Da_1 and Da_2. When attempting to find a solution where the size of T_{surf} is industrially-relevant, the numerical solver would always make a step to values of Q_{crat} and q_{crat} for which ode15s failed to converge partway along the channel, i.e. the step moved into the grey regions in Figure 4.3. This occurred both when applying continuation in Da_1 and Da_2 from a no reactions solution, starting with $T_{\mathrm{surf}} = 0.25$, and when applying continuation of T_{surf} from the solution given in Figure 4.4. It was only possible to achieve a solution where both $T_{\mathrm{surf}} = 0.25$ and an appreciable amount of SiO had been removed from the channel, by picking a small value of $\epsilon^2\mathrm{Re}$. However, this led to no appreciable difference between the solid and gas temperatures, which is a key behaviour we wished to capture with our model in this chapter. Applying continuation of $\epsilon^2\mathrm{Re}$ to this solution allowed us to find solutions only for a small range of higher reduced Reynolds numbers, which showed no qualitative change in the solutions. We will discuss why this lack of a solution at higher reduced Reynolds numbers may be a feature of the model rather a problem with the numerical scheme in Section 4.5.

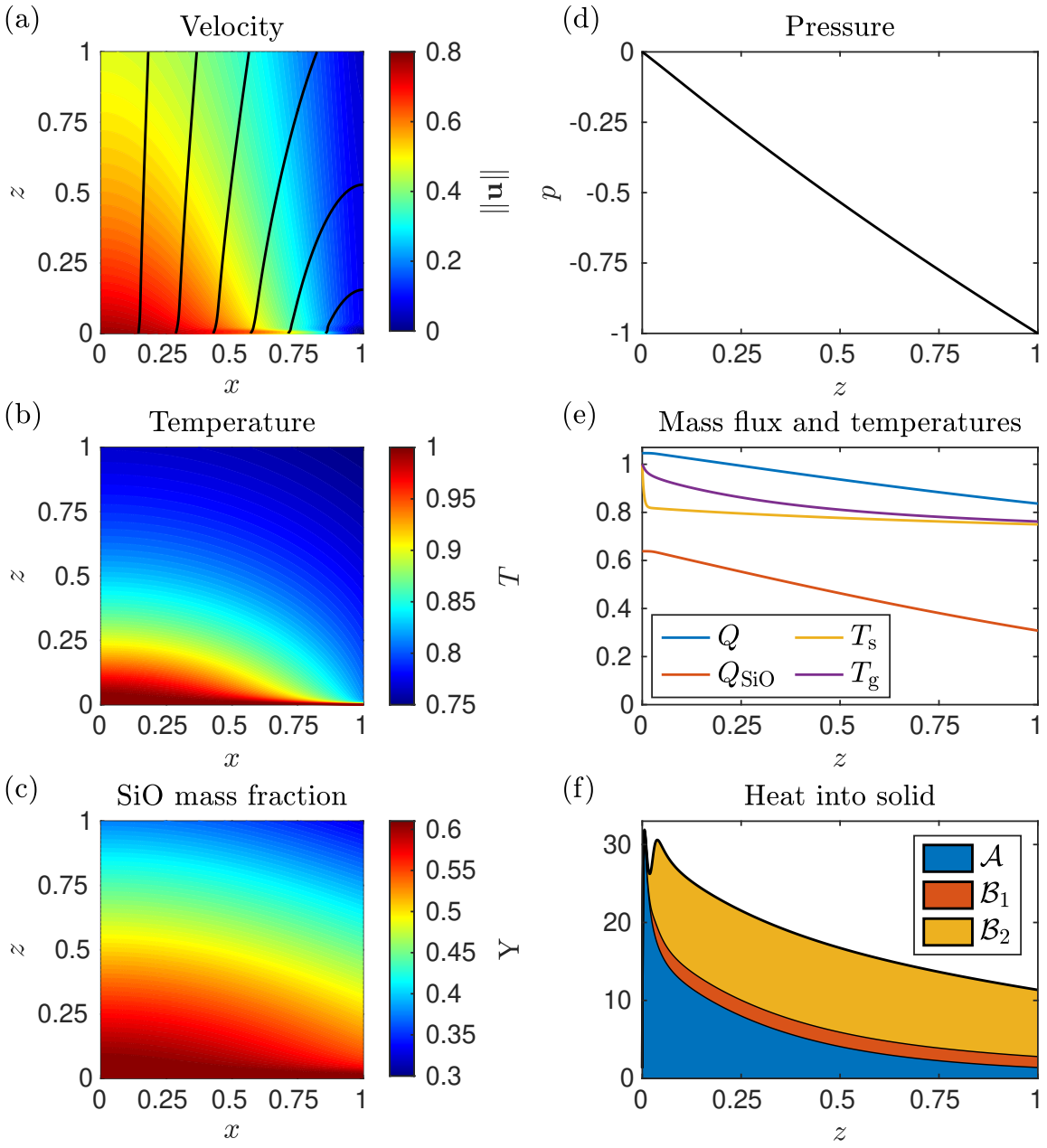


Figure 4.4: Solution to the coupled model when $\epsilon^2\mathrm{Re} = 1$, $T_{\mathrm{surf}} = 0.75$, $\mathrm{Da}_1 = \mathrm{Da}_2 = 0.1$, F_1, and F_2 are given by (2.82) with $T_{\mathrm{cond}} = 0.88$ and $\xi = 0.05$. The respective panels show: (a) the gas velocity magnitude $\|\boldsymbol{u}\|_2$ and streamlines, (b) the gas temperature T, and (c) the Mass fraction of SiO Y, all as functions of x and z. Also in: (d) the pressure p, (e) the total mass flux of gas Q, the mass flux of SiO Q_{SiO}, the solid temperature T_{s} and the average gas temperature T_{g}, defined by (4.26), and (f) the energy into the solid via conductive heat transfer and released by the reactions given in (4.39)–(4.40), all as functions of z. The total mass flux of gas at the crater is $Q_{\mathrm{crat}} = 1.05$, and the conductive heat flux into the solid at the crater is $q_{\mathrm{crat}} = -46.5$.

From Figure 4.4a, we can see that some of the streamlines pass into the interface at $x = 1$, due to the gas being consumed by reaction 2. We can also see that the magnitude of the average velocity decreases as z increases. This is caused by the gas becoming cooler, as shown in Figure 4.4b, and hence becoming denser by (4.16f). Figure 4.4c, shows that the mass fraction Y of SiO decreases with height up the furnace as material is consumed, and at a given height is lowest near the interface. Figure 4.4d shows the pressure profile is monotonically decreasing.

From Figure 4.4e, we can see that the solid temperature increases slowly as the solid moves downwards through the majority of the domain, then increases suddenly in a boundary layer near $z = 0$. In contrast the average gas temperature, defined by (4.26), and also shown in Figure 4.4e, decreases across the whole height of the furnace, exiting at a slightly higher temperature than the incoming solid. Figure 4.4e also shows both the total mass flux of gas, Q, and the mass flux of SiO, Q_{SiO}, decrease as z increases. Since the solid temperature is below the condensation temperature, $T_{\mathrm{cond}} = 0.88$ for reaction 2, over almost the entire height of the furnace, Q is decreasing everywhere, except a narrow region near $z = 0$.

Figure 4.4f shows how the relative contribution to the heating of the solid by heat transfer from the gas,

$$\mathcal{A} = -\frac{k}{A_\epsilon \left|\mathcal{C}_{\mathrm{s}}\right|} \left.\frac{\partial T}{\partial x}\right|_{x=1}, \tag{4.39}$$

and the energy released by reaction i (including the internal energy of any gas consumed),

$$\mathcal{B}_i = -\frac{\mathrm{Da}_i \mathrm{Pr}}{\mathrm{Sc} A_\epsilon \left|\mathcal{C}_{\mathrm{s}}\right|} \left(\left(\nu_{\mathrm{SiO}} + \nu_{\mathrm{CO}}\right) T\big|_{x=1} - \eta_i \right) \mathcal{R}_i|_{x=1}, \tag{4.40}$$

vary with z. From this plot we can see that the heat transfer from the gas decreases as z increases. From Figure 4.4e, we see that difference in average temperatures between the gas and solid also decreases as z increases, and we will explore the relationship between them further in Section 4.3.2. The amount of energy released by the reactions varies much less with z, and so represents the main contributor to the heating of the solid near the surface of the charge. The size of the total heat into the solid increases as z decreases, but there is no sudden jump to account for the sudden increase in solid temperature. This is because, for these parameter values, it is diffusive heat transfer from the crater into the solid, that raises to solid temperature to the crater temperature, with the gas and reactions only able to raise the solid temperature from 0.75 to 0.8 over the entire length of the furnace.

The results in Figure 4.4 demonstrate that the shooting method from Section 4.2.2 can produce a solution to the coupled model, even with multiple reactions whose rates

are temperature dependent. However, the process of obtaining such solutions is too unreliable to carry out any parameter analysis of the full model in the industrially-relevant parameter range, or to carry out sweeps to identify when multiple solutions exist to the model. Therefore, for the remainder of the chapter we will explore the dynamics of the model under the simplifying assumptions that either the reaction rates are zero or that the solid temperature is known.

4.3.2 Results without reactions

We now take $\mathrm{Da}_1 = \mathrm{Da}_2 = 0$, so that no reactions occur, and explore the solution structure and heat transfer behaviour of the coupled model.

In Figure 4.5 we plot the initial mass flux of gas, Q_{crat}, defined by (4.33a), and the diffusive heat flux from the crater into the solid, q_{crat}, defined by (4.36a), as functions of the reduced Reynolds number $\epsilon^2\mathrm{Re}$, for different values of T_{surf}. The behaviour of Q_{crat} when $T_{\mathrm{surf}} = 0.25$ and 0.5 is qualitatively the same as that of Q for case II of the model of a single gas species in Chapter 3, with two steady solutions below a critical value of $\epsilon^2\mathrm{Re}$, and none above. For consistency with that chapter, we refer to the two solutions as the low- and middle-flux solutions respectively. For both $T_{\mathrm{surf}} = 0.25$ and 0.5, q_{crat} tends to a constant as $\epsilon^2\mathrm{Re} \to 0$ along both solution branches, changing by less than an order of magnitude between solution branches on each occasion. The large size of q_{crat} along both solution branches implies that T_{s} will always heat up significantly near $z = 0$ due to heat supplied from the crater. Indeed, this can be seen in Figure 4.6a, where both the low- and middle-flux solutions for T_{s} are plotted as a function of z, for two different values of $\epsilon^2\mathrm{Re}$, with all the solutions showing a sudden increase near $z = 0$. Therefore, with the industrially-relevant value of T_{surf}, heat transfer from the gas alone appears to be insufficient to heat the solid to the crater temperature even with very high flow rates of gas of the middle-flux solution branch.

The behaviour of the model when $T_{\mathrm{surf}} = 0.75$ is slightly different from the lower values. This presents several numerical challenges, which mean we are able to only show part of the middle-flux branch for $T_{\mathrm{surf}} = 0.75$ in Figure 4.5. The relationship shown between $\epsilon^2\mathrm{Re}$ and Q_{crat} in Figure 4.5a for $T_{\mathrm{surf}} = 0.75$ has the same qualitative shape as the lower values of T_{surf}, with two branches of solutions below a critical value of $\epsilon^2\mathrm{Re}$. However, unlike for the lower values of T_{surf}, the diffusive heat flux from the crater q_{crat} shown in Figure 4.5b, becomes very small as $\epsilon^2\mathrm{Re}$ increases along the low-flux branch, with middle-flux branch at an approximately constant value around 1×10^{-6}. This massively complicates the numerical solution, since

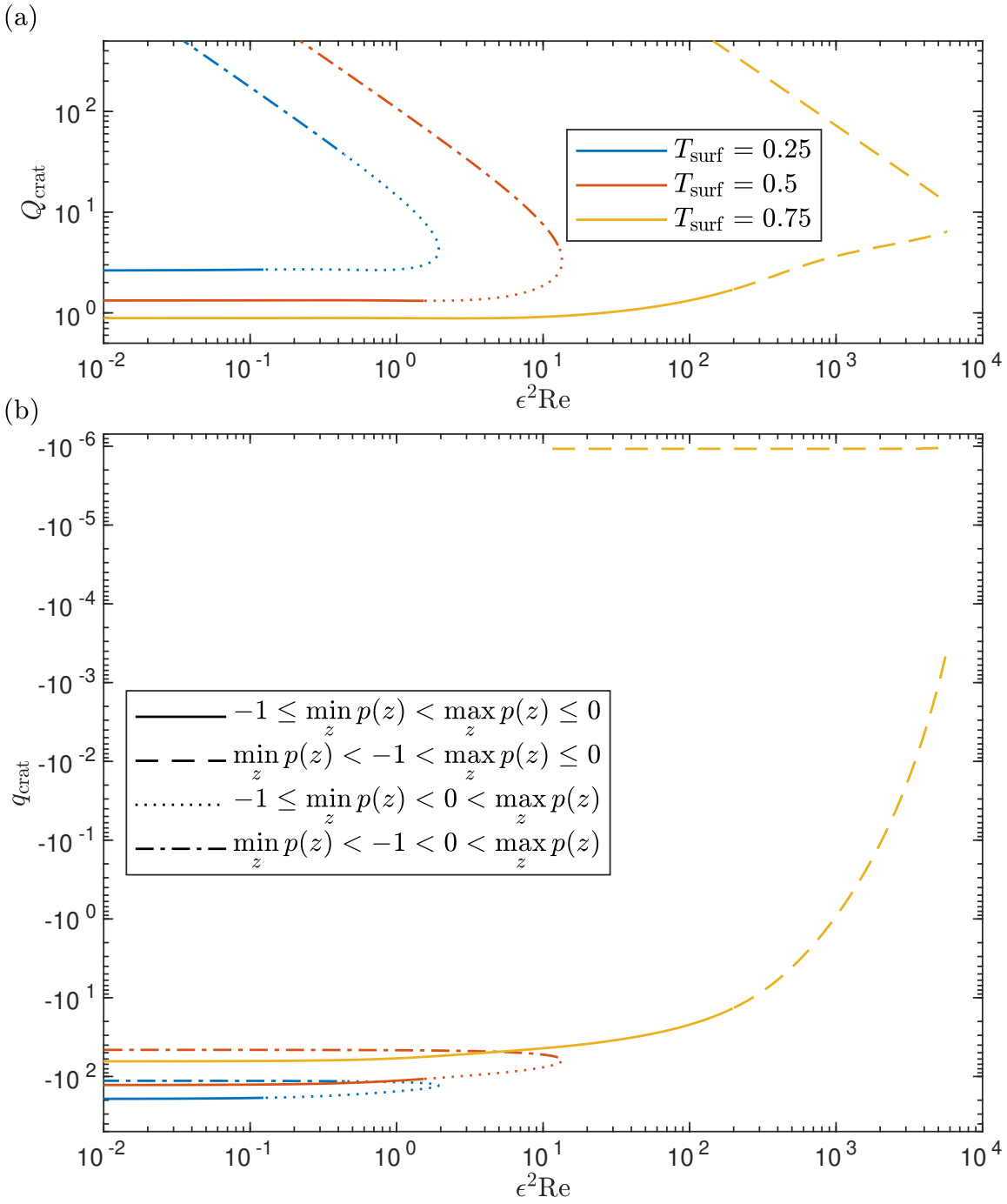


Figure 4.5: (a) The total mass flux of gas at the crater Q_{crat}, and (b) the diffusive heat flux into the solid at the crater q_{crat} as functions of the reduced Reynolds number $\epsilon^2\text{Re}$ for surface temperature drops, where: $T_{\text{surf}} = 0.25$ is blue, $T_{\text{surf}} = 0.5$ is red, and $T_{\text{surf}} = 0.75$ is yellow. Solutions with a pressure profile bounded by the crater and surface pressure are shown as a solid line, while solutions with a non-monotonic pressure whose extrma lie below or above these pressures are shown by a dashed and a dotted line, respectively. A solution that has both a too low minimum pressure and a too high maximum is shown as a dot-dash line.

there are at least seven orders of magnitude in difference between the sizes of the two shooting parameters, making estimates for the gradient of the system inaccurate. Moreover, we are required to use higher tolerances than we were for the other sweeps. However, we were still unable to resolve the behaviour around the point of maximum $\epsilon^2\mathrm{Re}$, leading to the gaps in the curve in Figure 4.5.

Due to the large range of $\epsilon^2\mathrm{Re}$ for which a solution exists, we only consider the temperature profiles of the low-flux solution when $T_{\mathrm{surf}} = 0.75$. These are shown in Figure 4.6b, for $\epsilon^2\mathrm{Re} = 0.1, 10$, and 1000, and shows that, at $\epsilon^2\mathrm{Re} = 1000$ there is no boundary layer near $z = 0$, unlike all the other solutions, and instead the solid begins heating immediately as it enters the furnace. This means the gradient of the solid temperature is very small at $z = 0$, which is consistent with the small value of q_{crat}. The shape of the temperature profile T_{s} is also different from the other solutions, being concave rather than convex. In Chapter 5, we will show that when the gas and solid temperatures are equal, this change in shape indicates that the direction of net advection of heat is changing from downwards to upwards, i.e. that overall more heat is being carried upwards by the gas than downwards by the solid.

In Chapter 3, we found that some solutions to the model for a single-phase gas had non-monotonic pressure profiles, with the minimum pressure along the channel being less than the surface pressure. When solving the coupled gas-solid problem, we also observe solutions with this behaviour, and such solutions are shown using a dashed line in Figure 4.5. However, some solutions to the coupled problem have non-monotonic pressure profiles where the maximum pressure is greater than the crater pressure and we have shown such solutions using a dotted line. Solutions where both these effects occur, i.e. the minimum pressure is lower than the surface pressure and the maximum pressure is above the crater pressure, are shown by dot-dashed lines. Examples of all such types of pressure profile are given in Figure 4.6a and c. These illustrate the general trend that the local maximum occurs before $z = 0.5$, while the local minimum occurs after $z = 0.5$. From Figure 4.5, we can see that the $T_{\mathrm{surf}} = 0.25$ and 0.5 curves follow the same trend of initially developing a maximum pressure greater than zero along the low-flux solution branch, before a minimum less than minus one appears on the low-flux solution branch. Therefore, we can conjecture that the local maximum is delaying the onset of the local minimum, since in the single-phase case in Chapter 3, the local minimum developed on the low-flux solution branch. The behaviour of the $T_{\mathrm{surf}} = 0.75$ solution is again different, with the maximum pressure always remaining the crater pressure, and a minimum pressure below the surface pressure developing for large reduced Reynolds numbers along the low-flux solution branch. The maximum

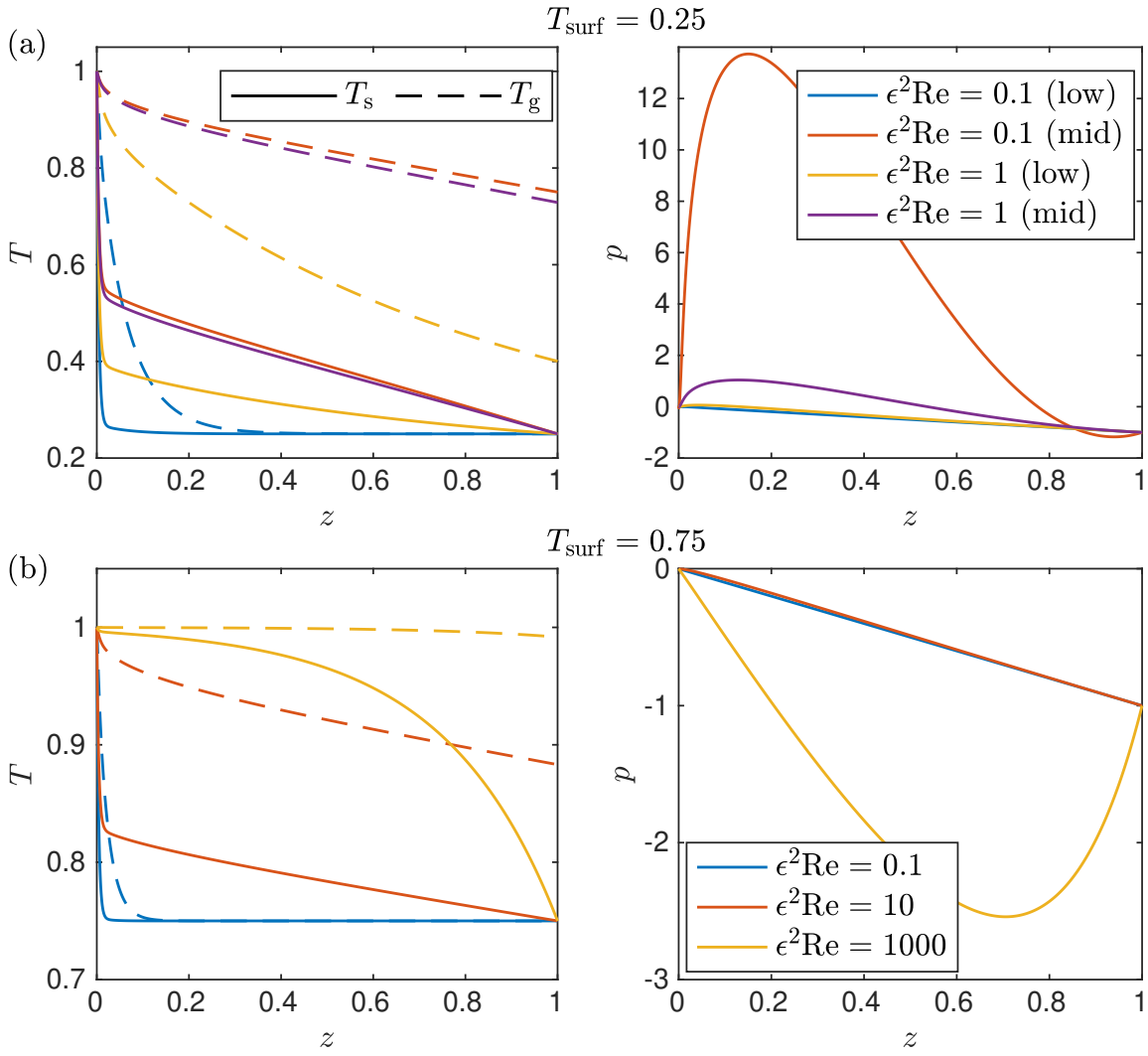


Figure 4.6: The solid temperature T_{s}, shown by a solid line, the average gas temperature T_{g}, defined by (4.26) and shown by a dashed line, along with the pressure p, all as functions of z, for a range of $\epsilon^2\text{Re}$ when $\text{Da}_1 = \text{Da}_2 = 0$, and (a) $T_{\text{surf}} = 0.25$ and (b) $T_{\text{surf}} = 0.75$. In (a) the low- and middle-flux solutions are distinguished by using different colours.

pressure being the crater pressure, appears to persist along the middle-flux solution branch when $T_{\text{surf}} = 0.75$ too.

We now consider the behaviour of the energy fluxes associated with the solutions from Figure 4.5. As no reactions occur, we have that $E_{\text{React}} = 0$. For identical reasons to those discussed in Section 3.2.4.4, the dimensional forms of all the energy fluxes will be proportional to $\epsilon^2\text{Re}$ times the dimensionless form, with the same proportionality constant. Hence, for ease of interpretability for the results, in Figure 4.7a-c, we plot the absolute value of the energy fluxes times the reduced Reynolds number as a function of the reduced Reynolds number. As both the solid velocity and solid temperature are fixed by the boundary conditions at $z = 0$ and $z = 1$, the values of $E_{\text{s,crat,A}}$ and $E_{\text{s,surf,A}}$ are fixed, and so appear as horizontal lines. For all values of T_{surf}, the energy in the gas from the crater increases with $\epsilon^2\text{Re}$, as does the energy exiting the gas phase through the surface, with the latter always remaining less than the former. However, the distance between them decreases as $\epsilon^2\text{Re}$ increases along the low-flux solution branch, and the two are almost equal along the middle-flux solution branch. This implies that a reduced proportion of available energy will be reaching the solid from the gas. For the $T_{\text{surf}} = 0.25$ and 0.5 solutions, the diffusive energy flux from the crater remains the same order of magnitude as $\epsilon^2\text{Re}$ varies along both solution branches. In general it is a similar order of magnitude to the useful output $E_{\text{s,surf,A}}$, indicating it contributes a significant amount to achieving the necessary heating, despite conduction being a small effect in the governing equations. For both these values of T_{surf}, the heat lost due to diffusion through the surface is negligible. The behaviour of the $T_{\text{surf}} = 0.75$ solution is different, with the diffusive energy flux from the crater initially starting a similar order of magnitude to the output energy, but decreasing rapidly for $\epsilon^2\text{Re} > 10$. At that point diffusive heat loss through the surface starts to become an important effect.

The energy efficiency, defined by (4.25), is plotted for each of these sets of fluxes in Figure 4.7d. For all values of T_{surf} this tends to one along the low-flux solution branch, suggesting no appreciable amount of energy is being lost in these solutions. As $\epsilon^2\text{Re}$ increases, the efficiency decreases, with the decrease increasing sharply once $\epsilon^2\text{Re} > 1$. From the energy fluxes we can see that this decrease is primarily due to the increasing loss in the gas exiting the surface of the charge. For $T_{\text{surf}} = 0.25$ and 0.5, the efficiency tends to a constant value along the middle-flux solution, which we can see is due to all the energy fluxes also tending to constant values. The minimum value of efficiency decreases as T_{surf} increases, with the efficiency for $T_{\text{surf}} = 0.75$ going to zero as $\epsilon^2\text{Re}$ increases.

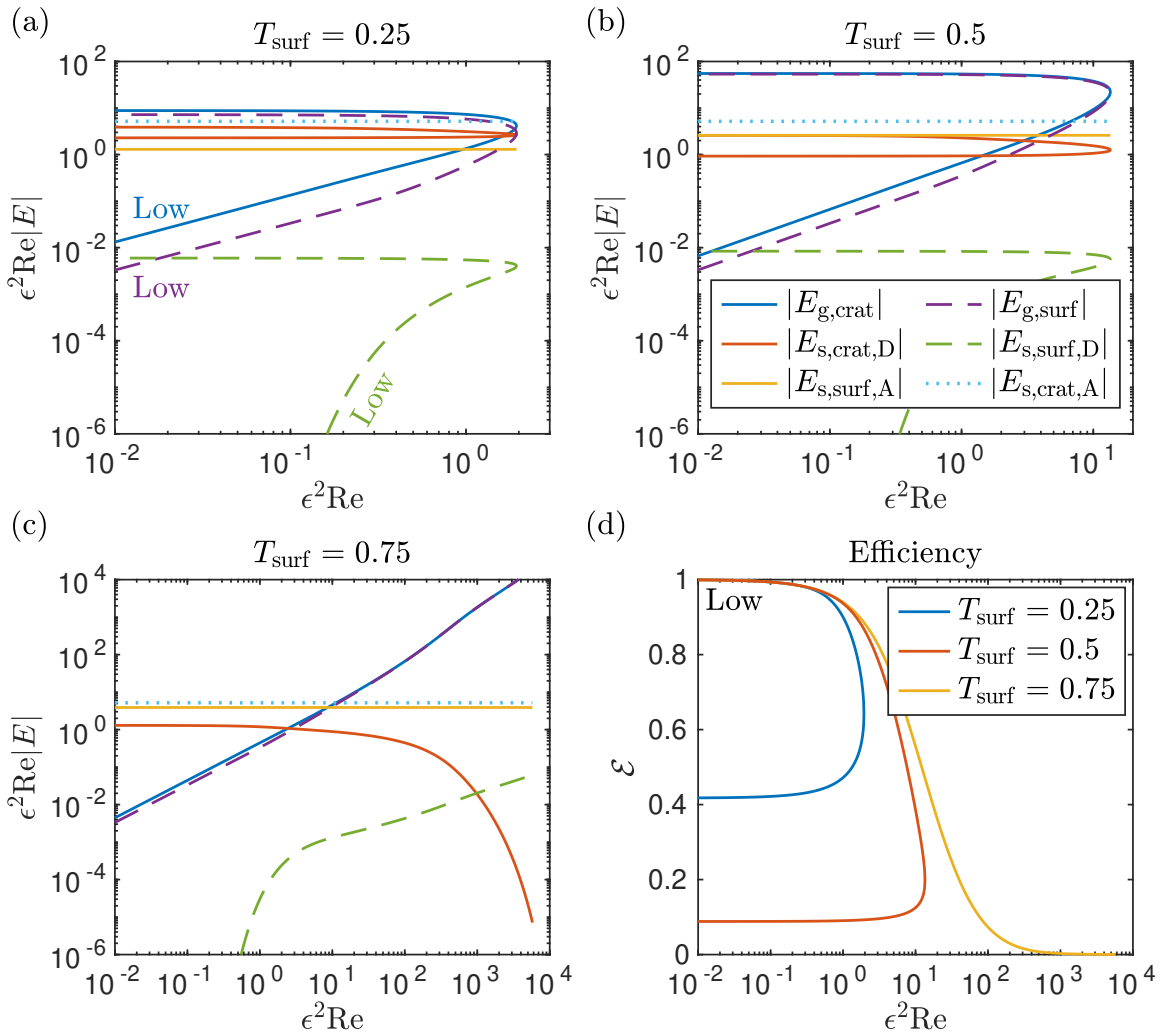


Figure 4.7: (a)-(c) The absolute value of the energy fluxes (4.21)–(4.22) multiplied by $\epsilon^2\text{Re}$ as a function of $\epsilon^2\text{Re}$ when $\text{Da}_1 = \text{Da}_2 = 0$ and (a) $T_{\text{surf}} = 0.25$, (b) $T_{\text{surf}} = 0.5$, (c) $T_{\text{surf}} = 0.75$. Energy fluxes representing an input of energy to the domain are represented by solid lines, while fluxes representing lost energy and useful output are represented by dashed and dotted lines respectively. (d) The Energy efficiency defined by (4.25) as a function of $\epsilon^2\text{Re}$ for the results from (a)-(c).

We can also use solutions of the coupled model to investigate the validity of the hypotheses of previous macroscale models used to study silicon furnaces. Recall from the literature review in Chapter 1 that studies of flow in porous media out of local thermal equilibrium rely on the constitutive assumption that the heat transfer between the fluid and solid structure is linearly proportional to the difference in average temperature between the two phases. As our model makes no such assumptions for the heat exchange, and is instead based purely on physical laws, we are able to use solutions of our model to determine the actual behaviour in this process. Fully determining the dependence of the heat exchange on all the parameters involved is beyond the scope of this thesis, particularly due to the complexity of our current model with the temperature directly coupling to the fluid behaviour, so we will focus on demonstrating the method by studying the dependence on the reduced Reynolds number.

In Figure 4.8a, we plot the profiles of T_{s} and T_{g}, associated with the low-flux solutions for three different values of $\epsilon^2\mathrm{Re}$ when $T_{\mathrm{surf}} = 0.5$ and $\mathrm{Da}_1 = \mathrm{Da}_2 = 0$. We choose to focus on this surface temperature as the range of values of $\epsilon^2\mathrm{Re}$ for which steady solutions exist extends beyond ten, allowing solutions where interia is important to be considered, but the overall behaviour of Q_{crat} and q_{crat} in Figure 4.5 is qualitatively the same as that for the industrially-relevant value of $T_{\mathrm{surf}} = 0.25$. We focus on the low-flux solution as we believe it to be more physically relevant. The results in the figure show that in the majority of the domain, the average temperatures of the gas and solid are approximately equal when $\epsilon^2\mathrm{Re} \ll 1$, and differ when $\epsilon^2\mathrm{Re} = O(1)$, supporting the hypothesis of Chapter 3. However, the $\epsilon^2\mathrm{Re} = 0.1$ solutions still shows a difference in temperature near $z = 0$, with the gas temperature being higher. This indicates that there is a boundary layer near the inlet where inertia is important. Unlike the $\epsilon^2\mathrm{Re} = 0.1$ solution, where the solid did not appreciably heat up from T_{surf} until near $z = 0$, both the $\epsilon^2\mathrm{Re} = 1$ and 10 solutions show the solid heating up throughout the domain, although still requiring a significant increase in the boundary layer near $z = 0$. The behaviour of the average gas temperature changes significantly between the $\epsilon^2\mathrm{Re} = 1$ solution, where the gas has almost cooled to T_{surf} as it exits the furnace, and the $\epsilon^2\mathrm{Re} = 10$ solution, where the gas is exiting at a significantly higher temperature than T_{surf}. This agrees with the sudden decrease in energy efficiency we observed in Figure 4.7d.

The evolution in the difference in average temperature can be seen more clearly in Figure 4.8b, where $T_{\mathrm{g}} - T_{\mathrm{s}}$ is plotted against the size of the source term in the energy equation of the solid (4.14), which represents the rate of energy transfer into the solid

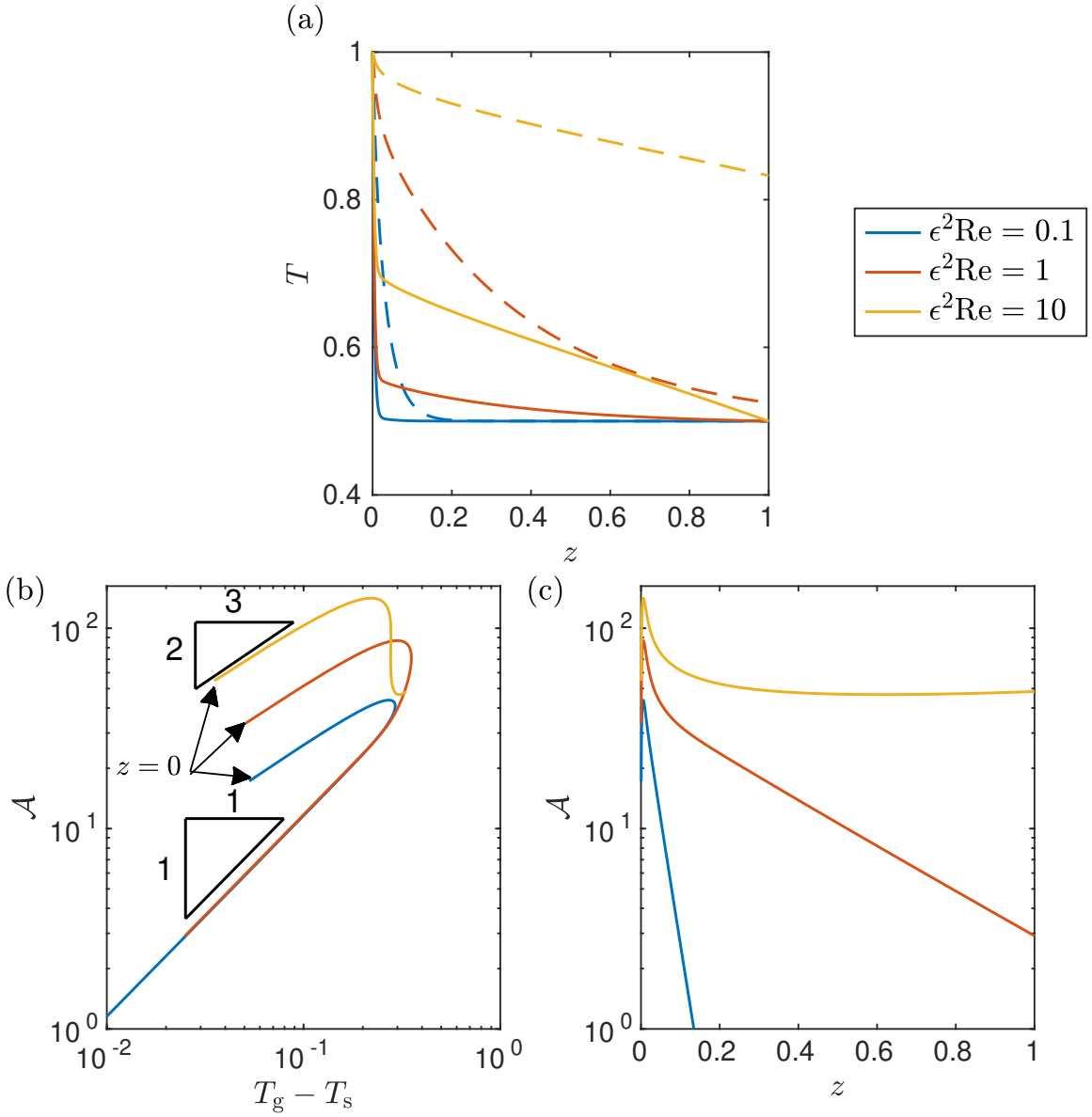


Figure 4.8: (a) The solid temperature T_s, shown as a solid line, and the average gas temperature T_g, defined by (4.26) and shown by dashed lines, varying with z. The solutions were computed with $T_{surf} = 0.5$, $Da_1 = Da_2 = 0$. (b) and (c) The amount of heat exchanged between the gas and the solid as a function of the difference between the average temperature of the gas and solid and distance along the channel, respectively.

due to heat transfer from the gas phase. We see in all three solutions the difference in temperature grows in a boundary layer near $z = 0$. Then, in the $\epsilon^2\mathrm{Re} = 0.1$ and 1 solutions, the difference in temperatures decreases again, but in the $\epsilon^2\mathrm{Re} = 10$ solution the difference remains approximately constant. In the $\epsilon^2\mathrm{Re} = 0.1$ and 1 solutions, we see that outside the boundary layer, there is indeed a linear relationship between the temperature difference and the heat exchange, agreeing with the constitutive law in the literature. However, in the region near $z = 0$, all three solutions show the heat exchange to be approximately proportional to $(T_\mathrm{g} - T_\mathrm{s})^{2/3}$. For the $\epsilon^2\mathrm{Re} = 10$ solution, we see from Figure 4.8c, which shows the heat exchanged as a function of z, that the amount of heat exchanged rapidly tends to a constant value as z increases. These results suggest that a heat exchange term linearly proportional to the difference in temperature between the fluid and solid in a porous media gives a good approximation of the 'true'-behaviour of our more realistic model of the furnace, over the majority of the domain, provided the reduced Reynolds number is small. However the approximation breaks down near $z = 0$ for all $\epsilon^2\mathrm{Re}$, and the relationship becomes nonlinear, but is well approximated by a power law in temperature difference. Future work to systematically explore this behaviour is discussed in Chapter 6.

4.4 Prescribed solid temperature

To investigate the effect of non-zero reaction rates we now consider the behaviour of the model for the gases, (4.16)–(4.17), subject to an imposed solid temperature T_s. This proves a simpler and more robust problem to solve numerically than the coupled problem with reactions, allowing us to sweep over different sizes of reaction rates. Our main goal here is to investigate how the reactions change the solution structure and explore the dependence of the SiO loss on the parameters in the model. As in Section 3.3, we will take T_s to be given by (3.42), and so be a linear function of z. For all the results in this section we use industrially-relevant parameter values with the exception of A_ϵ, for which we take the value of 0.02.

Previously, we modelled the temperature dependence of the rate of reaction 2 through the functions $F_2(T)$, given in (2.82). However, with T_s prescribed, F_2 becomes a function depending on position along the channel only, and so is unaffected by the dynamics of the problem. With the linear solid temperature, we are just delaying the start of reaction 2 until the gas reaches $z \approx (1 - T_\mathrm{cond})/(1 - T_\mathrm{surf})$. To simplify the interpretation of the results, we consider instead the problem where $F_2(T) = 1$, i.e. the same constant dependence as reaction 1. Then, the only difference between the

two reactions is chemical, namely that reaction 1 replaces one SiO molecule with a CO molecule, while reaction 2 removes two SiO molecules.

In Figure 4.9, we plot the initial mass flux of gas, Q_{crat}, defined by (4.33a), as a function of the reduced Reynolds number, $\epsilon^2\text{Re}$, for different values of the Damköhler numbers of reaction i, Da_i, for $i = 1, 2$ when $T_{\text{surf}} = 0.25$. This is now the only shooting parameter so it is straightforward to verify that the results in the figure represent a complete set of solutions using the approach from Chapter 3. In each case, the model has the same structure as the solutions to case II of the single-phase model in Chapter 3, with a region where two steady solutions exist, and a region where none exist. It also matches the qualitative behaviour of the coupled model in Figure 4.5 when $T_{\text{surf}} = 0.25$.

Figure 4.9a demonstrates that, when $\text{Da}_2 = 0$, varying Da_1 has no effect on the relationship between $\epsilon^2\text{Re}$ and Q_{crat}, which remains unchanged from the no reactions case. In particular, they coincide exactly with the solution curve when $\text{Da}_1 = \text{Da}_2 = 0$, which is identical to the solution for case II of the single-phase model, with the same parameter values. This is because reaction 1 merely exchanges a SiO molecule for a CO molecule, and due to our assumption that the molar weights are equal, this does not alter the total amount of mass of gas in the channel.

In contrast, when $\text{Da}_1 = 0$ but Da_2 varies, as shown in Figure 4.9b, the rate of the reaction does affect the relationship between $\epsilon^2\text{Re}$ and Q. In particular, the value of Q as $\epsilon^2\text{Re} \to 0$ along the low-flux branch, changes depending on whether Da_2 is zero or non-zero. Hence, if we want to solve the coupled problem when $\text{Da}_2 \neq 0$ by applying continuation in Da_2, starting from $\text{Da}_2 = 0$ may not necessarily be effective when $\epsilon^2\text{Re}$ is very small.

The value of Q_{crat} in the limit $\epsilon^2\text{Re} \to 0$ is equal to that predicted by the asymptotic solution to case III of the single-phase model, when $\text{Da}_2 = 0$. This is shown in Figure 4.9b by the lower black dot-dash line. The limit when $\text{Da}_2 \neq 0$ can be similarly predicted using the method of matched asymptotics, the outline of which we sketch out. As we are considering $\epsilon^2\text{Re} \to 0$, we have that $\epsilon^2\text{Re} \ll \text{Da}_2$. When this occurs, all of the SiO will be consumed in a boundary layer near $z = 0$. Evidence for this can be seen in Figure 4.10, which shows the z position of different quartiles of the fraction of Q_{SiO} remaining in the channel. When $\text{Da}_2 = 0.1$ or 1, all of the contours tend to $z = 0$ as $\epsilon^2\text{Re} \to 0$, indicating the SiO is being consumed almost immediately. In the outer solution, away from the crater we therefore have $Y = 0$, and so $Q_{\text{SiO}} = 0$. Inside the boundary layer there are large number of possible behaviours, depending on the assumed parameter sizes, but since we assume that z is small, we will find the

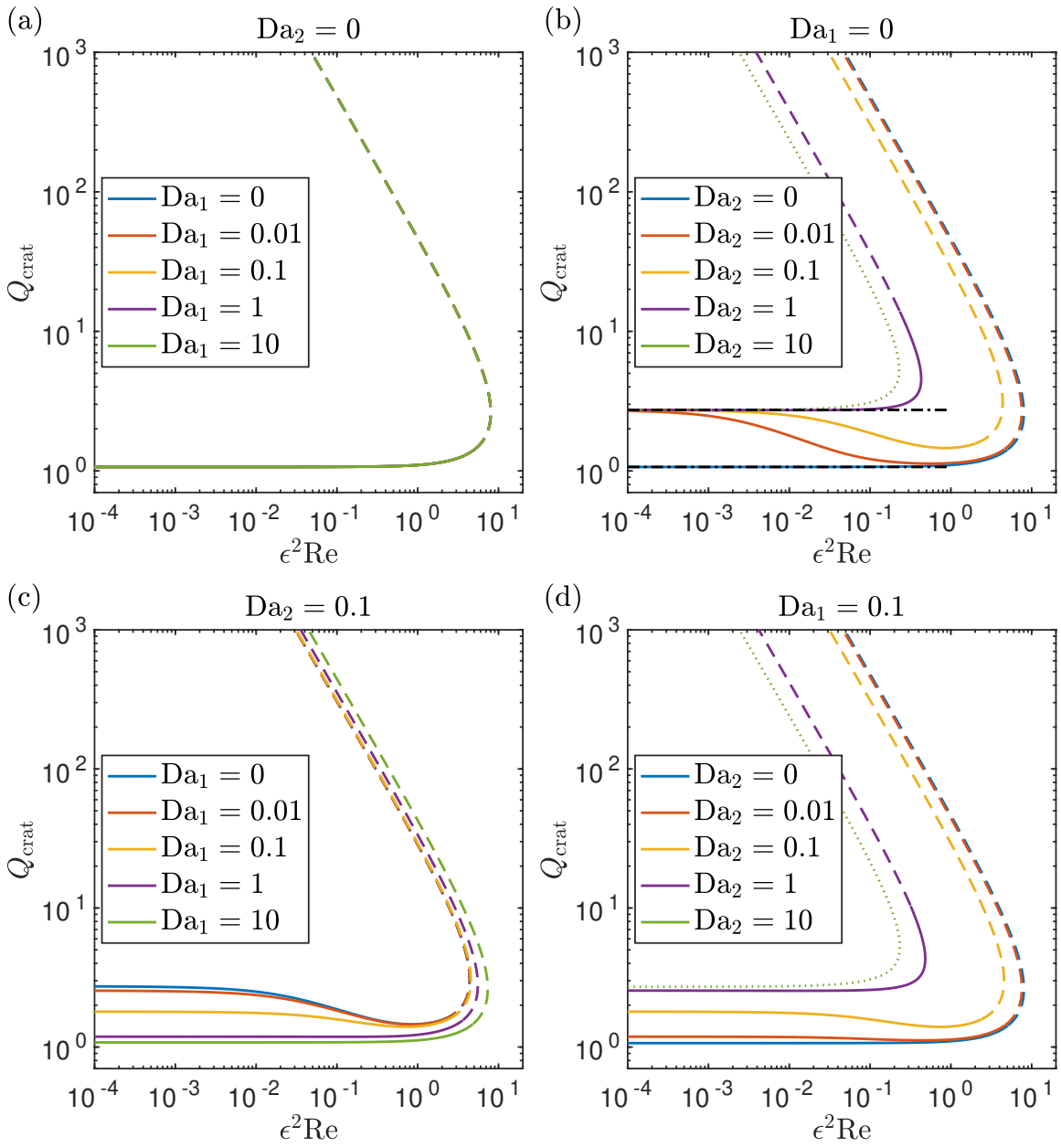


Figure 4.9: The gas mass flux at the crater Q_{crat} as a function of the reduced Reynolds number for different Damköhler numbers Da_1 and Da_2, obtained by solving the binary gas mixture problem (4.16)–(4.17) with an imposed linear solid temperature with $T_{\text{surf}} = 0.25$. A solution where the pressure profile is non-monotonic such that the minimum pressure is less than the pressure at the surface is shown by a dashed line, while a solution such that the maximal pressure is greater than the pressure in the crater is shown by a dotted line. In panel (b) the asymptotic solution when $\epsilon^2\text{Re} \ll 1$, with no reactions, given by (3.27f) and when reaction 2 occurs, given by (4.41) are shown by dot-dash black lines, with the latter the higher line.

pressure is constant in z in the boundary layer, and so equal to the crater pressure. This implies the pressure in the outer problem will tend to the crater pressure as it approaches the crater. Therefore, in the outer problem we have the crater and surface pressures at each end of the channel, and no SiO implying no reactions, which means the mass flux in the outer problem will be identical to the mass-flux for a single phase gas, given by (3.27f). To find the total mass flux of gas from the crater, we just need to relate it to the mass flux of gas in the outer. This is straightforward, as all the SiO gas is consumed in the boundary layer, but CO is neither created or removed. Hence, the outer mass flux is just the mass flux of CO from the crater. Hence, we use the imposed mass fraction of SiO at the crater to find, $Q_{\mathrm{CO}} = Q_{\mathrm{crat}}\,(1 - Y_{\mathrm{crat}})$, and

$$Q_{\mathrm{crat}} = \frac{2}{3\,(1 - Y_{\mathrm{crat}}) \int_0^1 T_{\mathrm{s}}(z)\mu\,(T_{\mathrm{s}}(z))\,\mathrm{d}z}. \tag{4.41}$$

This asymptotic result is also plotted in Figure 4.9b as the upper dot-dash black line, and it does indeed match up with the limit as $\epsilon^2\mathrm{Re} \to 0$ for $\mathrm{Da}_2 \neq 0$.

At larger reaction rates, the numerical results in Figure 4.9b stay close to the asymptotic limit for $\mathrm{Da}_2 \neq 0$, given by (4.41) for the whole of the low-flux solution, whereas for smaller reaction rates, the mass flux decrease as $\epsilon^2\mathrm{Re}$ increases. This is because the smaller reaction rates violate the requirement that $\epsilon^2\mathrm{Re} \ll \mathrm{Da}_2$, meaning that the SiO is no longer completely consumed in a boundary layer near the crater, and instead is being removed partway along the length of the channel. This can be seen in Figure 4.10, where the 0.25, 0.5, and 0.75 quartiles of $\mathrm{Da}_2 = 0.1$ increase from $z = 0$ to $z = 1$ as $\epsilon^2\mathrm{Re}$ increases, meaning that a greater proportion of SiO gas must be exiting the channel. Hence, the pressure drop must drive an increasing proportion of the initial gas flux at the crater through the entire length of the channel. In contrast the quartiles of SiO when $\mathrm{Da}_2 = 1$ show that less than 25 % of the SiO gas is reaching the surface at the maximum mass flux, and so the pressure drop never has to force the SiO through the entire length of the channel, so that the total initial mass flux can remain higher.

Figures 4.9c and d, show the effect of both reactions occurring when one of Da_1 and Da_2 is fixed. Unlike in Figure 4.9a, where varying Da_1 had no effect on the relationship between $\epsilon^2\mathrm{Re}$ and Q, Figure 4.9c shows altering Da_1 changes the relationship when Da_2 is non-zero. This is because varying Da_1 alters the amount of SiO converted into CO, and this CO must travel the remaining length of the channel because it cannot be removed by the reactions. The behaviour seen in Figure 4.9d, where Da_2 varies, more closely matches that seen in Figure 4.9b, however, unlike in Figure 4.9b, the low-flux

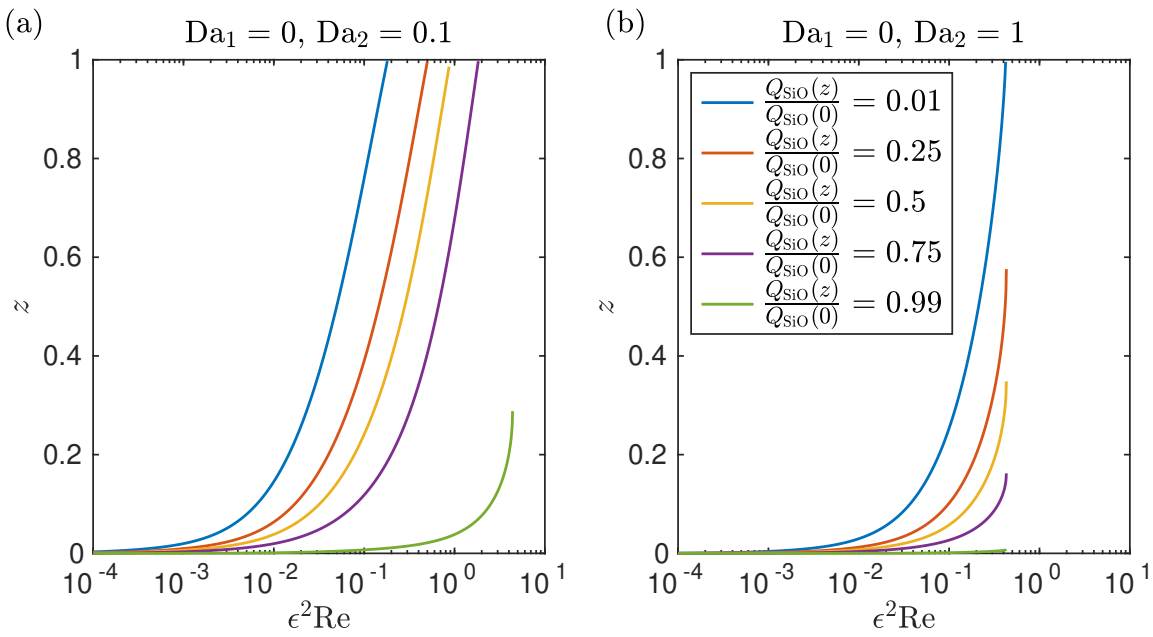


Figure 4.10: The positions of the 0.01, 0.25, 0.5, 0.75, and 0.99 quartiles of the fraction of the Q_{SiO} in the channel as a function of $\epsilon^2\mathrm{Re}$, when the solid temperature is fixed to be (3.42), $T_{\mathrm{surf}} = 0.25$, $\mathrm{Da}_1 = 0$, and (a) $\mathrm{Da}_2 = 0.1$, (b) $\mathrm{Da}_2 = 1$.

solutions tend to different limits as $\epsilon^2\mathrm{Re} \to 0$. This is because in the boundary layer near $z = 0$ when $\mathrm{Da}_2 \ll \epsilon^2\mathrm{Re}$, some SiO will be converted to CO by reaction 1 before it can be removed by reaction 2, implying Q_{CO} is no longer constant in this region.

Figures 4.9b and 4.9d show that increasing Da_2 increases the size of the range of $\epsilon^2\mathrm{Re}$ where multiple steady solutions exist, and, when Da_1 is non-zero, increases the total mass flux of gas from the crater in the low-flux solution as $\epsilon^2\mathrm{Re} \to 0$. In contrast, Figure 4.9c shows that increasing Da_1 when $\mathrm{Da}_2 \neq 0$ reduces the range of $\epsilon^2\mathrm{Re}$ where multiple steady solutions exist, and decreases the total mass flux of gas from the crater in the low-flux solution as $\epsilon^2\mathrm{Re} \to 0$. This is because a higher rate of reaction 1 increases the amount of CO gas that must be forced through the entire length of the channel.

Just as for the single-phase and the coupled model we find that the pressure can become non-monotonic with its extremal values outside of the interval $[-1,\ 0]$. Except when $\mathrm{Da}_2 = 10$, this behaviour is very similar to that of case II from Chapter 3, with the low-flux solution monotonic and the middle-flux solution non-monotonic, with the minimum pressure less than the surface pressure. However, the behaviour of the transition from a monotonic to a non-monotonic pressure is more complicated. For case II, we found that the transition always occurred on the low-flux solution branch, before the maximum value of $\epsilon^2\mathrm{Re}$. For the coupled model, we can see from

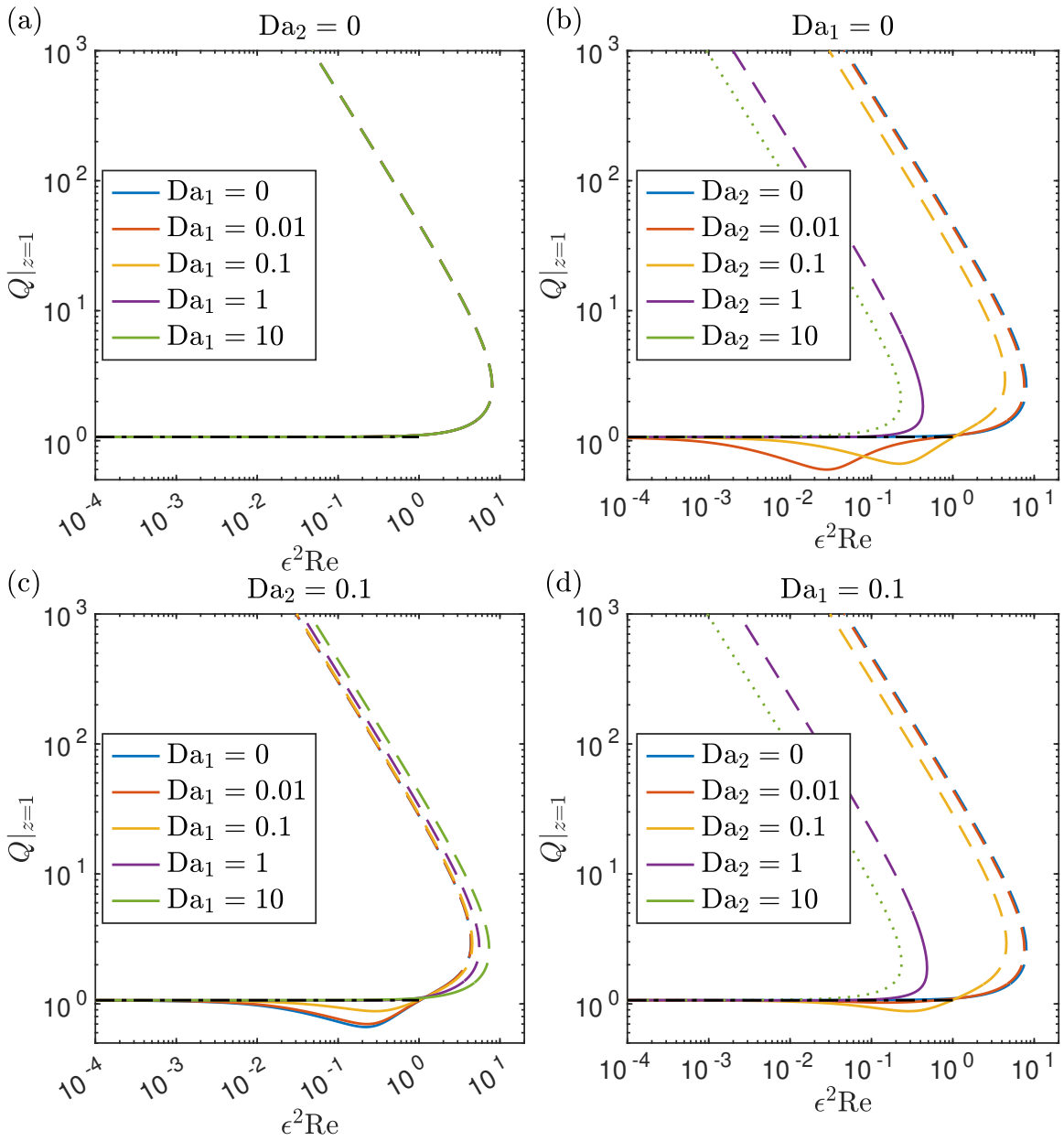


Figure 4.11: The gas mass flux at the surface $Q\big|_{z=1}$ as a function of the reduced Reynolds number for different Damköhler numbers Da_1 and Da_2, obtained by solving the binary gas mixture problem (4.16)–(4.17) with an imposed linear solid temperature with $T_{\mathrm{surf}} = 0.25$. A solution where the pressure profile is non-monotonic such that the minimum pressure is less than the pressure at the surface is shown by a dashed line, while a solution such that the maximal pressure is greater than the pressure in the crater is shown by a dotted line. In each panel the asymptotic solution when $\epsilon^2\mathrm{Re} \ll 1$, and no reactions occur, given by (3.27f) is shown by dot-dash black lines.

Figure 4.9, that varying Da_1 seems to have very little effect on the transition, with it always occurring at the same value of Q_{crat} for a given value of Da_2. However, increasing Da_2 while Da_1 remains fixed increases the value of Q_{crat} at which the transition to a non-monotonic solution occurs. This means that for small values of Da_2 the solution behaves like case II with the transition happening on the low-flux solution branch, but for larger values it happens instead on the middle-flux solution branch. If our hypothesis from Chapter 3, that non-monotonic pressure solutions correspond to unstable solutions, is correct, then the results in Figure 4.9b and d suggest that there is a range of $\epsilon^2\mathrm{Re}$ when $\mathrm{Da}_2 = 1$ with two stable steady solutions. When $\mathrm{Da}_2 = 10$, the behaviour on both solution branches changes completely, with the pressure non-monotonic, but with the maximum pressure exceeding the crater pressure. Therefore, if the hypothesis that non-monotonic pressure implies instability is correct, we have found that at higher Damköhler numbers no steady solution exists for any reduced Reynolds number.

While the total mass flux of gas is the primary quantity of mathematical interest, being the shooting parameter for the numerical problem, in practice it is the total mass flux of gas through the surface of the charge, $Q_{\mathrm{surf}} = Q\big|_{z=1}$, which can be observed by furnace operators. Therefore, in Figure 4.11 we plot Q_{surf}, for the same set of parameter values as in Figure 4.9. These results show that for all values of Da_1 and Da_2, the mass flux at the surface tends to the same limit as $\epsilon^2\mathrm{Re} \to 0$ along the low flux solution branch, and this limit is equal to the predicted value when no reactions occur by (3.27f), shown in the figure by a black dot-dash line. Further, when $\epsilon^2\mathrm{Re} \ll 1$, Q_{surf}, always remains below the predicted asymptotic limit. Physically, this can be interpreted as saying that mass flux of gas that can be driven down the channel by the imposed pressure drop without reactions is the maximum possible value, and any gas driven partway along the channel then removed reduces the amount of gas at the exit. Indeed, by comparing Figures 4.9b,c and 4.11b,c we can see that the reaction rates with the greatest value of Q_{crat}, have the lowest value of Q_{surf}, as some of the work done by pressure is used to push the reacted gases partway along the channel, leaving less to drive the gas that passes the entire length. However, this behaviour is under the assumption that the solid temperature is fixed, so may not hold for the coupled problem where varying the reaction rate will also alter the solid temperature profile.

We can also use our results to investigate the dynamics of the proportion of the SiO lost from the furnace, $\mathcal{L}$ defined in (4.20). In Figure 4.12, we plot $\mathcal{L}$ as a function of $\epsilon^2\mathrm{Re}$, for the same set of parameter values as in Figure 4.9. We can see from these

results that along the low-flux solution branch $\mathcal{L} \to 0$ as the solution goes towards the previously discussed solutions where the SiO is all consumed near $z = 0$. Increasing either Damköhler number increases the rate of increase of $\mathcal{L}$ with $\epsilon^2\mathrm{Re}$ on the low-flux solution branch. Hence, if the reaction rate is higher, then small fluctuations in $\epsilon^2\mathrm{Re}$ in industrial furnaces would cause a greater change in the amount of silicon recovered.

Along the middle-flux solution branch, $\mathcal{L}$ tends rapidly to a constant value as $\epsilon^2\mathrm{Re}$ decreases. When Da_2 is small this constant is close to one, but it decreases significantly as Da_2 increases. In contrast, Da_1 has only a small effect on the middle-flux solution, with $\mathcal{L}$ remaining close to one even when $\mathrm{Da}_1 = 10$.

4.5 Discussion

In Section 4.1, we derived a reduced model for the coupled behaviour of the gases and solids in a silicon furnace in the limit where the reduced Reynolds number is of order unity. This limit was chosen out of the possible industrially-relevant values, as it allows the gas temperature to be significantly higher than the solid temperatures, which is believed to occur in industrial furnaces.

In Section 4.2, under the simplifying assumption that ratio of molar masses $\mathcal{M} = 1$, we were able to extend the numerical method from Chapter 3 to solve the coupled problem as a shooting problem for two parameters Q_{crat} and q_{crat} representing the total mass flux of gas out of the crater and the conductive heat flux from the crater into the solid respectively. However, we found that there is a large set of values of Q_{crat} and q_{crat} for which our model breaks down as the solid temperature became negative. Since the industrially-relevant solutions often lay close to this region, it proved a significant challenge to converge to solutions to the coupled model in the industrially-relevant parameter regimes with reactions. Specifically, we could not find a solution with: a reduced Reynolds number of order unity to allow the gas and solid temperatures to differ; a realisticly low value of the surface temperature; and non-zero Damköhler numbers, so that exothermic reactions could contribute to the heating. Therefore, after demonstrating our model could converge to a solution of the coupled model with reactions when the surface temperature was unfeasibly large, we focused on the behaviour of the model under simplifying assumptions.

In Section 4.3, we considered the behaviour of the coupled model without reactions. By performing sweeps as the reduced Reynolds number varied for different surface temperatures, we found that the coupled model has two solutions below a

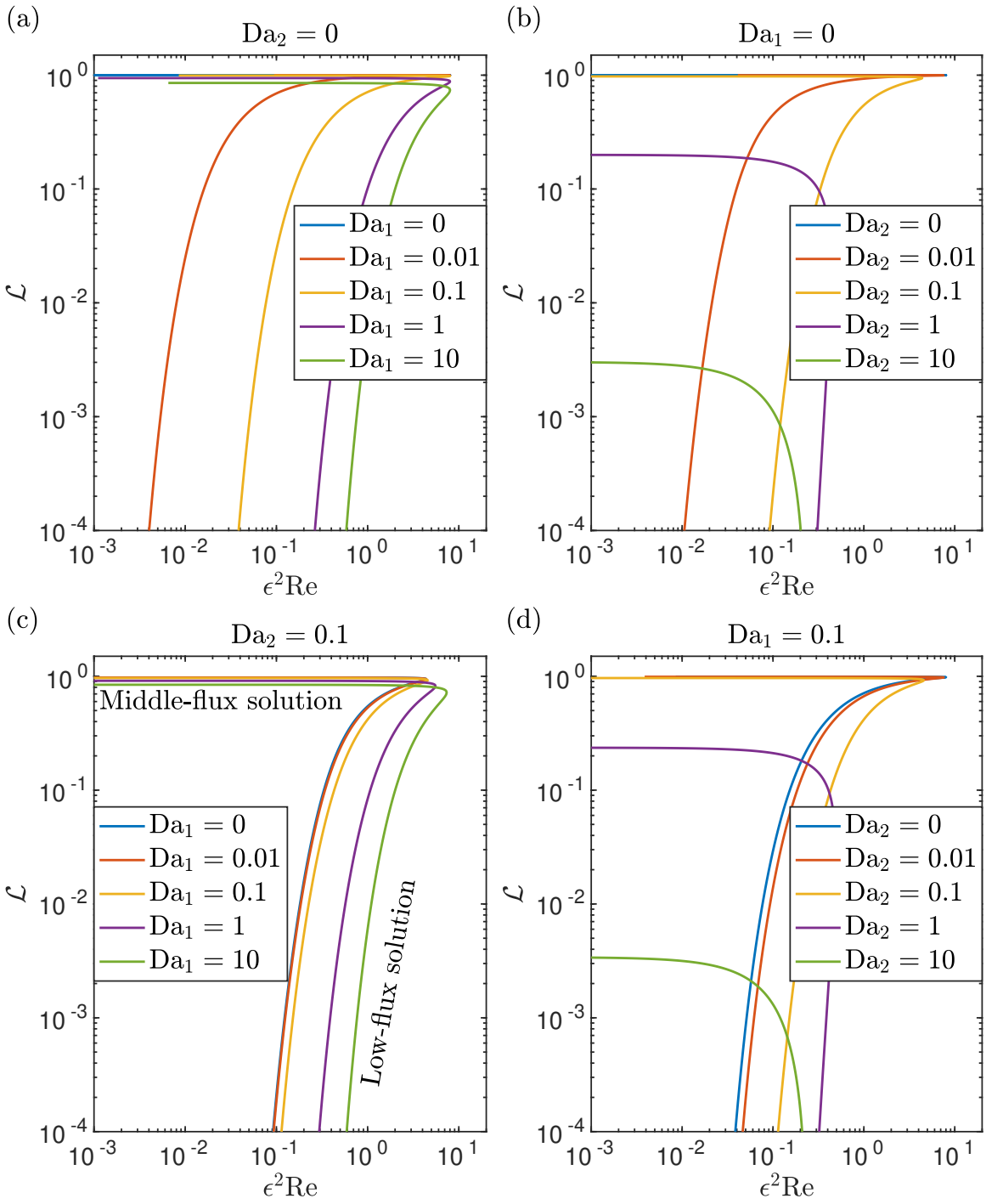


Figure 4.12: The proportion of SiO gas escaping the furnace $\mathcal{L}$, defined in (4.20) as a function of the reduced Reynolds number, for different Damköhler numbers Da_1 and Da_2, obtained by solving the binary gas mixture problem (4.16)–(4.17) with an imposed solid temperature with $T_{\mathrm{surf}} = 0.25$.

critical reduced Reynolds number, and none above, the same as the equivalent single-phase gas only model, case II, from Chapter 3. We found that when the surface temperature $T_{\text{surf}} = 0.25$ or 0.5, the majority of solid heating always occurred in a narrow region near the crater. However, when $T_{\text{surf}} = 0.75$ the increase in solid temperature can occur over the entire domain, or in a narrow region near the solid surface. As for the single-phase model in Chapter 3, we found that the solutions to the model could have non-monotonic pressure profiles, and now observe maximum pressures above the crater pressure, in addition to minimum pressures below the surface pressure. Using the coupled model, we investigated the relationship between the size of the heat transfer between the gas and solid and the difference in average temperature between them. For the small set of solutions considered, we found that a common hypothesis from the porous medium literature, namely that the heat exchange is linearly proportional to the temperature difference between the gas and solid, only held true when $\epsilon^2 \text{Re} \leq 1$. At greater reduced Reynolds numbers we found that the heat transfer could change while the temperature difference remained constant. Moreover, we found that for all reduced Reynolds numbers, there was a narrow region near the crater where the relationship was described by a power law with an index of approximately 2/3.

In Section 4.4 we studied the model when the solid temperature was prescribed, allowing us to study the effect of reactions on the gas flow. We found that reaction 2, which removes gas from the channel by condensation of SiO, could alter the relationship between the reduced Reynolds number and the total mass flux of gas, in particular reducing the maximum reduced Reynolds number for a solution exists as the reaction rates increased. We found that reaction 1, which swaps SiO molecules for CO molecules, had no effect on the gas flow unless it occurred together with reaction 2, where it affected the relationship by inhibiting reaction 2. However, this behaviour in reaction 1 is due to the assumption that the molar weights of C and SiO are equal; if this assumption was removed then reaction 1 would cause a small loss of mass from the gas, and so we would expect it to behave more like reaction 2.

While we have been unable to solve the full coupled model in an industrially-relevant regime in this chapter, the results we have found can give us an indication of the expected behaviour. When solving the coupled model without reactions in Section 4.3.2, we found that the maximum reduced Reynolds number for which a solution exists is of size $O(1)$, for exampling equalling two when $T_{\text{surf}} = 0.25$. Moreover, the results from Section 4.4 with a prescribed solid temperature, show that reaction rates decreased the maximum value of $\epsilon^2 \text{Re}$ for which a solution existed compared to the

no reactions value. Hence, we could conjecture that steady solutions to the coupled model in the industrially-relevant parameter regime with reactions may only exist for reduced Reynolds numbers less than two, i.e. they must be small. This suggests our inability to find solutions with the behaviour we were expecting may have been due to them not existing, rather than the deficiencies of our numerical solver. This motivates us to relax our requirement that the gas and solid temperatures should differ, and consider, in Chapter 5, an asymptotic solution of the coupled model when $\epsilon^2 \mathrm{Re} \ll 1$. This will provide a simpler model for the behaviour on the low-flux solution branch, allowing the coupling between the gases, solid, and reactions to be more easily studied, and the parameters swept over to find regimes where the predictions of our model qualitatively match observations of industrial furnaces.

Chapter 5

Counter-current flow of gases and solids in the small reduced Reynolds number limit

In this chapter, we study the model of the coupled behaviour between the gases and solid in a silicon furnace, developed in Chapter 2, in the limit of small reduced Reynolds number. Our motivation for considering this limit comes from the results in Chapter 4 which suggested that, with industrially-relevant parameter values and reactions included, we can expect steady solutions to the coupled model to only exist when $\epsilon^2 \mathrm{Re} < 1$. This means we can capture the behaviour of all the industrially-relevant solutions using a simpler model, allowing us to more easily explore the effect of variation of different parameters in the model.

The remainder of the chapter is structured as follows. In Section 5.1, we discuss the simplifications to the model used throughout this chapter and the assumed industrially-relevant parameter sizes. In Section 5.2, we consider the behaviour of the model for an arbitrary set of reactions with small Damköhler numbers using asymptotic analysis. In Section 5.3, we consider the behaviour of the model for a single reaction with an order unity Damköhler number and a strongly temperature-dependent reaction rate using the method of matched asymptotics.

5.1 Assumptions

In this chapter, unlike Chapters 3 and 4, we will work in the original three-dimensional geometry depicted in Figure 2.1. This will make it easier to relate the results of our model directly to silicon furnaces. Therefore, throughout this chapter, we will work in the cylindrical coordinate system defined by (2.59) and write u, v and w for the

radial, angular, and axial velocities, respectively. The analysis of this limit in the two-dimensional Cartesian geometries used in Chapters 3 and 4 follows the same structure, but results in slightly different algebraic expressions.

For simplicity, we will assume that the solid density is constant, i.e. $\rho_{\mathrm{s}} = 1$. This allows us to immediately solve the conservation of mass equation for the solid, (2.74a), and determine that

$$w_{\mathrm{s}} = -1, \tag{5.1}$$

i.e. the solid is moving downwards at a constant speed. This reduces the problem in Ω_{s} to a single equation for the temperature. We also assume that the viscosity, binary diffusion coefficient, and the thermal conductivity in both the gas mixture and solid are constant with temperature, i.e. $\mu = k = \mathcal{D} = k_{\mathrm{s}} = 1$.

To be consistent with Chapter 4, we assume that the ratio of molar masses $\mathcal{M} = 1$. However, the analysis in this chapter could be repeated relatively easily with this assumption removed, and only leads to a slightly more complicated model.

As previously mentioned, in this chapter we wish to consider the limit where $\epsilon^2\mathrm{Re} \ll 1$. When we considered this limit in Chapter 3, we assumed only that $\epsilon^2 \ll \epsilon^2\mathrm{Re} \ll 1$, where ϵ is the aspect ratio of the channel, based on the value of the industrially-relevant Reynolds number in Table 2.3. However, in this chapter, constructing the asymptotic solution will require us to consider higher-order behaviour in both the governing equations for: the gas (2.68), where the largest small parameter is $\epsilon^2\mathrm{Re}$, which controls the size of axial advective transport; and the energy equation for the solid, (2.74b), where the largest small parameter is of size $\epsilon^2\mathrm{Pe}_{\mathrm{s}}$, again controlling the size of axial advection. As in Chapter 4, we will make the assumption that $\mathrm{Pe}_{\mathrm{s}} = O(1)$, implying that axial advection and conduction will balance in the solid: this will enable us to avoid considering boundary layers near $z = 0$ or $z = 1$ in order to satisfy the temperature boundary conditions, (2.76b) and (2.77b) respectively. As previously mentioned, the industrially-relevant large value of Re in Table 2.3 precludes a balance between $\epsilon^2\mathrm{Re}$ and ϵ^2, and the relevant physical processes are instead determined by the relationship between $(\epsilon^2\mathrm{Re})^2$ and ϵ^2. To obtain the richest behaviour, we focus on the distinguished limit where these two terms balance, and hence take

$$\frac{1}{\mathrm{Re}} = \Gamma\epsilon \quad \text{where } \Gamma = O(1), \tag{5.2}$$

implying that the reduced Reynolds number may be rewritten as $\epsilon^2\mathrm{Re} = \epsilon/\Gamma$. The other possible balances in the problem can be investigated by taking the large and small Γ limits of the resulting solution. Similarly, we can explore the effect of true

value of the Péclet number, by sending $\mathrm{Pe_s} \to \infty$ in the resulting solutions. Based on Table 2.3, we will take $\Gamma = 0.025$ as representative of the industrially-relevant parameter values throughout this chapter.

We must also consider the relative sizes of the ratio of the gas and solids thermal conductivities, Λ, and ϵ. As in Chapter 4, our starting point for this is to rewrite the definition of the Péclet number as (4.2), into which we substitute (5.2) and rearrange, to obtain that

$$\Lambda = C_\Lambda \epsilon, \qquad \text{where } C_\Lambda = \frac{\mathrm{Pe_s}\Gamma}{\mathrm{Pr}} \frac{[w_\mathrm{g}][\rho_\mathrm{g}][c_{p,\mathrm{CO}}]}{[w_\mathrm{s}][\rho_\mathrm{s}][c_{p,\mathrm{s}}]} = O(1). \tag{5.3}$$

For comparison, in Chapter 4 we found that $\Lambda = O(\epsilon^2)$. The change in order of Λ is caused by moving from assuming $1/\mathrm{Re} = O(\epsilon^2)$ in Chapter 4, to assuming $1/\mathrm{Re} = O(\epsilon)$ in this chapter. Using the parameter values in Table 2.3, we find $\Lambda = 10$ as a representative industrially-relevant value. This suggests the assumption on the size of Λ in this chapter, 5.3, is better supported by the industrially-relevant parameter values than the assumed size in Chapter 4, given in (4.3).The value of C_Λ still remains order unity, even if you let $\mathrm{Pe_s} = 1$ in its definition.

The other parameters in the model, with the exception of the Damköhler numbers, Da_1 and Da_2, which we discuss below, are assumed to have the same sizes as given for the coupled model from Chapter 4, which were given in (4.1) and (4.4). Hence, the assumptions we take throughout this chapter may be summarised as

$$\alpha \ll \epsilon \sim \Lambda \sim \frac{1}{\mathrm{Re}} \ll \Delta p \tag{5.4a}$$

and

$$\mathrm{Pr},\ \mathrm{Sc},\ \mathrm{Pe_s},\ \gamma,\ \eta_1,\ \eta_2 = O(1). \tag{5.4b}$$

In the remainder of this chapter, we will consider two cases for the size of the Damköhler numbers. In Section 5.2, we will consider the case $\mathrm{Da}_i = O(\epsilon)$, which we will see allows the reaction to occur throughout the length of the channel. We therefore refer to this as the slow reaction case. In Section 5.3, we will consider the case the $\mathrm{Da}_i = O(1)$ for a single reaction, assumed to have a strongly temperature-dependent reaction rate. We will refer to this as the fast reaction case.

5.2 Slow reactions model

In this section, we will assume that

$$\mathrm{Da}_i = C_{\mathrm{Da},i}\epsilon \quad \text{where } C_{\mathrm{Da},i} = O(1), \tag{5.5}$$

for all reactions i. We will see later that this is the limit where reactions will occur along the entire length of the channel. We derive the leading-order model for an arbitrary set of reactions $\mathcal{R}_i$, then consider its solution using the form of $\mathcal{R}_i$ given in (2.81)–(2.82) to model reactions 1 and 2 in (1.2).

5.2.1 Reduction to a one-dimensional model

We seek an asymptotic solution to the governing equations for the gas, given in cylindrical coordinates in (B.1), the governing equation for conservation of energy in the solid (2.74b), and the boundary conditions (2.76)–(2.80), of the form

$$T \sim T^{(0)} + \epsilon T^{(1)} + \epsilon^2 T^2 + o\left(\epsilon^2\right), \tag{5.6}$$

and similarly for the other variables. Substituting the asymptotic series (5.6) into the governing equation for the solid, (2.74), then equating coefficients of ϵ, we find the $O(1)$ problem in Ω_s to be given by

$$\frac{1}{r}\frac{\partial}{\partial r}\left(r\frac{\partial T^{(0)}}{\partial r}\right) + \frac{1}{r^2}\frac{\partial^2 T^{(0)}}{\partial \theta^2} = 0 \text{ in } \Omega_\mathrm{s}, \tag{5.7}$$

with the relevant boundary conditions from (2.76)–(2.80) becoming

$$T^{(0)} = 1 \quad \text{on } \partial\Omega_{\mathrm{crat,g}}, \tag{5.8a}$$

$$\boldsymbol{\nabla} T^{(0)} \cdot \boldsymbol{n}_\mathrm{s} = 0 \quad \text{on } \partial\Omega_{\mathrm{Inter}}, \tag{5.8b}$$

$$T^{(0)} \text{ periodic} \quad \text{on } \partial\Omega, \tag{5.8c}$$

$$T^{(0)} = T_\mathrm{surf} \quad \text{on } \partial\Omega_{\mathrm{surf,g}}. \tag{5.8d}$$

Note that by multiplying (5.7) by $T^{(0)}$, then using Green's identity and the boundary conditions (5.8b)–(5.8c), including the requirement the solution be smooth over $\partial\Omega$, we obtain that

$$\int_{\mathcal{C}_\mathrm{s}} \|\boldsymbol{\nabla}_\perp T^{(0)}\|_2^2 \,\mathrm{d}A = 0, \tag{5.9}$$

where $\boldsymbol{\nabla}_\perp$ is the gradient operator in the plane normal to the z-axis. Since the integrand is non-negative, we conclude that $\boldsymbol{\nabla}_\perp T^{(0)} = 0$ in Ω_s, implying

$$T^{(0)}(r,\theta,z,t) = T^{(0)}(z,t) \quad \text{ in } \Omega_\mathrm{s}. \tag{5.10}$$

Thus, at leading-order, the temperature in Ω_s is independent of r and θ. By the continuity of temperature condition on the gas-solid interface, (2.78e), it follows that $T^{(0)}$ is independent of θ on $\partial\Omega_{\mathrm{Inter}}$. This means that, at leading-order, all the boundary

conditions and governing equations for the gas are rotationally symmetric. Hence, we conclude the solution inside the gas channel Ω_{g} must be independent of θ, i.e. the leading-order solution is axisymmetric. Thus, after substituting the asymptotic series (5.6) into the governing equations for the gas in polar coordianates (B.1) and grouping powers of ϵ, we can use axisymmetry to simplify the leading-order problem in Ω_{g} to

$$\frac{1}{r}\frac{\partial}{\partial r}\left(r\rho^{(0)}u^{(0)}\right)+\frac{\partial}{\partial z}\left(\rho^{(0)}w^{(0)}\right)=0, \tag{5.11a}$$

$$0=\frac{\partial p^{(0)}}{\partial r}, \tag{5.11b}$$

$$\frac{\partial p^{(0)}}{\partial z}=\frac{1}{r}\frac{\partial}{\partial r}\left(r\frac{\partial w^{(0)}}{\partial r}\right), \tag{5.11c}$$

$$0=\frac{1}{r}\frac{\partial}{\partial r}\left(r\frac{\partial T^{(0)}}{\partial r}\right), \tag{5.11d}$$

$$0=\frac{1}{r}\frac{\partial}{\partial r}\left(r\rho^{(0)}\frac{\partial Y^{(0)}}{\partial r}\right), \tag{5.11e}$$

$$\rho^{(0)}T^{(0)}=1, \tag{5.11f}$$

where $\rho^{(0)},u^{(0)},w^{(0)},p^{(0)},Y^{(0)},T^{(0)}$, are functions of r, z, and t. Substituting the asymptotic series (5.6) into the boundary conditions (2.76)–(2.78), we find the appropriate subset to impose on (5.11) is given by

$$u^{(0)}=0,\quad r\frac{\partial w^{(0)}}{\partial r}\to 0,\quad r\frac{\partial T^{(0)}}{\partial r}\to 0,\quad r\frac{\partial Y^{(0)}}{\partial r}\to 0\quad \text{as } r\to 0, \tag{5.12a}$$

$$Y=Y_{\mathrm{crat}},\quad p^{(0)}=0\quad \text{at } z=0, \tag{5.12b}$$

$$\left.\begin{aligned}\rho^{(0)}\frac{\partial Y^{(0)}}{\partial r}=0,\quad w^{(0)}=0,\quad T^{(0)}\big|_{r=1-}=T^{(0)}\big|_{r=1+},\\ \frac{1}{\Gamma}\rho^{(0)}u^{(0)}=-\sum_i\frac{C_{\mathrm{Da},i}}{\mathrm{Sc}}\left(\nu_{i,\mathrm{SiO}}+\nu_{i,\mathrm{CO}}\right)\mathcal{R}_i^{(0)}\end{aligned}\right\}\ \text{at } r=1, \tag{5.12c}$$

$$p^{(0)}=-1,\quad \text{at } z=1. \tag{5.12d}$$

For identical reasons to those discussed in Section 3.2.4 for the $\epsilon^2\mathrm{Re}\ll 1$ limit of the single-phase model, we have neglected some boundary conditions present at $z=0$ and $z=1$ in the full problem, (2.77a) and (2.76a) respectively. The conditions given by (5.12a) are also included to ensure the solution remains bounded as $r\to 0$. Here $\mathcal{R}_i^{(0)}$ is the leading-order reaction rate, obtained by substituting (5.6) into the definition of $\mathcal{R}_i$, and expanding via $\mathcal{R}_i=\mathcal{R}_i^{(0)}+\epsilon\mathcal{R}_i^{(1)}+\cdots$. For the model of reactions 1 and 2 in (1.2), given in (2.81)–(2.82), the leading-order reaction rates are given by

$$\mathcal{R}_i^{(0)}=\rho^{(0)}Y^{(0)}F_i^{(0)}\left(T^{(0)}\right), \tag{5.13a}$$

for $i = 1, 2$, where

$$F_1^{(0)}\left(T^{(0)}\right) = 1, \qquad F_2^{(0)}\left(T^{(0)}\right) = \frac{1}{1 + \exp\left(\dfrac{T^{(0)} - T_{\text{cond}}}{\xi}\right)}. \tag{5.13b}$$

Integrating (5.11d) twice with respect to r, and applying the boundary conditions (5.12a), (5.12c) gives that

$$T^{(0)} = T^{(0)}(z, t) \quad \text{in } \Omega_{\text{g}}, \tag{5.14}$$

and moreover, $T^{(0)}$ in Ω_{g} is equal to $T^{(0)}$ in Ω_{s}. Hence, at leading-order the gas and solid are in local thermal equilibrium. Similarly, we can use (5.11e), (5.12a), (5.12c) to show that

$$Y^{(0)} = Y^{(0)}(z, t) \quad \text{in } \Omega_{\text{g}}. \tag{5.15}$$

From (5.11f), it follows that $\rho^{(0)} = 1/T^{(0)}$, and so density is also a function only of z and t.

We can integrate the conservation of mass equation (5.11a) across the cross-section of Ω_{g}, i.e. $\mathcal{C}_{\text{g}}$, and apply the boundary conditions (5.12a) and (5.12c) to obtain an equation for the leading-order mass flux $Q^{(0)}(z, t)$,

$$\frac{\partial Q^{(0)}}{\partial z} = \sum_i \frac{2\pi C_{\text{Da},i}\Gamma\left(\nu_{i,\text{SiO}} + \nu_{i,\text{CO}}\right)}{\text{Sc}} \mathcal{R}_i^{(0)}, \tag{5.16}$$

where $Q^{(0)}$ is defined by substituting the asymptotic series (5.6) into the definition of Q, (2.83), and expanding $Q_i = Q_i^{(0)} + \epsilon Q_i^{(1)} + \cdots$ so that

$$Q^{(0)} = \int_{\mathcal{C}_{\text{g}}} \rho^{(0)} w^{(0)} \, \mathrm{d}A. \tag{5.17}$$

Using the conservation of mass and momentum equations, (5.11a)–(5.11c), it is straightforward to find that the velocities are given by,

$$u^{(0)} = \frac{1}{2\pi} T^{(0)} \frac{\partial Q^{(0)}}{\partial z} \left(r^3 - 2r\right), \tag{5.18}$$

$$w^{(0)} = \frac{2}{\pi} Q^{(0)} T^{(0)} \left(1 - r^2\right), \tag{5.19}$$

and the pressure is related to the total mass flux of gas according to

$$\frac{\partial p^{(0)}}{\partial z} = -\frac{8}{\pi} Q^{(0)} T^{(0)}. \tag{5.20}$$

Since we have no equations remaining to determine $Y^{(0)}$ and $T^{(0)}$, the problem is not yet closed, and we proceed to next order.

The $O(\epsilon)$ problem in Ω_s is given by

$$\frac{1}{r}\frac{\partial}{\partial r}\left(r\frac{\partial T^{(1)}}{\partial r}\right)+\frac{1}{r^2}\frac{\partial^2 T^{(1)}}{\partial \theta^2}=0 \text{ in } \Omega_\mathrm{s}, \tag{5.21}$$

with boundary conditions

$$\boldsymbol{\nabla} T^{(1)}\cdot\boldsymbol{n}_\mathrm{s}=-C_\Lambda\left.\frac{\partial T^{(0)}}{\partial r}\right|_{r=1-}=0 \quad \text{on } \partial\Omega_\mathrm{Inter}, \tag{5.22a}$$

$$T^{(1)} \text{ periodic} \quad \text{on } \partial\Omega, \tag{5.22b}$$

The second equality in (5.22a) follows from $T^{(0)}$ being independent of r in Ω_g. Hence, (5.21)–(5.22) is identical to the leading-order problem in the solid, (5.7)–(5.8), so by an identical argument, we can conclude that $T^{(1)}=T^{(1)}(z,t)$ in Ω_s, implying the $O(\epsilon)$ solution in Ω_g must be axisymmetric.

To close the leading-order problem, it is sufficient to only consider conservation of energy and conservation of SiO equations, (B.1e) and (B.1f), respectively, at $O(\epsilon)$. Using the axisymmetry, they are given by

$$\frac{1}{\Gamma}\left(\frac{1}{r}\frac{\partial}{\partial r}\left(ru^{(0)}\right)+\frac{\partial}{\partial z}\left(w^{(0)}\right)\right)=\frac{1}{\mathrm{Pr}}\frac{1}{r}\frac{\partial}{\partial r}\left(r\frac{\partial T^{(1)}}{\partial r}\right), \tag{5.23a}$$

$$\frac{1}{\Gamma}\left(\frac{1}{r}\frac{\partial}{\partial r}\left(r\rho^{(0)}Y^{(0)}u^{(0)}\right)+\frac{\partial}{\partial z}\left(\rho^{(0)}Y^{(0)}w^{(0)}\right)\right)=\frac{1}{\mathrm{Sc}}\frac{1}{r}\frac{\partial}{\partial r}\left(r\rho^{(0)}\frac{\partial Y^{(1)}}{\partial r}\right). \tag{5.23b}$$

The subset of the boundary conditions (5.8b)–(2.78), we require for these equations are

$$r\frac{\partial T^{(1)}}{\partial r}\to 0, \quad , r\frac{\partial Y^{(1)}}{\partial r}\to 0 \quad \text{as } r\to 0, \tag{5.24a}$$

$$\left.\begin{aligned} T^{(1)}\big|_{r=1-}&=T^{(1)}\big|_{r=1+},\\ \frac{1}{\Gamma}\rho^{(0)}Y^{(0)}u^{(0)}-\frac{1}{\mathrm{Sc}}\rho^{(0)}\frac{\partial Y^{(1)}}{\partial r}&=-\sum_i\frac{C_{\mathrm{Da},i}\nu_{i,\mathrm{SiO}}}{\mathrm{Sc}}\mathcal{R}_i^{(0)}\end{aligned}\right\} \quad \text{at } r=1. \tag{5.24b}$$

By substituting (5.18)–(5.19) into (5.23b), integrating twice with respect to r, and using (5.24), we obtain that the $O(\epsilon)$ gas temperature is given by

$$T^{(1)}=\frac{\mathrm{Pr}}{8\pi\Gamma}Q^{(0)}\frac{\partial T^{(0)}}{\partial z}\left(4r^2-r^4-3\right)+T^{(1)}\big|_{r=1+}(z,t), \tag{5.25}$$

in Ω_g. The solution for $T^{(1)}$ has a contribution from the $O(\epsilon)$ temperature in the solid, and so cannot be fully determined till the next order of the expansion. However, it is unnecessary to know $T^{(1)}\big|_{r=1+}$ in order to evaluate the r derivative of $T^{(1)}$ in Ω_g, and so evaluate the heat flux into the solid at $O(\epsilon^2)$ (see (5.30a) below).

By integrating (5.23a) over $\mathcal{C}_\mathrm{g}$, and using (5.24), we obtain an equation for the evolution of the leading-order mass flux of SiO,

$$\frac{\partial Q^{(0)}_{\mathrm{SiO}}}{\partial z} = \sum_i \frac{2\pi\Gamma C_{\mathrm{Da},i}\nu_{i,\mathrm{SiO}}}{\mathrm{Sc}}\mathcal{R}^{(0)}_i, \tag{5.26}$$

where $Q^{(0)}_{\mathrm{SiO}}$ is defined by substituting the asymptotic series (5.6) into the definition of Q_{SiO}, (2.84), and expanding $Q_{\mathrm{SiO}} = Q^{(0)}_{\mathrm{SiO}} + \epsilon Q^{(1)}_{\mathrm{SiO}} + \cdots$ so that

$$Q^{(0)}_{\mathrm{SiO}} = \int_{\mathcal{C}_\mathrm{g}} \rho^{(0)} w^{(0)} Y^{(0)} \,\mathrm{d}A. \tag{5.27}$$

Note, as $Y^{(0)}$ is independent of r, we have the following relationship

$$Q^{(0)}_{\mathrm{SiO}} = Q^{(0)} Y^{(0)}, \tag{5.28}$$

allowing us to eliminate $Y^{(0)}$ from the problem.

As we still do not have an equation to determine $T^{(0)}$, we proceed to the $O(\epsilon^2)$ problem in Ω_s, given by

$$\mathrm{Pe_s}\left(\frac{\partial T^{(0)}}{\partial t} - \frac{\partial T^{(0)}}{\partial z}\right) = \frac{1}{r}\frac{\partial}{\partial r}\left(r\frac{\partial T^{(2)}}{\partial r}\right) + \frac{1}{r^2}\frac{\partial^2 T^{(2)}}{\partial \theta^2} + \frac{\partial^2 T^{(0)}}{\partial z^2}, \tag{5.29}$$

with boundary conditions

$$\begin{aligned}\boldsymbol{\nabla} T^{(2)} \cdot \boldsymbol{n}_\mathrm{s} &= -C_\Lambda \left(\left(-\frac{\mathrm{Pr}}{\Gamma}\rho^{(0)} u^{(0)} T^{(0)} + \frac{\partial T^{(1)}}{\partial r}\right)\bigg|_{r=1-} - \sum_i \frac{C_{\mathrm{Da},i}\eta_i \mathrm{Pr}}{\mathrm{Sc}}\mathcal{R}^{(0)}_i \right) \\ &= -C_\Lambda \left(\frac{\mathrm{Pr}}{2\pi\Gamma}\frac{\partial}{\partial z}\left(Q^{(0)}T^{(0)}\right) - \sum_i \frac{C_{\mathrm{Da},i}\eta_i \mathrm{Pr}}{\mathrm{Sc}}\mathcal{R}^{(0)}_i \right), \end{aligned} \tag{5.30a}$$

on $\partial\Omega_{\mathrm{Inter}}$, and

$$T^{(2)} \quad \text{periodic} \tag{5.30b}$$

on $\partial\Omega$. In (5.30a), the second equality comes from substituting in (5.11f), (5.18), and (5.25), then using the chain rule to combine the first two terms.

By integrating (5.29) over $\mathcal{C}_\mathrm{s}$, the cross-section of Ω_s in the xy-plane, then applying the divergence theorem and using (5.30), we can eliminate $T^{(2)}$, and obtain,

$$\mathrm{Pe_s}\left(\frac{\partial T^{(0)}}{\partial t} + \frac{\partial}{\partial z}\left(\beta T^{(0)}\right)\right) = \frac{\partial^2 T^{(0)}}{\partial z^2} + \sum_i \frac{2\pi C_{\mathrm{Da},i} C_\Lambda \eta_i \mathrm{Pr}}{|\mathcal{C}_\mathrm{s}|\,\mathrm{Sc}}\mathcal{R}^{(0)}_i, \tag{5.31}$$

where

$$\beta = C_1 Q^{(0)} - 1, \quad \text{where } C_1 = \frac{C_\Lambda \mathrm{Pr}}{|\mathcal{C}_\mathrm{s}|\,\Gamma \mathrm{Pe_s}}. \tag{5.32}$$

Equation (5.31) allows us to solve for $T^{(0)}$, closing the leading-order problem. Physically, β represents the velocity of net advection of heat by gas and solid through the domain. If $\beta > 0$, then overall, more heat is being carried in the positive z-direction by the gas than is being carried in the negative z-direction by the solid. If $\beta < 0$, the converse is true. Since $Q^{(0)} > 0$ for the solution to be physical, we have that $\beta > -1$. Based on the industrially-relevant parameter values in Table 2.3, $C_1 \approx 0.015$. Hence, for solutions with $Q^{(0)} = O(1)$, β will always be negative implying heat is being advected downwards.

If we were to consider the large-Péclet sub-limit of the model, and so treat axial solid conduction as a small effect compared to advection, (as was done by [48]), then a boundary layer where conduction balances advection would be necessary to satisfy both the temperature boundary conditions (5.8a) and (5.8d), at $z = 0$ and $z = 1$ respectively, with the structure of those boundary layers changing depending on the sign of β. If $\beta > 0$ throughout the domain, then a boundary layer would be required near $z = 1$, but if instead $\beta < 0$ throughout the domain a boundary layer would be needed at $z = 0$. If the evolution of $Q^{(0)}$ is such that β changes sign throughout the domain, then an internal boundary layer will occur centred on the location where $\beta = 0$, with the existence of boundary layers at $z = 0$ and $z = 1$ dependent on the local sign of β.

In summary, we have reduced the problem to four ODEs (5.16), (5.20), (5.26), and (5.31) in terms of four variables $T^{(0)}$, $Q^{(0)}$, Q_{SiO}, and $p^{(0)}$ which depend only on a single space dimension, z, and time t. Up till now, we have derived the slow reactions model for an arbitrary set of chemical reactions, however, if we substitute in our model for reactions 1 and 2, (5.13a), leaving $F_i^{(0)}$ arbitrary, and group the constants, we may rewrite the problem as

$$\frac{\partial T^{(0)}}{\partial t} + \frac{\partial}{\partial z}\left(\beta T^{(0)}\right) = \frac{1}{\mathrm{Pe_s}}\frac{\partial^2 T^{(0)}}{\partial z^2} + \sum_i a_i \frac{Q_{\mathrm{SiO}}^{(0)}}{Q^{(0)}T^{(0)}} F_i\left(T^{(0)}\right), \tag{5.33a}$$

$$\frac{\partial Q^{(0)}}{\partial z} = \sum_i b_i \frac{Q_{\mathrm{SiO}}^{(0)}}{Q^{(0)}T^{(0)}} F_i\left(T^{(0)}\right), \tag{5.33b}$$

$$\frac{\partial Q_{\mathrm{SiO}}^{(0)}}{\partial z} = \sum_i c_i \frac{Q_{\mathrm{SiO}}^{(0)}}{Q^{(0)}T^{(0)}} F_i\left(T^{(0)}\right), \tag{5.33c}$$

$$\frac{\partial p^{(0)}}{\partial z} = -\frac{8}{\pi} Q^{(0)} T^{(0)}, \tag{5.33d}$$

where the constants a_i, b_i, and c_i are given by

$$a_i = 2\pi C_1 D_i \eta_i \quad b_i = 2\pi D_i\left(\nu_{i,\mathrm{SiO}} + \nu_{i,\mathrm{CO}}\right), \quad c_i = 2\pi D_i \nu_{i,\mathrm{SiO}}, \tag{5.34}$$

where

$$D_i = \frac{C_{\mathrm{Da},i}\Gamma}{\mathrm{Sc}} = \frac{\mathrm{Da}_i}{\epsilon^2 \mathrm{ReSc}}, \tag{5.35}$$

for all i. The remaining boundary conditions to impose are

$$p^{(0)} = 0, \quad T^{(0)} = 1, \quad Q^{(0)}_{\mathrm{SiO}} = Y_{\mathrm{crat}} Q^{(0)} \quad \text{at } z = 0, \tag{5.36a}$$

$$p^{(0)} = -1, \quad T^{(0)} = T_{\mathrm{surf}} \quad \text{at } z = 1, \tag{5.36b}$$

coming from (5.8a), (5.8d), (5.12b), and (5.12d). We also require an initial condition for $T^{(0)}$ to fully specify the problem.

In (5.33), (5.33a) is an advection-reaction-diffusion equation for temperature; (5.33b) is conservation of total mass for the gas; using (5.28), (5.33c) is an advection equation for mass fraction of SiO; and (5.33d) is conservation of momentum for the gas, which in Section 6.2 we show is equivalent to Darcy's law for flow in porous media. The new parameter grouping D_i expresses the ratio of the surface reaction rate to the convective mass transfer rate.

For the exothermic reactions, such as reactions 1 and 2 in (1.2), $a_i > 0$ since $\eta_i > 0$, with the converse true for exothermic reactions. For reactions where SiO is removed from the channel, again such as reactions 1 and 2, $b_i \leq 0$ and $c_i < 0$, with $b_i = 0$ if and only if the number of molecules of SiO consumed equals the number of CO molecules created.

Given a solution to (5.33), we can calculate the leading-order energy fluxes. Substituting (5.6) into (2.87)–(2.91), and expanding according to $E = E^{(0)} + \epsilon E^1 + \cdots$, we find that the leading-order energy fluxes are given by

$$E^{(0)}_{\mathrm{g,crat}} = -\int_{\mathcal{C}_{\mathrm{g}}} \left(\rho^{(0)} w^{(0)} T^{(0)}\right)\Big|_{z=0} \,\mathrm{dA} = -Q^{(0)}\Big|_{z=0}, \tag{5.37a}$$

$$E^{(0)}_{\mathrm{g,surf}} = \int_{\mathcal{C}_{\mathrm{g}}} \left(\rho^{(0)} w^{(0)} T^{(0)}\right)\Big|_{z=1} \,\mathrm{dA} = T_{\mathrm{surf}} Q^{(0)}\Big|_{z=1}, \tag{5.37b}$$

$$E_{\mathrm{s,crat,A}} = -\int_{\mathcal{C}_{\mathrm{s}}} \left(-\frac{\mathrm{Pe_s}\Gamma}{\mathrm{Pr}C_\Lambda} T^{(0)}\right)\Big|_{z=0} \mathrm{d}A = \frac{1}{C_1}, \tag{5.37c}$$

$$E_{\mathrm{s,crat,D}} = -\int_{\mathcal{C}_{\mathrm{s}}} \left(-\frac{\Gamma}{\mathrm{Pr}C_\Lambda} \frac{\partial T^{(0)}}{\partial z}\right)\Big|_{z=0} \mathrm{d}A = \frac{1}{C_1 \mathrm{Pe_s}} \left.\frac{\partial T^{(0)}}{\partial z}\right|_{z=0}, \tag{5.37d}$$

$$E_{\mathrm{s,surf,A}} = \int_{\mathcal{C}_{\mathrm{s}}} \left(-\frac{\mathrm{Pe_s}\Gamma}{\mathrm{Pr}C_\Lambda} T^{(0)}\right)\Big|_{z=1} \mathrm{d}A = -\frac{T_{\mathrm{surf}}}{C_1}, \tag{5.37e}$$

$$E_{\mathrm{s,surf,D}} = \int_{\mathcal{C}_{\mathrm{s}}} \left(-\frac{\Gamma}{\mathrm{Pr}C_\Lambda} \frac{\partial T^{(0)}}{\partial z}\right)\Big|_{z=1} \mathrm{d}A = -\frac{1}{C_1 \mathrm{Pe_s}} \left.\frac{\partial T^{(0)}}{\partial z}\right|_{z=1}, \tag{5.37f}$$

and

$$E_{\text{React}} = -\sum_i \int_{\partial\Omega_{\text{Inter}}} \frac{C_{\text{Da},i}\eta_i\Gamma}{\text{Sc}} \mathcal{R}_i^{(0)}\big|_{r=1}\,\mathrm{d}A$$
$$= -\sum_i \frac{2\pi C_{\text{Da},i}\eta_i\Gamma}{\text{Sc}} \int_0^1 \left(\frac{Q_{\text{SiO}}^{(0)}}{Q^{(0)}T^{(0)}} F_i\left(T^{(0)}\right)\right)\Bigg|_{r=1} \mathrm{d}z, \quad (5.37g)$$

where, as in (4.22) we have split the fluxes out of the solid into advective and diffusive components, as their signs may differ. This also gives a physical interpretation to C_1 as the reciprocal of the dimensionless energy flux from the solid into the crater, which we see is constant, due to our assumption that the solid density is constant.

Equations (5.37a)–(5.37b) imply that, the proportion of heat leaving the gas phase will be given by the difference in crater and surface temperature, just as it was for the two-dimensional single-phase model in Section 3.2.4.

5.2.2 No reactions solution

Before solving (5.33)–(5.36) in general, we consider the special case where $D_i = 0$ for all i, implying $a_i = b_i = c_i = 0$, and so no reactions will occur. This immediately allows us to deduce from (5.33b)–(5.33c) that

$$Q^{(0)} = Q_{\text{crat}}^{(0)}, \quad Q_{\text{SiO}}^{(0)} = Y_{\text{crat}} Q_{\text{crat}}^{(0)}, \tag{5.38}$$

where $Q_{\text{crat}}^{(0)} = Q^{(0)}\big|_{z=0}$, is the total mass flux of gas through the crater, which is an unknown constant to be determined. The problem depends only on three parameters Pe_s, T_{surf}, and C_1.

Restricting our attention to the steady behaviour of (5.33), we use that $Q^{(0)}$, and hence β are constants, meaning (5.33a) reduces to a second-order linear ODE with constant (although unknown) coefficients. Hence, it a standard calculation to solve (5.33a) using the temperature boundary conditions in (5.36) to obtain

$$T^{(0)} = 1 - (1 - T_{\text{surf}})\,\frac{1 - e^{\text{Pe}_\text{s}\beta z}}{1 - e^{\text{Pe}_\text{s}\beta}}. \tag{5.39}$$

We can substitute this expression for $T^{(0)}$ into (5.33d) and use the pressure boundary condition in (5.36a) at $z = 0$ to find the pressure, which is given by

$$p^{(0)} = -\frac{8Q_{\text{crat}}^{(0)}}{\pi}\left(\left(1 - \frac{1 - T_{\text{surf}}}{1 - e^{\text{Pe}_\text{s}\beta}}\right) z - \frac{1 - T_{\text{surf}}}{\text{Pe}_\text{s}\beta}\frac{1 - e^{\text{Pe}_\text{s}\beta z}}{1 - e^{\text{Pe}_\text{s}\beta}}\right). \tag{5.40}$$

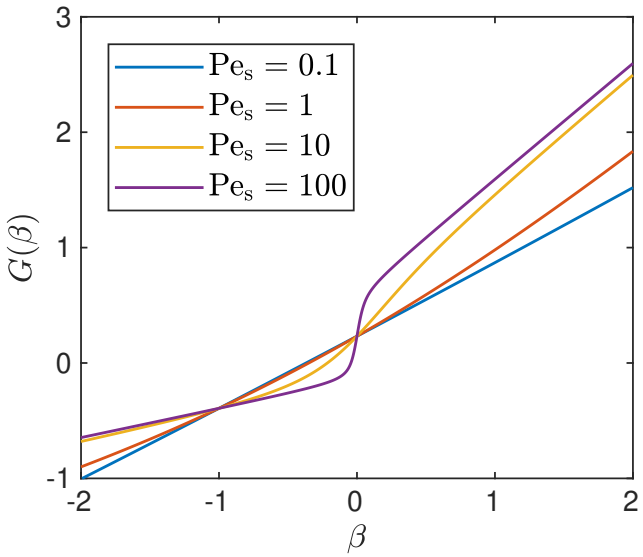


Figure 5.1: The function $G(\beta)$, defined by (5.41) when $T_{\text{surf}} = 0.25$, and $C_1 = 1$ as β varies at different values of $\mathrm{Pe_s}$.

Applying the boundary condition on pressure at $z = 1$, (5.36b), and using the definition of β, (5.32), allows us to obtain an algebraic equation for β,

$$0 = G(\beta) = (\beta + 1)\left(1 - (1 - T_{\text{surf}})\left(\frac{1}{1 - e^{\mathrm{Pe_s}\beta}} + \frac{1}{\mathrm{Pe_s}\beta}\right)\right) - \frac{\pi C_1}{8}, \tag{5.41}$$

and example profiles of $G(\beta)$ are plotted in Figure 5.1 for several values of $\mathrm{Pe_s}$. Note that G is bounded and well defined at $\beta = 0$, since

$$\begin{aligned}\lim_{\beta \to 0} G(\beta) &= (0 + 1)\left(1 - (1 - T_{\text{surf}})\left(\frac{1}{2}\right)\right) - \frac{\pi C_1}{8} \\ &= \frac{1 + T_{\text{surf}}}{2} - \frac{\pi C_1}{8}.\end{aligned} \tag{5.42}$$

Next, we observe that G is an increasing function of β, for all β. Moreover, we have that $G(\beta) \to -\infty$ as $\beta \to -\infty$, and $G(\beta) \to \infty$ as $\beta \to \infty$, so by the intermediate value theorem there must exist a root of G for all possible parameter values. Indeed, when $C_1 = 0$, $G(\beta) = 0$ implies $\beta = -1$. From (5.41) it is clear that varying the size of C_1 only translates $G(\beta)$ vertically, so it follows that for the industrially-relevant problem with $C_1 > 0$, the solution must satisfy $\beta > -1$. Therefore, for all possible physical parameter values there is a unique solution to $G(\beta) = 0$ such that $Q^{(0)} > 0$.

We solve (5.41) numerically for β using MATLAB's built-in nonlinear equation solver fzero, and so obtain $Q^{(0)}_{\text{crat}}$ by (5.32), completing the solution of the problem. In Figure 5.2 we show example solutions for different values of C_1 when $\mathrm{Pe_s} = 257$ and $\mathcal{T}_{\text{surf}} = 0.25$. These show that for the industrially-relevant value of $C_1 = 0.015$

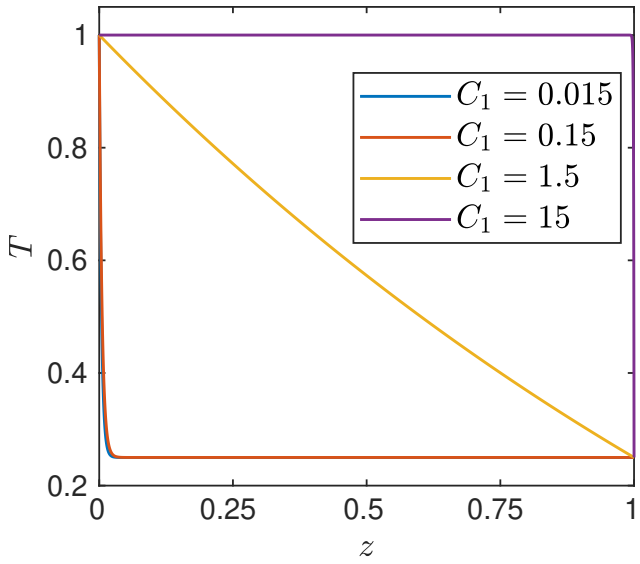


Figure 5.2: Temperature profiles for the no reaction solution, (5.39) , with $\mathrm{Pe_s} = 257$ and $T_{\mathrm{surf}} = 0.25$ as C_1 increases. The values of β for the solutions are -0.98, -0.77, -0.0022, and 4.9 in order of increasing C_1.

the majority of the heating occurs in a narrow layer near the crater. For this solution $\beta = -0.98$, indicating that the net advection of heat is almost entirely due to the solid movement. As C_1 increases, the solution transitions to one where all the increase in temperature happens in a boundary layer adjacent to the surface, implying the solid is heated up almost immediately. For this solution $\beta = 4.9$, which is positive, indicating the net advection of heat is now predominantly due to the gas flowing upwards.

Interestingly, as we vary C_1 between these two extreme values, we find that diffusion appears to dominate, around $C_1 = 1.5$, despite the large size of the Péclet number. Diffusion dominates for this solution because β becomes small, with $\beta = -0.0022$ for $C_1 = 1.5$. Physically, this means the advected energies in the gas and solid are almost exactly balancing. We can predict when this balance will occur in general by determining when β will change sign. We do this by setting the limit of $G(\beta)$ as $\beta \to 0$, given by, (5.42), to be equal to zero and so obtain the condition that

$$C_1 - \frac{4}{\pi}\left(T_{\mathrm{surf}} + 1\right) = 0. \tag{5.43}$$

For $T_{\mathrm{surf}} = 0.25$, equation (5.43) predicts that $C_1 = 1.592$, which is extremely close to our numerical value of $C_1 = 1.5$. While $|\beta| \ll 1$ represents a special class of solution to the no reactions model considered in this sub-section, we will see that when reactions are included, Q can vary, meaning β may change sign as z varies.

Given the solution (5.39), we can evaluate the energy fluxes (5.37), using (5.39), we find that

$$E^{(0)}_{\mathrm{g,crat}} = -Q^{(0)}_{\mathrm{crat}}, \qquad E^{(0)}_{\mathrm{g,surf}} = T_{\mathrm{surf}} Q^{(0)}_{\mathrm{crat}}, \tag{5.44a}$$

$$E_{\mathrm{s,crat,A}} = \frac{1}{C_1}, \qquad E_{\mathrm{s,crat,D}} = \frac{(1 - T_{\mathrm{surf}})\,\beta}{C_1\,(1 - e^{\mathrm{Pe_s}\beta})}, \tag{5.44b}$$

$$E_{\mathrm{s,surf,A}} = -\frac{T_{\mathrm{surf}}}{C_1}, \qquad E_{\mathrm{s,surf,D}} = -\frac{(1 - T_{\mathrm{surf}})\,\beta e^{\mathrm{Pe_s}\beta}}{C_1\,(1 - e^{\mathrm{Pe_s}\beta})} \tag{5.44c}$$

and $E_{\mathrm{React}} = 0$. It is a straightforward calculation to check the conservation of energy, (2.92), is indeed satisfied by (5.44), using the definition of β (5.32).

5.2.3 General solution

When reactions do occur, so that $F_i^{(0)}\left(T^{(0)}\right) \neq 0$ for some i, then in general it is not possible to solve (5.33)–(5.36) analytically. An exception is when $F_i^{(0)}\left(T^{(0)}\right) = T^{(0)}$, and $b_i = 0$ for all i, in which case the approach used for the no reaction solution in Section 5.2.2 can be extended, as described in Appendix D. However, outside of such special solutions, we must solve (5.33)–(5.36) numerically, which we do using MATLAB's built-in BVP solver bvp5c. To demonstrate that we have implemented (5.33)–(5.36) in bvp5c correctly, we compare the numerical solution to the previously mentioned special solution in Appendix D and find excellent agreement, with the error smaller than the required numerical tolerances.

In Figure 5.3 we plot the temperature and mass-flux of SiO obtained by solving (5.33)–(5.36) using the form of the reaction rates given in (5.13b) to model the rates of reactions 1 and 2 in (1.2). All the parameter values are based on industrial furnaces and given in Table 2.3 or the caption of the figure. In the figure, we vary $C_{\mathrm{Da,1}}$ and $C_{\mathrm{Da,2}}$ as the size of the reaction rates are not known. The results show that, in all cases, the majority of the change in temperature occurs near the crater at $z = 0$. This means that, the gases cool rapidly as they enter the charge, while the solid does not heat up till it nears the crater. Moreover, due to the large gradient in temperature at $z = 0$, it is diffusive heat transfer from the crater into the solid which is providing a significant portion of the energy used to heat up the solid. The results also show the size of $C_{\mathrm{Da,1}}$ and $C_{\mathrm{Da,1}}$ affects the amount of heating that occurs outside the narrow boundary layer at $z = 1$. When not all of the SiO is being consumed by reactions, increasing $C_{\mathrm{Da,2}}$ increases the temperature everywhere along the channel. However, from Figure 5.3c, we can see that if all the SiO is consumed partway along the channel, i.e. $Q_{\mathrm{SiO}} = 0$ for some z in $0 < z < 1$, then the temperature in the lower part of

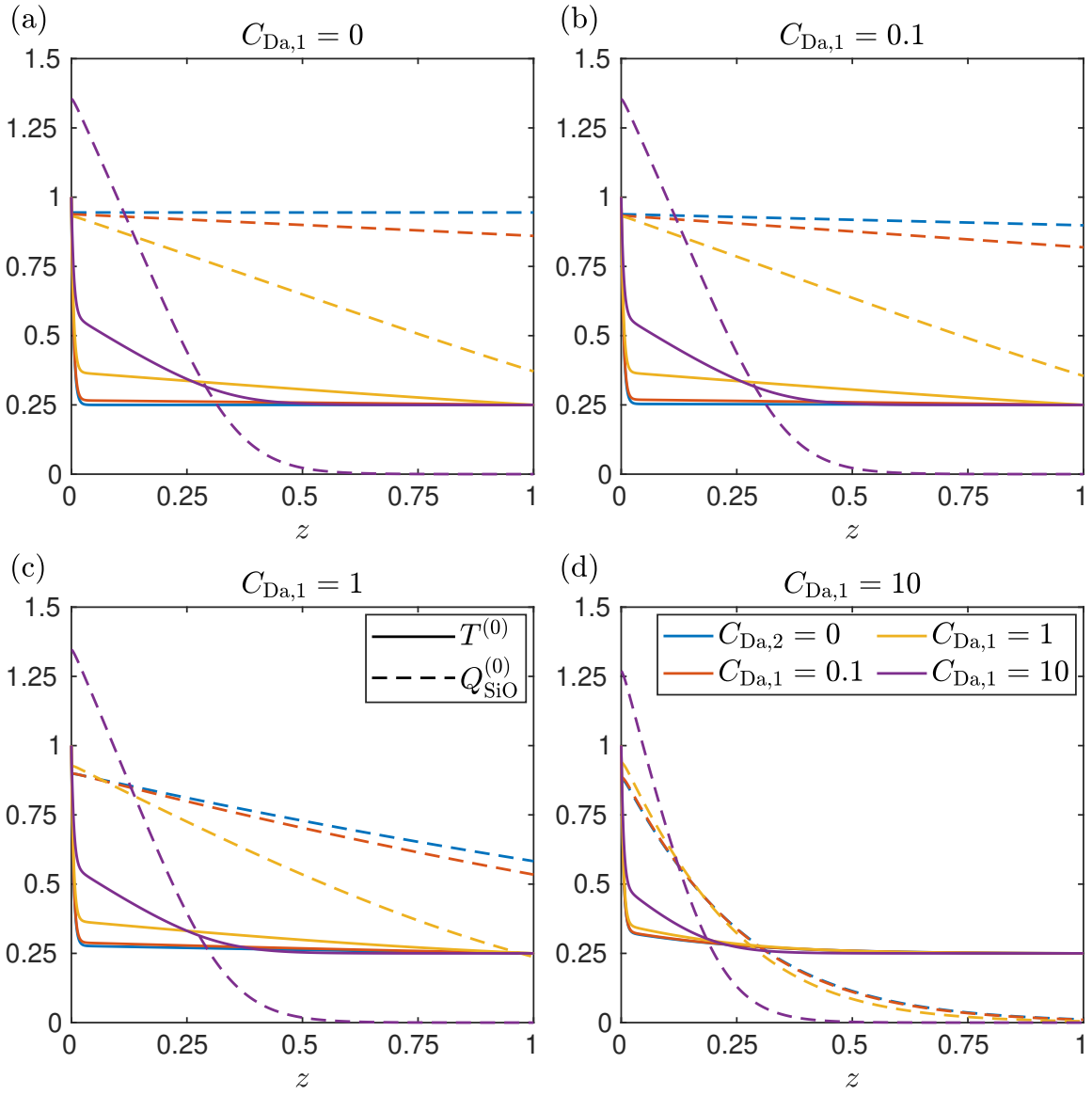


Figure 5.3: The leading-order temperature $T^{(0)}$, shown by solid lines, and mass flux of SiO $Q^{(0)}_{\mathrm{SiO}}$, shown by dashed lines obtained by solving (5.33)–(5.36) numerically for different values of $C_{\mathrm{Da},2}$ when: (a) $C_{\mathrm{Da},1} = 0$, (b) $C_{\mathrm{Da},1} = 0.1$, (c) $C_{\mathrm{Da},1} = 1$, and (d) $C_{\mathrm{Da},1} = 10$. The fixed parameter values are $\Gamma = 0.025$, $C_\Lambda = 10$, $|\mathcal{C}_\mathrm{s}| = 16 - \pi$, $\xi = 0.01$, $\mathrm{Pe}_\mathrm{s} = 256$.

the furnace becomes hotter, and the temperature in the lower part becomes cooler, compared to the solutions with smaller $C_{\mathrm{Da},2}$. The results in Figure 5.3 also show that increasing $C_{\mathrm{Da},2}$ increases the mass flux of gas through the furnace when $C_{\mathrm{Da},1}$ is fixed , but increasing $C_{\mathrm{Da},1}$ when $C_{\mathrm{Da},2}$ is fixed decreases the mass flux of gas since more SiO is converted to CO, and so must be flow through the entire length of the channel. This agrees with the interpretation of the results in Section 4.4 for vary the Damköhler numbers in the $\epsilon^2\mathrm{Re} = O(1)$ model with an imposed solid temperature.

In [23, 57], it is noted that the yield of silicon from the silicon production process is about 80 %, suggesting that between 10 to 25 % of the SiO created in the furnace escapes through the surface. The results in Figure 5.3, suggest taking $C_{\mathrm{Da},1} = C_{\mathrm{Da},2} = 1$ provides a good qualitative fit for typical size of the reaction rates in combination with the rest of our industrially-relevant parameter values. However, we have made a great many simplifications in our model, particularly to the solid which is reduced to a single species, leading to a large amount of uncertainty in its physical properties. Hence, in Figure 5.4, we plot how the temperature and total mass flux profiles vary as $\mathrm{Pe_s}$ varies. These show that as the Péclet number decreases, the temperature increases along the whole channel, while the mass flux of gas along the channel decreases. This makes sense as, physically, reducing the Péclet number corresponds to slowing the velocity of the solid, giving more time for the solid to accumulate heat, and less material to convert to gas. Moreover, the gas will be exposed to a hotter wall temperature, and become less dense by (5.11f), lowering the mass flux. Equivalently, the decreasing Péclet number could be due an increase in the thermal conductivity in the solid.

The solution with $\mathrm{Pe_s} = 64$ and $C_{\mathrm{Da},2} = 10$ exhibits the possibility of solutions for which reaction 2 begins partway along the furnace, unlike all the solutions in Figure 5.3 where it always occurred in the boundary layer near the crater wall. This is interesting industrially, as the as the condensate deposited by reaction 2 is believed to be important for sticking material together, to form the walls of the crater. Therefore changing the type of quartz added to the furnace, which Elkem have observed can alter the furnace behaviour [30], could be seen as altering the Péclet number. This would change the position clogging begins in the furnace, in turn altering the gas flow, and potentially the chemical balance. The results in Figure 5.4 show that a change by a factor of four is sufficient to alter the position of reaction 2.

Figures 5.4a and b show that when the Péclet number becomes small enough, solutions may exhibit a non-montonic temperature that, in particular, becomes hotter than the crater temperature. This is due to reaction 1 providing additional heat to

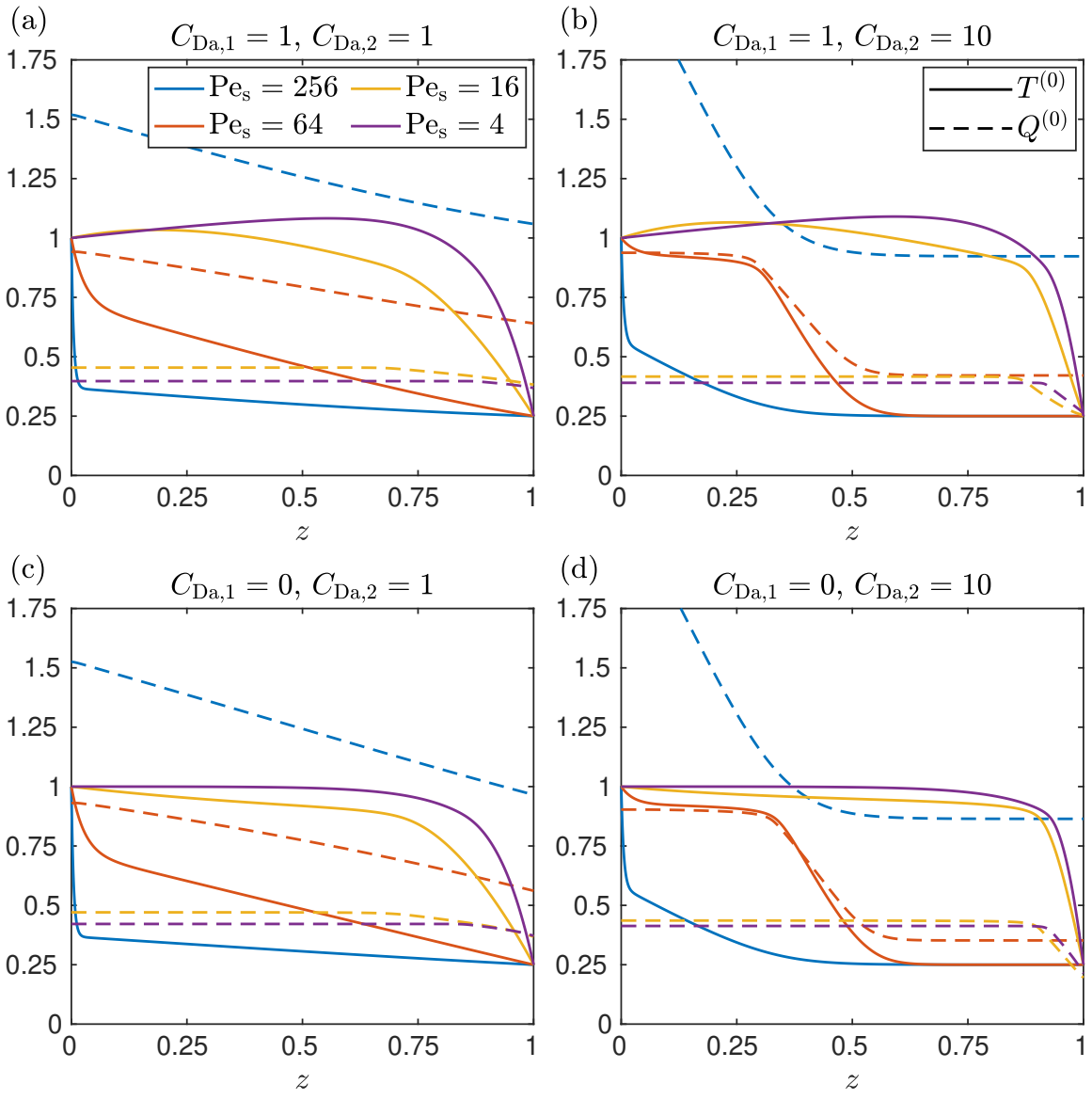


Figure 5.4: The leading-order temperature $T^{(0)}$, shown by solid lines, and total mass flux $Q^{(0)}$, shown by dashed lines, obtained by solving (5.33)–(5.36) numerically for different $\mathrm{Pe_s}$. The fixed parameter values are $\Gamma = 0.025$, $C_\Lambda = 10$, $|\mathcal{C}_\mathrm{s}| = 16 - \pi$, and $\xi = 0.01$.

the material, as it has no temperature restrictions on its reaction rate. To demonstrate this is phenomena is due to reaction 1, in Figures 5.3c and d, we show the same simulations but with $C_{\mathrm{Da},1} = 0$, and indeed, all the solutions have monotonic temperature profiles.

These preliminary results indicate how our model can be used to investigate behaviour for industrially-relevant parameter values. An interesting feature we can identify is that, when the size of $C_{\mathrm{Da},2}$ is large, then a large amount of SiO is consumed in a narrow region. This is in agreement with experimental results from pilot furnaces, which indicate that condensation resulting from reaction 2 is often found in narrow bands [74]. Hence, in the following section we will investigate the limit $\mathrm{Da}_2 = O(1)$ (i.e. $C_{\mathrm{Da},2} \to \infty$) of our model in order to easily estimate the location of these bands.

5.3 Fast reactions model

In this section, we investigate the $\mathrm{Da}_2 = O(1)$ limit of the coupled model, assuming $F_2(T)$ undergoes a rapid change in order of magnitude as the temperature varies. For simplicity, we neglect reaction 1, and so drop subscripts for reactions for this section. Assuming the form of reaction rate is given by (2.81) and (2.82), we have that

$$\mathcal{R} = \rho Y F(T) = \rho Y \frac{1}{1 + \exp\left(\dfrac{T - T_{\mathrm{cond}}}{\xi}\right)} \tag{5.45}$$

where $T_{\mathrm{surf}} < T_{\mathrm{cond}} < 1$. We assume that $\xi \ll 1$, so that F varies rapidly, and will fix its size relative to ϵ below. If $T > T_{\mathrm{cond}}$ then $F(T)$ is exponentially small (in terms of ξ), implying no reaction will occur at any order. If instead $T < T_{\mathrm{cond}}$ then $F(T) = O(1)$, and from the boundary condition (2.78a) at leading-order, we see that $Y = 0$ at leading-order on $\partial\Omega_{\mathrm{Inter}}$. Since the SiO transport equation (2.68f) has only transverse diffusion at leading-order, we have that Y is identically zero across the entire cross-section. This argument can be used iteratively to show that Y is zero at all orders, and so the reaction rate, which is proportional to Y, is again exponentially small. Therefore, to solve this problem we must use the method of matched asymptotics, identifying the region around $z = Z$ where $T \approx T_{\mathrm{cond}}$ such that the reaction rate is small and varying with temperature in a sense to be made formal below. Our analysis therefore has some similarities with counter-current diffusion flames [43], however, the reaction rate increasing as the temperature decreases means the problem also has similarities to endothermic reactions whose rate increases with

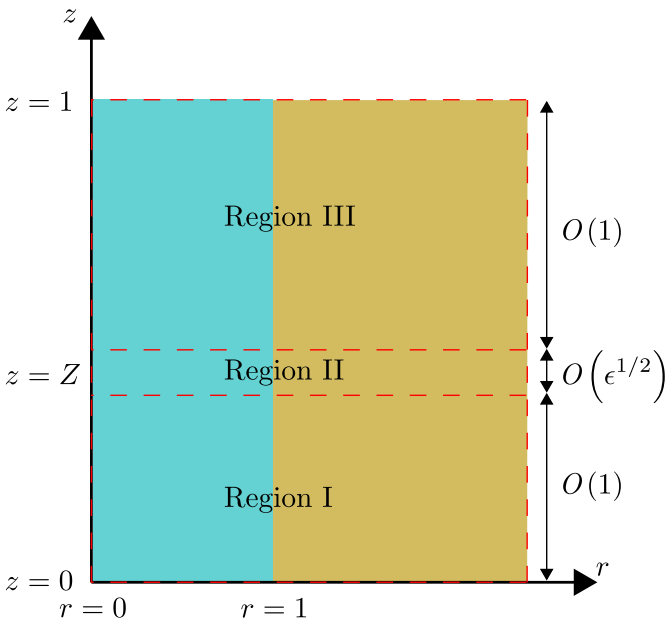


Figure 5.5: The different asymptotic regions in the $\mathrm{Da}_2 = O(1)$ limit.

temperature, as considered in [48], since in both cases the enthalpy change due to the reaction will oppose an increase in the reaction rate.

Since we are only considering a single temperature-dependent reaction we assume that the temperature varies monotonically. Therefore, as depicted in Figure 5.5, our solution will consist of 3 regions: region I where $T > T_{\mathrm{cond}}$ and the reaction rate $\mathcal{R}$ is exponentially small; region II where the reaction rate is small, i.e. $\mathcal{R} = O(\Delta_F)$, where $\Delta_F \ll 1$ is determined below; and region III where $T < T_{\mathrm{cond}}$ and again the reaction rate $\mathcal{R}$ is exponentially small.

In region II, we rescale to a thin region around a height Z up the furnace,

$$z = Z + \Delta_Z \bar{z}, \tag{5.46}$$

where $\Delta_Z \ll 1$ and $\bar{z} = O(1)$. With the benefit of hindsight, Z is determined by the condition

$$T\big|_{z=Z} = T_{\mathrm{cond}} + \xi \log\left(\frac{1}{\Delta_F}\right), \tag{5.47}$$

on $\partial\Omega_{\mathrm{Inter}}$. We assume that in region II

$$T = T_{\mathrm{cond}} + \xi \log\left(\frac{1}{\Delta_F}\right) + \Delta_T \bar{T}, \tag{5.48}$$

where $\bar{T} = O(1)$ and $\Delta_T \ll 1$ is determined below. Substituting this rescaled temperature into (5.45), we find that

$$\mathcal{R} = \Delta_F \rho Y \exp\left(-\frac{\Delta_T}{\xi}\bar{T}\right) + O\left(\Delta_F^2\right), \tag{5.49}$$

so $\mathcal{R} = O(\Delta_F)$, provided $\Delta_T = O(\xi)$. This is very reminiscent of the common approximation that over small intervals an Arrhenius law can be approximated by an inverse exponential [56, 59].

The sizes of Δ_F, Δ_T, and Δ_Z, can be determined by retaining a dominant balance in the rescaled governing equations (2.74) and (B.1), and the boundary conditions (2.77)–(2.80) in region II. We omit the details of this, and just note that the correct balances are

$$\frac{\epsilon^2 \mathrm{Re}}{\Delta_Z} \sim \Delta_F, \quad \frac{\epsilon^2 \mathrm{Re}\Lambda}{\Delta_T \Delta_Z} \sim \frac{\epsilon^2}{\Delta_Z^2}, \tag{5.50}$$

where the first condition comes from ensuring the leading order flux of gas into $\partial\Omega_{\mathrm{Inter}}$ balances the reaction rate, and the latter comes from ensuring a balance between axial diffusion in the solid with the energy released by the reactions. Later, we will see this latter balance is correct as axial diffusion in the solid is larger than axial advection in the solid in region II. Using our assumptions on the relative sizes of Re and Λ, (5.2) and (5.3) respectively, we can simplify these conditions to

$$\Delta_F \sim O\left(\frac{\epsilon}{\Delta_Z}\right), \quad \xi \sim \Delta_T \sim \Delta_Z \tag{5.51}$$

Therefore, for our analysis to be valid we require ξ to satisfy the condition

$$\epsilon \ll \xi \ll 1, \tag{5.52}$$

so that the reaction rate is small in region II. To keep the asymptotic expansion as simple as possible, we specify that

$$\xi = \frac{1}{C_\xi}\epsilon^{1/2}, \quad \text{where } C_\xi = O(1), \tag{5.53}$$

implying that $\Delta_F = \Delta_T = \Delta_Z = \epsilon^{1/2}$. The full rescaled governing equations resulting from this choice of ξ are presented in Section 5.3.3.

Due to the size of Δ_F, and the logarithmic term in (5.48), we must seek an

asymptotic solution of the form

$$
\begin{aligned}
T &\sim \sum_{m=0}^{\infty}\left[\sum_{n=0}^{m}\epsilon^{m/2}\left(\log\left(\frac{1}{\epsilon}\right)\right)^{n}T^{(\sigma(m,n))}\right] \\
&= T^{(0)} \\
&\quad + \epsilon^{1/2}\log\left(\epsilon^{-1}\right)T^{(1)} + \epsilon^{1/2}T^{(2)} \\
&\quad + \epsilon\left(\log\left(\epsilon^{-1}\right)\right)^{2}T^{(3)} + \epsilon\log\left(\epsilon^{-1}\right)T^{(4)} + \epsilon T^{(5)} \\
&\quad + \epsilon^{3/2}\left(\log\left(\epsilon^{-1}\right)\right)^{3}T^{(6)} + \epsilon^{3/2}\left(\log\left(\epsilon^{-1}\right)\right)^{2}T^{(7)} + \epsilon^{3/2}\log\left(\epsilon^{-1}\right)T^{(8)} + \epsilon^{3/2}T^{(9)} \\
&\quad + \epsilon^{2}\left(\log\left(\epsilon^{-1}\right)\right)^{4}T^{(10)} + \epsilon^{2}\left(\log\left(\epsilon^{-1}\right)\right)^{3}T^{(11)} + \epsilon^{2}\left(\log\left(\epsilon^{-1}\right)\right)^{2}T^{(12)} \\
&\qquad + \epsilon^{2}\log\left(\epsilon^{-1}\right)T^{(13)} + \epsilon^{2}T^{(14)} + \cdots,
\end{aligned}
\tag{5.54}
$$

where $\sigma(m,n) = \frac{1}{2}m(m+3) - n$. While this is much more complicated than (5.6), none of the additional terms are needed to obtain the leading-order solution in the outer regions. The extra terms arise due to the logarithmic term in (5.47). They are required to determine the full set of matching conditions for the leading-order problem inside region II, but we will see that solving that problem is unnecessary to obtain useful information from the model.

5.3.1 Region I

We first consider the solution in region I, where $T > T_{\text{cond}}$ and $F(T)$ is exponentially small. Hence, no reactions occur at any order and so the problem is identical to that for the slow reactions model in Section 5.2 with $\mathcal{R}_i = 0$. Seeking a solution of the form given by (5.54), we find that the additional terms in the asymptotic expansion introduce no additional terms in the derivation of the set of ODEs governing the leading-order behaviour compared to the slow reaction case. Hence, in a similar manner to Section 5.2, we find that $T^{(0)}$, $Q^{(0)}$, $Q^{(0)}_{\text{SiO}}$, and $p^{(0)}$, satisfy

$$\frac{\partial T^{(0)}}{\partial t} + \beta_{\text{I}}\frac{\partial T^{(0)}}{\partial z} = \frac{1}{\text{Pe}_{\text{s}}}\frac{\partial^2 T^{(0)}}{\partial z^2}, \tag{5.55a}$$

$$\frac{\partial Q^{(0)}}{\partial z} = 0, \tag{5.55b}$$

$$\frac{\partial Q^{(0)}_{\text{SiO}}}{\partial z} = 0, \tag{5.55c}$$

$$\frac{\partial p^{(0)}}{\partial z} = -\frac{8}{\pi}Q^{(0)}T^{(0)}, \tag{5.55d}$$

where

$$\beta_{\text{I}} = C_1 Q^{(0)} - 1, \tag{5.56}$$

is the overall velocity of heat advection in region I. The density in region I is given by (5.11f), while the velocity components of the gas are given by (5.18)–(5.19). The boundary conditions for (5.55) at $z = 0$ are unchanged from the slow reactions, so given by (5.36a). We will see later that both the leading-order temperature and pressure in region II are constant, so the matching conditions that close the problem in region I are

$$T^{(0)} \to T_{\text{cond}} \quad \text{as } z \to Z, \tag{5.57a}$$

$$p^{(0)} \to p_{\text{II}} \quad \text{as } z \to Z, \tag{5.57b}$$

where p_{II} is the unknown constant leading-order pressure in region II.

The problem given by (5.55), with boundary conditions (5.36a) and (5.57) is almost identical to the no-reactions special case for the slow reactions model, described in Section 5.2.2, so the solution is given by

$$\rho^{(0)} = \frac{1}{T^{(0)}}, \tag{5.58a}$$

$$u^{(0)} = 0, \tag{5.58b}$$

$$w^{(0)} = \frac{2}{\pi} Q_{\text{I}} T^{(0)} \left(1 - r^2\right), \tag{5.58c}$$

$$T^{(0)} = 1 - (1 - T_{\text{cond}}) \frac{1 - e^{\text{Pe}_{\text{s}} \beta_{\text{I}} z}}{1 - e^{\text{Pe}_{\text{s}} \beta_{\text{I}} Z^{(0)}}}, \tag{5.58d}$$

$$Y^{(0)} = Y_{\text{crat}}, \tag{5.58e}$$

$$Q^{(0)} = Q_{\text{I}}, \tag{5.58f}$$

$$Q_{\text{SiO}}^{(0)} = Y_{\text{crat}} Q_{\text{I}}, \tag{5.58g}$$

$$p^{(0)} = -\frac{8 Q_{\text{I}}}{\pi} \left(\left(1 - \frac{1 - T_{\text{cond}}}{1 - e^{\text{Pe}_{\text{s}} \beta_{\text{I}} Z^{(0)}}} \right) z - \frac{1 - T_{\text{cond}}}{\text{Pe}_{\text{s}} \beta_{\text{I}}} \frac{1 - e^{\text{Pe}_{\text{s}} \beta_{\text{I}} z}}{1 - e^{\text{Pe}_{\text{s}} \beta_{\text{I}} Z^{(0)}}} \right), \tag{5.58h}$$

where Q_{I} is the unknown total mass flux of the gas at the crater, and $Z^{(0)}$ is the unknown leading-order position of region II. Note that (5.58) was obtained without using (5.57b) to replace one of the unknowns with p_{II}, since this form is more convenient to work with. The values of Q_{I} and $Z^{(0)}$ will be determined in Section 5.3.3.

5.3.2 Region III

We now consider the solution in region III. In this region $T < T_{\text{cond}}$, and so, by the discussion above, $Y = 0$ along $\partial\Omega_{\text{Inter}}$. This changes the leading-order boundary condition on $\partial\Omega_{\text{Inter}}$ for $Y^{(0)}$ from a homogeneous Neumann to a homogeneous Dirichlet condition, meaning the leading-order mass fraction of SiO is zero everywhere in region

III. Besides this small change, the leading-order problem in region III is essentially identical to that in region I, and so, after obtaining the closure conditions, the ODEs governing $T^{(0)}$, $Q^{(0)}$, and $p^{(0)}$ are

$$\frac{\partial T^{(0)}}{\partial t} + \beta_{\mathrm{III}} \frac{\partial T^{(0)}}{\partial z} = \frac{1}{\mathrm{Pe_s}} \frac{\partial^2 T^{(0)}}{\partial z^2}, \tag{5.59a}$$

$$\frac{\partial Q^{(0)}}{\partial z} = 0. \tag{5.59b}$$

$$\frac{\partial p^{(0)}}{\partial z} = -\frac{8}{\pi} Q^{(0)} T^{(0)}, \tag{5.59c}$$

where

$$\beta_{\mathrm{III}} = C_1 Q^{(0)} - 1, \tag{5.60}$$

is the overall velocity of advection of heat in region III. The boundary conditions for (5.59) at $z = 1$, are unchanged from those for the slow reaction model, so are given by (5.36b). Since we will see later that $T^{(0)}$ and $p^{(0)}$ are constant at leading-order in region II, the matching conditions as $z \to Z$ are given by

$$T^{(0)} \to T_{\mathrm{cond}} \quad \text{as } z \to Z, \tag{5.61a}$$

$$p^{(0)} \to p_{\mathrm{II}} \quad \text{as } z \to Z. \tag{5.61b}$$

The leading-order solution in region III is given by

$$\rho^{(0)} = \frac{1}{T^{(0)}}, \tag{5.62a}$$

$$u^{(0)} = 0, \tag{5.62b}$$

$$w^{(0)} = \frac{2}{\pi} Q_{\mathrm{III}} T^{(0)} \left(1 - r^2\right), \tag{5.62c}$$

$$T^{(0)} = T_{\mathrm{surf}} - \left(T_{\mathrm{surf}} - T_{\mathrm{cond}}\right) \frac{1 - e^{\mathrm{Pe_s}\beta_{\mathrm{III}}(z-1)}}{1 - e^{\mathrm{Pe_s}\beta_{\mathrm{III}}\left(Z^{(0)}-1\right)}}, \tag{5.62d}$$

$$Y^{(0)} = 0, \tag{5.62e}$$

$$Q^{(0)} = Q_{\mathrm{III}}, \tag{5.62f}$$

$$Q^{(0)}_{\mathrm{SiO}} = 0, \tag{5.62g}$$

$$p^{(0)} = -\frac{8Q_{\mathrm{III}}}{\pi} \Bigg(\left(T_{\mathrm{surf}} - \frac{T_{\mathrm{surf}} - T_{\mathrm{cond}}}{1 - e^{\mathrm{Pe_s}\beta_{\mathrm{III}}\left(Z^{(0)}-1\right)}} \right) (z-1) - \frac{T_{\mathrm{surf}} - T_{\mathrm{cond}}}{\mathrm{Pe_s}\beta_{\mathrm{III}}} \frac{1 - e^{\mathrm{Pe_s}\beta_{\mathrm{III}}(z-1)}}{1 - e^{\mathrm{Pe_s}\beta_{\mathrm{III}}(Z^{(0)}-1)}} + \frac{\pi}{8Q_{\mathrm{III}}} \Bigg), \tag{5.62h}$$

where Q_{III} is the unknown constant total mass flux of gas through region III. As for region I, we could apply (5.61b) to eliminate one of Q_{III} and $Z^{(0)}$, but it will be more convenient to leave the solutions in their current form.

5.3.3 Region II

We now consider region II, where the reaction rate varies with temperature. As discussed above, in region II we rescale axial length and temperature as follows

$$z = Z + \epsilon^{1/2}\bar{z}, \quad T = T_{\text{cond}} + \frac{1}{2C_\xi}\epsilon^{1/2}\log\left(\frac{1}{\epsilon}\right) + \epsilon^{1/2}\bar{T}, \quad u = \epsilon^{-1/2}\bar{u}, \tag{5.63}$$

where we rescale the transverse velocity, so that the conservation of mass equation (B.1a) fully balances. We also use bar notation to denote all the other unscaled variables in this region. Then, under the assumptions (5.2)–(5.3), along with (5.63), we can rewrite the governing equations in region II as

$$\alpha\epsilon^{1/2}\frac{\partial\bar{\rho}}{\partial t} + \frac{1}{\bar{r}}\frac{\partial\left(\bar{r}\bar{\rho}\bar{u}\right)}{\partial\bar{r}} + \frac{\partial\left(\bar{\rho}\bar{w}\right)}{\partial\bar{z}} = 0, \tag{5.64a}$$

$$\frac{1}{\Gamma}\left(\alpha\epsilon\frac{\partial\left(\bar{\rho}\bar{u}\right)}{\partial t} + \frac{1}{\bar{r}}\frac{\partial\left(\bar{r}\bar{\rho}\bar{u}\bar{u}\right)}{\partial\bar{r}} + \frac{\partial\left(\bar{\rho}\bar{u}\bar{w}\right)}{\partial\bar{z}}\right) = -\frac{1}{\epsilon^2}\frac{\partial\bar{p}}{\partial\bar{r}} + \frac{1}{\epsilon}\frac{1}{\bar{r}}\frac{\partial\left(\bar{r}\bar{\tau}_{rr}\right)}{\partial r} + \frac{1}{\epsilon^{1/2}}\frac{\partial\bar{\tau}_{rz}}{\partial\bar{z}}, \tag{5.64b}$$

$$\frac{\epsilon}{\Gamma}\left(\alpha\epsilon^{1/2}\frac{\partial\left(\bar{\rho}\bar{w}\right)}{\partial t} + \frac{1}{\bar{r}}\frac{\partial\left(\bar{r}\bar{\rho}\bar{u}\bar{w}\right)}{\partial\bar{r}} + \frac{\partial\left(\bar{\rho}\bar{w}\bar{w}\right)}{\partial\bar{z}}\right) = -\frac{\partial\bar{p}}{\partial\bar{z}} + \frac{\epsilon^{1/2}}{\bar{r}}\frac{\partial\left(\bar{r}\bar{\tau}_{rz}\right)}{\partial\bar{r}} + \epsilon\frac{\partial\bar{\tau}_{zz}}{\partial\bar{z}}, \tag{5.64c}$$

$$\begin{aligned}\frac{\epsilon^{1/2}}{\Gamma}\left(\epsilon^{1/2}\alpha\frac{\partial\left(\bar{\rho}\bar{T}\right)}{\partial t} + \frac{1}{\bar{r}}\frac{\partial\left(\bar{r}\bar{\rho}\bar{u}\bar{T}\right)}{\partial r} + \frac{\partial\left(\bar{\rho}\bar{w}\bar{T}\right)}{\partial\bar{z}}\right) &= \frac{1}{\text{Pr}}\frac{1}{\bar{r}}\frac{\partial}{\partial\bar{r}}\left(\bar{r}\frac{\partial\bar{T}}{\partial\bar{r}}\right) + \frac{\epsilon^{1/2}}{\text{Pr}}\frac{\partial\bar{T}}{\partial\bar{z}^2} \\ &\quad + \frac{\text{Ec}}{\epsilon}\left(\epsilon^{1/2}\alpha\frac{\partial\bar{p}}{\partial t} + \bar{u}\frac{\partial\bar{p}}{\partial\bar{r}} + \bar{w}\frac{\partial\bar{p}}{\partial\bar{z}}\right) + \epsilon^2\text{Ec}\bar{\Phi},\end{aligned} \tag{5.64d}$$

$$\frac{\epsilon^{1/2}}{\Gamma}\left(\epsilon^{1/2}\alpha\frac{\partial\left(\bar{\rho}\bar{Y}\right)}{\partial t} + \frac{1}{\bar{r}}\frac{\partial\left(\bar{r}\bar{\rho}\bar{u}\bar{Y}\right)}{\partial\bar{r}} + \frac{\partial\left(\bar{\rho}\bar{w}\bar{Y}\right)}{\partial\bar{z}}\right) = \frac{1}{\text{Sc}}\frac{1}{\bar{r}}\frac{\partial}{\partial\bar{r}}\left(\bar{r}\bar{\rho}\frac{\partial\bar{Y}}{\partial\bar{r}}\right) + \frac{\epsilon}{\text{Sc}}\frac{\partial}{\partial\bar{z}}\left(\bar{\rho}\frac{\partial\bar{Y}}{\partial\bar{z}}\right), \tag{5.64e}$$

$$\Delta p\,\bar{p} + 1 = \bar{\rho}\left(T_{\text{cond}} + \frac{1}{2C_\xi}\epsilon^{1/2}\log\left(\frac{1}{\epsilon}\right) + \epsilon^{1/2}\bar{T}\right), \tag{5.64f}$$

where the components of the viscous stress tensor are given by

$$\bar{\tau}_{rr} = \epsilon^{1/2}\left(2\frac{\partial \bar{u}}{\partial \bar{r}} - \frac{2}{3}\left(\frac{1}{\bar{r}}\frac{\partial}{\partial \bar{r}}\left(\bar{r}\bar{u}\right) + \frac{\partial \bar{w}}{\partial \bar{z}}\right)\right), \tag{5.65a}$$

$$\bar{\tau}_{rz} = \frac{\partial \bar{w}}{\partial \bar{r}} + \epsilon\frac{\partial \bar{u}}{\partial \bar{z}}, \tag{5.65b}$$

$$\bar{\tau}_{zz} = \epsilon^{1/2}\left(2\frac{\partial \bar{w}}{\partial \bar{z}} - \frac{2}{3}\left(\frac{1}{\bar{r}}\frac{\partial}{\partial \bar{r}}\left(\bar{r}\bar{u}\right) + \frac{\partial \bar{w}}{\partial \bar{z}}\right)\right), \tag{5.65c}$$

and the rescaled viscous dissipation function is given by

$$\bar{\Phi} = \frac{2}{\epsilon}\left(\left(\frac{\partial \bar{u}}{\partial \bar{r}}\right)^2 + \left(\frac{\bar{u}}{\bar{r}}\right)^2 + \left(\frac{\partial \bar{w}}{\partial \bar{z}}\right)^2\right) + \left(\frac{\partial \bar{u}}{\partial \bar{z}} + \frac{1}{\epsilon}\frac{\partial \bar{w}}{\partial \bar{r}}\right)^2 - \frac{2}{3}\frac{1}{\epsilon}\left(\frac{1}{\bar{r}}\frac{\partial}{\partial \bar{r}}\left(\bar{r}\bar{u}\right) + \frac{\partial \bar{w}}{\partial \bar{z}}\right)^2. \tag{5.66}$$

In the above statement of the governing equations for the gas, we have neglected all non-axisymmetric terms, since, as for all the other problems discussed in this chapter, they will play no role in determining the leading-order behaviour. However, as for the other problems, we do not know this *a priori* and must prove it as part of the solution.

Applying the scaling (5.63) to the solid governing equation (2.74), we obtain that in region II,

$$\epsilon^{3/2}\mathrm{Pe_s}\left(\epsilon^{1/2}\frac{\partial \bar{T}}{\partial t} - \frac{\partial \bar{T}}{\partial \bar{z}}\right) = \frac{1}{\bar{r}}\frac{\partial}{\partial \bar{r}}\left(\bar{r}\frac{\partial \bar{T}}{\partial \bar{r}}\right) + \frac{1}{\bar{r}^2}\frac{\partial^2 \bar{T}}{\partial \bar{\theta}^2} + \epsilon\frac{\partial^2 \bar{T}}{\partial \bar{z}^2}. \tag{5.67}$$

Applying the scaling (5.63) to the boundary conditions (2.76)–(2.80), gives that

$$\bar{u} = 0, \quad \bar{r}\frac{\partial \bar{w}}{\partial \bar{r}} \to 0, \quad \bar{r}\frac{\partial \bar{T}}{\partial \bar{r}} \to 0, \quad \bar{r}\frac{\partial \bar{Y}}{\partial \bar{r}} \to 0, \tag{5.68}$$

at $\bar{r} = 0$;

$$\frac{1}{\Gamma}\bar{\rho}\bar{u} = -\frac{\mathrm{Da}}{\mathrm{Sc}}\left(\nu_{\mathrm{SiO}} + \nu_{\mathrm{CO}}\right)\bar{\rho}\bar{Y}e^{-C_\xi \bar{T}}, \tag{5.69a}$$

$$\frac{\epsilon^{1/2}}{\Gamma}\bar{\rho}\bar{Y}\bar{u} - \frac{1}{\mathrm{Sc}}\bar{\rho}\frac{\partial \bar{Y}}{\partial \bar{r}} = -\epsilon^{1/2}\frac{\mathrm{Da}\nu_{\mathrm{SiO}}}{\mathrm{Sc}}\bar{\rho}\bar{Y}e^{-C_\xi \bar{T}}, \tag{5.69b}$$

$$\bar{w} + \alpha = 0, \tag{5.69c}$$

$$\bar{T}\big|_{r=1-} = \bar{T}\big|_{r=1+}, \tag{5.69d}$$

$$\left.\frac{\partial \bar{T}}{\partial \bar{r}}\right|_{\bar{r}=1+} = C_\Lambda\epsilon\left(\left(-\frac{\mathrm{Pr}}{\Gamma}\bar{\rho}\bar{u}\left(T_{\mathrm{cond}} + \frac{\epsilon^{1/2}}{2C_\xi}\log\left(\epsilon^{-1}\right) + \epsilon^{1/2}\bar{T}\right) + \frac{\partial \bar{T}}{\partial \bar{r}}\right)\Big|_{\bar{r}=1-} - \left.\frac{\mathrm{Da}\eta\mathrm{Pr}}{\mathrm{Sc}}\bar{\rho}\bar{Y}e^{-C_\xi \bar{T}}\right|_{r=1}\right), \tag{5.69e}$$

along $r = 1$;

$$\bar{T} \text{ periodic} \tag{5.70a}$$

on $\partial\Omega$; and

$$\bar{T} = 0, \tag{5.71}$$

at $\bar{r} = 1$, $\bar{z} = 0$, with this final condition coming from the definition of Z, (5.47). We also require matching conditions as $\bar{z} \to \pm\infty$ into regions I and III respectively, which will be discussed shortly.

We seek an asymptotic solution of the form given by (5.54) for $\bar{u}, \bar{w}, \bar{\rho}, \bar{p}, \bar{Y}$ to the problem defined by (5.64), (5.67)–(5.71). We also seek a solution for the temperature in the same manner, but in a slight abuse of notation, we take

$$\bar{T}^{(0)} = T_{\text{cond}}, \quad \bar{T}^{(1)} = \frac{1}{2C_\xi}, \tag{5.72}$$

the known $O(1)$, and $O\left(\epsilon \log\left(\epsilon^{-1}\right)\right)$ temperatures in region II, so that the expansion for $\bar{T}$ starts at $\bar{T}^{(2)}$.

The leading-order governing equation in Ω_{s} is therefore

$$0 = \frac{1}{\bar{r}} \frac{\partial}{\partial \bar{r}} \left(\bar{r} \frac{\partial \bar{T}^{(2)}}{\partial \bar{r}} \right) + \frac{1}{\bar{r}^2} \frac{\partial^2 \bar{T}^{(2)}}{\partial \theta^2}, \tag{5.73}$$

subject to the boundary conditions

$$\bar{\boldsymbol{\nabla}} \bar{T}^{(2)} \cdot \mathbf{n} = 0 \quad \text{on } \partial\Omega_{\text{Inter}}, \tag{5.74a}$$

$$\bar{T}^{(2)} \text{ periodic} \quad \text{on } \partial\Omega. \tag{5.74b}$$

By identical arguments as for (5.7)–(5.8) in Section 5.2.1, we conclude $\bar{T}^{(2)}$ depends only on $\bar{z}$ in Ω_{s}, and the leading-order boundary conditions at $\bar{r} = 1$ imply the leading-order solution in Ω_{g} is axisymmetric. Exploiting this, the leading-order governing equations in region II of Ω_{g} are

$$\frac{1}{\bar{r}} \frac{\partial \left(\bar{r} \bar{\rho}^{(0)} \bar{u}^{(0)} \right)}{\partial \bar{r}} + \frac{\partial \left(\bar{\rho}^{(0)} \bar{w}^{(0)} \right)}{\partial \bar{z}} = 0, \tag{5.75a}$$

$$0 = -\frac{\partial \bar{p}^{(0)}}{\partial \bar{r}}, \tag{5.75b}$$

$$0 = -\frac{\partial \bar{p}^{(0)}}{\partial \bar{z}}, \tag{5.75c}$$

$$0 = \frac{1}{\text{Pr}} \frac{1}{\bar{r}} \frac{\partial}{\partial \bar{r}} \left(\bar{r} \frac{\partial \bar{T}^{(2)}}{\partial \bar{r}} \right), \tag{5.75d}$$

$$0 = \frac{1}{\mathrm{Sc}}\frac{1}{\bar{r}}\frac{\partial}{\partial \bar{r}}\left(\bar{r}\bar{\rho}\frac{\partial \bar{Y}^{(0)}}{\partial \bar{r}}\right), \tag{5.75e}$$

$$1 = \bar{\rho}^{(0)} T_{\mathrm{cond}}, \tag{5.75f}$$

with the leading-order form of the boundary conditions being given by

$$\bar{u}^{(0)} = 0, \quad \bar{r}\frac{\partial \bar{w}^{(0)}}{\partial \bar{r}} \to 0, \quad \bar{r}\frac{\partial \bar{T}^{(2)}}{\partial \bar{r}} \to 0, \quad \bar{r}\frac{\partial \bar{Y}^{(0)}}{\partial \bar{r}} \to 0, \tag{5.76}$$

at $\bar{r} = 0$, and

$$\frac{1}{\Gamma}\bar{\rho}^{(0)}\bar{u}^{(0)} = -\frac{\mathrm{Da}}{\mathrm{Sc}}\left(\nu_{\mathrm{SiO}} + \nu_{\mathrm{CO}}\right)\bar{\rho}^{(0)}\bar{Y}^{(0)}e^{-C_\xi \bar{T}^{(2)}}, \tag{5.77a}$$

$$\bar{\rho}^{(0)}\frac{\partial \bar{Y}^{(0)}}{\partial \bar{r}} = 0, \tag{5.77b}$$

$$\bar{w}^{(0)} = 0, \tag{5.77c}$$

$$\bar{T}^{(2)}\big|_{r=1-} = \bar{T}^{(2)}\big|_{r=1+}, \tag{5.77d}$$

at $r = 1$.

Using (5.75d), along with the boundary conditions (5.76)–(5.77), we can deduce that

$$\bar{T}^{(2)} = \bar{T}^{(2)}\big|_{\bar{r}=1+}, \tag{5.78}$$

in Ω_{g}, so that the leading-order gas and solid temperatures must be equal, and depend only on z. Similarly, using (5.75e), we find $\bar{Y}^{(0)} = \bar{Y}^{(0)}(\bar{z})$. The two momentum equations (5.75b)–(5.75c) together imply that, to leading-order, the pressure in region II is constant in $\bar{r}$ and $\bar{z}$, meaning

$$\bar{p}^{(0)} = p_{\mathrm{II}}, \tag{5.79}$$

where p_{II} is the unknown constant that previously appeared in the matching conditions (5.57b), and (5.61b) from regions I and III respectively. The equation of state (5.75f) implies that

$$\bar{\rho}^{(0)} = \frac{1}{T_{\mathrm{cond}}}, \tag{5.80}$$

giving that the leading-order density is constant in region II.

By integrating the conservation of mass equation (5.75a), over $\mathcal{C}_{\mathrm{g}}$ and using the boundary conditions (5.76) and (5.77a), we obtain that

$$\frac{\partial \bar{Q}^{(0)}}{\partial \bar{z}} = \frac{2\pi \mathrm{Da}\Gamma}{\mathrm{Sc}T_{\mathrm{cond}}}\left(\nu_{\mathrm{SiO}} + \nu_{\mathrm{CO}}\right)\bar{Y}^{(0)}e^{-C_\xi \bar{T}^{(2)}}. \tag{5.81}$$

As before, we must consider the behaviour at higher orders to obtain sufficient closure conditions for the leading-order problem as $\bar{T}^{(2)}$ remains undetermined. The

solution at $O\left(\epsilon^{1/2}\log\left(\epsilon^{-1}\right)\right)$ in both Ω_{g} and Ω_{s} has no direct relevance for obtaining the closure conditions in region II, so we proceed straight to the $O\left(\epsilon^{1/2}\right)$ problem.

At $O\left(\epsilon^{1/2}\right)$ in the solid Ω_{s}, $\bar{T}^{(4)}$ satisfies an identical problem to (5.73)–(5.74), and so we find that $\bar{T}^{(4)}$ is independent of $\bar{r}$ and $\bar{\theta}$, implying the $O\left(\epsilon^{1/2}\right)$ solution of the gas may be taken to be axisymmetric. Hence, the relevant governing equations at $O\left(\epsilon^{1/2}\right)$ for the gas are given by

$$0 = -\frac{\partial \bar{p}^{(2)}}{\partial \bar{r}}, \tag{5.82a}$$

$$0 = -\frac{\partial \bar{p}^{(2)}}{\partial \bar{z}} + \frac{1}{r}\frac{\partial}{\partial \bar{r}}\left(r\frac{\partial \bar{w}^{(0)}}{\partial \bar{r}}\right), \tag{5.82b}$$

$$\frac{1}{\Gamma}\left(\frac{1}{\bar{r}}\frac{\partial\left(\bar{r}\bar{\rho}^{(0)}\bar{u}^{(0)}\bar{Y}^{(0)}\right)}{\partial \bar{r}} + \frac{\partial\left(\bar{\rho}^{(0)}\bar{w}^{(0)}\bar{Y}^{(0)}\right)}{\partial \bar{z}}\right) = \frac{1}{\mathrm{Sc}}\frac{1}{\bar{r}}\frac{\partial}{\partial \bar{r}}\left(\bar{r}\bar{\rho}^{(0)}\frac{\partial \bar{Y}^{(2)}}{\partial \bar{r}}\right), \tag{5.82c}$$

subject to the boundary conditions

$$\bar{r}\frac{\partial \bar{Y}^{(2)}}{\partial \bar{r}} \to 0 \quad \text{as } \bar{r} \to 0, \tag{5.83a}$$

$$\frac{1}{\Gamma}\bar{\rho}^{(0)}\bar{Y}^{(0)}\bar{u}^{(0)} - \frac{1}{\mathrm{Sc}}\bar{\rho}^{(0)}\frac{\partial \bar{Y}^{(2)}}{\partial \bar{r}} = -\frac{\mathrm{Da}\nu_{\mathrm{SiO}}}{\mathrm{Sc}}\bar{\rho}^{(0)}\bar{Y}^{(0)}e^{-C_\xi \bar{T}^{(2)}} \quad \text{at } \bar{r} = 1. \tag{5.83b}$$

By integrating (5.82c) over $\mathcal{C}_{\mathrm{g}}$, and using (5.83), we obtain an equation for the leading order mass flux of SiO in region II,

$$\frac{\partial \bar{Q}^{(0)}_{\mathrm{SiO}}}{\partial \bar{z}} = \frac{2\pi \mathrm{Da}\Gamma\nu_{\mathrm{SiO}}}{\mathrm{Sc}T_{\mathrm{cond}}}\bar{Y}^{(0)}e^{-C_\xi \bar{T}^{(2)}}. \tag{5.84}$$

Using the $O(1)$ conservation of mass equation (5.75a), and the $O\left(\epsilon^{1/2}\right)$ momentum equations (5.82a)–(5.82b), we obtain an equation for the $O\left(\epsilon^{1/2}\right)$ pressure,

$$\frac{\partial \bar{p}^{(2)}}{\partial \bar{z}} = -\frac{8T_{\mathrm{cond}}}{\pi}\bar{Q}^{(0)}, \tag{5.85}$$

which allows us to determine the $O(1)$ velocities in region II

$$\bar{u}^{(0)} = \frac{1}{2\pi}T_{\mathrm{cond}}\frac{\partial \bar{Q}^{(0)}}{\partial \bar{z}}\left(\bar{r}^3 - 2\bar{r}\right), \tag{5.86}$$

$$\bar{w}^{(0)} = \frac{2}{\pi}T_{\mathrm{cond}}\bar{Q}^{(0)}\left(1 - \bar{r}^2\right), \tag{5.87}$$

in terms of $\bar{Q}^{(0)}$.

To close the problem, we consider the governing equation for the solid at $O(\epsilon)$, again omitting the details of the $O\left(\epsilon\left(\log\left(\epsilon^{-1}\right)\right)^2\right)$, and $O\left(\epsilon\log\left(\epsilon^{-1}\right)\right)$ solutions, as

they do not contribute to the $O(\epsilon)$ dynamics. The $O(\epsilon)$ governing equation in Ω_s is given by

$$0 = \frac{1}{\bar{r}}\frac{\partial}{\partial \bar{r}}\left(\bar{r}\frac{\partial \bar{T}^{(5)}}{\partial \bar{r}}\right) + \frac{1}{\bar{r}^2}\frac{\partial^2 \bar{T}^{(5)}}{\partial \theta^2} + \frac{\partial^2 \bar{T}^{(2)}}{\partial \bar{z}^2}, \tag{5.88}$$

in $\partial\Omega_\mathrm{s}$, subject to the boundary conditions

$$\bar{\boldsymbol{\nabla}}\bar{T}^{(5)} \cdot \boldsymbol{n} = -C_\Lambda\Bigg(\left(-\frac{\mathrm{Pr}}{\Gamma}\bar{\rho}^{(0)}\bar{u}^{(0)}T_\mathrm{cond} + \frac{\partial \bar{T}^{(2)}}{\partial \bar{r}}\right)\Bigg|_{\bar{r}=1-} - \frac{\mathrm{Da}\eta}{\mathrm{Sc}}\bar{\rho}^{(0)}\bar{Y}^{(0)}e^{-C_\xi \bar{T}^{(2)}}\Bigg) \tag{5.89a}$$

$$= -\frac{C_\Lambda \mathrm{PrDa}}{\mathrm{Sc}T_\mathrm{cond}}\left(\left(\nu_\mathrm{SiO} + \nu_\mathrm{CO}\right)T_\mathrm{cond} - \eta\right)\bar{Y}^{(0)}e^{-C_\xi \bar{T}^{(2)}}, \tag{5.89b}$$

at $\bar{r} = 1$; and

$$\bar{T}^{(2)}\text{periodic} \tag{5.89c}$$

on $\partial\Omega$. Here (5.89b) was obtained using (5.86). By integrating (5.88) over $\mathcal{C}_\mathrm{s}$, then applying the divergence theorem, we obtain the equation

$$0 = \frac{\partial^2 \bar{T}^{(2)}}{\partial \bar{z}^2} + \frac{2\pi C_\Lambda \mathrm{PrDa}}{\mathrm{Sc}T_\mathrm{cond}|\mathcal{C}_\mathrm{s}|}\left(\eta - \left(\nu_\mathrm{SiO} + \nu_\mathrm{CO}\right)T_\mathrm{cond}\right)\bar{Y}^{(0)}e^{-C_\xi \bar{T}^{(2)}}, \tag{5.90}$$

which closes the leading-order problem in region II.

In summary, the problem in region II can be reduced to four ODEs (5.81), (5.84), (5.85), and (5.90), in terms of four variables $\bar{T}^{(2)}$, $\bar{Q}^{(0)}$, $\bar{Q}^{(0)}_\mathrm{SiO}$, and $\bar{p}^{(2)}$, which may be re-written as

$$0 = \frac{\partial^2 \bar{T}^{(2)}}{\partial \bar{z}^2} + a_\mathrm{II}\frac{\bar{Q}^{(0)}_\mathrm{SiO}}{\bar{Q}^{(0)}}e^{-C_\xi \bar{T}^{(2)}}, \tag{5.91a}$$

$$\frac{\partial \bar{Q}^{(0)}}{\partial \bar{z}} = b_\mathrm{II}\frac{\bar{Q}^{(0)}_\mathrm{SiO}}{\bar{Q}^{(0)}}e^{-C_\xi \bar{T}^{(2)}}, \tag{5.91b}$$

$$\frac{\partial \bar{Q}^{(0)}_\mathrm{SiO}}{\partial \bar{z}} = c_\mathrm{II}\frac{\bar{Q}^{(0)}_\mathrm{SiO}}{\bar{Q}^{(0)}}e^{-C_\xi \bar{T}^{(2)}}, \tag{5.91c}$$

$$\frac{\partial \bar{p}^{(2)}}{\partial \bar{z}} = -\frac{8T_\mathrm{cond}}{\pi}\bar{Q}^{(0)} \tag{5.91d}$$

where

$$a_\mathrm{II} = 2\pi C_1 \tilde{D}\mathrm{Pe}_\mathrm{s}\left(\eta - \left(\nu_\mathrm{SiO} + \nu_\mathrm{CO}\right)T_\mathrm{cond}\right), \tag{5.92a}$$

$$b_\mathrm{II} = 2\pi\tilde{D}\left(\nu_\mathrm{SiO} + \nu_\mathrm{CO}\right), \tag{5.92b}$$

$$c_\mathrm{II} = 2\pi\tilde{D}\nu_\mathrm{SiO}, \tag{5.92c}$$

$$\tilde{D} = \frac{\mathrm{Da}\Gamma}{\mathrm{Sc}T_\mathrm{cond}} \tag{5.92d}$$

subject to the single boundary condition

$$\bar{T}^{(2)} = 0 \quad \text{at } \bar{z} = 0, \tag{5.93}$$

and matching conditions with the outer solutions in regions I and III.

Since Q and Q_{SiO} are constant at leading-order in regions I and III (see (5.58) and (5.62)), four of the matching conditions are given by

$$\bar{Q}^{(0)} \to Q_{\mathrm{I}}, \quad \bar{Q}^{(0)}_{\mathrm{SiO}} \to Y_{\mathrm{crat}} Q_{\mathrm{I}} \quad \text{as } \bar{z} \to -\infty, \tag{5.94a}$$

$$\bar{Q}^{(0)} \to Q_{\mathrm{III}}, \quad \bar{Q}^{(0)}_{\mathrm{SiO}} \to 0 \quad \text{as } \bar{z} \to \infty. \tag{5.94b}$$

To find the remaining matching conditions, we must also consider the switchback $O\left(\epsilon^{1/2}\log\left(\epsilon^{-1}\right)\right)$ and $O\left(\epsilon^{1/2}\right)$ problems in regions I and III to obtain matching conditions for $\bar{T}^{(2)}$ and $\bar{p}^{(2)}$. However, as this is unnecessary to find $Q_{\mathrm{I}}, Q_{\mathrm{III}}$, and $Z^{(0)}$ in order to determine the outer solutions, and a full analytic solution of (5.91) is not possible, we do not consider this in this thesis.

5.3.4 Solution to the outer problems

Since we are not concerned with obtaining a full solution to (5.91) (since no closed form analytic solution exists), we match using only the leading-order term in each region. By definition $\bar{T}^{(0)} = T_{\mathrm{cond}}$ is constant in region II, giving the matching conditions previously stated in in (5.57a), and (5.61a). Moreover, by (5.79), the leading-order pressure is constant in region II, which gives us the matching conditions previously stated in (5.57b), and (5.61b). As these latter two expressions are equal we can eliminate p_{II}, and obtain the algebraic equation

$$\begin{aligned} Q_{\mathrm{I}}\left(\left(1 - \frac{1-T_{\mathrm{cond}}}{1-e^{\mathrm{Pe_s}\beta_{\mathrm{I}}Z^{(0)}}}\right)Z^{(0)} - \frac{1-T_{\mathrm{cond}}}{\mathrm{Pe_s}\beta_{\mathrm{I}}}\right) \\ = Q_{\mathrm{III}}\Bigg(\left(T_{\mathrm{surf}} - \frac{T_{\mathrm{surf}}-T_{\mathrm{cond}}}{1-e^{\mathrm{Pe_s}\beta_{\mathrm{III}}\left(Z^{(0)}-1\right)}}\right)\left(Z^{(0)}-1\right) \\ - \frac{T_{\mathrm{surf}}-T_{\mathrm{cond}}}{\mathrm{Pe_s}\beta_{\mathrm{III}}} + \frac{\pi}{8Q_{\mathrm{III}}}\Bigg), \end{aligned} \tag{5.95}$$

which depends on three variables Q_{I}, Q_{III} and $Z^{(0)}$.

Next, as the reaction terms in (5.91) are all scalar multiples of each other, it is possible to find two first integrals to (5.91). By combining (5.91b)–(5.91c), we deduce that

$$c_{\mathrm{II}}\bar{Q}^{(0)} - b_{\mathrm{II}}\bar{Q}^{(0)}_{\mathrm{SiO}} = Q_{\mathrm{I}}\left(c_{\mathrm{II}} - b_{\mathrm{II}}Y_{\mathrm{crat}}\right),, \tag{5.96}$$

where we have used the matching condition for $Q^{(0)}$ and $Q^{(0)}_{\mathrm{SiO}}$ as $\bar{z} \to -\infty$, (5.94a), to find the constant of integration. Using the other matching condition for $Q^{(0)}$ and $Q^{(0)}_{\mathrm{SiO}}$ as $\bar{z} \to +\infty$, (5.94b), we obtain a relationship between the total mass fluxes in regions I and III,

$$Q_{\mathrm{III}} = \left(1 - \frac{b_{\mathrm{II}} Y_{\mathrm{crat}}}{c_{\mathrm{II}}}\right) Q_{\mathrm{I}}. \tag{5.97}$$

To obtain the second first integral, we combine (5.91a) and (5.91c), giving

$$c_{\mathrm{II}} \frac{\partial \bar{T}^{(2)}}{\partial \bar{z}} + \bar{a}_{\mathrm{II}} \bar{Q}^{(0)}_{\mathrm{SiO}} = B, \tag{5.98}$$

where B is a constant. Next, we note that in region II,

$$\frac{\partial T}{\partial z} \sim \frac{\partial \bar{T}^{(2)}}{\partial \bar{z}} + o(1), \tag{5.99}$$

so we may match the z-derivative of $T^{(0)}$ in regions I and III, to the $\bar{z}$-derivative of $\bar{T}^{(2)}$ in region II. Doing this as $\bar{z} \to \pm\infty$ allows us to eliminate B, and obtain the algebraic equation

$$\begin{aligned}(1 - T_{\mathrm{cond}})\,\mathrm{Pe_s}\beta_{\mathrm{I}} \frac{e^{\mathrm{Pe_s}\beta_{\mathrm{I}} Z^{(0)}}}{1 - e^{\mathrm{Pe_s}\beta_{\mathrm{I}} Z^{(0)}}} + \frac{a_{\mathrm{II}}}{c_{\mathrm{II}}} Y_{\mathrm{crat}} Q_{\mathrm{I}} \\ = (T_{\mathrm{surf}} - T_{\mathrm{cond}})\,\mathrm{Pe_s}\beta_{\mathrm{III}} \frac{e^{\mathrm{Pe_s}\beta_{\mathrm{III}}\left(Z^{(0)} - 1\right)}}{1 - e^{\mathrm{Pe_s}\beta_{\mathrm{III}}\left(Z^{(0)} - 1\right)}},\end{aligned} \tag{5.100}$$

which depends on Q_{I}, Q_{III} and $Z^{(0)}$. Hence, equations (5.95), (5.97), and (5.100) form a system of three algebraic equations we can solve for Q_{I}, Q_{III} and $Z^{(0)}$. This fully determines the leading-order outer solutions in regions I and III, (5.58) and (5.62), respectively. Moreover, since the coefficients of the reaction terms in the system of ODEs (5.91), defined in (5.92a)–(5.92c), appear only in ratios of each other in the algebraic system, the only parameters required to determine Q_{I}, Q_{III} and $Z^{(0)}$ are: the condensation temperature T_{cond}; the surface temperature T_{surf}; the Péclet number of the solid $\mathrm{Pe_s}$; the stoichiometric constants ν_{SiO} and ν_{CO}; the dimensionless enthalpy of the reaction η; and C_1, defined in (5.32), which we showed in (5.37) to be the inverse of the dimensionless advected energy flux in the solid. Therefore, if only the condensation reaction occurs, then the position at which condensation occurs does not, to leading-order, actually depend on the Damköhler number, and hence on the reaction rate itself, only on the form in which the reaction rate depends on temperature. The presence of other reactions which provide heating would change the location of the condensation, and we discuss how this analysis can be extended to this situation in Section 5.4.

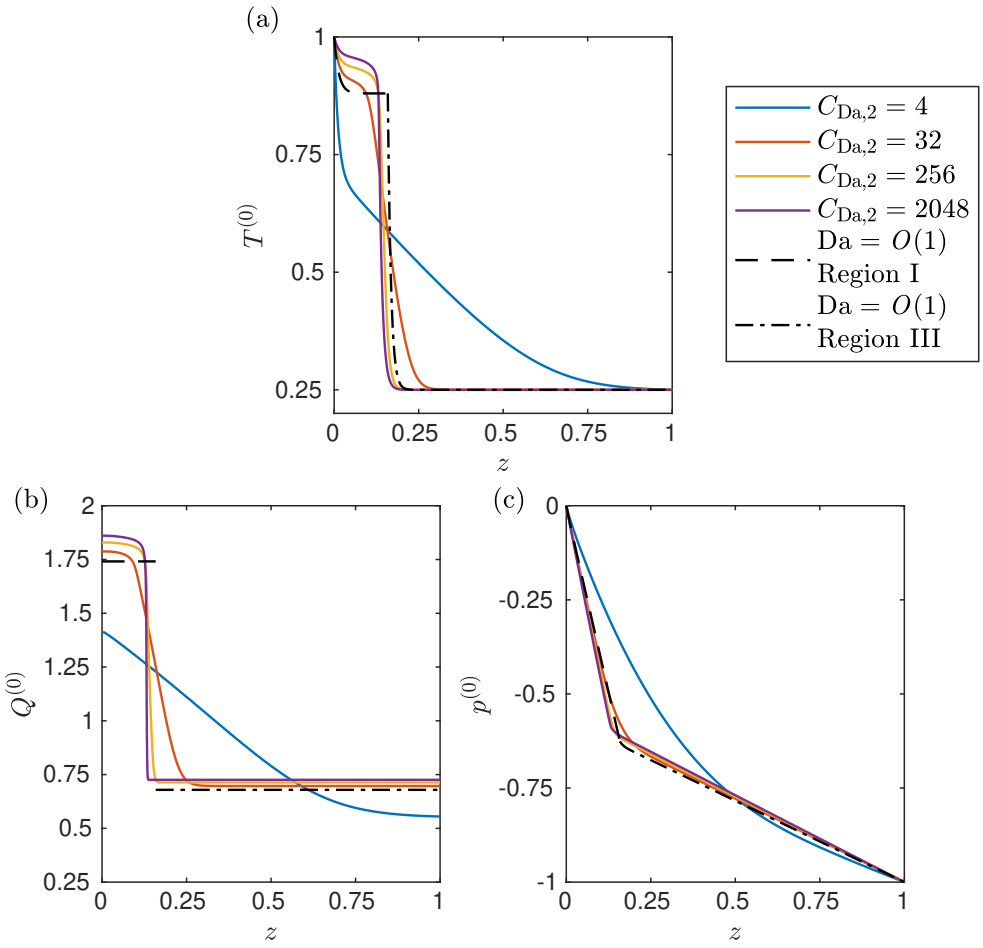


Figure 5.6: Numerical solutions of the slow reactions model, shown as solid lines for different values of $C_{\mathrm{Da},2}$, and the outer solutions to the fast reaction model, with region I shown by a dashed line and region III shown by a dash-dot line. The fixed parameter values are $\Gamma = 0.025$, $C_\Lambda = 10$, $|\mathcal{C}_\mathrm{s}| = 16 - \pi$, $\xi = 0.01$, $\mathrm{Pe}_\mathrm{s} = 256$, with the other values given in Table 2.3.

In Figure 5.6 we compare the outer solutions of the fast reaction model in regions I and III, (5.58) and (5.62), respectively, to numerical solutions of the slow reaction model, (5.33) and (5.36), as we increase the size of $C_{\mathrm{Da},2}$ in the slow reaction model. We set $C_{\mathrm{Da},1} = 0$ and all other parameters are kept at the same industrially-relevant parameter values for both models. There is good agreement in the position at which the reaction will occur between both models, but the agreement between the temperature and mass flux in region I is fairly poor. However, we recall the correct asymptotic expansion for the fast reaction model, (5.54), has a correction of size $\epsilon^{1/2}\log(\epsilon^{-1})$. Hence, even for the smallest industrially-relevant aspect ratio of the channel, given as $\epsilon = 3.33 \times 10^{-4}$ in Table 2.3, gives a correction of size 0.15. Hence, the converge of the asymptotic solution to the fast reaction model is fairly poor, and the difference

between the solutions of the slow and fast solutions is within the error we would expect.

5.4 Discussion

In this chapter, we considered the model for the coupled behaviour of the gas and solid in the industrially-relevant limit of small reduced Reynolds number. In Section 5.2, we used asymptotic analysis to derive a set of one-dimensional ODEs which govern the leading-order behaviour of the coupled system, for an arbitrary set of reactions, under the assumption the that Damköhler number of the reactions was small, and found that this implied reactions would occur slowly along the entire length of the channel. We were able to solve the problem analytically for the special case of no reactions, and the more general case numerically using MATLAB's built-in bvp solver bvp5c. We showed that without reactions, a unique steady solution always exists for the model. We also obtained a condition for the transition between solutions where the net flux of heat through the furnace moves downwards with the solid, and when it will move upwards with the gas. Using our estimates of the industrially-relevant parameter values, we found that the majority of heating occurred in a narrow boundary layer adjacent to the crater and was primarily due to diffusive heat transfer from the crater. This implied that the SiO condensation reaction began almost immediately, and using our reaction model, it occurred over the whole height of the furnace, unless the reduced Damköhler numbers were high enough to consume all of the SiO. However, by decreasing the size of the Péclet number by a single order of magnitude, we found that the start of condensation could be delayed to partway up the furnace. This is interesting industrially, as it suggests that the height at which a crust of condensed material (which must be broken up manually by the stoking process) will form is sensitive to the properties of the solid material.

To investigate the dependence of the position of the condensation reaction further, in Section 5.3 we consider the behaviour of the model for a single, strongly temperature-dependent reaction with order unity Damköhler number using the method of matched asymptotics. We found an asymptotic structure similar to that for a flame [43], with the reaction confined to a narrow region whose position must be determined as part of the solution. While we were unable to obtain a solution in this narrow region, we were able to extract sufficient information through matching to obtain a simple set of algebraic equations to determine the leading-order outer solutions away from the reaction, and the position of the reacting layer. A key property of these

equations, potentially making them very useful for industrial applications is that the rate of reaction does not appear within the algebraic system; since there is limited data for many of the reactions in the furnace, this gives our model a great advantage over others, such as [78], who also considered the position of condensate deposition in a furnace.

The preliminary analysis of the coupled behaviour between the gas and the solid for small reduced Reynolds number performed in this chapter, has shown that the model has some very interesting, and possibly industrially-relevant behaviour in this limit. A next step could be to consider parameter sweeps of the Péclet number, and ratio of gas and solid thermal conductivities, to explore the effect of variation in the properties of the raw materials. Also, unlike the previous chapters, the models considered here are simple enough that their time-dependent behaviour could reasonably be explored. This would allow us to understand how the temperature in the furnace evolves over a single stoking cycle, and so give an indication as to whether the steady solutions from Chapter 4 would ever be reached in a real furnace.

The approach outlined in Section 5.3 could be extended to also incorporate additional reactions j where $\mathrm{Da}_j \ll 1$, using the analysis from Section 5.2 in the outer regions. However, without an analytic solution for the slow reaction problem, such as found in Appendix D, for the special case where the reaction rate is linearly proportional to temperature, it would be necessary to obtain a numerical solution to the problem in each region.

None of the results in this chapter showed any evidence of a non-montonic pressure solution, despite the results of Chapter 4 suggesting that such solutions are possible for small reduced Reynolds number without reactions (see Figure 4.5). It would therefore be interesting to see if by proceeding to $O(\epsilon)$ in the asymptotic solution, if we were able to predict this onset of non-montonicity, and hence gain mechanistic insight into both the cause of this phenomenon and its stability.

Chapter 6

Discussion

To conclude, we discuss and summarise the research presented in this thesis. In Section 6.1 we summarise our work and highlight the key findings. In Section 6.2 we discuss some possible extensions of our model and analysis. Finally, in Section 6.3, we discuss the practical implications of our results for silicon furnace operators. We also describe the insight our results gives to those developing improved models of silicon furnaces in future.

6.1 Summary of results

In this thesis, we have developed a detailed model for the flow of gas ascending through the charge material in a silicon furnace, coupled to a simple model for the descending solid material, based on the idealisation of the microstructure of the charge as a solid perforated by a regular array of channels. The coupling occurs through heat transfer between the phases and exothermic reactions occurring on the gas-solid interface. This model, which is presented in Chapter 2, represents a formidable challenge to solve numerically due to the non-linear governing equations, counter-current motion of the gases and solid, and the disparate size of the parameter values in the model. This motivated us to consider simplified forms of this model for the remainder of the thesis to gain insight into the crucial physical and chemical effects.

In Chapter 3, we studied the problem of a steady single-phase gas flow in a narrow channel subject to an imposed temperature on the walls, to gain insight into the behaviour of the gas in the full model. We derived a set of reduced models in the limit of small aspect ratio of the channel and small pressure drop along the channel, considering the full range of industrially-relevant reduced Reynolds numbers, $\epsilon^2\mathrm{Re}$. The solutions of these reduced models were validated against solutions of the full compressible Navier-Stokes equations, obtained using the finite element software

COMSOL. When considering the $\epsilon^2\mathrm{Re} = O(1)$ limit, we predict a bifurcation, with two solutions with different mass fluxes below a critical reduced Reynolds number and no solutions above the critical reduced Reynolds number. However, when considering the behaviour for large $\epsilon^2\mathrm{Re}$, which brought internal heating of the gas into the energy equation, and was previously neglected, we found that the bifurcation diagram transformed into an 'S'-shaped curve, meaning a solution existed for all $\epsilon^2\mathrm{Re}$, with three solutions existing in a finite interval. However, to solve for the behaviour in this limit, we considered a self-consistent composite model which is not a valid asymptotic limit of the problem. While all our numerical solutions to the compressible Navier-Stokes equations agreed with the prediction of the reduced models, COMSOL was unable to converge to some solutions our reduced models predicted. As these solutions corresponded almost exactly with solutions to the reduced model with non-monotonic pressure profiles, we conjectured that this suggested these solutions were unstable. Our results also showed that when $\epsilon^2\mathrm{Re}$ is small, to leading-order the gas temperature would equal the temperature of the surrounding solid, whereas for larger values of $\epsilon^2\mathrm{Re}$, the gas could become significantly hotter than the solid.

In Chapter 4, we considered a simplified version of the coupled model for the gases and solid based on the industrially-relevant parameter values. Informed by our results from Chapter 3, we focused on the case $\epsilon^2\mathrm{Re} = O(1)$, believing it must be the correct limit to match the observation that, in the furnace gases appear to cool as they pass through the charge, but still exit the furnace at a hotter temperature than the surrounding solid. However, the resulting numerical problem proved challenging to solve numerically, since the industrially-relevant solutions lies close to a region of solution space where the solid temperature becomes negative, with the solver often stepping into that region, and hence crashing. Therefore, we focused on two slightly simpler problems: first, where there are no reactions between the gases and solid; and second, where the solid temperature is imposed. When solving the coupled problem without reactions, we found a similar solution structure to the single-phase model, with two steady solutions below a critical reduced Reynolds number, and no steady solution above. We also demonstrated this model could be used to investigate the validity of the common constitutive relationship that heat exchange between different phases in porous media is linearly proportional to the difference in temperatures between the phases. We found the constitutive relation to be generally valid when $\epsilon^2\mathrm{Re} < 1$, but broke down when $\epsilon^2\mathrm{Re} > 1$. The constitutive relationship also broke down in a narrow layer near the crater for all values of $\epsilon^2\mathrm{Re}$, suggesting instead a power law in difference in temperature with an exponent of $2/3$ might be more appropriate. When

considering the gas problem with reactions, subject to an imposed wall temperature, we again found the solution structure of two solutions below a critical value of $\epsilon^2\mathrm{Re}$ and none above. However, we did find that increasing the rate of the condensation of SiO reaction would lower this critical value. Combining the insight gained from these simplified models, we concluded that the coupled problem with reactions was unlikely to have any steady solutions for $\epsilon^2\mathrm{Re} > 1$. The observations of silicon furnace are therefore best explained in terms of our model as either examples of unsteady solutions, or by recalling from Chapter 1, that the temperature measurements of the outwards flowing gas are not taken at the immediate surface of the charge, so may be substantially altered by the combustion of the material in the furnace hood.

In Chapter 5, motivated by the conclusion of Chapter 4, we considered the behaviour of the coupled model in the limit of small reduced Reynolds number. This provided a much simpler model, albeit one where the gas and solids share a common temperature at leading-order. In the limit of small Damköhler numbers, which express the ratio between the rate of reaction and the rate of diffusion of SiO, the reactions occurred along the entire length of the channel and the problem reduced to a simple one-dimensional BVP which could be solved numerically. We found that the behaviour of the solution changed depending on the direction of net transport of heat, as is typical of counter-current flow problems [48]. As condensate deposited by reaction 2 in (1.2) is often found in narrow bands in the furnace, we also considered the limit of order unity Damköhler number with a strongly temperature-dependent reaction rate. This analysis followed a very similar structure to that typically used for flames, with the reaction confined to a narrow region in the channel [43]. Although we were unable fully solve the problem with order unity Damköhler number, we were able extract sufficient information to obtain a set of algebraic equations governing equations for the position at which the condensation reaction occurs.

6.2 Future work

There is a wide range of possible extensions to the work presented here, either to improve the applicability of our results to silicon furnaces, or from mathematical interest. We discuss these below. Note, we do not address improving the performance of the numerical solver in Chapter 4 here, as this is discussed within that chapter.

Reactions and conservation of mass The model as presented in Chapter 2 is currently unphysical as the reactions do not conserve mass. Currently gas can be created or removed by the reactions, but no corresponding change will occur

in the solid. To fix this, we would need to treat the interface as a free-boundary, whose position must be determined as part of the solution by a kinematic condition. Once this effect is included in the model, it would become possible to investigate the effect of clogging of the gas channel due to condensate deposited by reaction 2. Extending our analysis of the coupled model in the $\epsilon^2\mathrm{Re} \ll 1$ limit would be relatively straightforward, as we would simply find the cross-sections now depend on height. However, extending the numerical methods used for the $\epsilon^2\mathrm{Re} = O(1)$ limit to account for an evolving domain would more complicated. A possible approach would be to use a front fixing method, as described in [14], to map the problem to a fixed domain.

Throughout this thesis we have assumed the rate of reaction 2, the condensation reaction tends to a constant rate below the condensation temperature, taken to be 2000 K. However, in [8] it is shown experimentally that the rate actually begins to decrease again below 1920 K, becoming zero around 1200 K, which is assumed to be due to the activation energy of the reaction. Therefore a large amount of condensate can be deposited in a narrow layer, but some SiO will still leave the furnace. This is interesting mathematically, as the reaction rate becomes exponentially small in both directions, creating additional asymptotic structures, and industrially, as allowing a fraction of SiO to escape the furnace, even in the presence of a fast condensation reaction, seems to reflect the actual process occurring in the furnace.

It would also be interesting to explore the effect of including some of the endothermic reactions from (1.2) into our model. However, with the exception of reaction 5, the other endothermic reactions require multiple solid (or liquid) species to be able to react together. Therefore the solid model would have to be extended to account for the amounts of different solid species. Further, it would be strange to restrict these reactions to the gas-solid interface, and so we would also need to treat Ω_s as a porous medium, complicating the model still further.

Case I as a valid asymptotic limit An unsatisfactory part of Chapter 3 is that case I, was not an asymptotic limit of the full model. For this reason we chose not to consider its behaviour as part of the coupled model in the subsequent chapters. However, if we instead considered the asymptotic limit $\epsilon^2\mathrm{Re} = O(1)$, $\Delta p = O(1)$, then we also obtain the governing equations for case I, (3.8), except the equation of state (3.8e) is replaced by the full ideal gas law (3.2e). We did not consider this limit in this thesis, as our numerical methods rely heavily on transforming the problem using

the substitution $1 = \rho T$. However, we could instead rewrite (3.2e) as

$$1 = \frac{\rho T}{1 + \Delta p\, p}, \tag{6.1}$$

and by substituting this into the governing equations (3.8c) and (3.8d), introducing the streamfunction (3.12), and using that $\partial p/\partial x = 0$, obtain the new transformed problem

$$\epsilon^2 \mathrm{Re}\left(\psi_{xz}\psi_x T + \psi_x^2 T_z - \psi_z \left(\psi_x T\right)_x\right) = \left(\frac{\Delta p \psi_x^2 T}{1 + \Delta p p} - (1 + \Delta p\, p)\right) p_z + \left(\left(\mu \left(\psi_x T\right)_x\right)\right)_x, \tag{6.2a}$$

$$\epsilon^2 \mathrm{Re}\left(\psi_x T_z - \psi_z T_x\right) = \frac{1}{\mathrm{Pr}} \left(k T_x\right)_x + \mathrm{Ec}\left(\frac{\psi_x T p_z}{1 + \Delta p\, p} + \frac{\mu}{\left(1 + \Delta p\, p\right)^2} \left(\left(\psi_x T\right)_x\right)^2\right), \tag{6.2b}$$

which can be solved by a similar method used for the original transformed problem (3.13). Note that here we have not differentiated the momentum equation with respect to x, as it is no longer possible to eliminate pressure from the governing equations. We conjecture that the results from this new limit would be very similar to those for case I. This is because the only additional term, compared to case I, is $\Delta p\, p$, and from Figure 3.8, we can see that $\Delta p\, p \ll 1$ (since the solid lines are always orders of magnitude smaller than the corresponding dashed lines). Hence, we postulate that solutions to the new problem to only be a small perturbation from the solution to case I.

Stability of solutions with non-monotonic pressure A major question about the results obtained in this thesis, but particularly Chapter 3, is the stability of the different solution branches identified. In Chapter 3, we conjectured that those solutions with non-monotonic pressure profiles were unstable, as typically was unable to converge to them, but would readily converge to solutions on the same branch for different parameter values, if the reduced model predicted the pressure profile to be monotonic. In [70] a similar problem was studied to case III, but with $\Delta p = O(1)$, and a constant heat flux on the walls, which they found had a maximum value for which steady solutions would exist. When they carried out time-dependent simulations with values beyond this critical value they found the gas would exit out of both the inlet and and outlet, and the axial velocity tended to zero. As we have no equivalent existence problem for case III, we are primarily interested in time-dependent simulations of cases I and II. Such simulations would be challenging to carry out, as our numerical method for cases I and II is based on a streamfunction formulation, and it is not possible to define a streamfunction for an unsteady compressible flow unless $\partial \rho/\partial t = 0$, so that

the conservation of mass equation (3.2a) is satisfied. An alternative approach would be to perform a linear stability analysis, but we do not pursue this further in this thesis, due to the complicated two-dimensional base state.

Constant heat flux into a gas channel Throughout Chapter 3, we investigated the behaviour of the model of a single-phase gas subject to a prescribed wall temperature. It would be interesting to investigate how the behaviour of the model changes when the prescribed wall temperature condition is replaced with a constant heat flux. In particular, we could investigate how the bound on the maximum applicable heat flux for steady solutions found by [70] in the limit $\epsilon^2\mathrm{Re} \to 0$ varies as $\epsilon^2\mathrm{Re}$ increases.

Homogenisation and macroscale heat transfer The setup of the model presented would allow for homogenisation via the method of multiple scales to be easily used to obtain effective equations for the macroscale behaviour of our coupled model in the xy-plane [15]. The behaviour of horizontal temperature gradients is interesting industrially, since the material nearer the electrode is hotter, and hence consumed more rapidly [33]. However, the geometry of the channels prohibits any macroscale transverse motion of the gas. Hence homogenisation would be most useful, in conjunction with the extension of an evolving channel due to condensation as discussed above, as a tool to see how the shape of the channels evolves with distance from the electrodes over time.

In Section 4.3.2, we investigated the validity of the macroscale constitutive law that heat exchange between gases and solid in porous medium is linearly proportional to the difference in average temperatures. However, the current coupled model was too complicated to easily explore the parameter space, or obtain analytic expressions. It would be interesting to instead consider a simpler problem in a similar geometry, for example with a prescribed incompressible fluid flowing through the gas channel. Then, only the temperature problems for the fluid and solid would remain, allowing the full range of parameter values to be explored using a combination asymptotic and numerical techniques, and the relationship between the heat flux and difference of average temperatures could be studied rigorously.

6.3 Industrial implications

The motivation for this thesis was to use mathematical modelling to further our understanding of the behaviour of a silicon furnace, with a particular focus on the role movement of material plays. We have focused on understanding the behaviour of the gas flowing through the furnace, due to its important role in the temperature

distribution by transporting heat up from the crater, and in determining the chemical behaviour, through the distribution of SiO gas. Our approach of developing a physics-based model for the mesoscale behaviour of the gas within the charge, which we describe in Chapter 2, meant that all the parameters in our model could be readily estimated from the physical properties of the materials involved. In contrast, many of the previous models of silicon furnaces have contained lumped parameters describing a macroscale quantity of the system which cannot be measured in practice. While the ease of parameterisation of our model meant that the full problem was too complicated to solve, we were able to exploit the size of the dimensionless parameters to derive simplified models, which could be solved either numerically or analytically. Our approach of simplifying the charge structure to an array of vertical channels meant that a solution on the microscale, of a single channel has a clear interpretation as macroscale behaviour.

While the model in Chapter 3 of the gas flow for an imposed temperature does not apply directly to the furnace, it would be directly useful for other applications such as heat exchangers.

The models in Chapters 4 and 5 consider the limits where $\epsilon^2\mathrm{Re} = O(1)$, and $\epsilon^2\mathrm{Re} \ll 1$, respectively. We found that: in the former the temperatures of the gases and solid could differ, although the existence of a steady gas flow seems unlikely; and in the latter, the temperatures of the gas and solid will be approximately equal, and a steady gas flow likely does exist. To show when this transition will occur physically, in Figure 6.1, we show the value of $\epsilon^2\mathrm{Re} = 1$, as a function of crater pressure p^*_{crat}, and channel radius a^*. The other dimensional parameter values are given in Table 2.1 and have well established values. This shows that if the channel radius is below 2 mm, we always be in the $\epsilon^2\mathrm{Re} < 1$ regime in the furnace and gas temperature will equal the solid, irrespective of the crater pressure. Conversely, if the channel radius is above 5 mm, then $\epsilon^2\mathrm{Re} > 1$ for almost all crater pressures, and the gas will always be hotter than the solid. However knowing, for example, the density and bulk density of the charge material is not sufficient information to estimate the size of the channels. Instead, data such as is reported in [63], where the pressure drop as air is blown through cold charge material, in an attempt to measure its permeability, are needed to estimate the radii of channels equivalent to real charge material.

In Chapter 5, we obtained an analytic relationship between the pressure gradient and the mass flux when $\epsilon^2\mathrm{Re} \ll 1$, (5.33d), which we can re-write as

$$\frac{\partial p^{(0)}}{\partial z} = -\frac{8}{\pi}\frac{Q^{(0)}}{\rho^{(0)}} = -\frac{8}{\pi}\int_{\mathcal{C}_{\mathrm{g}}} w^{(0)} dA, \tag{6.3}$$

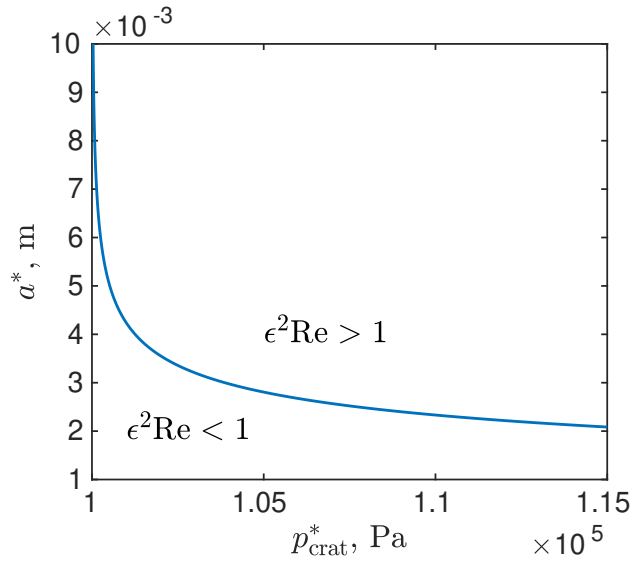


Figure 6.1: The reduced Reynolds number $\epsilon^2\mathrm{Re}$ varying with the crater pressure p^*_{crat} and channel radius a^*, with the other parameter values given in Table 2.1.

using that $\rho^{(0)}$ depends only on z. Hence, we have that the average fluid velocity in the z-direction, will be is linearly proportional to the pressure gradient in the z-direction, in other words, the behaviour of the leading-order gas flow when $\epsilon^2\mathrm{Re} \ll 1$ is simply Darcy's law [55], which is unaffected by the non-isothermal nature of the flow. This is not necessarily obvious, since it is known the permeability of a porous material with gas flowing through it will differ from its permeability to a liquid, and that the effective permeability for a gas will depend on pressure and the physical properties of the gas [94]. As previously mentioned the gases and solids share a common temperature at leading-order in this limit. We also found no correction to Darcy's law to account for the change in momentum due to the gas flux into the solid, which again is not obvious, as such corrections have been found in other applications [41]. When $\epsilon^2\mathrm{Re} = O(1)$, the situation considered in Chapter 4, we found that the relationship between pressure and mass flux is nonlinear and we found no equivalent expression to (6.3).

When modelling the temperature(s) in the furnace our results indicate that when $\epsilon^2\mathrm{Re}$ is small, the furnace should either be modelled as having a common temperature for both the gas and solid, or with a linear exchange of heat between the phases with a large heat transfer coefficient (i.e. the constant of proportionality). If $\epsilon^2\mathrm{Re} = O(1)$, then our work indicates that the difference in temperature plays a small role in the rate of heat exchange, so the linear constitutive law is a poor choice, despite it prevalence in the literature.

The work in this thesis has considered the behaviour of the temperature distribution of silicon furnaces under a variety of operating conditions. For any realistic set of parameter values, both with and without exothermic reactions, we have found that a significant portion of the heating of the solid material occurs in a thin layer near the crater wall, with the energy supplied by diffusive heat transfer from the crater. Since [45] showed that electrical heating effects also only penetrate a small distance from the crater, our combined work would appear to imply that the solid material remains relatively cold for much of its descent through the furnace. This in turn suggests that the majority of the chemical behaviour of the furnace will be confined to the narrow hot region, where the temperature is sufficient for the endothermic, silicon creating reactions.

Appendix A

Physical properties of CO, SiO, and gas mixtures

A.1 Kinetic gas theory for transport coefficients

To apply the binary mixture model in Chapter 2, we need a way to estimate the viscosity, thermal conductivity, and binary diffusivity in the mixture. To do this we use the kinetic theory of dilute gases and mixtures (also called Chapman-Enskog theory), described in [29]. Here, dilute means that molecular collisions in the mixture are all assumed to involve only two molecules. To apply the kinetic theory of gases we must specify a potential governing the interactions between pairs of molecules; for this we choose to use the Lennard-Jones potential, which is the simplest model for soft attractive and repulsive interactions between non-polar molecules. The Lennard-Jones potential depends upon two parameters, σ_X [Å=10^{-10}m], the collision diameter for low energy collisions (the distance where the interaction potential is zero), and $\epsilon_X/k_{\text{Bolt}}$ [K], where ϵ_X is the depth of the potential well (the maximum energy of attraction) and k_{Bolt} is the Boltzmann constant. Values of these parameters for interactions between two molecules of CO and SiO respectively are given in table A.1. To model the mixture, we also need to parameterise the Lennard-Jones potential for interactions between a CO and a SiO molecule. For this we use empirical 'combining laws', dependent on the parameters for each pure gas species,

$$\sigma_{XY} = \frac{1}{2}\left(\sigma_X + \sigma_Y\right), \qquad \epsilon_{XY} = \sqrt{\epsilon_X \epsilon_Y}. \tag{A.1}$$

Species	σ_X	$\epsilon_X/k_{\text{Bolt}}$	Reference
CO (g)	3.706 Å	88 K	[29]
SiO (g)	3.374 Å	569 K	[54]

Table A.1: The intermolecular pair potential parameters for CO (g) and SiO (g).

A.1.1 Viscosity

From the kinetic theory of dilute gases, the viscosity μ_X^* [kg m^{-1} sec-1] of a pure monatomic gas of species X is given by

$$\mu_X^* = \left(2.67 \times 10^{-6}\right) \frac{\sqrt{T^* \hat{M}_X}}{\sigma_X^2 \Omega^{(2,2)} \left(\frac{T^* k_{\text{Bolt}}}{\epsilon_X}\right)}, \tag{A.2}$$

where $\hat{M}_X$ [g mol^{-1}] is the molecular weight of species X, and $\Omega^{(2,2)}$ is a dimensionless function determined by a series of integrals describing the interaction between a pair of molecules. To find the value of $\Omega^{(2,2)}$ we use linear interpolation of the values tabulated in [29]. To compute the viscosity of the mixture, we use an empirical expression from [6], giving

$$\mu_{\text{mix}}^* = \sum_X \left[\frac{(c_X^*/c^*)\, \mu_X^*}{\sum_Y \left[(c_Y^*/c^*)\, \Phi_{XY}\right]} \right], \tag{A.3}$$

where

$$\Phi_{XY} = \frac{1}{\sqrt{8}} \left(1 + \frac{\hat{M}_X}{\hat{M}_Y}\right)^{-1/2} \left(1 + \left(\frac{\mu_X^*}{\mu_{Y^*}}\right)^{1/2} \left(\frac{\hat{M}_Y}{\hat{M}_X}\right)^{1/4}\right)^2. \tag{A.4}$$

This expression has the property that as the fraction of species X tends to one, the viscosity of the mixture tends to the viscosity of that species. From (A.3), it is clear that viscosity will depend on the temperature and the amount of each species, but not on the pressure. In Figure A.1 we plot the viscosity of CO and SiO from (A.2), the mixture viscosity from (A.3) using the mass fraction at the crater given in table 2.1, all as functions of temperature. This plot shows that the difference between the viscosities of the two species will remain small over the temperature range of interest, and so in general the temperature of the gas will play a more important role than the mass fraction in determining the mixture viscosity.

Figure A.1 also shows the viscosity of CO predicted by a power law model,

$$\mu_{\text{CO}}^* = \mu_{\text{CO,ref}}^* \left(\frac{T^*}{T_{\text{ref}}^*}\right)^n, \tag{A.5}$$

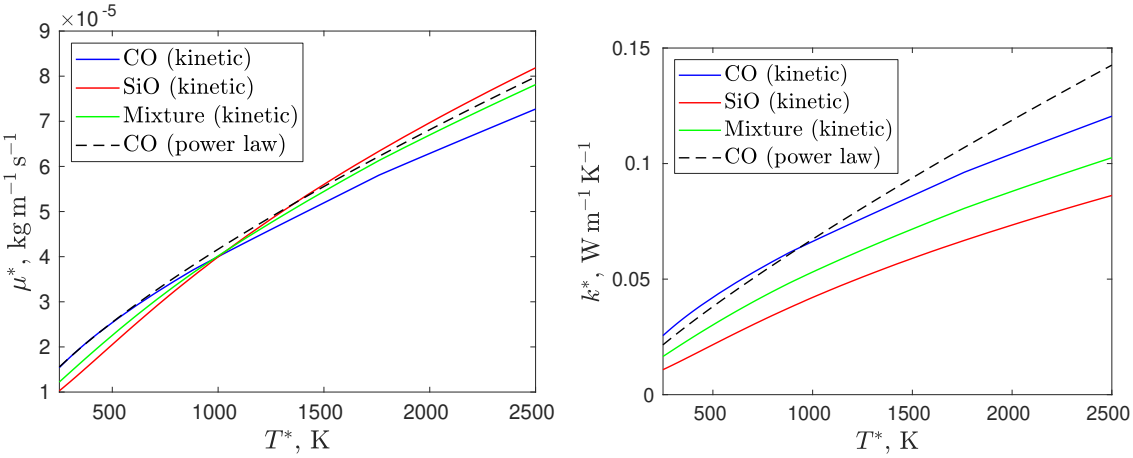


Figure A.1: (a) The viscosity and (b) the thermal conductivity of CO, SiO, and a mixture with equal molar fractions of CO and SiO calculated using kinetic gas theory are shown varying with temperature. The model for viscosity and thermal conductivity of CO gas calculated using the empirical power law model from [91] are is shown by black dashed lines.

where $\mu^*_{\mathrm{CO,ref}}$ is a reference value of the viscosity at temperature T^*_{ref}, and n is a dimensionless parameter, using parameter values from [91]. Comparing between the two models for CO, we see very good agreement at lower temperatures, as this is the range of the experimental data used to fit the parameters in the power law, and reasonable agreement at the higher temperatures. This suggests the power law model (A.5), which is much cheaper to evaluate numerically, are likely to be qualitatively similar to the kinetic model.

A.1.2 Thermal conductivity

For the thermal conductivity k^*_X $[\mathrm{J\,m^{-1}\,s^{-1}\,K^{-1}}]$ of species X, we do not use the expression for a monotonic gas as we did for viscosity. This is because the thermal conductivity of polyatomic gases is poorly approximated by the theory of monatomic gases, to a greater degree than viscosity, since there can be an exchange between the internal kinetic energy of particles in collisions involving polyatomic molecules, but not when both molecules are monatomic [29]. Instead, we use the empirical Eucken formula [29] for polyatomic molecules,

$$k^*_X = \frac{1000R^*}{\hat{M}_X}\left(\frac{1}{\gamma-1}+\frac{9}{4}\right)\mu^*_X, \tag{A.6}$$

where R^* is the universal gas constant $[\mathrm{J\,K^{-1}\,mol^{-1}}]$ and γ is defined in (2.71). We again use an empirical expression from [6] to combine these to get the thermal con-

ductivity of the mixture, namely

$$k^*_{\text{mix}} = \sum_X \left[\frac{(c^*_X/c^*)\, k^*_X}{\sum_Y \left[(c^*_Y/c^*)\, \Phi_{XY} \right]} \right], \tag{A.7}$$

where Φ_{XY} was defined in (A.4). The thermal conductivities of CO and SiO from (A.6) and the mixture conductivity from (A.7) are plotted in Figure A.1. As for viscosity, a power law model with experimentally determined parameters [91],

$$k^*_{\text{CO}} = k^*_{\text{CO,ref}} \left(\frac{T^*}{T^*_{\text{ref}}} \right)^{\nu}, \tag{A.8}$$

is also plotted in Figure A.1. These show reasonable agreement between the power law and the kinetic theory values for CO, but the agreement is worse than for viscosity, as (A.6) is empirical.

A.1.3 Binary diffusion coefficient

The value of binary diffusion coefficient $\mathcal{D}^*_{XY}$ [$\text{m}^2\,\text{sec}^{-1}$] between two different species of gas X and Y, can be estimated using dilute kinetic gas theory, and is found by [29], to be given by,

$$\mathcal{D}^*_{XY} = \left(2.67 \times 10^{-2}\right) \frac{\sqrt{(T^*)^3 \, \frac{\hat{M}_X + \hat{M}_Y}{2\hat{M}_X \hat{M}_Y}}}{p^* \sigma^2_{XY} \Omega^{(1,1)} \left(\frac{T^* k_{\text{Bolt}}}{\epsilon_{XY}} \right)}, \tag{A.9}$$

where p^* is the pressure [Pa] and $\Omega^{(1,1)}_{XY}$ is another dimensionless function whose values come from evaluating integrals describing the dynamics of the interaction between the molecules. As before, we evaluate $\Omega^{(1,1)}$ by linearly interpolating the values tabulated in [29]. Note that unlike μ^*_{mix} and k^*_{mix}, $\mathcal{D}^*_{XY}$ does not depend on the molar fraction of each species. However, it does depend on the pressure as well as the temperature.

A.2 Specific heat capacity

As SiO gas only exists at very high temperatures, we also need a method to estimate its thermal conductivity, in order to apply the binary mixture model from Chapter 2. For consistency, we will also estimate the specific heat capacity of CO using the same method.

Using statistical mechanics, and the principle of equipartition of energy, it is shown, by e.g. [11], that the specific heat capacity of species X , $c^*_{p,X}$ [$\text{J}\,\text{kg}^{-1}\,\text{K}^{-1}$], is given by

$$c^*_{p,X} = \left(\frac{f_X + 2}{2} \right) \frac{R^*}{M_X}, \tag{A.10}$$

where f_X is the number of internal degrees of freedom. As diatomic molecules, both CO and SiO have seven degrees of freedom: three translational, two rotational, and two vibrational. At room temperature, quantum effects mean that there is no contribution from the vibrational degrees of freedom to the heat capacity for many common gases [11]. However, due to the high temperatures in the furnace, we will assume that these degrees of freedom have 'unfrozen' and contribute fully to the heat capacity. For CO, (A.10) predicts $c^*_{p,\mathrm{CO}} = 1.34 \times 10^3\,\mathrm{J\,kg^{-1}\,K^{-1}}$, which is very close to the experimental value of $1.29 \times 10^3\,\mathrm{J\,kg^{-1}\,K^{-1}}$ at 2800 K given in [91].

Appendix B

Dimensionless governing equations for the gas in cylindrical coordinates

The dimensionless governing equations for the gas (2.68) are given, in cylindrical coordinates, by

$$\alpha\frac{\partial\rho}{\partial t}+\frac{1}{r}\frac{\partial\left(r\rho u_r\right)}{\partial r}+\frac{1}{r}\frac{\partial\left(\rho v_\theta\right)}{\partial\theta}+\frac{\partial\left(\rho w_z\right)}{\partial z}=0, \tag{B.1a}$$

$$\begin{aligned}\epsilon^2\mathrm{Re}\left(\alpha\frac{\partial\left(\rho u_r\right)}{\partial t}+\frac{1}{r}\frac{\partial\left(r\rho u_r u_r\right)}{\partial r}+\frac{1}{r}\frac{\partial\left(\rho u_r v_\theta\right)}{\partial\theta}+\frac{\partial\left(\rho u_r w_z\right)}{\partial z}-\frac{\rho v_\theta^2}{r}\right)\\ =-\frac{1}{\epsilon^2}\frac{\partial p}{\partial r}+\frac{1}{\epsilon}\frac{1}{r}\frac{\partial\left(r\tau_{rr}\right)}{\partial r}+\frac{1}{\epsilon}\frac{1}{r}\frac{\partial\tau_{r\theta}}{\partial\theta}+\frac{\partial\tau_{rz}}{\partial z}-\frac{1}{\epsilon}\frac{\tau_{\theta\theta}}{r},\end{aligned} \tag{B.1b}$$

$$\begin{aligned}\epsilon^2\mathrm{Re}\left(\alpha\frac{\partial\left(\rho v_\theta\right)}{\partial t}+\frac{1}{r}\frac{\partial\left(r\rho u_r v_\theta\right)}{\partial r}+\frac{1}{r}\frac{\partial\left(\rho v_\theta v_\theta\right)}{\partial\theta}+\frac{\partial\left(\rho v_\theta w_z\right)}{\partial z}+\frac{\rho u_r v_\theta}{r}\right)\\ =-\frac{1}{\epsilon^2}\frac{1}{r}\frac{\partial p}{\partial\theta}+\frac{1}{\epsilon}\frac{1}{r^2}\frac{\partial}{\partial r}\left(r^2\tau_{r\theta}\right)+\frac{1}{\epsilon}\frac{1}{r}\frac{\partial\tau_{\theta\theta}}{\partial\theta}+\frac{\partial\tau_{\theta z}}{\partial z},\end{aligned} \tag{B.1c}$$

$$\begin{aligned}\epsilon^2\mathrm{Re}\left(\alpha\frac{\partial\left(\rho w_z\right)}{\partial t}+\frac{1}{r}\frac{\partial\left(r\rho u_r w_z\right)}{\partial r}+\frac{1}{r}\frac{\partial\left(\rho v_\theta w_z\right)}{\partial\theta}+\frac{\partial\left(\rho w_z w_z\right)}{\partial z}\right)\\ =-\frac{\partial p}{\partial z}+\frac{1}{r}\frac{\partial\left(r\tau_{rz}\right)}{\partial r}+\frac{1}{r}\frac{\partial\tau_{\theta z}}{\partial\theta}+\epsilon\frac{\partial\tau_{zz}}{\partial z},\end{aligned} \tag{B.1d}$$

$$\epsilon^2\mathrm{Re}\left(\alpha\frac{\partial\left(\rho T\right)}{\partial t}+\frac{1}{r}\frac{\partial\left(r\rho u_r T\right)}{\partial r}+\frac{1}{r}\frac{\partial\left(\rho v_\theta T\right)}{\partial\theta}+\frac{\partial\left(\rho w_z T\right)}{\partial z}\right)$$
$$-\epsilon^2\mathrm{Re}\left(1-\kappa\right)\left(\alpha\frac{\partial\left(\rho TY\right)}{\partial t}+\frac{1}{r}\frac{\partial\left(r\rho u_r TY\right)}{\partial r}+\frac{1}{r}\frac{\partial\left(\rho v_\theta TY\right)}{\partial\theta}+\frac{\partial\left(\rho w_z TY\right)}{\partial z}\right)$$
$$=\frac{1}{\mathrm{Pr}}\frac{1}{r}\frac{\partial}{\partial r}\left(rk\frac{\partial T}{\partial r}\right)+\frac{1}{\mathrm{Pr}}\frac{1}{r}\frac{\partial}{\partial\theta}\left(\frac{1}{r}k\frac{\partial T}{\partial\theta}\right)+\frac{\epsilon^2}{\mathrm{Pr}}\frac{\partial}{\partial z}\left(k\frac{\partial T}{\partial z}\right)$$
$$+\mathrm{Ec}\left(\alpha\frac{\partial p}{\partial t}+u_r\frac{\partial p}{\partial r}+\frac{v_\theta}{r}\frac{\partial p}{\partial\theta}+w_z\frac{\partial p}{\partial z}\right)+\epsilon^2\mathrm{Ec}\Phi, \quad \text{(B.1e)}$$

$$\epsilon^2\mathrm{Re}\left(\alpha\frac{\partial\left(\rho Y\right)}{\partial t}+\frac{1}{r}\frac{\partial\left(r\rho u_r Y\right)}{\partial r}+\frac{1}{r}\frac{\partial\left(\rho v_\theta Y\right)}{\partial\theta}+\frac{\partial\left(\rho w_z Y\right)}{\partial z}\right)$$
$$=\frac{1}{\mathrm{Sc}}\frac{1}{r}\frac{\partial}{\partial r}\left(r\rho\mathcal{D}\frac{\partial Y}{\partial r}\right)+\frac{1}{\mathrm{Sc}}\frac{1}{r}\frac{\partial}{\partial\theta}\left(\frac{1}{r}\rho\mathcal{D}\frac{\partial Y}{\partial\theta}\right)+\frac{\epsilon^2}{\mathrm{Sc}}\frac{\partial}{\partial z}\left(\rho\mathcal{D}\frac{\partial Y}{\partial z}\right), \quad \text{(B.1f)}$$

$$\Delta p\, p+1=\rho T\left(1-\left(1-\mathcal{M}\right)Y\right), \quad \text{(B.1g)}$$

where the components of the dimensionless viscous stress tensor $\boldsymbol{\tau}$ are given by

$$\tau_{rr}=\epsilon\mu\left(2\frac{\partial u_r}{\partial r}-\frac{2}{3}\left(\frac{1}{r}\frac{\partial\left(ru_r\right)}{\partial r}+\frac{1}{r}\frac{\partial v_\theta}{\partial\theta}+\frac{\partial w_z}{\partial z}\right)\right), \quad \text{(B.2a)}$$
$$\tau_{\theta\theta}=\epsilon\mu\left(2\left(\frac{1}{r}\frac{\partial v_\theta}{\partial\theta}+\frac{u_r}{r}\right)-\frac{2}{3}\left(\frac{1}{r}\frac{\partial\left(ru_r\right)}{\partial r}+\frac{1}{r}\frac{\partial v_\theta}{\partial\theta}+\frac{\partial w_z}{\partial z}\right)\right), \quad \text{(B.2b)}$$
$$\tau_{zz}=\epsilon\mu\left(2\frac{\partial w_z}{\partial z}-\frac{2}{3}\left(\frac{1}{r}\frac{\partial\left(ru_r\right)}{\partial r}+\frac{1}{r}\frac{\partial v_\theta}{\partial\theta}+\frac{\partial w_z}{\partial z}\right)\right), \quad \text{(B.2c)}$$
$$\tau_{r\theta}=\epsilon\mu\left(r\frac{\partial}{\partial r}\left(\frac{v_\theta}{r}\right)+\frac{1}{r}\frac{\partial u_r}{\partial\theta}\right), \quad \text{(B.2d)}$$
$$\tau_{rz}=\mu\left(\frac{\partial w_z}{\partial r}+\epsilon^2\frac{\partial u_r}{\partial z}\right), \quad \text{(B.2e)}$$
$$\tau_{\theta z}=\mu\left(\epsilon^2\frac{\partial v_\theta}{\partial z}+\frac{1}{r}\frac{\partial w_z}{\partial\theta}\right), \quad \text{(B.2f)}$$

and the dimensionless viscous dissipation function Φ is given by

$$\frac{\Phi}{\mu}=2\left(\left(\frac{\partial u_r}{\partial r}\right)^2+\left(\frac{1}{r}\frac{\partial v_\theta}{\partial\theta}+\frac{u_r}{r}\right)^2+\left(\frac{\partial w_z}{\partial z}\right)^2\right)$$
$$+\left(r\frac{\partial}{\partial r}\left(\frac{v_\theta}{r}\right)+\frac{1}{r}\frac{\partial u_r}{\partial\theta}\right)^2+\left(\frac{1}{\epsilon}\frac{\partial w_z}{\partial\theta}+\epsilon\frac{\partial v_\theta}{\partial z}\right)^2+$$
$$\left(\epsilon\frac{\partial u_r}{\partial z}+\frac{1}{\epsilon}\frac{\partial w_z}{\partial r}\right)^2-\frac{2}{3}\left(\frac{1}{r}\frac{\partial(ru_r)}{\partial r}+\frac{1}{r}\frac{\partial v_\theta}{\partial\theta}+\frac{\partial w_z}{\partial z}\right)^2. \quad \text{(B.3)}$$

Appendix C

Finite difference schemes for solving reduced models

In this thesis, we solve three problems numerically via finite differences, namely the transformed problem for both cases I and II from Chapter 3, (3.12)–(3.16), and the transformed coupled model from Chapter 4, (4.29)–(4.36). Due to the similarities between the problems, we will present our finite difference scheme for a combined problem containing the union of the terms across all three models, essentially corresponding to the coupled model if the assumptions of case I rather than case II were used for the gas phase. The actual scheme used for each model is obtained by removing the unnecessary terms.

C.1 Methodology

C.1.1 Gas

In Ω_{g}, the variables ψ, T, and Y all depend on both x and z. We therefore apply the method of lines to discretise the x-derivatives in (3.13) and (4.29c), approximating them on a uniformly spaced mesh of $N_x + 2$ points; $x_i = i/(N_x + 1)$, for $i = 0, 1, \ldots, N_x + 1$. As (3.13a) contains third and fourth x-derivatives for T and ψ, respectively, we introduce ghost points x_{-1} and x_{N_x+2} to approximate these derivatives at the x_1, x_{N_x}. In order to have sufficient equations to determine the values of ψ, T, and Y at these ghost points, we also require the energy equation (3.13b) and the conservation of SiO equation (4.29c) to hold on the boundaries at x_0 and x_{N_x+1}. The integral in (3.14) is approximated using the trapezium rule.

Introducing the notation $\psi_i(z) = \psi(x_i, z)$, $\dot{\psi}_i = \partial\psi_i/\partial z$, and $\Delta x = x_i - x_{i-1}$, and

similarly for the other variables, (3.13a) becomes

$$\left(\frac{\dot{\psi}_{i+1}-2\dot{\psi}_i+\dot{\psi}_{i-1}}{(\Delta x)^2}\right)\left(\frac{\psi_{i+1}-\psi_{i-1}}{2\Delta x}\right)T_i + 2\left(\frac{\psi_{i+1}-2\psi_i+\psi_{i-1}}{(\Delta x)^2}\right)\left(\frac{\psi_{i+1}-\psi_{i-1}}{2\Delta x}\right)\dot{T}_i + \left(\frac{\psi_{i+1}-\psi_{i-1}}{2\Delta x}\right)^2\left(\frac{\dot{T}_{i+1}-\dot{T}_{i-1}}{2\Delta x}\right) - \dot{\psi}_i\left(\frac{\alpha_{i+1}-2\alpha_i+\alpha_{i-1}}{(\Delta x)^2}\right) = \frac{1}{\epsilon^2\mathrm{Re}}\left(\frac{\nu_{i+1}-2\nu_i+\nu_{i-1}}{(\Delta x)^2}\right), \quad \text{(C.1)}$$

for $i = 1, \ldots, N_x$; (3.13b) and (4.29c) become

$$\left(\frac{\psi_{i+1}-\psi_{i-1}}{2\Delta x}\right)\dot{T}_i - \dot{\psi}_i\left(\frac{T_{i+1}-T_{i-1}}{2\Delta x}\right) - \frac{\mathrm{Ec}}{\epsilon^2\mathrm{Re}}\left(\frac{\psi_{i+1}-\psi_{i-1}}{2\Delta x}\right)T_i\dot{p} = \frac{1}{\epsilon^2\mathrm{RePr}}\left(\frac{\chi_{i+1/2}-\chi_{i-1/2}}{\Delta x}\right) + \frac{\mathrm{Ec}}{\epsilon^2\mathrm{Re}}\frac{\nu_i^2}{\mu_i}, \quad \text{(C.2)}$$

and

$$\left(\frac{\psi_{i+1}-\psi_{i-1}}{2\Delta x}\right)\dot{Y}_i - \dot{\psi}_i\left(\frac{Y_{i+1}-Y_{i-1}}{2\Delta x}\right) = \frac{1}{\epsilon^2\mathrm{ReSc}}\left(\frac{\omega_{i+1/2}-\omega_{i-1/2}}{\Delta x}\right), \quad \text{(C.3)}$$

for $i = 0, \ldots, N_x + 1$; (3.14), (3.15), and (4.32) become

$$H = p + \epsilon^2\mathrm{Re}\frac{\Delta x}{2}\sum_{i=1}^{N_x+1}\left[T_i\left(\frac{\psi_{i+1}-\psi_{i-1}}{2\Delta x}\right)^2 + T_{i-1}\left(\frac{\psi_i-\psi_{i-2}}{2\Delta x}\right)^2\right], \quad \text{(C.4)}$$

$$\dot{H} = \nu_{N_x+1}, \quad \text{(C.5)}$$

and

$$\dot{Q} = \frac{2}{\epsilon^2\mathrm{Re}}\sum_j \frac{\mathrm{Da}_j}{\mathrm{Sc}}\left(\nu_{j,\mathrm{SiO}} + \nu_{j,\mathrm{CO}}\right)\mathcal{R}_j\left(T_{N_x+1}, Y_{N_x+1}\right), \quad \text{(C.6)}$$

where

$$\psi_{i+1/2} = \frac{\psi_{i+1}+\psi_i}{2}, \quad T_{i+1/2} = \frac{T_{i+1}+T_i}{2}, \quad Y_{i+1/2} = \frac{Y_{i+1}+Y_i}{2}, \quad \text{(C.7)}$$

$$\mu_i = \mu\left(T_i\right), \quad k_i = k\left(T_i\right), \quad \mathcal{D}_i = \mathcal{D}\left(T_i\right), \quad \text{(C.8)}$$

$$\mu_{i+1/2} = \mu\left(T_{i+1/2}\right), \quad k_{i+1/2} = k\left(T_{i+1/2}\right), \quad \mathcal{D}_{i+1/2} = \mathcal{D}\left(T_{i+1/2}\right), \quad \text{(C.9)}$$

$$\chi_{i+1/2} = k_{i+1/2}\left(\frac{T_{i+1}-T_i}{\Delta x}\right), \quad \omega_{i+1/2} = \frac{\mathcal{D}_{i+1/2}}{T_{i+1/2}}\left(\frac{Y_{i+1}-Y_i}{\Delta x}\right), \quad \text{(C.10)}$$

$$\alpha_i = \frac{\psi_{i+1/2}-\psi_{i-1/2}}{\Delta x}T_i, \quad \nu_i = \mu_i\left(\frac{\left(\frac{\psi_{i+1}-\psi_i}{\Delta x}T_{i+1/2} - \frac{\psi_i-\psi_{i-1}}{\Delta x}T_{i-1/2}\right)}{\Delta x}\right). \quad \text{(C.11)}$$

The nonlinear terms in (C.1)–(C.11) have been approximated by repeatedly applying second-order accurate central finite differences of width Δx to each first-order derivative operator, introducing terms that are evaluated at the midpoints of the mesh. We use the arithmetic mean to calculate the values of $\psi_{i+1/2}$, $T_{i+1/2}$, and $Y_{i+1/2}$ at these midpoints, while for $\mu_{i+1/2}$, $k_{i+1/2}$, and $\mathcal{D}_{i+1/2}$, we evaluate the functions forms of μ, k, and $\mathcal{D}$ at $T_{i+1/2}$, as testing revealed this to improve accuracy, compared to using the mean of their values at meshpoints, without greatly increasing the run-time.

The boundary conditions at $x = 0$ and $x = 1$, (4.33b) and (4.33c), become

$$\psi_0 = 0, \quad \frac{\psi_1 - 2\psi_0 + \psi_{-1}}{(\Delta x)^2} = 0, \quad \frac{T_1 - T_{-1}}{2\Delta x} = 0, \quad \frac{Y_1 - Y_{-1}}{2\Delta x} = 0, \tag{C.12a}$$

$$\psi_{N_x+1} = \frac{Q}{2}, \quad \frac{\psi_{N_x+2} - \psi_{N_x}}{2\Delta x} = 0, \quad T_{N_x+1} = T_{\mathrm{s}}, \tag{C.12b}$$

$$\frac{\mathcal{D}_{N_x+1}}{T_{N_x+1}} \frac{Y_{N_x+2} - Y_{N_x}}{2\Delta x} = -\sum_j \mathrm{Da}_j \left(\left(Y_{N_x+1} - 1 \right) \nu_{\mathrm{SiO},j} + Y_{N_x+1} \nu_{\mathrm{CO},j} \right) \mathcal{R}_j \left(T_{N_x+1}, Y_{N_x+1} \right). \tag{C.12c}$$

When solving a problem with a given solid temperature, (C.1)–(C.12) form a system of equations that can be solved via a shooting method for Q_{crat}, as described in Section 3.2.3. If T_{s} is unknown, then they must be coupled to the equations given in Section C.1.2.

For a given value of Q_{crat}, we solve (C.1)–(C.12), along with the data at $z = 0$, using MATLAB's inbuilt DAE solver ode15s using adaptive time-stepping in the z direction, giving the solution on a mesh $0 = z_0 < z_1 < \cdots < z_{N_z} = 1$. To improve the efficiency of the code, we use complex step differentiation to compute the Jacobian to machine precision using the PMAD package described in [71].

Letting $\psi_i^n = \psi\left(x_i, z_n\right)$, and similarly for T and Y, we can determine the corresponding values of ρ, u and w by using the expressions

$$\rho_i^n = \frac{1}{T_i^n}, \quad u_i^n = -T_i^n \dot{\psi}_i^n, \quad w_i^n = T_i^n \left(\frac{\psi_{i+1}^n - \psi_{i-1}^n}{2\Delta x} \right), \tag{C.13}$$

derived from (3.8e) and (3.12).

C.1.2 Solid

The transformed problem in Ω_{s}, (4.34)–(4.35) depends only on z, so there is no need to extend the x-mesh into Ω_{s}. Hence, using second-order central differences to

approximate the terms in the gas phase, (4.34)–(4.35) becomes

$$q = k_{\mathrm{s}}\dot{T}_{\mathrm{s}}, \tag{C.14}$$

and

$$0 = \frac{\mathrm{Pe}_{\mathrm{s}}}{k_{\mathrm{s}}}q + \dot{q} + \sum_j \frac{\mathrm{Da}_j\eta_j\mathrm{Pr}}{\mathrm{Sc}A_\epsilon|\mathcal{C}_{\mathrm{s}}|}\mathcal{R}_j\left(T_{N_x+1}, Y_{N_x+1}\right) - \frac{1}{A_\epsilon|\mathcal{C}_{\mathrm{s}}|}\left(\epsilon^2\mathrm{RePr}\dot{\psi}_{N_x+1}T_{N_x+1} + k_{N_x+1}\frac{T_{N_x+2}-T_{N_x}}{2\Delta x}\right). \tag{C.15}$$

C.1.3 Initial conditions

To solve the problem (C.1)–(C.15), obtained by the method of lines, we must also specify conditions at $z = 0$. Applying our discretisation to (4.33a) and (4.36a), we obtain

$$\dot{\psi}_i = 0, \quad T_i = 1, \quad Y_i = Y_{\mathrm{crat}} \quad p = 0, \quad T_{\mathrm{s}} = 1, \quad q = q_{\mathrm{crat}}, \tag{C.16}$$

at $z = 0$, for $i = 1, 2, \ldots, N_x$. However, as (C.1)–(C.12) form a set of DAEs, it is necessary supply the value and derivative (usually called initial slope) of every variable at $z = 0$, such that (C.1)–(C.12) are satisfied. We obtain that by solving the BVP (3.17)–(3.18) using one of the methods described in the main text.

C.2 Validation

To validate the implementation of the numerical scheme described above, we solve cases I and II of the single-phase model, and the coupled gas-solid model when $N_x = 2^m$ for different integer values of m. To allow for comparisons between different solutions, we interpolate the solution onto a fixed z mesh of size $N_z = 2^m$, with the same accuracy as the solution on the adaptive mesh used by ode15s. Then, letting $\tilde{T}_i^n$ denote the solution on the finest mesh, where $m = M$, we define the relative error of temperature on the size 2^m mesh as

$$\mathrm{error}_{\mathrm{Mesh}}(T) = \max_{i,n=0,1,\ldots,2^m}\left\{\frac{\left|T_i^n - \tilde{T}^{2^{(M-m)}n}_{2^{(M-m)}i}\right|}{\left|\tilde{T}^{2^{(M-m)}n}_{2^{(M-m)}i}\right|}\right\}, \tag{C.17}$$

and similarly for the other variables. In Figure C.1 we then plot this relative error as a function of N_x, for the representative parameter values $\epsilon^2\mathrm{Re} = 10$, $\Delta T = 0.5$, taking $\Delta p = 1/26$ when solving case I, and $\mathrm{Da}_i = 0.1$, $F_i(T) = 1$, for $i = 1, 2$ when solving the coupled gas-solid problem. The tolerance used by ode15s, fzero, and fsolve is held

fixed at 10×10^{-6}. We see the expected second-order convergence for solutions to case I and II, until the error size reaches 10×10^{-6}. For the coupled model again see the expected second-order converge, but only until the error size reaches 10×10^{-3}. This is because the coupled model has a greater number of shooting parameters to determine, and therefore additional errors can occur when the values of both Q_{crat} and q_{crat} differ between values of N_x. To show this more clearly, in Figure C.1 we also plot the relative error as the solver tolerances vary, defined by

$$\text{error}_{\text{Tol}}(T) = \max_{i,n=0,1,\ldots,2^M} \left\{ \frac{\left| T_i^n - \tilde{T}_i^n \right|}{\left| \tilde{T}_i^n \right|} \right\}, \tag{C.18}$$

where $\tilde{T}_i^n$ is the solution with the smallest tolerance, and the mesh size is fixed as $N_x = 2^M$. We see the expected first order converge for all three models, but the coupled model requires a much smaller tolerance to begin converging at that rate.

From these results we see that the error is reducing at the expected rates for all solution components, suggesting the numerical scheme has been implemented correctly, and the choice of $N_x = 2000$, with a tolerance of 10×10^{-6} will give an error of at most 1×10^{-4} in any solution component.

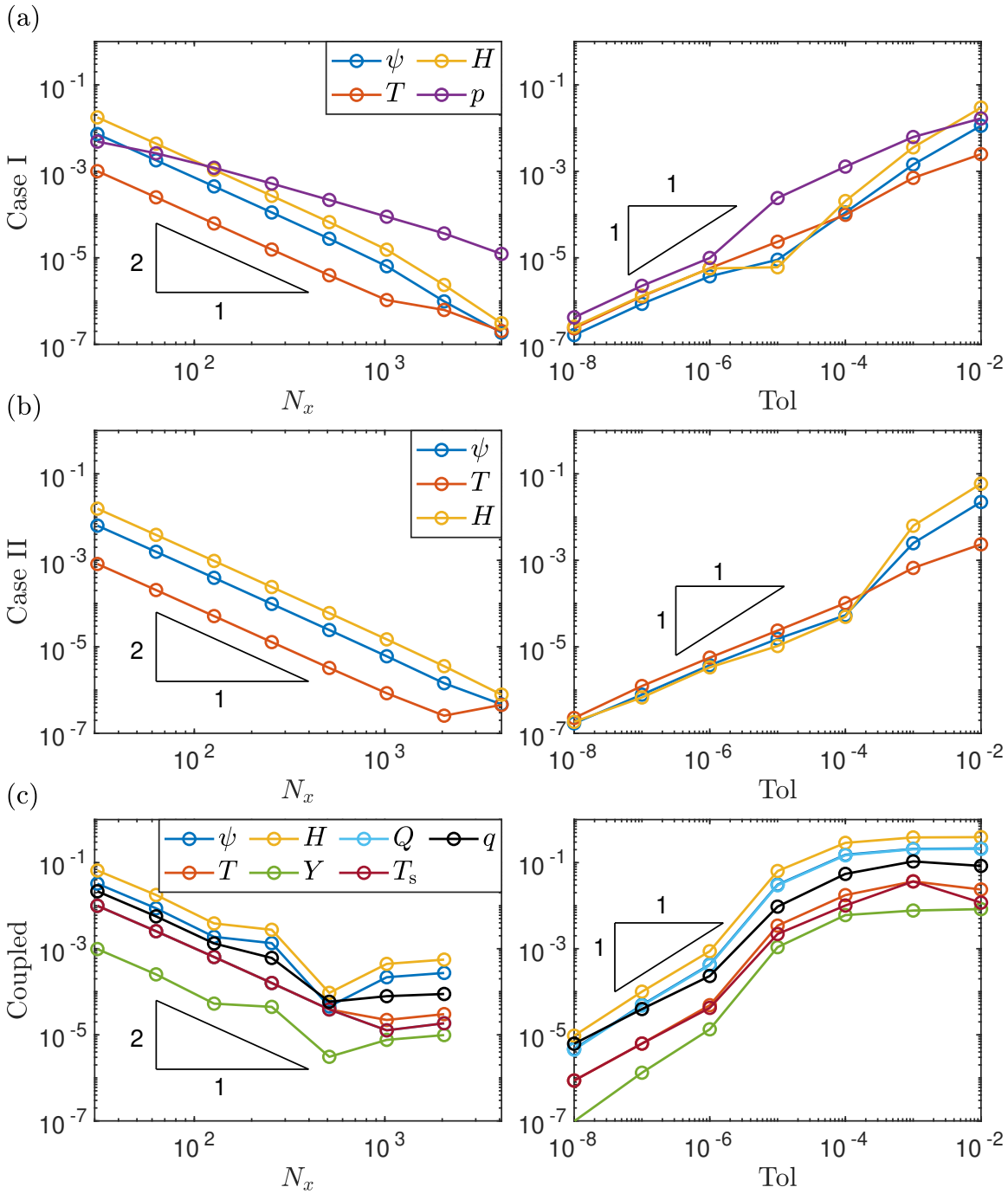


Figure C.1: The relative error for each solution component, as a function of N_x when the tolerance of solvers is 1×10^{-6}, and as a function of solver when $N_x = 2048$. The problem solved is (a) Case I of the single-phase model; (b) Case II of the single-phase model; (c) Coupled gas-solid model with $\mathrm{Da}_1 = \mathrm{Da}_2 = 0.1$, $\mathrm{Pe}_s = 257$, and $A_\epsilon = 0.02$.

Appendix D

Special case of slow reaction asymptotic analysis

We will consider a special case of (5.33)–(5.36) where an analytic solution is possible. We assume that only a single reaction occurs, allowing the subscripts on F, a, b, and c to be dropped, and take

$$F(T^{(0)}) = T^{(0)}, \quad b = 0. \tag{D.1}$$

This latter assumption is appropriate to model reaction 1 in (1.2).

Using (D.1), equations (5.33b)–(5.33c) decouple from $T^{(0)}$, and so using the boundary conditions (5.36a) we find that

$$Q^{(0)} = Q^{(0)}_{\text{crat}}, \tag{D.2}$$

$$Q^{(0)}_{\text{SiO}} = Y_{\text{crat}} Q^{(0)}_{\text{crat}} e^{cz/Q^{(0)}_{\text{crat}}}, \tag{D.3}$$

where the unknown constant $Q^{(0)}_{\text{crat}}$ is the leading-order total mass flux of gas from the crater. This means that (5.33a) reduces to a second-order linear differential equation with constant coefficients and an exponential forcing term. Assuming resonance does not occur, i.e.

$$\text{Pe}_{\text{s}}\beta \neq \frac{c}{Q^{(0)}_{\text{crat}}}, \tag{D.4}$$

then, using the boundary conditions (5.36), we can write the solution as

$$T^{(0)} = 1 - \left(1 - T_{\text{surf}} - \widetilde{C}\left(1 - e^{c/Q^{(0)}_{\text{crat}}}\right)\right)\frac{1 - e^{\text{Pe}_{\text{s}}\beta z}}{1 - e^{\text{Pe}_{\text{s}}\beta}} - \widetilde{C}\left(1 - e^{cz/Q^{(0)}_{\text{crat}}}\right), \tag{D.5}$$

where

$$\widetilde{C} = \frac{a\text{Pe}_{\text{s}} Y_{\text{crat}}\left(Q^{(0)}_{\text{crat}}\right)^2}{c\text{Pe}_{\text{s}}\beta Q^{(0)}_{\text{crat}} - c^2}, \tag{D.6}$$

is a constant (dependent on $Q^{(0)}_{\text{crat}}$). We can then integrate (5.33d) and use the boundary condition at $z = 0$, (5.36a), to find the pressure

$$p^{(0)} = -\frac{8Q_{\text{crat}}}{\pi}\left(\left(1 - \frac{1 - T_{\text{surf}} - \widetilde{C}\left(1 - e^{c/Q^{(0)}_{\text{crat}}}\right)}{1 - e^{\text{Pe}_{\text{s}}\beta}} - \widetilde{C}\right) z \right.$$
$$\left. - \frac{1 - T_{\text{surf}} - \widetilde{C}\left(1 - e^{c/Q^{(0)}_{\text{crat}}}\right)}{\text{Pe}_{\text{s}}\beta}\frac{1 - e^{\text{Pe}_{\text{s}}\beta z}}{1 - e^{\text{Pe}_{\text{s}}\beta}} - \frac{\widetilde{C}Q^{(0)}_{\text{crat}}}{c}\left(1 - e^{cz/Q^{(0)}_{\text{crat}}}\right)\right) \quad \text{(D.7)}$$

Finally, by evaluating $p^{(0)}$ at $z = 1$ and applying the boundary condition (5.36b), we obtain an algebraic equation, $\widetilde{G}\left(Q^{(0)}_{\text{crat}}\right) = 0$, to determine $Q^{(0)}_{\text{crat}}$, where

$$\widetilde{G}\left(Q^{(0)}_{\text{crat}}\right) = \frac{8Q^{(0)}_{\text{crat}}}{\pi}\left(1 - \frac{1 - T_{\text{surf}} - \widetilde{C}\left(1 - e^{c/Q^{(0)}_{\text{crat}}}\right)}{1 - e^{\text{Pe}_{\text{s}}\beta}} - \widetilde{C}\right.$$
$$\left. - \frac{1 - T_{\text{surf}} - \widetilde{C}\left(1 - e^{c/Q^{(0)}_{\text{crat}}}\right)}{\text{Pe}_{\text{s}}\beta} - \frac{\widetilde{C}Q^{(0)}_{\text{crat}}}{c}\left(1 - e^{c/Q^{(0)}_{\text{crat}}}\right)\right) - 1. \quad \text{(D.8)}$$

We can solve $\widetilde{G}\left(Q^{(0)}_{\text{crat}}\right) = 0$ numerically using an identical method as used for $G(\beta) = 0$ in Section 5.2.2. It is easy to check *a posteriori* that the no resonance condition (D.4) is satisfied.

If the assumption that $b = 0$ is removed from (D.1), then it is still possible to solve (5.33b)–(5.33c) for $Q^{(0)}$ and $Q^{(0)}_{\text{SiO}}$ using Lambert-W functions, but (5.33a) no longer has constant coefficients, so cannot readily be solved analytically.

In Figure D.1a we plot the both the analytical solution (D.2), (D.3), (D.5), and (D.7) obtained by numerically solving $\widetilde{G}\left(Q^{(0)}_{\text{crat}}\right) = 0$ along with the solution obtained by numerically solving (5.33)–(5.36) using the method described in Section 5.2.3 with tolerances of 1×10^{-6}. There is excellent agreement between the two methods, in particular from Figure D.1b where we display the absolute value of the difference between the two solutions, which is always far below 1×10^{-6}. This provides evidence that our numerical solver for the general problem has been correctly implemented.

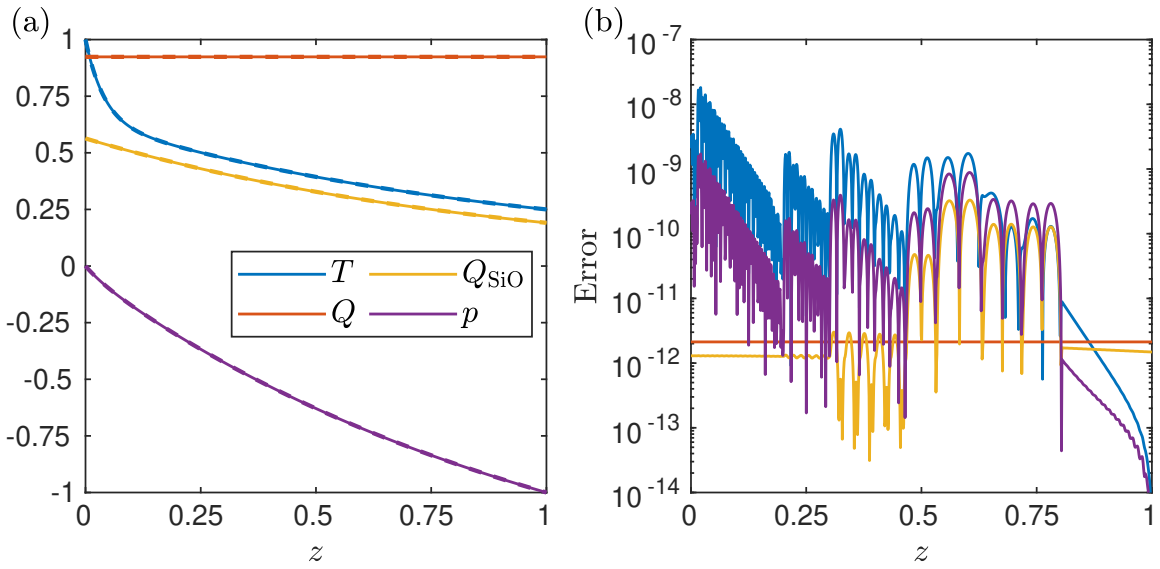


Figure D.1: (a) The analytic solution of (5.33b)–(5.33c) when $F(T) = T$ and $b = 0$ shown as a solid line, and the numerical solution using MATLAB's bvp5c shown by dashed lines. The other parameter values are $T_{\text{surf}} = 0.25$, $\text{Pe}_{\text{s}} = 25$, $C_\Lambda = 1$, $\text{Pr}_{\text{g}} = 0.991$, $\Gamma = 1$, $|\mathcal{C}_{\text{s}}| = 16 - \pi$, $Y_{\text{crat}} = 0.61$, $a = 1$, $c = -1$. (b) The error between the numerical and analytic solutions given in (a).

Bibliography

[1] J. C. Adams and J. C. Williams. Viscous compressible laminar flow in slender axisymmetric channels with adiabatic walls. *Appl. Sci. Res.*, 21(1):113–137, 1969.

[2] B. Andresen. *Process model for carbothermic production of silicon metal*. PhD thesis, NTNU, Norway, 1995.

[3] S. Bennett, P. Asinari, and P. J. Dellar. A lattice Boltzmann model for diffusion of binary gas mixtures that includes diffusion slip. *Int. J. Numer. Meth. Fl.*, 69(1):171–189, 2012.

[4] H. R. Van den Berg, C. A. Ten Seldam, and P. S. Van der Gulik. Compressible laminar flow in a capillary. *J. Fluid Mech.*, 246:1–20, 1993.

[5] H. R. Van den Berg, C. A. Ten Seldam, and P. S. Van der Gulik. Thermal effects in compressible viscous flow in a capillary. *Int. J. Thermophys.*, 14(4):865–892, 1993.

[6] R. B. Bird, W. E. Stewart, and E. N. Lightfoot. *Transport phenomena*. Wiley, New York ; Chichester, 2nd edition, 2002.

[7] C. J. W. Breward and K. B. Kiradjiev. A simple model for desulphurisation of flue gas using reactive filters. *J. Eng. Math.*, 129(1):1–28, 2021.

[8] A. Broggi. *Condensation of SiO and CO in silicon and ferrosilicon production*. PhD thesis, NTNU, Norway, 2021.

[9] H. Byrne and J. Norbury. Stable solutions for a catalytic converter. *SIAM J. Appl. Math.*, 54(3):789–813, 1994.

[10] H. Byrne and J. Norbury. The effect of solid conversion on travelling combustion waves in porous media. *J. Eng. Math.*, 32(4):321–342, 1997.

[11] S. Chapman and T. G. Cowling. *The mathematical theory of non-uniform gases: an account of the kinetic theory of viscosity, thermal conduction and diffusion in gases*. Cambridge University Press, 3rd edition, 1970.

[12] J. F. Clarke and C. A. Cooper. Some gas flows which obey Charles' law. *J. Fluid Mech.*, 80(3):423–432, 1977.

[13] R. J. Cooper, J. Billingham, and A. C. King. Flow and reaction in solid oxide fuel cells. *J. Fluid Mech.*, 411:233–262, 2000.

[14] J. Crank. *Free and moving boundary problems*. Clarendon Press, 1987.

[15] M. P. Dalwadi, I. M. Griffiths, and M. Bruna. Understanding how porosity gradients can make a better filter using homogenization theory. *P. Roy. Soc. A-Math. Phy.*, 471(2182):20150464, 2015.

[16] Deendarlianto, T. Höhne, D. Lucas, and K. Vierow. Gas–liquid countercurrent two-phase flow in a PWR hot leg: A comprehensive research review. *Nucl. Eng. and Des.*, 243:214–233, 2012.

[17] V. D. Djordjevic and C. Crnojevic. Friction dominated, subsonic compressible flow in channels of slowly varying cross section. *Int. J. Heat Fluid Fl.*, 20(2):166–171, 1999.

[18] A. Ern, V. Giovangigli, and M. D. Smooke. Numerical study of a three-dimensional chemical vapor deposition reactor with detailed chemistry. *J. Comput. Phys.*, 126(1):21–39, 1996.

[19] V. Fitt, J. R. Ockendon, and M. Shillor. Counter-current mass transfer. *Int. J. Heat Mass Tran.*, 28(4):753–759, 1985.

[20] A. C. Fowler and M. Robinson. Counter-current convection in a volcanic conduit. *J. Volcanol. Geoth. Res.*, 356:141–162, 2018.

[21] P. Fullick. *Physics*. Heinemann Educational, 1994.

[22] F. Golfier, M. Quintard, and S. Whitaker. Heat and mass transfer in tubes: An analysis using the method of volume averaging. *J. Porous Media*, 5(3), 2002.

[23] R. González-Fariña. *Modelling the mechanisms of microsilica particle formation and growth*. DPhil thesis, University of Oxford, UK, 2020.

[24] R. González-Fariña, A. Münch, J. M. Oliver, and R. A. Van Gorder. Modeling microsilica particle formation and growth due to the combustion reaction of silicon monoxide with oxygen. *SIAM J. Appl. Math.*, 80(2):1003–1033, 2020.

[25] P. S. Hagan and M. M. KŁosek. Explicit half-range expansions for Sturm–Liouville operators. *Eur. J. Appl. Math.*, 10(5):447–475, 1999.

[26] P. S. Hagan and J. R. Ockendon. Half-range analysis of a counter-current separator. *J. Math. Anal. Appl.*, 160(2):358–378, 1991.

[27] S. A. Halvorsen. A unidimensional dynamic model for the (ferro-) silicon process—a reliable tool for identifying the state of the furnace? In *Proceedings of the Conference Inverse Problems and Optimal Design in Industry*, pages 229–238. Springer, 1994.

[28] T. H. Hannesson. The Si process drawings. Elkem Iceland, 2016.

[29] J. O. Hirschfelder, R. B. Bird, and C. F. Curtiss. *Molecular theory of gases and liquids*. Wiley, New York, 1954.

[30] Internal Elkem data. Private communication, 2022.

[31] S. T. Johansen, H. Tveit, S. Grådahl, A. M. Valderhaug, and J. Byberg. Environmental aspects of ferro-silicon furnace operations-an investigation of waste gas dynamics (revised edition). In *The 8th International Ferroalloys Congress, Peking*, 1998.

[32] K. F. Jusnes. *Phase transformations and thermal degradation in industrial quartz*. PhD thesis, NTNU, Norway, 2020.

[33] M. Kadkhodabeigi. *Modeling of Tapping Processes in Submerged Arc Furnaces*. PhD thesis, NTNU, Norway, 2011.

[34] A. C. King, J. Billingham, and R. J. Cooper. Performance modelling of solid oxide fuel cells. *Combust Theor Model*, 5(4):639, 2001.

[35] R.-J. Koopmans, J. S. Shrimpton, G. T. Roberts, and A. J. Musker. A one-dimensional multicomponent two-fluid model of a reacting packed bed including mass, momentum and energy interphase transfer. *Int. J. Multiphas. Flow*, 57:10–28, 2013.

[36] M. Ksiazek, M. Tangstad, and E. Ringdalen. Five furnaces five different stories. In *Silicon for the Chemical and the Solar Industry XIII. Kristiansand, Norway*, pages 33–42, 2016.

[37] K. J. Kuijlaars, C. R. Kleijn, and H. E. A. van den Akker. Multi-component diffusion phenomena in multiple-wafer chemical vapour deposition reactors. *Chem. Eng. J. Bioch. Eng.*, 57(2):127–136, 1995.

[38] J. Kunze and R. Degel. New trends in submerged arc furnace technology. In *Tenth International Ferroalloys Congress*, volume 1, page 4, 2004.

[39] H. M. Kvamsdal, G. Haugen, and H. F. Svendsen. Flue-gas cooling in post-combustion capture plants. *Chem. Eng. Res. Des.*, 89(9):1544–1552, 2011.

[40] P.-Y. Lagrée. Thermal mixed convection induced locally by a step change in surface temperature in a Poiseuille flow in the framework of triple deck theory. *Int. J. Heat Mass Tran.*, 42(14):2509–2524, 1999.

[41] D. Lasseux, F. J. Valdés-Parada, J.-F. Thovert, and V. Mourzenko. Exuding porous media: deviations from Darcy's law. *J. Fluid Mech.*, 911, 2021.

[42] G. Li, S.-H. Huang, and Z. Li. Gas-phase dynamics in graphene growth by chemical vapour deposition. *Phys. Chem. Chem. Phys.*, 17(35):22832–22836, 2015.

[43] A. Linan. The asymptotic structure of counterflow diffusion flames for large activation energies. *Acta Astronaut.*, 1(7-8):1007–1039, 1974.

[44] J. R. Lister and P. J. Dellar. Solidification of pressure-driven flow in a finite rigid channel with application to volcanic eruptions. *J. Fluid Mech.*, 323:267–283, 1996.

[45] E. K. Luckins. *Mathematical modelling of electrical, thermal, and chemical processes occurring within a silicon furnace*. DPhil thesis, University of Oxford, UK, 2021.

[46] E. K. Luckins, J. M. Oliver, C. P. Please, B. M. Sloman, A. M. Valderhaug, and R. A. Van Gorder. Modelling alternating current effects in a submerged arc furnace. *IMA J. Appl. Math.*, 87(3):492–520, 2022.

[47] E. K. Luckins, J. M. Oliver, C. P. Please, B. M. Sloman, and R. A. Van Gorder. Homogenised model for the electrical current distribution within a submerged arc furnace for silicon production. *Eur. J. Appl. Math.*, 33(5):828–863, 2022.

[48] E. K. Luckins, J. M. Oliver, C. P. Please, B. M. Sloman, and R. A. Van Gorder. Modelling and analysis of an endothermic reacting counter-current flow. *J. Fluid Mech.*, 949:A21, 2022.

[49] J. C. Merchuk, Y. Rosenblat, and I. Berzin. Fluid flow and mass transfer in a counter-current gas–liquid inclined tubes photo-bioreactor. *Chem. Eng. Sci.*, 62(24):7414–7425, 2007.

[50] J. W. Mitchell and G. E. Myers. An analytical model of the counter-current heat exchange phenomena. *Biophys. J.*, 8(8):897–911, 1968.

[51] J. J. Moré. The levenberg-marquardt algorithm: implementation and theory. In *Numerical analysis*, pages 105–116. Springer, 1978.

[52] T. G. Myers, F. Font, and M. G. Hennessy. Mathematical modelling of carbon capture in a packed column by adsorption. *Appl. Energ.*, 278:115565, 2020.

[53] W. Nachbar, F. Williams, and S. S. Penner. The conservation equations for independent coexistent continua and for multicomponent reacting gas mixtures. *Q. Appl. Math.*, 17(1):43–54, 1959.

[54] M. K. Næss. *Mechanisms and kinetics of liquid silicon oxidation.* PhD thesis, NTNU, Norway, 2013.

[55] D. A. Nield and A. Bejan. *Convection in Porous Media.* Springer, 4th edition, 2013.

[56] H. Ockendon and J. R. Ockendon. Variable-viscosity flows in heated and cooled channels. *J. Fluid Mech.*, 83(1):177–190, 1977.

[57] P P. Fidjestøl and M Dastol. The history of silica fume in concrete- from novelty to key ingredient in high performance concrete. In *Proceedings of the Congresso Brasileiro do Concreto. 4th-9th Sept*, 2008.

[58] M. V. Papalexandris. On the applicability of Stokes' hypothesis to low-Mach-number flows. *Continuum Mech. Therm.*, 32(4):1245–1249, 2020.

[59] J. R. A. Pearson. Variable-viscosity flows in channels with high heat generation. *J. Fluid Mech.*, 83(1):191–206, 1977.

[60] R. Prud'homme. *Flows of reactive fluids*. Springer, 2010.

[61] R. K. Prud'Homme, T. K. Chapman, and J. R. Bowen. Laminar compressible flow in a tube. *Appl. Sci. Res.*, 43(1):67–74, 1986.

[62] E. Ringdalen. Changes in quartz during heating and the possible effects on Si production. *JOM*, 67(2):484–492, 2015.

[63] E. Ringdalen, K. E. Einarsrud, and A. Nordhus. Gas flow and pressure drop in charge material in silicon production. *JOM*, 74(11):3971–3979, 2022.

[64] C. M. Rooney, C. P. Please, and S. D. Howison. Homogenisation applied to thermal radiation in porous media. *Eur. J. Appl. Math.*, 32(5):784–805, 2021.

[65] A. A. Rostami, A. S. Mujumdar, and N. Saniei. Flow and heat transfer for gas flowing in microchannels: a review. *Heat Mass Transfer*, 38:359–367, 2002.

[66] E. Scheepers, Y. Yang, A. T. Adema, R. Boom, and M. A. Reuter. Process modeling and optimization of a submerged arc furnace for phosphorus production. *Metall. Mater. Trans. B*, 41(5):990–1005, 2010.

[67] A. Schei, J. K. Tuset, and H. Tveit. *Production of high silicon alloys*. Tapir, Trondheim, Norway, 1998.

[68] H. Schlichting and K. Gersten. *Boundary-layer theory*. Springer, 8th edition, 2000.

[69] L. W. Schwartz. A perturbation solution for compressible viscous channel flows. *J. Eng. Math.*, 21(1):69–86, 1987.

[70] A. Shajii and J. P. Freidberg. Theory of low mach number compressible flow in a channel. *J. Fluid Mech.*, 313:131–145, 1996.

[71] L. F. Shampine. Accurate numerical derivatives in MATLAB. *ACM T. Math. Software*, 33(4), 2007.

[72] L. F. Shampine, M. W. Reichelt, and J. A. Kierzenka. Solving index-1 DAEs in MATLAB and Simulink. *SIAM Rev.*, 41(3):538–552, 1999.

[73] F. Sharipov and V. Seleznev. Data on internal rarefied gas flows. *J. Phys. Chem. Ref. Data*, 27(3):657–706, 1998.

[74] B. M. Sloman. *Mathematical modelling of silicon furnaces.* DPhil thesis, University of Oxford, UK, 2018.

[75] B. M. Sloman, C. P., Please, and R. A. Van Gorder. Melting and dripping of a heated material with temperature-dependent viscosity in a thin vertical tube. *J. Fluid Mech.*, 905, 2020.

[76] B. M. Sloman, C. P. Please, and R. A. Van Gorder. Asymptotic analysis of a silicon furnace model. *SIAM J. Appl. Math.*, 78(2):1174–1205, 2018.

[77] B. M. Sloman, C. P. Please, and R. A. Van Gorder. Homogenization of a shrinking core model for gas–solid reactions in granular particles. *SIAM J. Appl. Math.*, 79(1):177–206, 2019.

[78] B. M. Sloman, C. P. Please, R. A. Van Gorder, A. M. Valderhaug, R. G. Birkeland, and H. Wegge. A heat and mass transfer model of a silicon pilot furnace. *Metall. Mater. Trans. B*, 48(5):2664–2676, 2017.

[79] Y. Sone. Flows induced by temperature fields in a rarefied gas and their ghost effect on the behavior of a gas in the continuum limit. *Annu. Rev. Fluid Mech.*, 32(1):779–811, 2000.

[80] I. A. Sutherland. Recent progress on the industrial scale-up of counter-current chromatography. *J. Chromatogr. A*, 1151(1-2):6–13, 2007.

[81] S. R. Tieszen. On the fluid mechanics of fires. *Annu. Rev. Fluid Mech.*, 33(1):67–92, 2001.

[82] P. Vadasz. Explicit conditions for local thermal equilibrium in porous media heat conduction. *Transport Porous Med.*, 59(3):341–355, 2005.

[83] D. C. Venerus. Laminar capillary flow of compressible viscous fluids. *J. Fluid Mech.*, 555:59–80, 2006.

[84] D. C. Venerus and D. J. Bugajsky. Compressible laminar flow in a channel. *Phys. Fluids*, 22(4):046101, 2010.

[85] C. G. Wagner and R. Beals. Constructing solutions to two-way diffusion problems. *J. Phys. A-Math. Theor.*, 52(11):115204, 2019.

[86] B. Weigand, J. Braun, S. O. Neumann, and K. J. Rinck. Freezing in forced convection flows inside ducts: A review. *Heat Mass Transfer*, 32(5):341–351, 1997.

[87] S. Whitaker. Transport processes with heterogeneous reaction. In *Concepts and design of chemical reactors*, pages 1–94. Gordon and Breach New York, 1986.

[88] S. Whitaker. Coupled transport in multiphase systems: a theory of drying. In *Advances in Heat Transfer*, volume 31, pages 1–104. Academic press, 1998.

[89] S. Whitaker. Derivation and application of the Stefan-Maxwell equations. *Rev. Mex. Ing. Quim.*, 8(3):213–243, 2009.

[90] S. Whitaker. Making connections at interfaces. *Rev. Mex. Ing. Quim.*, 8(1):1–33, 2009.

[91] F. White. *Viscous fluid flow.* McGraw-Hill, 2nd International edition, 1991.

[92] J. C. Williams. Viscous compressible and incompressible flow in slender channels. *AIAA J.*, 1(1):186–195, 1963.

[93] R. W. Winters and R. E. Davies. The role of countercurrent mechanisms in urine concentration: a review. *Ann. Intern. Med.*, 54(4):810–826, 1961.

[94] Y.-S. Wu, K. Pruess, and P. Persoff. Gas flow in porous media with Klinkenberg effects. *Transport Porous Med.*, 32(1):117–137, 1998.

[95] S. H. Yi, B. R. Cho, and C. H. Rhee. Prediction of channelling caused by breakthrough of cohesive zone in blast furnace. *Ironmak. Steelmak.*, 25(4):303, 1998.

[96] J. B. Young and B. Todd. Modelling of multi-component gas flows in capillaries and porous solids. *Int. J. Heat Mass Tran.*, 48(25-26):5338–5353, 2005.